Numerical N-body approach to binary asteroid formation and evolution

Carlo Comito

Università degli Studi di Torino
Scuola di Dottorato in Scienza ed Alta Tecnologia

Université de Nice - Sophia Antipolis - UFR Sciences
École Doctorale de Sciences Fondamentales et Appliquées

Tesi per ottenere il titolo di / Thèse pour obtenir le titre de

Dottore di ricerca in Scienza e Alta Tecnologia - Fisica e Astrofisica
dell'Università degli Studi di Torino
XXIV ciclo: anni 2009 - 2010 - 2011
e / et
Docteur en Sciences - specialité: Sciences de l'Univers
de l'Université de Nice-Sophia Antipolis
années universitaires 2009/10 - 2010/11 - 2011/12

Numerical N-body approach to binary asteroid formation and evolution

Carlo COMITO

diretta da / dirigée par :	**Alberto CELLINO**	**Eric BOIS**
		Paolo TANGA
discussa a / soutenue à :	TORINO	
il / le :	3 aprile 2012 / 3 avril 2012	

Controrelatore:	Adriano CAMPO BAGATIN	*profesor titular*
Rapporteurs:	Daniel HESTROFFER	*astronome*
	Paolo PAOLICCHI	*professore associato*

Commissione / Jury:

Paolo PAOLICCHI	*professore associato*	Presidente / Président
Alberto CELLINO	*primo ricercatore*	Relatore / Directeur
Marc FOUCHARD	*maître de conferences*	Esaminatore / Examinateur
Paolo TANGA	*astronome adjoint*	co-Relatore / co-Directeur

Università degli Studi di Torino
Scuola di Dottorato in Scienza ed Alta Tecnologia

Indirizzo di Fisica ed Astrofisica

Université de Nice - Sophia Antipolis - UFR Sciences
École Doctorale de Sciences Fondamentales et Appliquées

Specialité de Sciences de l'Univers

Numerical N-body approach to binary asteroid formation and evolution

Carlo Comito

Tutor: Silvano Massaglia

Relatori: Alberto Cellino
Eric Bois
Paolo Tanga

Riconoscimento

La co-tutela del dottorato nel corso del quale questa tesi è stata originata è stata in parte finanziata dalla borsa di mobilità del *Progetto Vinci* dell'Università Italo-Francese

Contents

Introduction

Despite extensive observational and theoretical studies from the ground and from space, the intimate nature of the minor bodies of the Solar System remains essentially unknown.

In particular the asteroids, in the commonly accepted scenario, suffered an intense collisional life, as a result of the dynamical processes that shaped our planetary system. It is commonly accepted that catastrophic processes, such as disruption and gravitational reaccumulation, deeply modified their structure, creating highly fragmented bodies.

At least a fraction of them would have a very low internal cohesion, resulting in objects that are essentially kept together by gravity. The internal properties of these "gravitational aggregates" remain however poorly known, as most observational constraints are related to the surface properties of asteroids.

Binary asteroids are a peculiar case of primary importance for understanding the physics and the evolution of such objects, since their observations more easily convey useful data on their internal structure.

In fact, first of all, they can provide fairly accurate estimates of their total masses, from the characteristics of the mutual orbit. Binary asteroids lightcurves provide a direct measure on the sizes of the components and their orbits, even for objects not spatially resolved. A precious knowledge of the density can thus be obtained.

Rotation states and shapes can also be more easily determined, permitting useful estimates about the internal stresses and more accurate geo-morphological models in microgravity conditions.

The existence of binaries themselves, and the variety thereof, is directly linked to main processes that have sculpted the asteroid belt. Any determination of their physical properties is thus seminal to our understanding of both their formation, and the global picture of the asteroids' evolution.

Many possible mechanisms have been proposed for the origin of asteroid binaries: from tidal encounters, to energetic cratering impacts driving mass into orbit; from direct binary re-accumulation after a catastrophic collision to fission by angular momentum increase. All of them, and their domain of applicability, are currently under test both by observations and by theoretical modeling.

The aim of this work is to explore the behavior of spinning gravitational aggregates,

when they are close to their upper angular momentum limit before mass shedding. Further spin-up provides insights on the splitting processes, closely related to the formation of asteroid satellites.

We model asteroids numerically, by a specialized N-body code, as "perfect rubble-piles": aggregates of mono-dispersed rigid spheres subject to their mutual gravity and inelastic collisions. In search for the instabilities possibly leading to a binary, we increase their rotation rate to a threshold where major instabilities set in, and explore the resulting reshaping and formation of satellites.

We also tentatively study the question of the long-term orbital stability of the systems obtained and discuss the current limitations of our approach.

Eventually, the results are examined in a wider context, by comparison to other theoretical or numerical studies, and to observations.

This Thesis is structured as follows:

In Chapter 1 we briefly outline the techniques for the observation of binary asteroids and give an overview on their current inventory. We also briefly review the current understanding of the processes leading to the formation of satellites.

In Chapter 2 we present models for approaching the study of the equilibrium shapes for gravitational aggregates.

In Chapter 3 we present the numerical approach we use for our study, its limitations and properties, mainly based upon the experience built during the doctorate work; previous related results that we obtained are also briefly recalled.

In Chapter 4 we study the possibility of forming binary asteroids starting from bodies that have accumulated an excess of angular momentum beyond the fissioning limit.

In Chapter 5 we use a gradual spin-up for simulating the application of a slow-acting perturbing force to an otherwise stable body, for exploring the splitting as a function of complex initial conditions.

Chapter 1

The observation of asteroids

1.1 The minor bodies within the Solar System

The number of the minor Solar System bodies whose orbit has been computed ranges in the hundreds of thousands[1]. According to their orbital parameters, they are grouped in a few classes, the more important of which being:

Near-Earth Objects (NEOs) (or **Near Earth Asteroids (NEAs)**), a collection of objects whose orbit is near, or crosses, the orbit of the Earth (and of the other inner planets)

Main Belt (MB) , a large toroidal region between ~ 2.06 and 3.28 AU from the Sun, between the orbits of Mars and Jupiter, where most objects internal to Neptune's orbit are located

(Jupiter) Trojans , two groups in 1:1 orbital resonance with Jupiter, roughly dispersed around the leading and trailing points 60° apart from the planet[2]

Trans Neptunian Objects (TNOs) , a vast group with semimajor axes beyond the orbit of the giant planets (a>30AU)

with other minor groupings existing based on orbital characteristics.

The objects orbiting the Sun at or closer than Jupiter's orbit semimajor axis constitute the traditional *asteroid* population, and are mainly rocky objects of densities $\sim 1 \div 3\, g/cm^3$, with lighter and lighter objects as we move away from the Sun.

The TNOs total mass and number is estimated at orders of magnitude larger than MB objects, though only a very limited fraction has been discovered so far, with probably many large (500+km in size) objects yet to be discovered. The discovery of a larger and larger number of them had the International Astronomical Union[3] officially define a "planet" as an object:

[1] cf. http://hamilton.dm.unipi.it/astdys/index.php?pc=1.0.0

[2] the L_4 and L_5 Lagrangian points

[3] XXVI General Assembly, Prague, 24th August 2006;
http://www.iau.org/static/resolutions/Resolution_GA26-5-6.pdf

- orbiting the Sun,
- having sufficient mass for the self-gravitation to overcome rigid body forces, assuming a hydrostatic equilibrium shape,
- having cleared the neighbourhood around its orbit.

The objects not respecting the third criterion are classified as "dwarf planets", which are hydrostatically relaxed objects sharing their orbital space with other similarly-sized (or larger) bodies .

The modern classification of *minor bodies* thus includes the many other irregularly-shaped objects orbiting the Sun at different distances, for which self gravitation must play together with other forces to determine the overall behaviour.

1.1.1 solar system formation

Under the Standard Model of planetary systems formation (cf. [V.S. Safronov, 1969]), while the Sun was forming, part of the original protostellar cloud remained in orbit around it in a disk of gas and dust.

This mass in a relatively short time started to coalesce into larger and larger *planetesimal* bodies by the means of a runaway mechanism, which mutually disturbed their orbits, driving a greater part of the original mass either unto the Sun or into outer space. Eventually, a relatively small number of *proto-planets* emerged, that rapidly swept their orbits gathering almost all remaining matter. The length of the process can be estimated in $\sim 10\,My$ by radionuclides dating ([G.W. Lugmair, A. Shukolyukov, 2001])[4].

The planets, due to the heat gathered by the colliding planetesimal that formed them and to the decay of primitive radionuclides trapped deep inside their surface (McSween et al. in [ASTEROIDS III]), were initially composed of molten rock and metal, that allowed for internal differentiation into metal-rich cores and more rocky mantels. Eventually, the terrestrial planets' outer layer cooled and solidified [5].

It is understood that for the asteroids this process has been partial at best[6].

1.1.2 the asteroids today

The Main Belt is today a depleted zone with a mass $\sim 3.3{\cdot}10^{21}$ kg ($\sim 5.5{\cdot}10^{-4} M_{\oplus}$), and is the remnant of an early stage of Solar System history. The rapid growth of Jupiter

[4] It is possible [K. Tsiganis et al., 2005] for Saturn, Uranus and Neptune to have been formed closer to the Sun than where they orbit today. An outer orbiting belt of planetesimal, that never coalesced into large planets due to the low density of the disk far away from the Sun, could have at first slowly disturbed the giant planets orbits up to a point when mutual resonances eventually drove these into their current orbits, dispersing the greatest part of the planetesimal belt. A part of these objects being pulled towards the Sun, they are considered the impactors responsible for a so-called *Late Heavy Bombardment* ([R. Gomes et al. (2005)]) ($\sim 6 \cdot 10^8$ years into Solar System age) of the inner Solar System objects as recorded by their cratered surfaces.

[5] the giant planets still conserve a thick layer of lighter elements (mainly H and He) from the protoplanetary disk, swept away from the inner system by the solar wind

[6] though still observable in some of the largest ones, either original unshattered bodies (4 Vesta) or the largest members of dynamical families (e.g. 8 Flora)

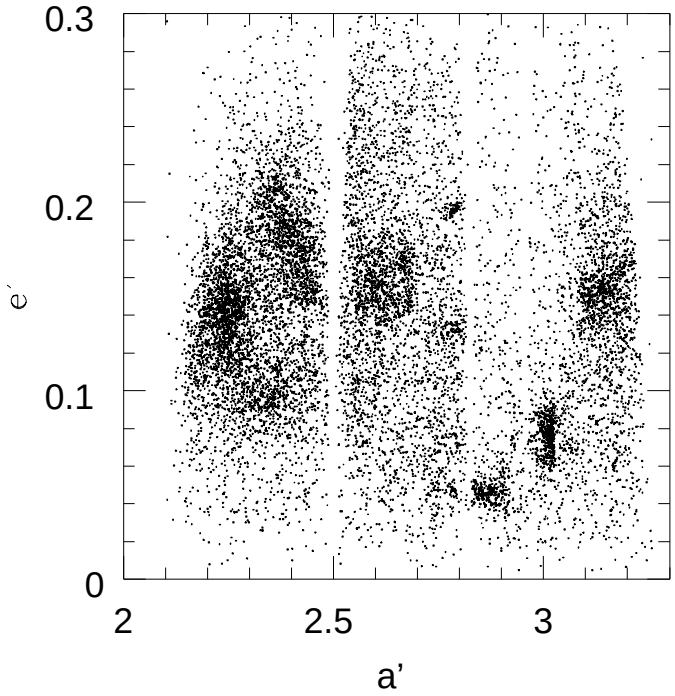

Figure 1.1: Distribution of proper elements for the ∼12,500 asteroids whose orbit was known in 1995: the families can easily be seen. Image by P. Paolicchi

(and secondarily of Mars) has highly destabilised the orbits of the planetesimal of this region, rapidly depopulating the zone and blocking the growth of a major planet.

This influence of the different gravitational perturbers on the survived population induces a slow evolution of the asteroids orbits, with short-period variations of their instantaneous values (the so-called "osculating parameters") around fairly stable averages: such *proper elements* (cf. [A. Milani, Z. Knežević, 1994]) are the parameters considered for e.g. the determination of dynamical families (cf. fig. 1.1). Generally, the orbit of an asteroid is often the first and simplest parameter to find, strictly needed for its subsequent recovery.

The current size distribution of asteroids is compatible at first order with the power law $dn_R/dR \propto R^{\zeta}$ (R. Davis e al. in [ASTEROIDS III]); this has been shown ([J.W. Dohnanyi, 1969]) to be the resulting distribution for a population where the objects periodically collide with projectiles energetic enough to shatter them, with a relaxing time of but a few million years for the estimated density of the Main Belt.

As the asteroids are fragmented, part of the material re-accumulates into a new gravitational aggregate object and part is dispersed. If we examine the proper elements (a' - e') plane for asteroid orbits, the presence of *families* of body with similar orbits can be seen. In many cases, tracing back their history showed them to be compatible with the origin from a single parent body ([P. Michel et al., 2001]). This is also the possible source for many binary asteroids (see § 1.3.2).

While Main Belt objects are today mainly stable, the orbits of those crossing the Earth's are highly unstable. The current NEOs population, because of the frequent close encounters with the inner planets, would be lost in a few million years. A mechanism is thus responsible for continually replenish this class of objects with bodies taken from the Main Belt.

the asteroids as gravitational aggregates

Under the Standard Model for Solar System formation, the history of asteroids is a very collisional one with frequent impacts that can highly fragment them, and the presence of the families witnessing this. Their highly collisional history is a first clue that many asteroids not being simple monolithic objects, but rather gravitational aggregates or *rubble-piles*[7].

Following the current estimates, the average time between catastrophic collisions for the largest bodies in the Solar System is calculated to be of the order of Solar System age, while the smaller bodies may have been shattered multiple times.

Another evidence comes from the distribution of rotation rates (see fig. 1.2). Simple statistics of rotation periods make conspicuous the fact that an intrinsic limit seems to exist on their distribution in the nearby of $T \sim 2.2\,\mathrm{h}$ for asteroid larger than $R \approx 50\,m$.

[P. Pravec, A.W. Harris, 2000] notes that this limit corresponds to a rotation speed near the dispersion limit for (spherical) bodies without internal cohesion, faster ones being won by centrifugal forces. If a substantial part of medium and large asteroids were monolithic, such an abrupt transition would hardly be observed.

Binary asteroids and space probes can give reliable values for the mass and density of a number of asteroids, and large asteroids' masses can be estimated by different means. A comparison with the calculated density of many medium and large asteroids with that of meteorites found on Earth and supposed of being of analogous composition shows us that, excepting the very biggest (Ceres, Palls, Vesta), whose cases must be treated separately, most other cases are examples of either a high fracturing (but still within the limits compatible with a certain global cohesion) or a real global fragmentation, with macroporosities equal to or larger than 30% (cf. fig. 1.3).

Cratering observation on asteroid surfaces is also both an indication of high collisional rate and of the fact that the impacts that would create some of the largest craters (see fig. 1.5) would as well easily shatter them were not they already fragmented with large part of the impact energy dissipated by the low resulting elasticity.

Even the presence of binaries themselves, some of which may have been formed by fission of a fast spinning parent body, also suggest asteroids to be aggregates instead of monoliths.

[7] sometimes these are used interchangeably in literature, while some authors suggest using the first term for asteroids where the main binding force is self-gravity

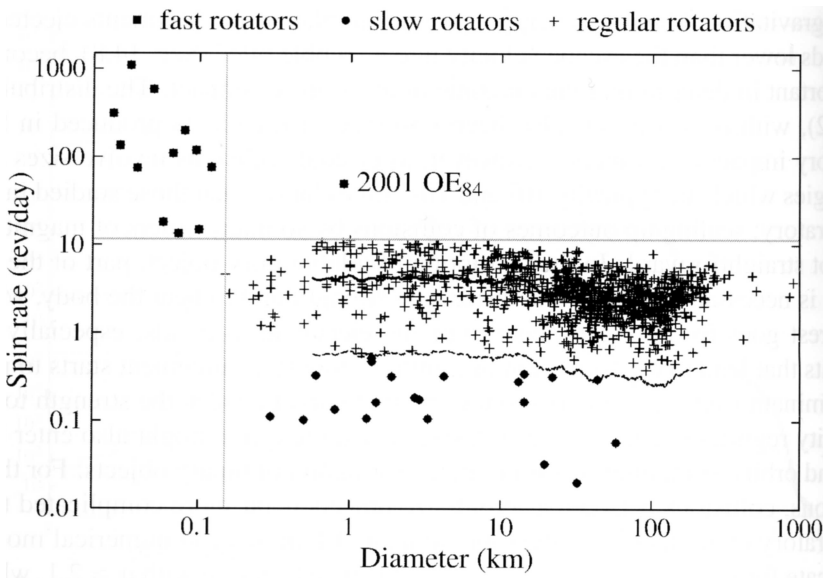

Figure 1.2: Diameter-spin rate relation for a thousand asteroids: the $T \simeq 2.2$ hours limit is apparent for asteroids larger than 150 m. From [Phys.Sol.Sys., p. 402], data from P. Pravec.

1.1.3 why do we study binary asteroids ?

The discovery of binary asteroids in the last 20 years has not been simply the answer to a long sought after question[8].

Asteroids are intrinsically difficult to observe and measure because of their tiny dimension, and binary systems appears a natural solution to many such problems.

The most difficult quantity to measure for asteroids is mass, and for most single asteroids (except some very large ones) only a very rough estimate is known; for binaries, however, the total mass of the system can immediately be computed once the mutual orbit has been determined. The determination of the dimensions also benefits from lightcurves containing features coming from mutual eclipses and occultations of the two components (see § 1.2.1), which can directly give information even on visually unresolved systems. Determination of shapes and rotation states is simplified as well for eclipsing binaries with the information given by mutual shadowing bodies.

This is an important point for all the models about asteroid internal behaviour, which can find a reliable validation test-bed in the binaries.

The study of asteroids, validated by the easily obtainable data for binaries, can improve our understanding of diverse fields among which collisional physics, granular systems, petrography, celestial mechanics, photometry, spectroscopy, astrobiology.

[8][C. André, 1901]

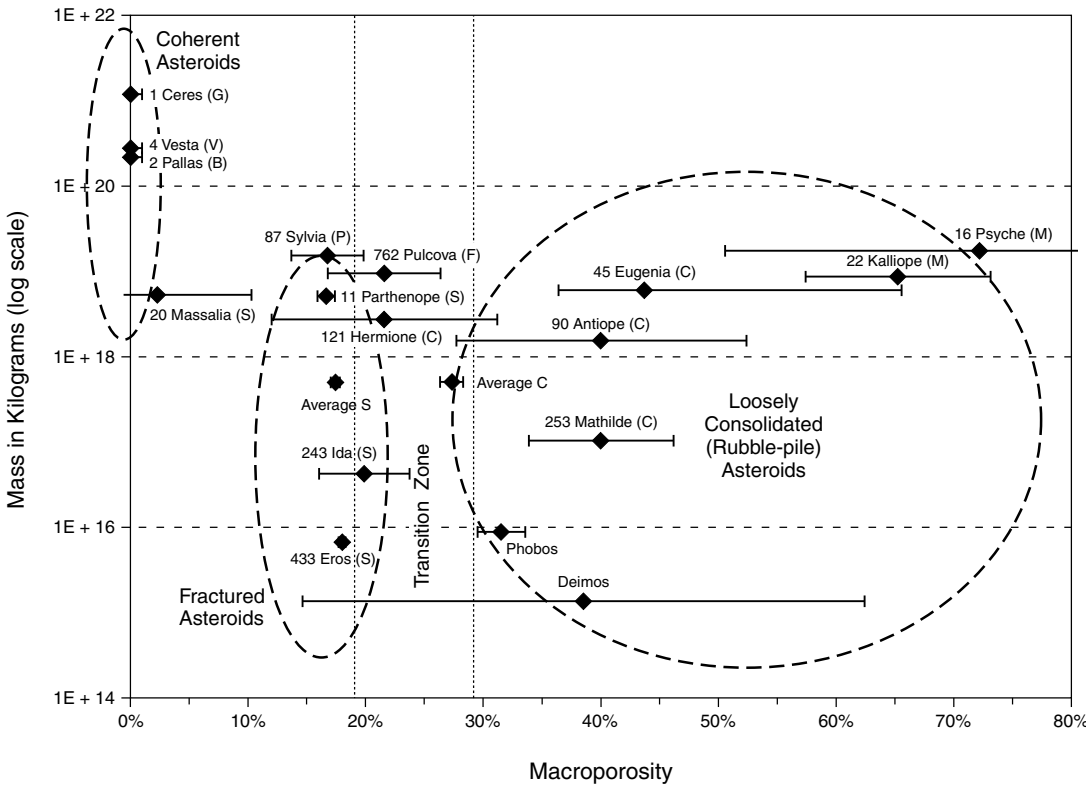

Figure 1.3: macroporosity for some large asteroids and the two martian moons, obtained subtracting from the total porosity, as calculated based upon composition and density, the measured microporosity of analogously composed meteorites. From (D.T. Britt et al., in [ASTEROIDS III])

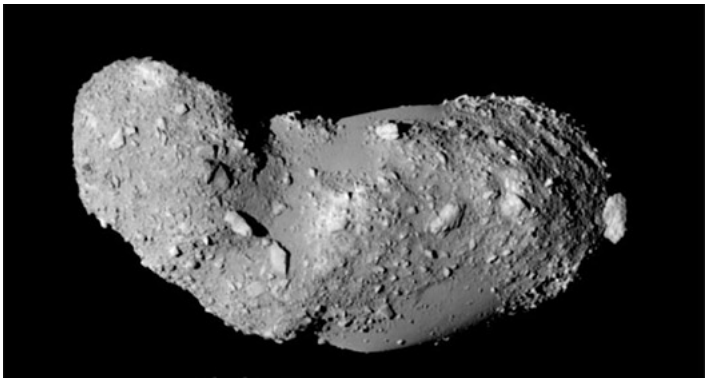

Figure 1.4: The small "contact binary" asteroid 25143 Itokawa, visited in September 2005 by the space probe Hayabusa in the first attempted (and successful) sample return mission. Its two main blocks are $\sim$ 500 and 200 m long. also, pebbles on the surface are visible. Image from JAXA

Figure 1.5: Asteroid 253 Mathilde photographed by NEAR probe on 27 June 1997: the large crater in the foreground suggests that in order to resist the high impact that generated it, the asteroid must consist of highly inelastic material, like multiple fragments kept together by gravity. Image from NASA

1.2 Physical parameters and observation techniques

For convenience, we will call quantities relative to the primary and the secondary with a convenient subscript "1" or "2", indicating the mean radius with R, the mass with M, the density with ρ, the angular velocity with Ω and the rotation period with P.

Contrary to orbit determination, the determination of physical parameters (mass, dimension, shape, rotational state) of the asteroids has always been a problem because of their tiny dimension. In fact, even in the most potent telescopes available up to relatively recent times they appear as point-like, distinguishable from the stellar background only thanks to their rapid angular motion on the celestial sphere.

The detection of binary asteroids poses some additional constraints.

Satellites for an asteroids are to be looked for in the region between the Roche[9] ($\sim$1.5 R_1) and the Hill distance[10] (roughly a hundred primary radii for NEAs to some hundreds for MB asteroids).

[9] where the tidal forces from the primary are greater than the secondary self-gravitation:

$$R_{Roche} \sim \left(\frac{3\rho_1}{\rho_2}\right)^{1/3} R_1 \approx 1.5\, R_1$$

[10] the distance at which the gravitation of the Sun prevails over the primary's in determining the orbit of a test mass, thus being the maximal distance a satellite can reach without being captured in an independent heliocentric orbit:

$$R_{Hill} \simeq \frac{\tilde{a}}{R_\odot} R_1 \sqrt[3]{\frac{\rho_1}{3\rho_{Sun}}} \quad ,$$

$\tilde{a}$ being $a(1-e)$. For comparison Earth's Hill radius is $\approx 215 R_{Earth}$, while for asteroidal systems at comparable distance it would be somewhat less due to both lower density and higher eccentricity

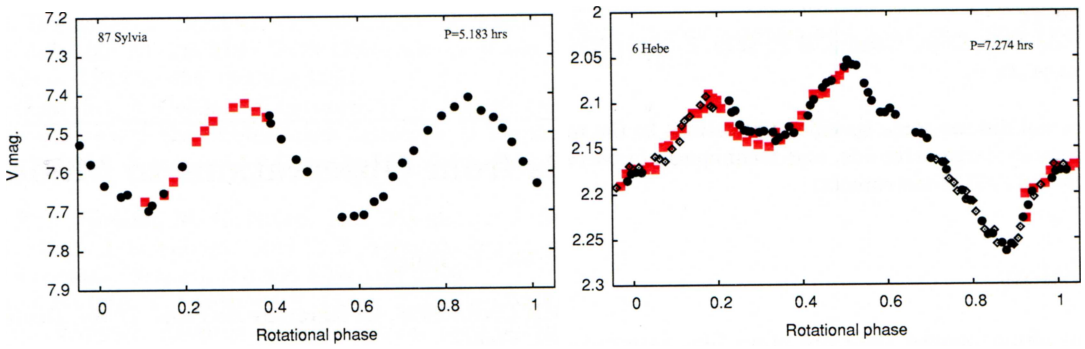

Figure 1.6: light curves of two asteroid from the Asteroid Photometric Catalogue; left: 87 Silvia, observed on 3rd (black circles) and 6th (red squares) of February 1987, data from Weidenshilling e al., 1990; right: 6 Ebe, observed on 18th (red squares), 23rd (black circles) and 27th (hollow squares) of June 1987, data from Hutton & Blain, 1988. from [D. Hestroffer, P. Tanga, 2006]

This is even for MB asteroids a sufficiently large region (up to some arcsec) for a secondary to be found with traditional telescopes; though much smaller distances have been the norm so far, with the separation smaller than atmospheric seeing ($\sim 1''$).

1.2.1 photometry and lightcurves

Visible and near IR photometry allows for important measures on asteroids.

By observing the variation of magnitude over a suitable time interval (hours or days) we can obtain a *lightcurve* for an object (see fig. 1.6), whose temporal variation is interpretable as variation of the surface section directed towards the observer[11].

These curves (generally sinusoidal and periodic), usually allow us to immediately retrieve the rotation period of the object, which is simply the light curve period (two minima and two maxima, usually slightly different).

The curve amplitude also gives an estimation of the object relative dimensions, information to be filtered by keeping in mind the aspect angle between the body rotation axis and the observing direction (supposing an approximately ellipsoidal shape, we can infer the axes ratios).

By knowing the asteroid's spectroscopic class we can also derive an estimate of the asteroid absolute size (and very roughly of mass).

The hypothesis of asteroids having an ellipsoidal shape is less respected for smaller bodies (<∼500m): some of these present irregular light curves, with several maxima and minima (albeit, usually two), in which even non uniform albedo can play a role.

However, at least a good estimate in possible in most cases[12].

[11] supposing a uniform albedo

[12] yet, some bodies can pose problems because of their irregular rotation, like with the Halley comet or the asteroid 4179 Toutatis, whose angular momentum is not aligned along one of main axes of inertia and which presents a classical precession motion; in the case of sufficiently rigid or lowly spinning

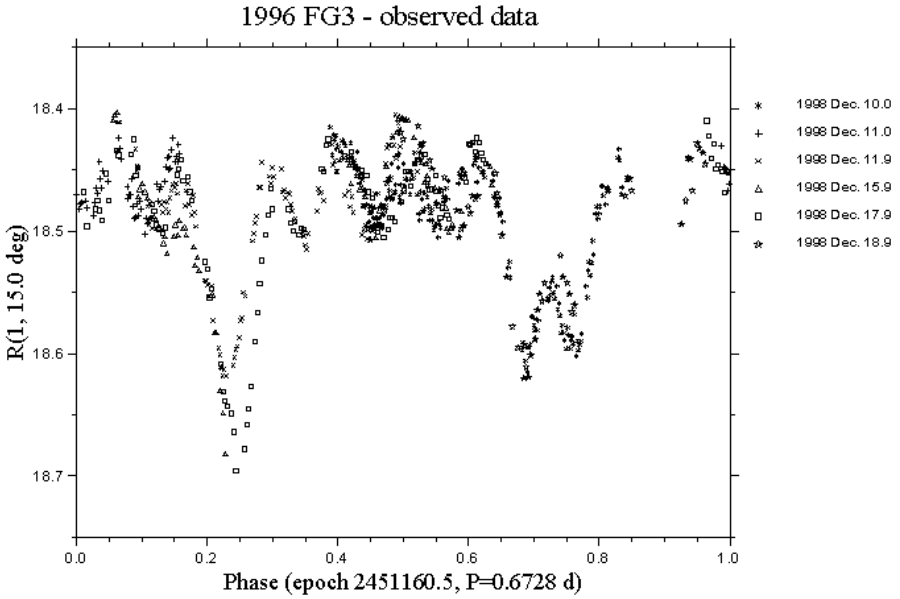

Figure 1.7: light curve of (175706) 1996 FG_3 showing occultation of the primary and eclipsing of the secondary superimposed to the primary rotation rate. from [P. Pravec et al., 2000]

A number of binaries have been discovered by irregularity in the lightcurves. The detection is possible when the primary's rotation is asynchronous and the mutual orbit is favourably oriented as for the secondary to periodically occult the primary and/or be eclipsed by it: this result in a double periodicity where the two frequencies are interpreted as primary's rotation and mutual orbital rates (see fig. 1.7).

Other selection effects include close orbits, for one or several full periods to be observed, and large secondaries ($\sim$ a fifth of primary in length).

1.2.2 direct imaging

Obtaining satisfactory asteroid pictures from Earth to extract data about their size has long been hampered by the small apparent dimensions for most asteroids, inferior to atmospheric seeing ($\sim 1''$).

Resolving binaries poses similar problems: the point-spread function of the primary is usually larger than the typical secondaries distances of observed binary asteroids. Yet, some TNOs have been discovered to be binaries, thanks to their high average separation[13].

Today we can obtain direct images of a number of asteroids, as well as reveal binaries thanks to different techniques, mainly adaptive optics (AO) or space telescopes.

---

bodies, the relaxation time to re-orient their spin along the highest inertia could be of the order of Solar System age, or longer ([D. Hestroffer, P. Tanga, 2006]).

[13] indeed, Pluto was identified as a binary in 1978 before the discovery of the transneptunian object group

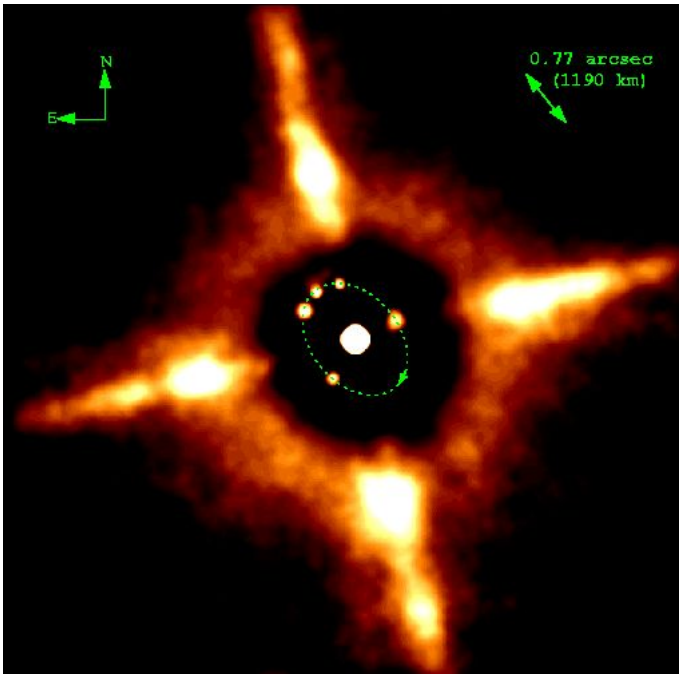

Figure 1.8: Adaptive optic image of MB 45 Eugenia at five different times, showing the motion of its satellite in a circular orbit of radius $\sim 11\,R_1$, taken at the Canada-France-Hawaii Telescope. Primary brightness has been reduced to enhance sharpness; the outer pattern is due to diffraction from the secondary mirror support. image by CFHT.

Adaptive optic substitutes a traditional mirror with a surface formed by many mobile mirrors, which is constantly deformed in real time to counter the microvariations of atmospheric refraction. The best telescopes can theoretically resolve down to 0.05" or less in the H-band (IR); however to calibrate the system they need a reliable point-like source.

For deep astronomy observations this is usually a nearby star. For observing asteroids, which move fast, the background is not usable, and the asteroid itself must be used. This degrades the image somewhat, and the calibration itself is not possible for too faint objects.

Once observations spanning a few orbits have been made, a fairly estimate for the orbit can be extracted using the standard techniques used for binary stars[14].

Visual observation of a binary usually allows for a good determination of the relative size of the two objects.

Two binary MB systems (45 Eugenia in 1998, and the double 90 Antiope in 2000) discovered through adaptive optics are shown in fig. 1.8 and 1.9.

For a handful of asteroids space probes have made close fly-bys, and have taken highly detailed pictures of them (cf. fig. 1.4, 1.5 and 1.10).

Space probes have also been used in the search of binaries: it is to remember how

[14] An indetermination for the direction of the pole may still be present

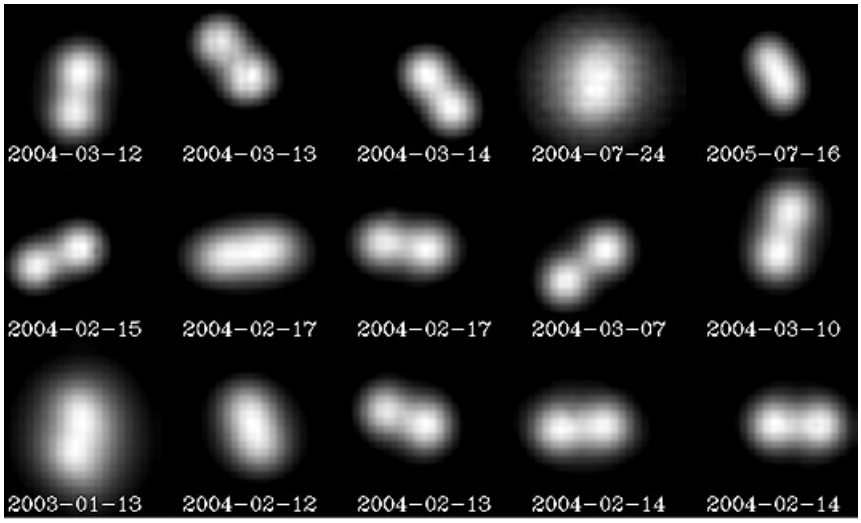

Figure 1.9: Adaptive optic images of MB 90 Antiope, taken at the VLT site. Its double nature is manifest. image by ESO

the first discovered double asteroid, 243 Ida, has revealed (by chance) its nature thanks to a later manual examination of the photographs taken by the Galileo probe in 1993 ([M. Belton, R. Carlson, 1994], see fig. 1.10).

1.2.3 radar astronomy

An independent technique for the determination of size and rotation status of the asteroids is given by radar astronomy.

A series of powerful electromagnetic impulses is sent from Earth towards the object, which reflects and sends them back to the observer. The return signal presents variations in its return time depending on the asteroid shape, and in its frequency by Doppler effect depending on overall velocity and spin of the asteroid. With those informations it is possible to extract its shape and rotational state with a fairly low incertitude.

Because of the huge power necessary to detect the faint return signal (signal intensity of the return beam decreases with the fourth power of the distance), a use of the major terrestrial radar telescopes is necessary, and the only objects suited for this kind of survey are the NEOs.

A number of these revealed their binary structure through the presence of a narrow frequency band superimposed to a broader spectrum: as successive signals showed a periodic oscillation of the narrow band, this can be easily interpreted as the variation in Doppler effect from an orbiting secondary, which can be usually distinctly resolved.

The peculiar shape of 4179 Toutatis has also been revealed by radar (see fig. 1.11).

1.2.4 occultations

A direct measuring method for an asteroid dimension is based on the observation of a *stellar occultation* by the body itself: when it is found passing in front of a star, the

Figure 1.10: image of the asteroid 243 Ida taken from the Galileo probe on 28th August 1993; on the right a small satellite, Dactyl, is clearly visible. image from NASA

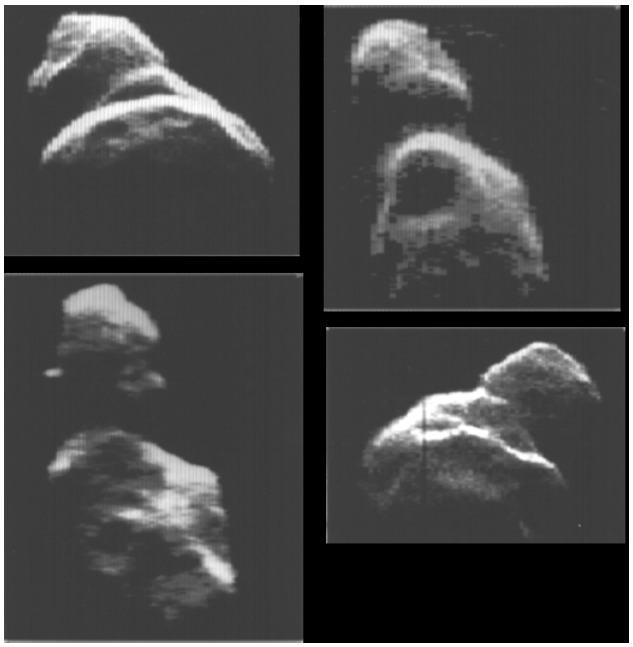

Figure 1.11: radar images of the Mars-crosser asteroid 4179 Toutatis obtained on 8, 9, 10 and 13 December 1992. from NASA

latter is occulted: from the measure of the occultation time it is in principle possible to extract the diameter of the occulting body. In practice, the efficiency of this technique is limited by many factors, like the difficulty of finding a suitable candidate occultation, the planning (several measurements must be made from different points at once), the site availability and the right atmospheric conditions.

Only of a limited number of asteroids, generally the major ones ($30 \div 40$ km of diameter), faithful data are available. Being nonetheless a rather precise, direct method for apparent diameter measure, it is useful as a gauge for photometric methods.

1.2.5 spectroscopy

The main and historically most important method to obtain information on the composition of the asteroids is the one linked to analyses of reflected radiation spectra: by studying the absorption profiles and confronting them with laboratory samples we can infer the (superficial, at least) composition of an observed object.

1.2.6 determination of mass

As mentioned above, the most difficult parameter to determine for an asteroid is its mass.

It can theoretically be computed based on the influence it has over the orbit of a second asteroid that happens to pass nearby, which will be somewhat deviated from its original unperturbed trajectory. In practice, this system meets noteworthy obstacles both in the smallness of the perturbation itself produced by even a medium-large asteroid, which would require very close fly-bys (which are rare) and very precise observations before and after the encounter, and because, even with these most favourable conditions, the perturbation effects from third bodies must be subtracted as much as possible (effects that are larger the longer the arc of the orbit observed, and thus the easier would seem the calculation of the overall perturbation).

The most favourable situation is that of binary asteroids, whose total mass can immediately be extracted from the revolution period and the mutual distance. Knowing additionally the relative sizes of the two objects we can even determine each one's mass, supposing a similar density.

If to a good estimation of the mass we add informations about the absolute size of the body, computation of the density is immediate. Asteroid density is generally low, as discussed before, with most objects being on the ($1 \div 3$ g/cm^3) variation band[15], sensibly less than that of the rocks that appear to form them. This fact is one of the main reasons leading astronomers to believe them being of highly internal porosity, in the most extreme cases even larger than 50% (cf. fig. 1.3).

[15] noteworthy exceptions however exist, especially among the very largest ones like 4 Vesta (the second most massive object of the Main Belt, of which it contains $\sim 8.5\%$ of the total mass): a peculiar object of density $\sim 3.4\, g/cm^3$ with a basaltic surface which would appear to be the only object with a certain internal composition differentiation which has survived almost intact the collisional evolution phase of the Belt, apart from some fragments today comprised almost exclusively in the Vesta family itself

1.3 Inventory of binary asteroids

In the last 20 years the discovery of binaries has been abundant.

Many NEOs are today known to have satellites, with an estimated binary population of $(15 \pm 4)\%$ ([P. Pravec et al., 2006]), compatible with the findings of double craters on Earth ([ASTEROIDS II, S.J. Weidenshilling et al., p.643]). Most systems are much more efficient for NEOs, these being much nearer to Earth than main belt objects. Yet, the nature of their orbits have them often be observable only for defined periods spaced multiple years apart, a problem that does not exist for more distant objects. For NEOs in particular, an abundance of small (sub-km) objects with fast orbiting secondaries can be observed.

Observations in the Main Belt, while not as easy, have nevertheless shown a relative abundance of binaries, among with a population of synchronous ones.

It is also well known for several TNOs to be binary objects (including Pluto itself).

1.3.1 binary asteroid populations

The discovered binaries appear as a diverse set of objects: they widely differ in size, mass ratio, spin rates, density, orbit shape ([P. Descamps, F. Marchis, 2008], [P. Pravec, A.W. Harris, 2007]).A still incomplete classification can though be schematized, with some groups that start appearing from the continually increasing data. See fig. 1.12[16].

large primary, small mass-ratio binaries

This is Pravec and Harris group L[17], concentrated in the Main Belt.

Prominent examples would be 22 Kalliope, 45 Eugenia, 87 Sylvia, 107 Camilla, 121 Hermione.

These are large primaries with R_1 from 45 to 135 km with small satellites (mass ratio $< 1\%$, but mainly $<0.1\%$). The primaries are among the fastest spinning object for their size range (periods in the $4 \div 7$h range). The total $\overline{L}$ is in the $0.25 \div 0.3$ range, and the systems lie in the vicinity of the Maclaurin-Jacobi bifurcation point in the $(\overline{L} - \overline{\Omega}^2)$ plane, justifying their fast rotations (see fig. 1.13 and 2.4). A possible creation scenario ([P. Descamps, F. Marchis, 2008]) involves a mechanism for extracting material from fast spinning large bodies (impacts?) and putting it into orbit forming a small satellite.

asynchronous small binaries

This is Pravec and Harris group A, composed of NEAs, Mars Crossers and small Main Belt asteroids. The primaries are of medium to small size ($R_1 <\sim 5$km) with substantial secondaries (mass ratio in the $1 \div 10\%$ range).

Their angular momentum content $\overline{L}$ is mainly comprised in the $0.3 \div 0.5$ range, which is compatible with a fragmentation from a fast spinning parent body. A candidate for

[16] for considerations about the meaning of the "normalised" angular momentum $\overline{L}$ see § 2.1.4 and eq. 2.31

[17] note that for some authors the "mass ratio" is actually M_1/M_2, while in the present work we use the reciprocal ratio M_2/M_1

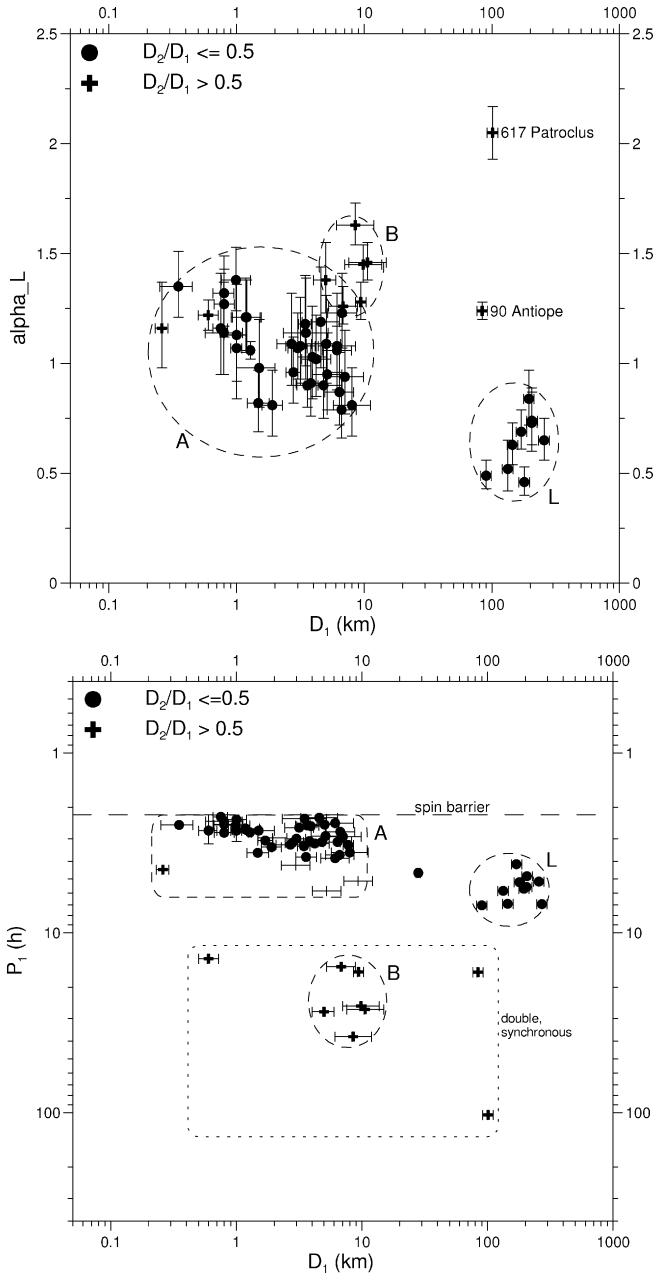

Figure 1.12: Grouping of the best known asteroid binaries according to [P. Pravec, A.W. Harris, 2007] (see § 1.3.1): the plotted quantities are the primary diameter D_1 and rotation period P_1, and the normalised angular momentum "α_L" of the couple which uses a different normalisation factor than the $\overline{L}$ used in the present work ($\overline{L} = 2/5\,\alpha_L$).

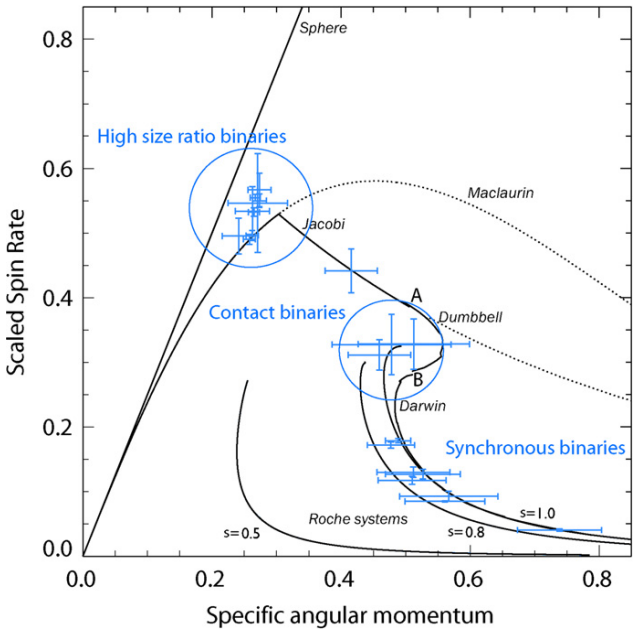

Figure 1.13: The positions of the binary groups in the $(\overline{L} - \overline{\Omega}^2)$ plane, compared with some hydrostatic sequences (see chapter 2 and fig. 2.4 - also note how these are called "high ratio", while the inverse convention on ratio is used in the present thesis). Image from [P. Descamps, F. Marchis, 2008].

spinning the bodies up to their fragmentation limit is thought to be the YORP effect (cf. 1.3.3).

synchronous similar-size small binaries

This is Pravec and Harris group B, composed of mainly Main Belt bodies with large secondaries (mass ratio >0.5) which can be thought of as double bodies.

There certainly is an observational bias against them in the difficulty of detecting this kind of objects from lightcurves analysis (see § 1.2.1). The sizes are on the same range as for the previous group, with a high $\overline{L}$ in the $0.6 \div 0.65$ range. The primary rotation periods are high, compatible with the synchronous state.

It is not clear if these are a tail of the previous population that could have reached synchronicity thanks to their high mass ratio and their location in the main belt (the highly unstable heliocentric orbits that inner planet crossers have may constitute a bias against observing them among the NEAs, as they may lack the time needed to reach a synchronous state).

To note is their location in the $(\overline{L} - \overline{\Omega}^2)$ plane near the region of the "mass ratio = 1.0" binaries from [I. Hacisu, Y. Eriguchi, 1984] (see fig. 2.4 and 2.5).

contact binaries

These are somewhat wanna-be binaries whose two components lie unto each other, touching. Interestingly, their angular momentum and spin locate them in the region of the "Dumbbell sequence" (2.5) in the $(\overline{L} - \overline{\Omega}^2)$ plane.

Of course, these are not true binaries, and their spin rate is not a direct indication for their mass. They are the witness that a gentle encounter has occurred between two asteroids, likely constituting an earlier de-spun couple.

others

Other yet unclassified objects include some wide binaries (with orbital semiaxis $> \sim$ 50 primary radii) as well some objects like two different fairly large (R $\sim$ 42 and 50) double synchronous asteroids: 90 Antiope in the outer Main Belt and the trojan 617 Patroclus.

Antiope's $\overline{L}$ is ~ 0.50 is within the range of the small populations', while Patroclus' high $\overline{L}$ of ~ 0.82 is, as of now, anomalous.

1.3.2 the origin of binaries

Binary objects are observed in all the major population of asteroids (NEOs, Main Belt, Trojans, TNOs), but their diverse nature suggests different kinds of formations as well ([ASTEROIDS III, W.J. Merlin et al., p. 289], [P. Descamps, F. Marchis, 2008], [P. Pravec, A.W. Harris, 2007]).

planetary close encounters

The high percentage of binaries among NEOs is generally considered due to a tidal effect from the inner planets that, in the occasion of maybe multiple close encounters, may have disrupted an initial rubble-pile or fragmented body. As tidal forces and other non-gravitational (e.g. YORP) effects can as easily disrupt an otherwise formed binary, and with the estimated life expectancy for a NEO before being expelled from the inner planets zone measured in some $\sim 10^7 years$ [S.A. Jacobson, D.J. Scheeres, 2011], it looks clear that this must be a dynamical equilibrium situation ([W.F. Bottke, H.J. Melosh, 1996]).

cratering ejecta

High energy impacts cratering an asteroid and releasing material into orbit are also a possible source for binary formation, while some problems remain: for example, on how to put fragments into stable orbits, as a normal elliptical trajectory would have them fall back on the primary in just a half "revolution". Theoretical considerations ([ASTEROIDS II, S.J. Weidenshilling et al., p.643]) about the range of ejecta velocities needed and the subsequent evolution would justify for these binaries a fast (P$<$6 h) rotating primary and a small satellite in a prograde orbit (possibly a gravitational aggregate).

The case of Ida (length $\sim$ 56 km) must be mentioned. By the available images, its cratering ([C.R. Chapman et al., 1996]) would indicate a long age for the primary

(>2 My). The estimated time between impacts that would destroy Ida's moon Dactyl (D$\sim$ 1.4 km) is estimated in ([D.R. Davis et al., 1996]) 240 My at most. This indicates a much younger age for Dactyl, whose likely origin is from re-accumulated ejecta from a large impact on Ida. In fact, it is possible for Dactyl to have been broken several times in the course of its history, its round shape and regolith presence being clues of it being an aggregate.

shattering and re-accumulation

A more extreme case could be of a catastrophic collision directly fissioning the body, and possibly accumulating a sufficient amount of angular momentum for the couple to enter into mutual orbit. The presence of families, witnessing past shattering events, can be a clue for some fragments remaining in orbit after the original creation event rather than being dispersed.

The accumulation of angular momenta of binary asteroids around values corresponding to the critical threshold for centrifugal disruption of a single body ([P.Pravec, A.W. Harris, 2007]) also suggests many of them to have been formed from a breakup of an original body subjected to fragmentation and re-accumulation, a grazing collision accelerating the spin of a body above the threshold and detaching a fragment by centrifugal fission, or, as recently suggested, and explored in the present work (cf. chapter 5), a progressive spinning up due to non-collisional forces that again pushes a parent body beyond the rotationally stable region.

The results we present in chapter 4 may be a step into the understanding of catastrophically originated binaries.

primordial binaries

Binary presence in more distant populations from the Sun (especially TNOs, but also trojans or Main Belt) of binaries whose age is compatible with that of the Solar System also suggests that a fraction of them might well be primordial, i.e. a relic from the early Solar System creation period.

1.3.3 YORP effect and binaries

More recently, YORP has also been suggested as the origin of some binaries.

The YORP (Yarkovsky-O'Keefe-Radzievskii-Paddack) effect is a mechanism that transfers (rotational) angular momentum to a (small) body orbiting the Sun because of anisotropic reflection and/or re-emission of photons by the irregular asteroid surface[18]. This mechanism has been directly measured in 2007 ([S.C. Lowry et al., 2007]) for the asteroid (54509) 2000 PH_5 (a $\sim$ 120 m NEO subsequently renamed "YORP"), with a rapidly changing rotation period whose changing rate is of the order of halving it in $\sim 6 \cdot 10^5$ years, along with erratic axial tilt and precession.

The mechanism is potentially capable of slowly spinning-up a body leading it to mass shedding by centrifugal force.

[18] the YORP effect is a variation of the Yarkovsky effect that exerts a torque on the asteroid varying its orbit, proposed for the first time in 1888, though for different purposes than asteroid studies ([G. Beekman, 2006])

Figure 1.14: a model of the asteroid (66391) 1999 KW_4 as obtained by radar data; the average slope on the surface of the primary is $\sim 28^{\circ}$ ([D.J. Scheeres et al., 2006]). image by NASA

a previous study

In [K.J. Walsh et al., 2008], a study has been performed to show how binaries may have been formed by the action of YORP. In particular, they tried to reproduce the binary asteroid (66391) 1999 KW_4 (see fig. 1.14): a NEA with a fast rotating primary (P$\approx$2.8h) of $R_1 \approx 750m$ and $\rho \approx 2g/cm^3$ and a close orbiting satellite ($a/R_1 \approx 3.9$ in circular orbit around it with a mass ratio of $\approx 5.7\%$).

The primary is peculiar as it presents a characteristic ridge along the equator: due to its fast rotation, a small rock placed on it would be just on the verge of entering orbit, moving with a velocity barely below the escape velocity. The tested hypothesis is that due to its initial shape, an asteroid has been accelerated by YORP effect up to having part of its surface mass migrate towards the equator (at lower potential energy), initially creating the ridge. As this configuration favoured YORP spin-up, the increasing angular momentum pumped on the body would start to gently detach material from the ridge and put it in orbit around the parent body. As more and more material was gathered in orbit, it was possible for it to eventually start to coalesce into a secondary just outside the Roche distance from the primary, the secondary continuing to grow into the mass it has today by intercepting all mass continually being emitted from the primary.

They ran a series of simulations by considering a range of spherical or ellipsoidal starting bodies, to which they applied a slow and steady angular acceleration in the form of small sudden "kicks" spaced by a short period for the body to readjust.

They used both spherical and elongated ellipsoidal shapes (with 2:1:1 axes ratios), with both high ($\phi \approx 40^{\circ}$) and low ($\phi \approx 0^{\circ}$) angle of friction[19] rubble-piles.

What they observed with the high friction structures, contrary to the expectations of classical hydrostatics, is that with the increasing of their angular momentum the elongated bodies start to alter their shape and turn into more spherical ones, essentially by losing particles from the ends which are expelled from the system. As soon as the body assumes a more spherical nature (or if it starts as such), the emitted particles, now coming from all around the equator, start being emitted with negative energy and remaining in orbit. Eventually, they manage to gather into a secondary that monopolise

[19] see § 2.3

the situation englobing most emitted mass from the primary.

In their study, this mechanism is prevented when using low friction structures. Here, acting more like the classical hydrostatic result would dictate, the fast spinning bodies tend to rapidly assume elongated shapes, retaining them during the mass loss process and preventing any secondary to form.

Somewhat middle results are obtained with moderate friction, with the secondary formation being more and more favoured as the angle of friction is increased.

In their study, "no large-scale 'fission' event" occurs.

It is our and others' opinion (cf. [S.A. Jacobson, D.J. Scheeres, 2011]) that this behaviour is not entirely physical. The lifespan of each of the small fragments put in orbit is generally short: under the influence of the primary, their orbits continually change, quickly exploring the whole a-e parameters space and are expelled from the system with a probability very near to 1 (cf. § 1.3.4 below). This happens in a relatively short time compared to the typical timescale of YORP, the mechanism considered responsible for the spin-up, to the point that particles dissipation is faster than their creation. The time the system is left evolving between spin-up kicks is an artificially shortened interval to simply allow the primary to reach gravitational equilibrium, and its length is not calibrated on the speed of the physical spin-up process; to maintain these particles in orbit during the successive spin-ups and eventually allow them to coalesce is thus a contradictory approach (yet, some particles do survive long orbiting very axisymmetric primaries, see § 1.3.4).

[K.A. Holsapple, 2010] also suggests that the (very) finite "resolution" of the body, composed of $\sim$ 1000 particles may play a role in allowing the particles to leave the surface and determining the critical primary spin conditions.

In § 3.1.1 we analyse some of the reasons behind this observed behaviour, and in chapter 5 we present new findings for the possible efficiency of small-scale perturbations that may be induced by YORP.

1.3.4 a NEAs binary asteroid cycle model

Models on the stabilities and evolution of binaries have been produced.

In [S.A. Jacobson, D.J. Scheeres, 2011] the authors show a semi-analytical model that may explain different kinds of binary systems and the possibilities for their evolution in the NEAs region. In fig. 1.15, a summary of their results is shown.

Via the numerical simulation of a large number (some hundreds) of systems, they draw a scenario of how binaries are formed and disrupted among the NEAs.

They assume YORP (see § 1.3.3) as a major driving force, that initially spins up the bodies having just been diverted in the NEAs region from outside. These bodies are mostly gravitational aggregates, and as they reach a limit spin, they fission; the fissioning surface is actually pre-determined by the internal arrangements of the components (taken as free parameters), which determine a correspondent spin limit (see [D.J. Scheeres, 2009 I]).

After the separation, the newly formed binary has exactly the right energy to put the

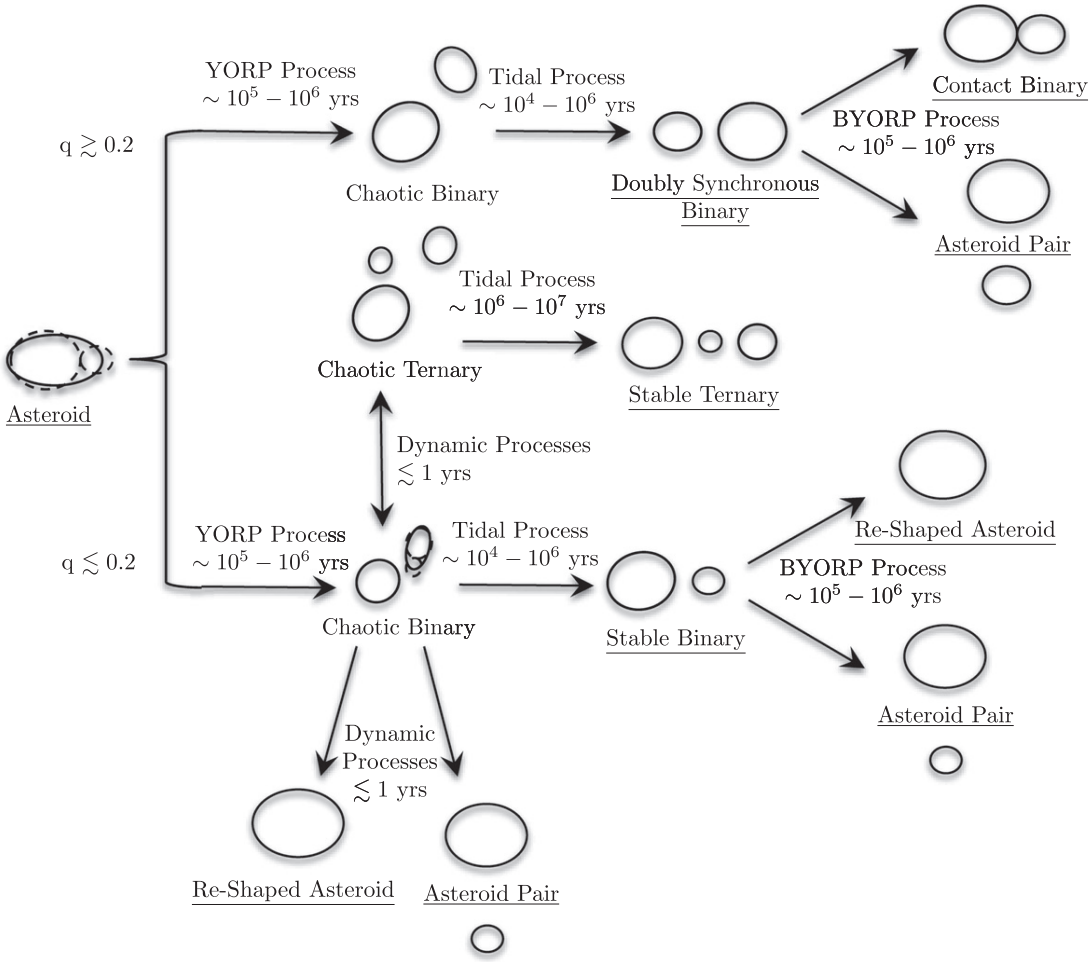

Figure 1.15: a scheme of the binary asteroids cycle proposed in [S.A. Jacobson, D.J. Scheeres, 2011] (see § 1.3.4); q is the secondary/primary mass ratio.

secondary into orbit[20]. They model the binary components as two ellipsoidal shapes with parallel axes of rotation (and parallel to the system angular momentum), and calculate the (approximated) mutual interaction forces between them as they orbit each other, including a tidal dissipation term.

From this point on, they follow the history of the binary with the aid of numerical integration of the analytical equations.

The post-fission dynamics are dominated by chaotic spin-orbit interactions. Patterns are however observed for the systems as a whole, which can be classified into two main regimes, according to the M_2/M_1 mass ratio[21].

For systems with $M_2/M_1 >\sim 0.2$, the free energy of the system (kinetical + mutual gravitational, but neglecting the internal gravitational energy for the two bodies considered rigid) necessary to fission the parent body is negative: as a consequence, if no further fission occurs, the system is bound. Moreover, their tidal evolution is fast, and eventually reach the full synchronous regime. The typical time to reach this state varies with mass ratio and the model used, but is estimated at ~ 4 My for the less favourable case (and being 20 times smaller for just a 0.3 mass ratio). As the permanence time in the NEAs region is larger than this, synchronous binaries are expected among the NEAs and to still be detected[22]. From there, other non-gravitational forces are modeled that may contract or expand the couple, leading to either a newly re-formed contact binary via a gentle impact or an asteroid pair.

For system with $M_2/M_1 <\sim 0.2$, the free energy at fissioning is positive. Spin-orbit coupling will lead the secondary to rapidly explore the (a-e) plane exchanging angular momentum and energy with the primary. Eventually, the satellite finds a way out of the gravitational well and escapes the primary. The tiny fraction ($\sim 2\%$) of those who survive for 10^3 years are all with almost perfect spheroidal shape ($a_2/a_1>0.98$). Secondary YORP fissioning (favoured by the small secondary mass) is also competing against spin-orbital interactions, and the evolution of ternary systems (modeled by ellipsoid + 2 spheres) is considered as well.

The lower bound for the mass of the secondary for it to remain in stable orbit of $\sim 20\%\,\mathrm{M}_1$ is in partial agreement with the results we find in chapter 5.

The main limitation of this work is that in does not take care of the very internal dynamics of the binary creation process, with e.g. the initial mass ratio being determined randomly, only considering the external conditions (limit rotation rate for detaching) at the moment of formation.

[20] they assume pre-fission objects are in a minimum-energy configuration

[21] "q" in fig. 1.15

[22] we remember the bias against observing them via lightcurves, cf. § 1.2.1

Chapter 2

Asteroid modeling

A classic first-order model for the description of asteroids shapes in general, and of rubble piles in particular, is provided by the hydrostatic theory[1], which still represents a useful term of comparison to infer the intensity of the body forces inside gravitational aggregates.

A limit of analytical solid models lies in the fact that generally, in order to give a solution to the equilibrium problem, it is necessary to know quite precisely the previous history of a body; in an elastic material model, any shape is in principle an equilibrium one given a suitable *relaxed* initial shape, upon which the models do not give prediction; in the Mohr-Coulomb plastic model, briefly analysed in sect. § 2.3, the theory gives a maximum limit on the range of shapes outside of which a deformation necessarily happens, but for a larger precision many data on the single asteroids are to be known than are available.

The discovery that many asteroids of large dimensions could be gravitational aggregates with much internal void could be in line with a fluid description, yet granular physics is now beginning to be more and more used in the description of asteroids in search of a faithful model that can describe the physics of this class of celestial objects.

2.1 Hydrostatic fluid equilibrium

A first modeling corresponds to an ideal frictionless fluid exposed to its own (isotropic) pressure and gravity [Ell.fig.equil.].

2.1.1 the virial equation

Let's assume an inertial reference frame with matter distribution $\rho(\mathbf{x}, t)$; this generates a Newtonian potential:

$$\mathfrak{V}(\mathbf{x}) = G \int_V \frac{\rho(\mathbf{x}')}{|\mathbf{x} - \mathbf{x}'|} \, d\mathbf{x}' \tag{2.1}$$

[1] studies date as far back as Newton: see [I. Newton, 1687, liber II, prop XVIII and XIX]

to which a gravitational potential energy is associated:

$$\mathfrak{W} = -\frac{1}{2}\int_V \rho\,\mathfrak{V}\,d\mathbf{x}' \quad . \tag{2.2}$$

Called $u_i(\mathbf{x},t)$ the matter velocity field, kinetic energy ends being

$$\mathfrak{K} = \frac{1}{2}\int_V \rho|\mathbf{u}|^2\,d\mathbf{x} \quad . \tag{2.3}$$

For ease, let's define the following tensorial quantities:

$$\mathfrak{V}_{ij}(\mathbf{x}) = G\int_V \rho(\mathbf{x}')\frac{(x_i-x_i')(x_j-x_j')}{|\mathbf{x}-\mathbf{x}'|^3}\,d\mathbf{x}' \tag{2.4}$$

$$\mathfrak{W}_{ij} = -\frac{1}{2}\int_V \rho\mathfrak{V}_{ij}\,d\mathbf{x} \tag{2.5}$$

$$\mathfrak{K}_{ij} = \frac{1}{2}\int_V \rho u_i u_j\,d\mathbf{x} \tag{2.6}$$

whose traces are, respectively, $\mathfrak{V}$, $\mathfrak{W}$ and $\mathfrak{K}$, and let's further define the momenta relative to the centre of mass:

$$I = \int_V \rho\,d\mathbf{x} = M \tag{2.7}$$

$$I_i = \int_V \rho\,x_i\,d\mathbf{x} \tag{2.8}$$

$$I_{ij} = \int_V \rho\,x_i x_j\,d\mathbf{x} \quad . \tag{2.9}$$

It is worthwhile to additionally define a global pressure integral

$$\Pi = \int_V \rho\,d\mathbf{x} \quad . \tag{2.10}$$

The motion is governed by the equation:

$$\rho\frac{du_i}{dt} = -\frac{\partial p}{\partial x_i} + \rho\frac{\partial\mathfrak{V}}{\partial x_i} \tag{2.11}$$

where

$$\frac{d}{dt} = \frac{\partial}{\partial t} + u_i\frac{d}{dt} \tag{2.12}$$

is the derivative associated with the matter element.
Total mass conservation allows us to write:

$$\frac{d}{dt}\int_V \rho(\mathbf{x},t)\,d\mathbf{x} = \frac{dM}{dt} = 0 \quad . \tag{2.13}$$

the momenta expansion

The general case solution is complex.
A suitable way of managing it consists in the computation of the equation "momenta", where its members are multiplied by 1, x_j, $x_j x_k$, $x_j x_k x_l$, etc... and then integrated over the whole volume V.

At first order we simply get:

$$\frac{d}{dt}\int_V \rho\, u_i\, d\mathbf{x} = -\int_S p\, dS_i - G\int_V\int_V \rho(\mathbf{x})\rho(\mathbf{x}')\frac{x_i - x_i'}{|\mathbf{x}-\mathbf{x}'|^3}\, d\mathbf{x}d\mathbf{x}' \tag{2.14}$$

where S is the *free surface* delimiting the volume V occupied by the fluid.
The surface integral is zero because pressure must cancel out on the border, and the double volume integral is zero because of the antisymmetry with respect to $\mathbf{x}$ and $\mathbf{x}'$; the 2.14 reduces then to

$$\frac{d}{dt}\int_V \rho\, u_i\, d\mathbf{x} = \frac{d^2}{dt^2}\int_V \rho\, x_i\, d\mathbf{x} = \frac{d^2 I_i}{dt^2} = 0 \tag{2.15}$$

which expresses the system's linear momentum conservation.

The second order term gives

$$\frac{d}{dt}\int_V \rho\, u_i x_j\, d\mathbf{x} = 2\mathfrak{K}_{ij} + \mathfrak{W}_{ij} + \delta_{ij}\Pi \tag{2.16}$$

which corresponds to nine real equations. Isolating the antisymmetric and the symmetric terms with respect to the (i,j) couple we obtain (being the right-side member completely symmetric)

$$\frac{1}{2}\frac{d}{dt}\int_V \rho(u_i x_j - u_j x_i)\, d\mathbf{x} = 0 \quad , \tag{2.17}$$

which expresses the angular momentum conservation, and

$$\begin{aligned}\frac{1}{2}\frac{d}{dt}\int_V \rho(u_i x_j + u_j x_i)\, d\mathbf{x} &= \\ \frac{1}{2}\frac{d^2 I_{ij}}{dt^2} &= 2\mathfrak{K}_{ij} + \mathfrak{W}_{ij} + \delta_{ij}\Pi\end{aligned} \tag{2.18}$$

which takes into account the body shape variation.

2.1.2 the virial equation in a rotating system

Being interested in the equilibrium rotating shapes, it is convenient to write the equations in a rotating reference frame with (constant) velocity $\mathbf{\Omega}$; equation (2.11) assumes then the form

$$\rho\frac{du_i}{dt} = -\frac{\partial p}{\partial x_i} + \rho\frac{\partial \mathfrak{V}}{\partial x_i} + \frac{1}{2}\rho\frac{\partial}{\partial x_i}|\mathbf{\Omega}\times\mathbf{x}|^2 + 2\rho\epsilon_{ijk}u_j\Omega_k \tag{2.19}$$

where we suitably introduced the centrifugal and Coriolis forces.

(2.16) is replaced by

$$\frac{d}{dt}\int_V \rho\, u_i x_j\, d\mathbf{x} = 2\mathfrak{K}_{ij} + \mathfrak{W}_{ij} + \Omega^2 I_{ij} - \Omega_i\Omega_k I_{jk} + \delta_{ij}\Pi + 2\epsilon_{ilm}\Omega_m \int_V \rho\, u_l x_j\, d\mathbf{x} \quad . \tag{2.20}$$

By supposing no internal mass motions, in (2.20) we can substitute $\mathbf{u} = 0$ overall on the body; by aligning for ease the x_3 axis along the Ω direction we obtain the relation:

$$\mathfrak{W}_{ij} + \Omega^2(I_{ij} - \delta_{i3}I_{3j}) = -\delta_{ij}\Pi \tag{2.21}$$

which must be satisfied by any rotating body in equilibrium with stationary Ω angular velocity with respect to an inertial frame.

(2.21) has as general solution (we remember the simmetricity of $\mathfrak{W}_{ij}$ and I_{ij})

$$\begin{gathered}\mathfrak{W}_{11} + \Omega^2 I_{11} = \mathfrak{W}_{22} + \Omega^2 I_{22} = \mathfrak{W}_{33} = -\Pi \\ \mathfrak{W}_{12} + \Omega^2 I_{12} = 0 \\ \mathfrak{W}_{13} = \mathfrak{W}_{23} = 0 \\ I_{13} = I_{23} = 0\end{gathered} \tag{2.22}$$

where, in particular, I_{ij} is not necessarily diagonal, but has the form

$$I_{ij} = \begin{pmatrix} I_{11} & I_{12} & 0 \\ I_{21} & I_{22} & 0 \\ 0 & 0 & I_{33} \end{pmatrix} \tag{2.23}$$

and analogously for $\mathfrak{W}_{ij}$.

This fact was discovered for the first time by Jacobi in 1834, and represents the noteworthy result of foreseeing stable constantly spinning shapes not presenting rotational symmetry. Obviously it is always possible in these cases to redefine the axes as to diagonalise I_{ij} (and $\mathfrak{W}_{ij}$), where we will then nevertheless have $I_{11} \neq I_{22}$.

2.1.3 homogeneous ellipsoids

The virial equation in the form (2.11) is sufficiently general to be applied to many different models, according to the relation between pressure $p(\mathbf{x})$ and density $\rho(\mathbf{x})$, from which indirectly the $\mathfrak{V}_{ij}, \mathfrak{W}_{ij}, I_{ij}, \mathfrak{K}_{ij}, \Pi$ quantities depend, by the means of complex relations.

The simplest model is the study of triaxial ellipsoids at constant and uniform density $\rho(\mathbf{x})$; in such a case the computation is greatly simplified, and the aforementioned quantities can explicitly be written.

Called a_1, a_2, a_3 the three semiaxes, supposed aligned with the coordinate frame, let's define for ease the following quantities:

$$\begin{aligned} A_i &= \alpha_1\alpha_2\alpha_3 \int_0^\infty \frac{du}{\Delta(\alpha_1^2 + u)} \\ \mathfrak{I} &= a_1^2\alpha_1\alpha_2\alpha_3 \int_0^\infty \frac{du}{\Delta} \quad , \end{aligned} \tag{2.24}$$

where

$$\alpha_i = \frac{a_i}{a_1} \tag{2.25}$$

$$\Delta = \sqrt{(\alpha_1^2 + u)(\alpha_2^2 + u)(\alpha_3^2 + u)} \tag{2.26}$$

and in which the integrals depend exclusively upon the shape α_i; furthermore, the relation

$$\sum_{i=1}^{3} a_i^2 A_i = \mathfrak{I} \tag{2.27}$$

holds.

For $\mathfrak{W}_{ij}$ and I_{ij} we thus have:

$$\begin{aligned} I_{ij} &= \frac{1}{5} M a_i^2 \delta_{ij} \\ \mathfrak{W}_{ij} &= -2\pi G \rho A_i I_{ij} \\ \mathfrak{W} &= -\frac{2}{5} \pi G \rho M \mathfrak{I} \end{aligned} \tag{2.28}$$

in which the dependence from M, ρ and the shape α_i is suitably factored.

2.1.4 the Maclaurin sequence

The first discovery of a rotationally symmetric sequence of stable, pole-flattened, shapes (so-called *spheroids*) happened in 1742 by Maclaurin.

By imposing in (2.22) the homogeneity and rotational symmetry around x_3 ($I_{11} = I_{22}$) we obtain the relation

$$2A_1 I_{11} - \overline{\Omega}^2 I_{11} = 2A_3 I_{33} \tag{2.29}$$

where $\overline{\Omega} = \Omega / \sqrt{\pi G \rho}$ is a suitable renormalization on the angular velocity, as to eliminate dependence on ρ. From (2.28), and the explicit calculation of the A_i (elliptic integrals) we get the relation

$$\overline{\Omega}^2 = \frac{2\sqrt{1-e^2}}{e^3}(3 - 2e^2)\sin^{-1} e - \frac{6}{e^2}(1 - e^2) \tag{2.30}$$

binding ellipticity $e = \sqrt{1 - a_3^2/a_1^2}$ to the angular velocity; (2.30) possesses solution for any value $0 < e < 1$, which can thus act as parametrization of the Maclaurin sequence.

Another important parameter of the sequence is the angular momentum L: by defining, as with the angular velocity Ω, a suitable renormalised value to eliminate mass and volume dependence, we have:

$$\overline{L} = \frac{L}{\sqrt{GM^3 \bar{a}}} = \frac{\sqrt{3}}{5} \left(\frac{a_1}{\bar{a}} \right)^2 \overline{\Omega} \tag{2.31}$$

where we define the mean radius $\bar{a}^3 = a_1 a_2 a_3$.

In figure 2.1 the variation of $\overline{\Omega}$ and $\overline{L}$ is tabulated along the Maclaurin sequence: it is to note in particular that, while $\overline{L}$ is monotone and tending to infinity, $\overline{\Omega}$ reaches a maximum around the value $e = 0.92995$ before decreasing back to zero.

$\Omega^2/\pi G\rho$	$L/(GM^3\bar{a})^{\frac{1}{2}}$	e	$\Omega^2/\pi G\rho$	$L/(GM^3\bar{a})^{\frac{1}{2}}$	e	$\Omega^2/\pi G\rho$	$L/(GM^3\bar{a})$
0	0	0·75	0·31947	0·25792	0·91	0·44507	0·41563
0·00534	0·02539	0·80	0·36316	0·29345	0·92	0·44816	0·43302
0·01204	0·03829	0·81	0·37190	0·30153	0·93	0·44933	0·45254
0·02146	0·05144	0·81267	0·37423	0·30375	0·94	0·44785	0·47480
0·03363	0·06491	0·82	0·38059	0·31001	0·95	0·44264	0·50074
0·04862	0·07882	0·83	0·38917	0·31893	0·95289	0·44022	0·50912
0·06647	0·09329	0·84	0·39761	0·32835	0·96	0·43193	0·53194
0·08727	0·10846	0·85	0·40583	0·33833	0·97	0·41257	0·57123
0·11108	0·12450	0·86	0·41378	0·34895	0·98	0·37802	0·62486
0·13799	0·14163	0·87	0·42136	0·36029	0·99	0·31030	0·71209
0·16807	0·16013	0·88	0·42845	0·37247	0·995	0·24371	0·79443
0·20135	0·18037	0·89	0·43490	0·38563	0·999	0·12540	0·97380
0·23783	0·20286	0·90	0·44053	0·39994	0·9999	0·04286	1·22633
0·27734	0·22834						

Figure 2.1: trends of $\overline{\Omega}^2$ and $\overline{L}$ as a function of e for the Maclaurin spheroids. from [Ell.fig.equil., p. 78])

Maclaurin sequence instabilities

The virial equation gives even a method for the study of perturbations at the equilibrium (or with respect to any flux even in the absence of equilibrium).
Be $\boldsymbol{\xi}(\mathbf{x},t)$ the (supposed small) variation of position of a matter element at time t with respect to the unperturbed position $\mathbf{x}$ at the same time. Be then the *Lagrangian variation* the variation induced on the generic local quantity $Q(\mathbf{x},t)$ linked to the matter element that in the unperturbed flux was described by the field $Q_0(\mathbf{x},t)$:

$$\Delta Q(\mathbf{x},t) = Q(\mathbf{x}+\boldsymbol{\xi}(\mathbf{x},t),t) - Q_0(\mathbf{x},t) \tag{2.32}$$

where, in particular, $\Delta\mathbf{u} = \frac{d\boldsymbol{\xi}}{dt}$, and be instead the *Eulerian variation* the difference between the same quantities with respect to the same point in space $\mathbf{x}$ at the same time t:

$$\delta Q(\mathbf{x},t) = Q(\mathbf{x},t) - Q_0(\mathbf{x},t) \quad . \tag{2.33}$$

In general, these relations hold

$$\left[\Delta; \frac{d}{dt}\right] = 0 \qquad \left[\delta; \frac{\partial}{\partial t}\right] = 0 \tag{2.34}$$

$$\Delta = \delta + \xi_i \frac{\partial}{\partial x_i} \quad . \tag{2.35}$$

For the integral quantities, they are subject to the transformation

$$J_0 = \int_V Q_0(\mathbf{x},t)\, d\mathbf{x} \quad \longrightarrow \quad J = \int_{V+\Delta V} Q(\mathbf{x},t)\, d\mathbf{x} \tag{2.36}$$

where the volume $V + \Delta V$ is that delimited by the surface $S + \boldsymbol{\xi}(S,t)$.

To the first order in $\boldsymbol{\xi}$, the δJ variation can be written:

$$\delta J = \int_V (\Delta Q + Q\, \boldsymbol{\nabla}\cdot\boldsymbol{\xi})\, d\mathbf{x} \tag{2.37}$$

linking to each other $\boldsymbol{\xi}$, Q and J, and allowing us to write the variations of the quantities appearing in the different momenta of the virial equation.

A suitable application of (2.32-2.37) to the virial equation (2.19) leads to linking together the $\boldsymbol{\xi}$ perturbation with the linear variations of the global quantities $\mathfrak{W}_{ij}$ and I_{ij} (small perturbations), allowing us to study the systems proper frequencies at equilibrium.

In the case of the Maclaurin sequence, supposing a perturbation of the kind

$$\boldsymbol{\xi}(\mathbf{x}, t) = e^{i\sigma t}\boldsymbol{\xi}_0(\mathbf{x}) \quad , \tag{2.38}$$

we can notice how in correspondence of $e \simeq 0.81267$ one of the characteristic frequencies relative to the second order of the virial gets to zero: here the (2.38) periodicity of the function is lost, and we have a case of indifferent equilibrium with respect to the corresponding (small) perturbation.
This frequency is associated to a perturbation leading the Maclaurin spheroid to deform into a triaxial ellipsoid: in correspondence of this point, in fact, the Maclaurin sequence meets a *bifurcation*, from which the Jacobi triaxial ellipsoids sequence branches off (see below).

Another point to notice is the one in correspondence of $e \simeq 0.95289$ in which two real solutions coincide, and beyond which they change into complex solutions, causing the rise of an unstable equilibrium.

A last interesting fact to notice is that if in the virial equation we insert additional dissipative terms due to internal frictions, the Maclaurin sequence becomes unstable from the Jacobi bifurcation point: for a Maclaurin spheroid beyond the branching point even a small dissipative term would lead to global instability.

2.1.5 the Jacobi sequence

Let's define for ease the quantities (cf. eq. 2.24)

$$\begin{aligned} A_{ij} &= \frac{\alpha_1\alpha_2\alpha_3}{a_1^2}\int_0^\infty \frac{du}{\Delta(\alpha_i^2+u)(\alpha_j^2+u)} \\ B_{ij} &= \frac{\alpha_1\alpha_2\alpha_3}{a_1^2}\int_0^\infty \frac{u\,du}{\Delta(\alpha_i^2+u)(\alpha_j^2+u)} = A_j - a_i^2 A_{ij} \quad , \end{aligned} \tag{2.39}$$

and let's consider again the (2.22) in the form:

$$\overline{\Omega}^2 a_1^2 - 2A_1 a_1^2 = \overline{\Omega}^2 a_2^2 - 2A_2 a_2^2 = -2A_3 a_3^2 \quad , \tag{2.40}$$

and add to the three members $2a_1^2 a_2^2 A_{12}$.
The pair of resulting equalities

$$a_1^2(\overline{\Omega}^2 - 2B_{12}) = a_2^2(\overline{\Omega}^2 - 2B_{12}) = 2(A_{12}a_1^2 a_2^2 - A_3 a_3^2) \tag{2.41}$$

is satisfied, once the $a_1 = a_2$ case, corresponding to the Maclaurin shapes, is excluded, if and only if

$$\begin{aligned} a_1^2 a_2^2 A_{12} &= a_3^2 A_3 \\ \overline{\Omega}^2 &= 2B_{12} \end{aligned} \tag{2.42}$$

a_2/a_1	a_3/a_1	$\Omega^2/(\pi G\rho)$	$L/(GM^3\overline{a})^{\frac{1}{2}}$	a_2/a_1	a_3/a_1	$\Omega^2/(\pi G\rho)$	$L/(GM^3\overline{a})^{\frac{1}{2}}$
1·00	0·582724	0·374230	0·303751	0·48	0·372384	0·302642	0·369473
0·96	0·570801	0·373987	0·303959	0·44	0·349632	0·287267	0·385940
0·92	0·558330	0·373190	0·304602	0·40	0·325609	0·269678	0·406073
0·88	0·545263	0·371785	0·305749	0·36	0·300232	0·249693	0·430872
0·84	0·531574	0·369697	0·307467	0·32	0·273419	0·227153	0·461750
0·80	0·517216	0·366837	0·309837	0·28	0·245083	0·201946	0·500777
0·76	0·502147	0·363114	0·312956	0·24	0·215143	0·174052	0·551140
0·72	0·486322	0·358424	0·316938	0·20	0·183524	0·143610	0·618069
0·68	0·469689	0·352649	0·321923	0·16	0·150166	0·111044	0·710927
0·64	0·452194	0·345665	0·328081	0·12	0·115038	0·077281	0·848770
0·60	0·433781	0·337330	0·335618	0·08	0·078166	0·044168	1·079302
0·56	0·414386	0·327493	0·344796	0·04	0·039688	0·015415	1·58276
0·52	0·393944	0·315989	0·355941	0	0	0	∞

Figure 2.2: trends of a_3/a_1, $\overline{\Omega}^2$ and $\overline{L}$ as a function of a_2/a_1 for the Jacobi ellipsoids. from [Ell.fig.equil., p. 103])

hold.

In such a case, they give a solution for an arbitrary value of α_2 (for simplicity, we can always assume it to be < 1), to which an angular speed and a third axis length will correspond as shown in fig. 2.2; as it can be observed, the rotation axis a_3 is always the shortest of the three. The trends of $\overline{\Omega}^2$ and $\overline{L}$ are shown in fig. 2.3 together with the Maclarin sequence.

Jacobi sequence instabilities

Even the Jacobi sequence presents several critical points of instability. The most noteworthy is the one corresponding to $\alpha_2 \simeq 0.432232$, where the sequence definitively loses stable equilibrium in favour of an *egg*-like configuration (**Poincaré sequence**). The corresponding instability is proper of the third order of the virial equations (quadratic dependance on the coordinates).

2.1.6 other constant-density sequences

The search for equilibrium shapes even in presence of the restricted problem of uniform density body model remains an infinite degrees of freedom problem, and several approaches have been used, like successive approximations or numerical integration, to find stable shapes or sequences, including shapes where a fission of the body into two or more parts is considered.
An example of some of these is given in figure 2.4.

A sequence to note is the so called *Dumbbell sequence* (see fig. 2.5), which branches off from the unstable part of the Jacobi sequence, from a triaxial ellipsoid to a body with a more and more pronounced central narrowing, which increases in size up to eventually separate the body into two separate equal mass and symmetric fragments. This kind of sequence is the one approximately followed by our bodies in the simulations presented in chapter 5.

Note that more than one binary sequence are in fact present, based upon different mass ratios, and that no stable known sequence exists connecting them to the known single body stable shapes region (apart for the 1:1 mass ratio), fact that imposes for

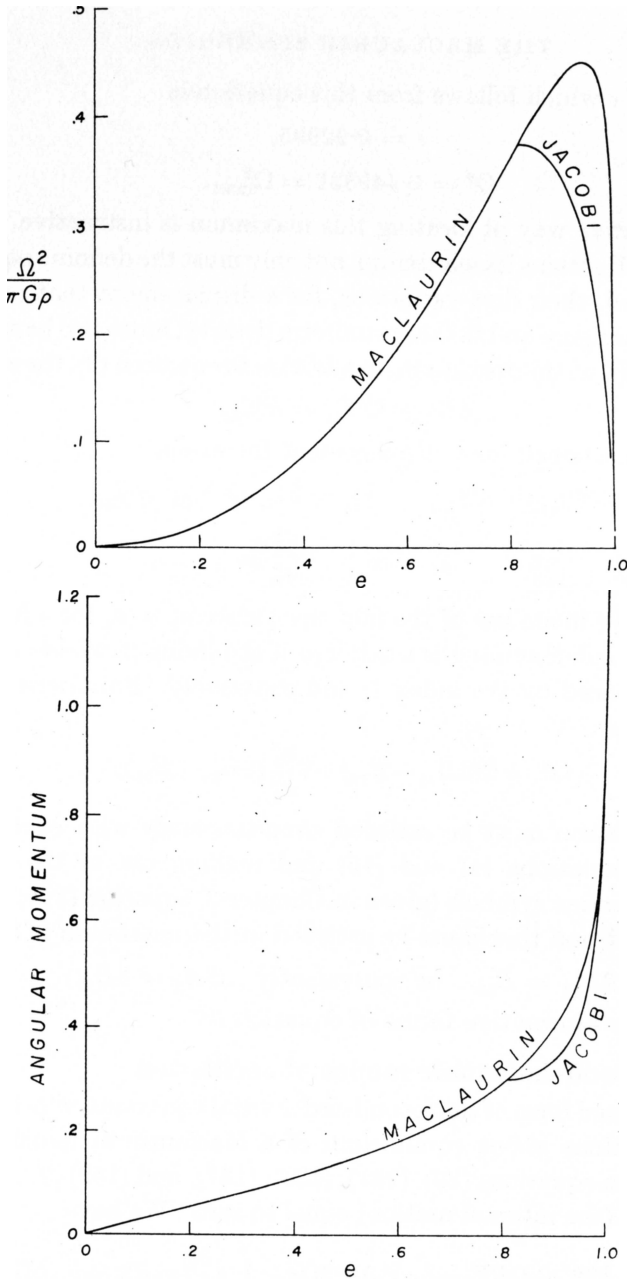

Figure 2.3: trends of the Maclarin and Jacobi sequences compared. from [Ell.fig.equil., p. 79]

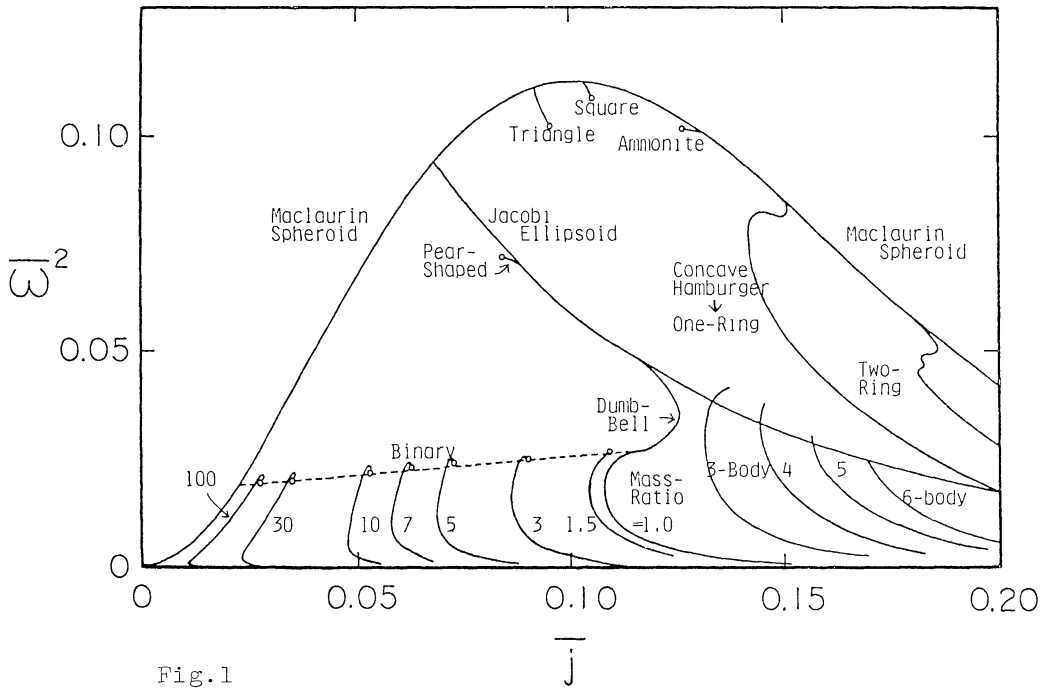

Figure 2.4: some hydrostatic equilibrium sequences at constant density ('j' is the angular momentum; note that normalization factors are different from the ones used in this work: for comparison, the Maclaurin-Jacobi bifurcation has $(\overline{L};\overline{\Omega}^2)$ coordinates $\approx(0.30\ ;\ 0.37)$). from [I. Hacisu, Y. Eriguchi, 1984]

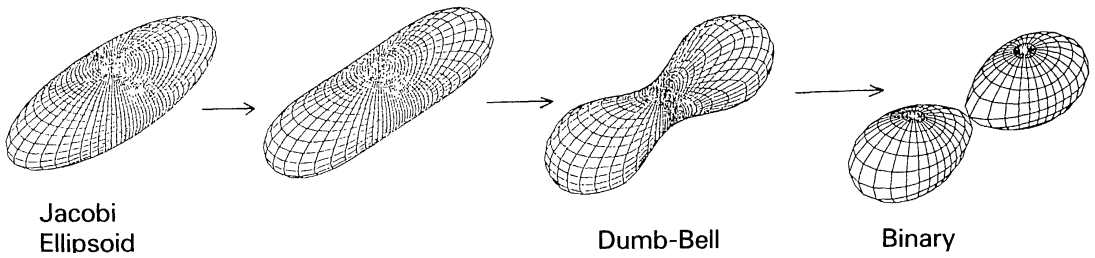

Figure 2.5: the Dumbbell sequence of shapes. from [I. Hacisu, Y. Eriguchi, 1984]

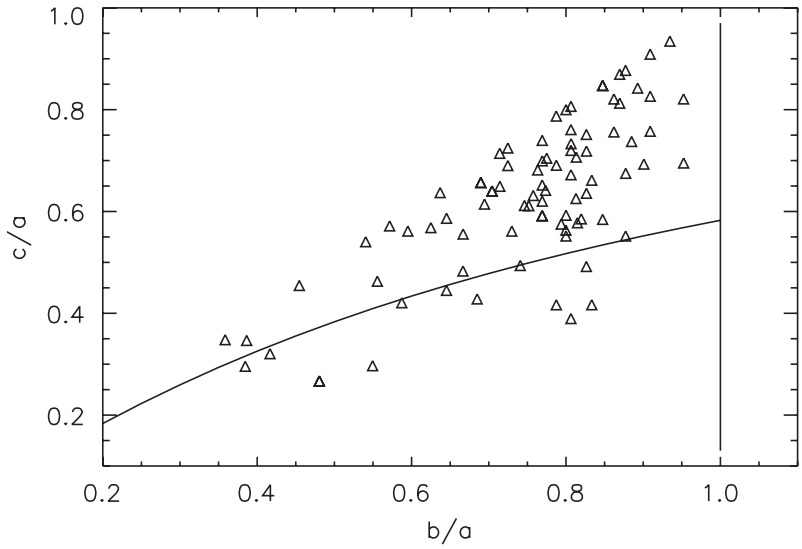

Figure 2.6: [P. Magnusson, C. Neese, 1996] database asteroids for which we know both axes ratios, compared to the Maclaurin and Jacobi sequences. from [P. Tanga et al., 2009 I]

them a necessarily chaotic or catastrophic origin. Of course these are but mathematical solutions for perfectly cohesionless and synchronous fluid systems, fact that must be considered when comparing them to real objects.

An important fact, which must enter a theory determining and predicting real objects' shapes, is that the effective reaching of a particular equilibrium shape instead of another depends more or less strongly on the previous body history. Theoretically, for any non equilibrium situation, the correct solution of the variational equations gives the right velocity field to which the body is subjected, and that will lead it to a new equilibrium point; in practice, the constant density (and mass) model must however be abandoned in favour of more complex models to take into account, for example, the initial creation phases themselves of the original object.

2.2 Real objects distribution

Available asteroid observations show that gravitational aggregates candidates do not correspond strictly to hydrostatic equilibrium shapes, but are rather dispersed within a quite wide region around them (cf. fig. 2.6).

If the classical Maclaurin and Jacobi sequences constitute a reference regarding their equilibrium shapes, and especially so for gravitational aggregates, other factors come into play in the case of solid, or granular, material, for which alternative models are to be considered.

2.3 Elasto-plastic material

The behaviour of the internal forces in a material and its small scale effects can be modeled in different ways. A global approach considers the use of the *stress tensor* σ_{ij} defined as

$$\sigma_{ij}(\mathbf{x}) = \frac{dF_i(\mathbf{x})}{dA_j} \tag{2.43}$$

where $\mathbf{F}$ is the contact force acting on the oriented surface $\mathbf{A}$ at the internal point $\mathbf{x}$ (negative in case of compressive forces); it describes the status of the internal forces in terms of normal ($\sigma_{xx}, \sigma_{yy}, \sigma_{zz}$) and tangential ($\sigma_{xy}, \sigma_{xz}, \sigma_{yz}$: the tensor is symmetrical) components acting along the different directions.

According to the model used, $\boldsymbol{\sigma}$ must be subjected to some restrictions if the body has to be in equilibrium without any permanent deformation or breaking in the material occurring.

To obtain $\boldsymbol{\sigma}$, in the case of a triaxial ellipsoid, we assume ([K.A. Holsapple, 2001]), for body symmetry, a shape like:

$$\sigma_{ii} = k_{i0} + k_{ij}x_j^2 \qquad \sigma_{ij} = \kappa_{ij}x_i x_j \tag{2.44}$$

dependent upon 15 parametres, which have to be determined with as many relations.

Three are given by the equation for general equilibrium with mass forces:

$$\frac{\partial \sigma_{ij}}{\partial x_j} = \rho \frac{\partial V}{\partial x_i} \tag{2.45}$$

where V is the potential to which matter is subjected: in the case of body spinning around the z axis, it is equal to the sum of gravitational $\mathfrak{V}$ and centrifugal

$$\mathfrak{C} = \frac{-\omega^2}{2}(x^2 + y^2) \tag{2.46}$$

potentials.

Secondly, we must impose that the stress vector on the surface of the body be zero everywhere (free surface). The latter is given by:

$$\mathbf{t} = \hat{\mathbf{n}} \cdot \boldsymbol{\sigma} \tag{2.47}$$

where $\hat{\mathbf{n}}$ is the normal to the surface in $\mathbf{x}$, proportional to $(x/a^2, y/b^2, z/c^2)$. Substituting the surface equation

$$\frac{x^2}{a^2} + \frac{y^2}{b^2} + \frac{z^2}{c^2} = 1 \tag{2.48}$$

and imposing it be zero in every point, we obtain for each of the 3 equations (2.47) 3 fixed combinations for the coefficients of (2.44) which must be set to zero, determining 9 further parameters.

To completely determine $\boldsymbol{\sigma}$ it is finally necessary to impose a specific model: for a perfect fluid we will have for example

$$\sigma_{xx} = \sigma_{yy} = \sigma_{zz} \qquad \sigma_{xy} = \sigma_{xz} = \sigma_{yz} = 0 \quad .$$

Another possibility consists of using the Hook law to couple $\boldsymbol{\sigma}$ to the strain tensor $\boldsymbol{\epsilon}$, but that requires an a priori knowledge of a supposedly "original" shape which has been deformed into the actual current one via deformations elastically induced by pressure forces.

This approach is of difficult use in the case of asteroids, whose knowledge of such a *rest* shape is possible only by knowing the whole previous history of a body and the possible breaks that may already have occurred, which further requires a much broader formulation of the original problem that must include besides a variable mass even a precise analysis of the fluxes induced by the overcoming of the elastic bonds breaking the threshold (so called *yielding*). Additionally, such an approach may be dependent upon a supposed continuity inside the body, which is not necessarily apt for the modeling of highly porous bodies, as many medium to large asteroids appear to be.

An interesting possibility as to what pertains to rubble-piles is offered by the use of the *Mohr-Coulomb model* for the maximum stresses: a certain wide set of materials (even of high granularity, like a particular kind of sand or mould) can be schematised as having a resistance (*strength*) to yielding due to tangential forces which is a linear function of the normal compressive force acting on the same surface (plus a *rest* cohesion parameter): when a tangential force overcome this threshold, a definitive yielding occurs that breaks the original elastic bonds (plastic deformation, fracture, mutual reorganization of the grains positions). According to this model, for a generic material the law:

$$(\sigma_1 + \sigma_3)\sin\phi - 2Y\cos\phi \leqslant (\sigma_3 - \sigma_1) \tag{2.49}$$

holds, where (negative) σ_1 and σ_3 are the greatest (least compressive) and least (most compressive) eigenvalues of $\boldsymbol{\sigma}$, Y the *cohesion stress*, i.e. the tangential yielding force without compression (akin to a static friction), dependent upon the material, and ϕ a coefficient (*angle of repose* or *angle of friction*), depending on the material, which expresses the proportional dependence between compressive and tangential yielding forces.

Rubble piles are usually assumed to be cohesionless: by supposing $Y = 0$, we have:

$$\operatorname{tg}\phi \geqslant \frac{1 - \sigma_1/\sigma_3}{2\sqrt{\sigma_1/\sigma_3}}. \tag{2.50}$$

This last relation, if applied to the six intersection points between the axes and the ellipsoid surface, allows us to determine the last three parameters of (2.44): in each of these points, having chosen the body axes as the reference frame axes in which to write $\boldsymbol{\sigma}$, the three tangential stresses are zero for symmetry reasons, and the tensor is thus diagonal. On the other hand, the normal component at the surface must also be zero[2] and, positive stresses (tractions) not being possible, this leads to it being the maximal one $= \sigma_1$; because of the (2.49) or the (2.50), σ_3 must also be zero, and thus all three.

2.3.1 the stability band

With these constraints, the resulting stress is:

$$\sigma_{ii} = -\rho c_i a_i^2 \mathcal{S} \tag{2.51}$$

[2] cf. (2.47)

where

$$\mathcal{S} = 1 - \sum_i \left(\frac{x_i}{a_i}\right)^2$$

and c_i are the coefficients of the potential

$$V(\mathbf{x}) = V_0 + \sum_i c_i x_i^2$$

that in the case of a body subjected only to its own gravity and centrifugal forces are (cf. (2.24), (2.28) and (2.46))

$$\begin{aligned} c_1 &= \rho\pi G A_1 - \frac{\omega^2}{2} \\ c_2 &= \rho\pi G A_2 - \frac{\omega^2}{2} \\ c_3 &= \rho\pi G A_3 \quad . \end{aligned} \tag{2.52}$$

The resulting tensor is thus always diagonal when written in the reference with the axes aligned to the body ones, and the ratios between the components are independent from the position inside the body: this means that, in case of overcoming of the (2.50) limit, a global yielding on the whole body is expected rather than a local fracture (what effectively is observed in all our simulations).

Thanks to (2.50) it is then possible to confront a generic shape $\boldsymbol{\alpha}$ rotating at fixed angular velocity with the repose angle needed to sustain it: the result is a "stability zone" at fixed $\phi = \tilde{\phi}$ around the classical equilibrium sequences of Maclaurin and Jacobi, within which a body composed of a material with a given angle of repose $\geqslant \tilde{\phi}$ can exist at equilibrium.

A comparison with the available data on size and rotation period of asteroids (see fig. 2.7) shows that most lie within a region characterised by an angle ϕ dependent upon the spectral class.

In [P. Tanga et al., 2009 II] (see § 3.10.2) we found that in fact $\phi \sim 5^\circ$ is enough to fit most asteroids and ran a series of numerical simulations to support this.

2.4 Granular system physics

If we want to make progress into understanding the physics of asteroids, their nature as rubble-piles and the finite size of their components cannot be neglected. Granular system physics does offer some insight into this problem, though it is a complex field of study that has been up to recent past (end of 20th century) poorly investigated.

A *granular system* may be thought of as a physical system where the single components (called *grains*) are macroscopic in nature (i.e. not subjected to thermodynamic fluctuations) and in close (i.e. touching) interaction, each interaction being traceable down to the component level; and yet, due to the high number of such grains, the overall behaviour is determined by complex laws.

The friction angle (see § 2.3) for a granular material is an example of such overall property not easily discernible from the single grains.

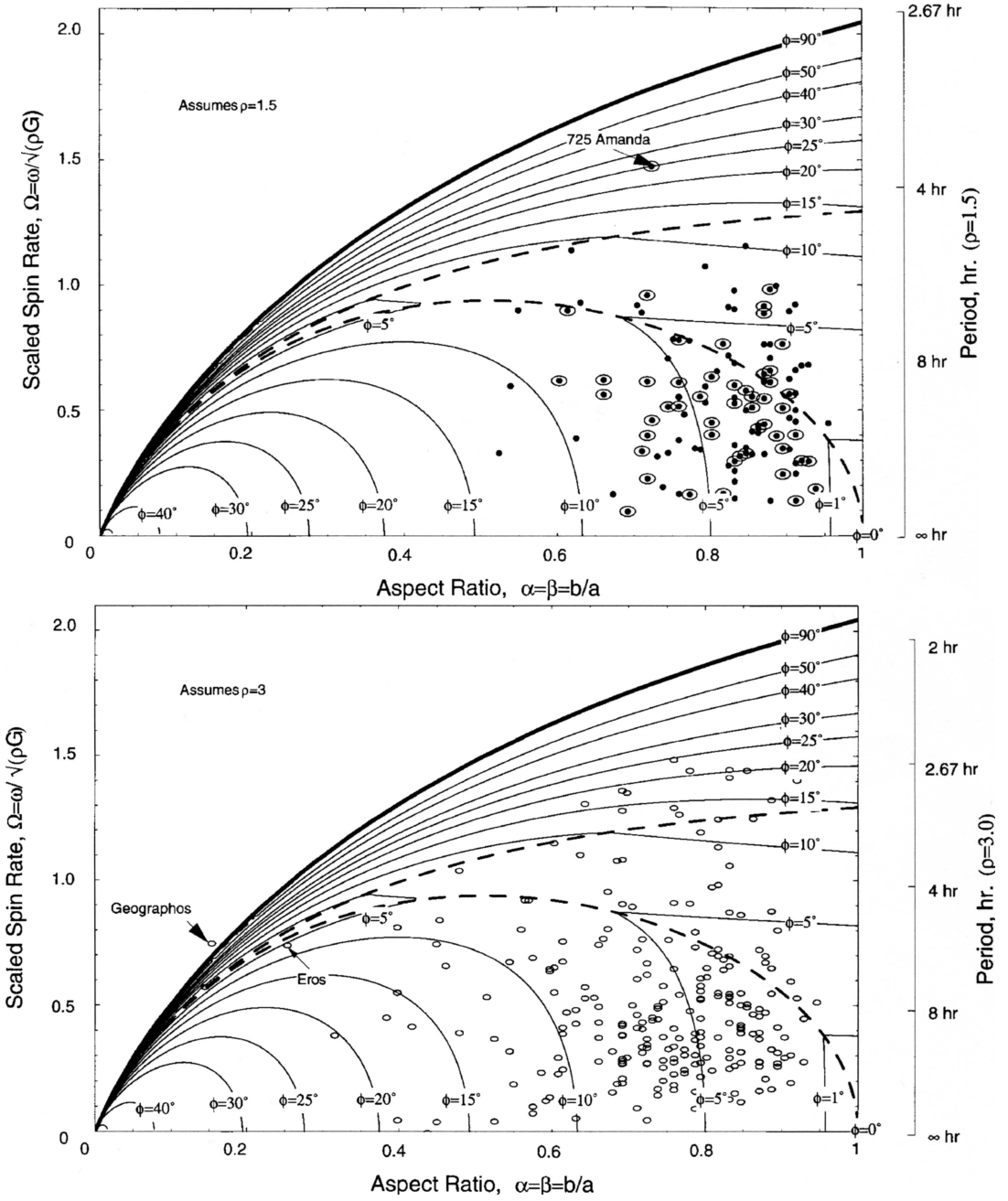

Figure 2.7: C (above) and S (below) -type asteroids compared to the (minimal) repose angle ϕ necessary to sustain their shapes; the a_2/a_1 ratio is the only generally known with a certain precision. For these graphs $a_3 = a_2$ has been supposed for all cases, with a mean density of 1.5 g/cm^3 for C-type asteroids C and 3 g/cm^3 for S-type asteroids. All asteroids lie within a zone defined by $\phi \lesssim 12^\circ$ and 25° respectively. from [K.A. Holsapple, 2001]; asteroids data from (P. Pravec, A. Harris)

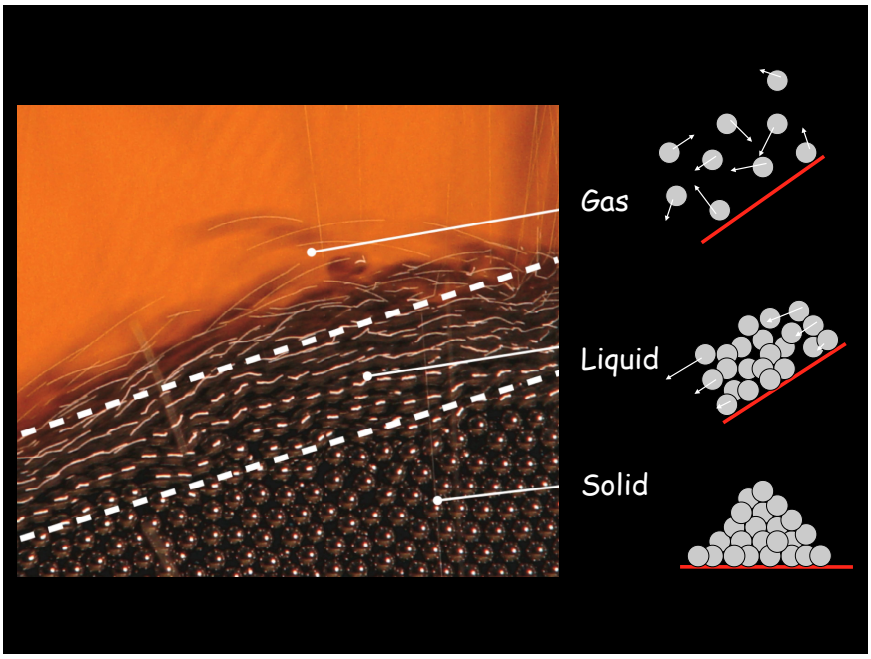

Figure 2.8: the different regimes of a granular system, according to the energy level. image by A. Pouliquen

Rubble-pile asteroids present in this regard a highly heterogeneous set of grains, from fine dust of micrometric size to large rocks of several hundred metres.

According to the energetic level of the ensemble, these systems have the property of behaving under different regimes: solid-like, e.g. in a rubble-pile at equilibrium, liquid-like, e.g. a snow and land avalanche, or in extreme cases even gas-like (see fig. 2.8).

At rest, a granular system may be characterized by many macroscopic variables typical of continuous materials, such as elasticity or plasticity, which rely in part on the characteristics of single grains (which may be deformable) and in part on the structure as a whole (shape, packing efficiency). When a global shape change occurs (we can think to the squeezing of a pack of sugar), the response of the whole is generally a non-linear stress-deformation relation.

The physics of friction is of paramount importance in granular systems, as the contact forces are their characteristic feature; a key in setting apart a solid from a liquid behaviour lies in the more or less abrupt overcoming of the static frictions that characterize a system, beyond which a more fluid structure behaviour settles in.

In a static (solid-like) granular continuum, the pressure forces are suitably unloaded from one grain to another in a complex pattern, which largely depends on external conditions, previous history of the material and, going down to the grain-to-grain level, partly random behaviour. When energy is injected into the system (i.e. in the form of elastic compression by pressure), the unloading pattern determines if and where the solid breaks and a deformation or slide occurs.

In fact, the very nature of microscopic contacts between grains due to the way two otherwise macroscopically similar (same grain nature, size, volume, shape, temperature) systems have been built does determine very different possible behaviours to macroscopic external stimuli (pressures, gravity). This may be an important factor to consider for the evolution of the asteroids, which is not expressly modeled in the code we use for our simulations.

A higher cohesion may also arise as the result of a liquid intermixing with the grains (e.g. a wet sand castle) or to the microdeformations of grains themselves (solid bridges) that may naturally form with time in a static system at equilibrium, putting again the previous history of the system as an important variable.

As the global behaviour is strongly dependent upon the external conditions, Earth-based results may lack full validity in the microgravity environment of an asteroid, for example by reducing the energy needed for a grain to move from its equilibrium configuration and determine a local or global deformation. This may change our understanding of the behaviour of e.g. asteroid regolith (which also determines in turn the spectroscopic properties observed from Earth) or gravitational aggregate macroscopic properties (e.g. the angle of friction for its material).

The two fields of granular physics and gravitational aggregates studies are today starting to exchange ideas and results to reach a better comprehension of their respective areas of study, and some experimental and numerical studies are being published ([B. Rozitis et al., 2009], [P. Sánchez, D.J. Scheeres, 2011]).

Chapter 3

Numerical methods

The simulations on binary formation presented here (see chapters 4 and 5) have been obtained using the software **pkdgrav**, a gravitational N-body simulator managing multiparticle systems under the effect of gravity, originally written for cosmological simulations by researchers from the University of Washington, successively modified by adding a collision treatment for dynamical simulations in the Solar System ([T.R. Quinn et al., 2000], [D.C. Richardson et al., 2000]), and later modified in part to suit specific needs of gravitational aggregates.

It has been and is being used as basis for a growing literature on the rubble pile and granular subjects (i.e. [P. Michel et al., 2001], [P. Tanga et al., 2004], [D.C. Richardson et al., 2005], [J.F. Consigli et al., 2006], [K.J. Walsh et al., 2008], [P. Tanga et al., 2009 I], [P. Tanga et al., 2009 II]) and is one the best N-body gravitational simulators, using parallel computing libraries in order to allocate work among several processors.

3.1 The *perfect rubble pile* model

The software uses spherical constant-density rigid spheres as basic mass units.

This considerably simplifies computations: firstly, the gravitational field generated by each sphere is equivalent to that of a point mass, and allows an exact fast computation for whatever configuration of particles; secondly it simplifies intrinsic angular momentum managing in two ways: the tensor of inertia is always diagonal and a multiple of the identity (and consequently the intrinsic angular momentum is always proportional to spin), and all reciprocal collisions occur on a contact point belonging to the line connecting the particles' centres (where the reciprocal exerted torque and intrinsic/orbital angular momentum exchange only depends on the relative surface velocities of the contact points).

The modeling of an asteroid by means of spherical particles, called of "perfect rubble pile", is a first attempt at using a numerical integration of the N-body problem for the study of gravitational aggregates.

A body composed of spherical particles tends to have, for geometric reasons, a certain internal quantity of empty space (voids): if on one side this reproduces the fact that, according to the models, real rubble piles go as far as having a worthwhile quantity

of internal empty space, this artificiality in the choice of components can produce some spurious behaviour.

When several particles pile up on each others, is it natural for them to settle in such a way to minimise the empty spaces amongst them, thus reducing the potential energy, and for a certain packing to appear.

3.1.1 the tightest theoretical packing: the "crystalline structure"

The best (densest) theoretically obtainable packing[1] with homogeneously sized spheres reaches a *filling coefficient* (the ratio between the volume of the spheres and the volume of the envelope) of $\pi\sqrt{2}/6 \simeq 74.048\%$; such a value can be reached with an ordered packing in the following way:

- along a plane we set down a layer of spheres with a hexagonal cell structure: this is the most efficient packing for equal circles in a plane:

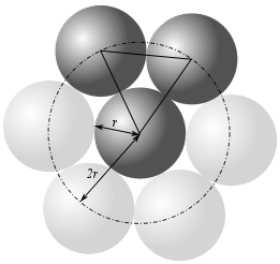

- we put then on top of it a second layer similar to the first so that the positions of the second spheres correspond to holes in the first one
- only a hole out of two of the first layer disposition has been covered by a sphere of the second one; the third layer, similar to the previous two, has thus two possibilities of being positioned: either exactly overlapping the first, or level with the holes of the first layer not covered by the second one
- the generic n-th layer has 2 possibilities: either exactly overlapping the (n-2)th, or the third case different from that and the (n-1)th layer.

Calling a the first layer disposition, b the second one's, and c the third possibility different from a and b, every packing can be described by the sequence of layers which compose it, and is a combination of two main trends (cf. fig. 3.1):

abcabc , which reproduces a ***face-centered cubic*** *crystal*

ababab , called ***hexagonal compact***.

[1] mathematically, it still is a conjecture, even if Gauss proved it to be nevertheless the best regular packing

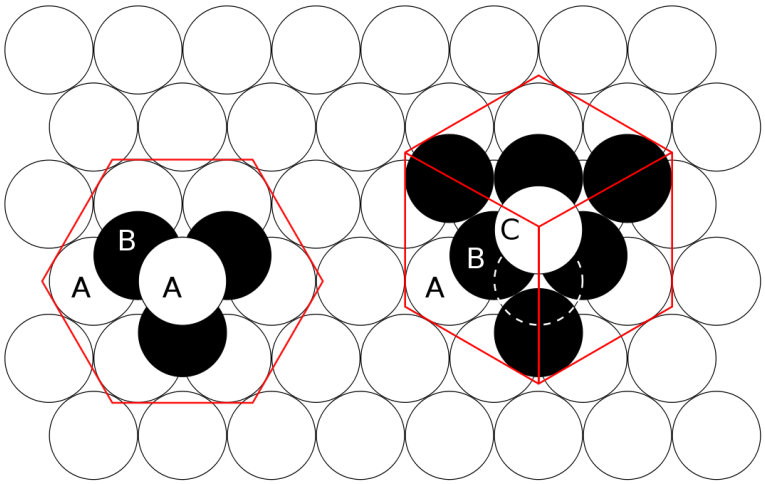

Figure 3.1: crystalline packing: on the left, hexagonal prism crystal; on the right, cubic crystal. images from wikipedia

experimental evidences

The geometric packing has occasionally been used ([D.C. Richardson et al., 2005], [K.J. Walsh et al., 2008]) to examine under which conditions yielding occurs, and which are the resulting shapes after such occurrences, including the possibility of YORP-induced satellite formation (cf. § 1.3.3).

These studies have examined the behaviour of mainly *prolate* ellipsoids ($a_2 = a_3$) of different ellipticity under different spinning conditions. Their results (cf. fig. 3.2) show a very high strength for the aggregates in the low spinning regime, where almost any shape is permitted, up to spin limits at which a mass loss occurs and the remaining fragment reverts towards the hydrostatic sequences.

[K.J. Walsh et al., 2008] in particular, uses the crystalline structure as the "high friction" rubble piles with which the growing secondary mechanism is achieved, noting that in the non-crystalline packing (see below) this mechanism is prevented. In that case, a general reshaping of the body out of the spheroid shape occurs at high spin, which frustrates the possibility for expelled particles to remain in orbit (the medium friction case is a crystalline core surrounded by an amorphous packing of smaller scale spheres, which shows intermediate behaviour).

The crystalline structure presents various features that makes it unfit for a wide study on the possible shapes that a rubble pile may assume. First, it is an artificial construction arising only where it is expressly built up: every time there is a naturally driven concentration of spherical particles, they tend instead to assume an unordered packing. Similarly, when a crystalline body breaks down because of instabilities, it inevitably assumes the more natural amorphous structure.

Second, the crystalline structure shows a tremendously anisotropic behaviour (cf. [C. Comito, 2008, § 7.3]), going as far as having an angle of repose of $\sim 70^\circ$ against compressions acting along its construction layers' attitude, and very low ($<10^\circ$) along

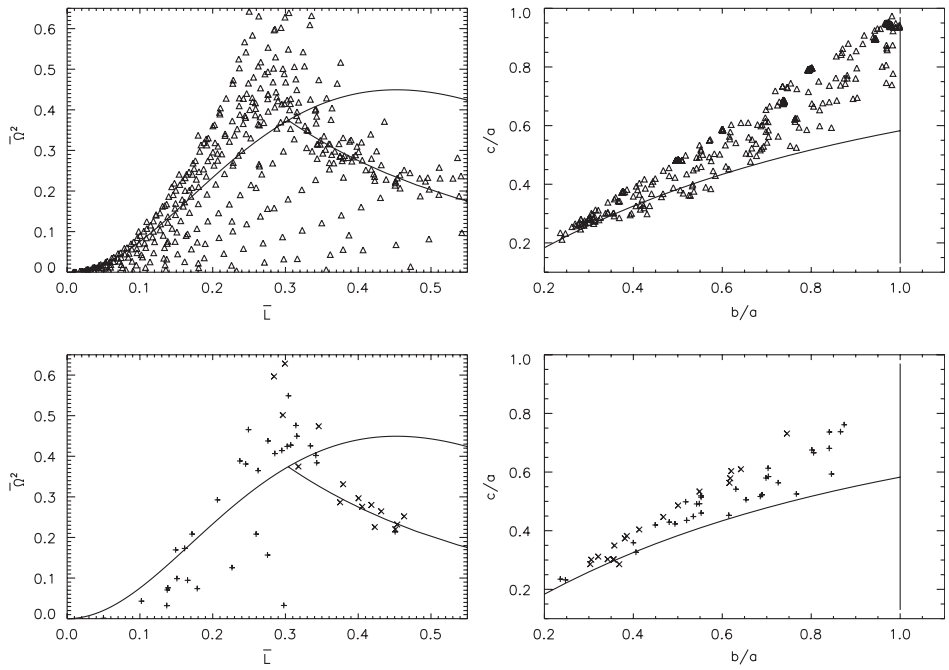

Figure 3.2: results of [D.C. Richardson et al., 2005]: above, all the simulations; below, only those with mass loss: '+' for losses up to 10%, '×' for those above 10%. from [P. Tanga et al., 2009 I]

the perpendicular direction[2].

Third, and perhaps most importantly, it does not allow for smooth transitions between shapes and for the exploration of the full range of possible configurations.

These reasons have been shown ([C. Comito, 2008] and see § 5.6.4) to strongly influence the results exposed above. Even the YORP-forming study (where a body is slowly spin up, see § 1.3.3) can be subject to similar problems, which somewhat limit the capability of this peculiar double asteroid formation process, which we expand in chapter 5.

For these reasons, to explore the shape space available for rubble-piles, we definitely used an unordered, amorphous rubble-pile structure (see fig. 3.3).

3.1.2 the "natural" packing: the "amorphous structure"

The crystal structure packing is not the natural packing obtained piling up spheres of homogeneous size.

It has been studied ([H.M. Jaeger, S.R. Nagel, 1992]) as, subjected to an external pressure, the spheres tend to assume a mainly irregular configuration, where every one tends to settle, within limits, at the centre of one of the faces of a tetrahedron formed

[2]In fact, this high angle of repose may come in handy if an internal friction or non-zero cohesion has to be modeled (or to take into account irregularly shaped components), but only when needed along a specific predetermined plane

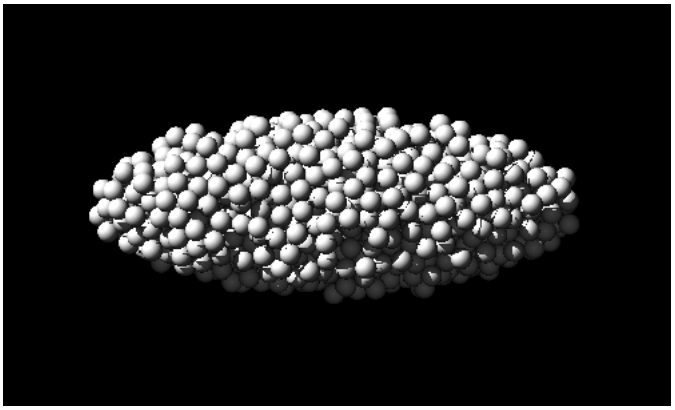

Figure 3.3: example of an aggregate created with a random ("amorphous") packing; cf. § 3.1.2

by other four (the tetrahedron not perfectly tessellating the space, this structure is discontinuous).

The irregular packing has a filling coefficient of about 64%, significantly lower than for the crystalline case, a fact that leaves inside the bodies more than a third of void space; this value is on the other hand fully compatible with the available estimates for asteroids believed to be rubble piles (cf. fig. 1.3).

This kind of packing is the one naturally observed in the case of re-accumulation simulations of particles from an initially dispersed cloud, of re-aggregation following a large mass loss from an initial body, or of a body reshaping after a massive yielding, and shows good isotropic properties.

The crystalline structure is of course completely prevented if spheres of different sizes are used; such mixing results in a very fluid-like behaviour ([K.J. Walsh et al., 2008], [C. Comito, 2008]) that appears unsuited for describing a rocky aggregate; the thesis work is thus concentrated on same-size unordered particles aggregates, which offer a suitable middle ground of study.

3.1.3 the "frozen" aggregates

`pkdgrav` can also manage multi-spheres blocks as rigid aggregates, by forcing the mutual distances of their component particles to remain constant. These "frozen" blocks can be set in the starting conditions and also be created at run-time when two particles (or blocks) collide with a predefined low mutual velocity (usually a fraction of the mutual escape velocity). Similarly, they can be broken at run-time in the case of a collision causing the differential stress between particles to exceed a certain strength threshold.

This has of course the effect of greatly increasing the computational burden on the computers, which makes the resulting simulations unsuitable for the present first exploring work on the nature of multiparticles binary fragmentation.

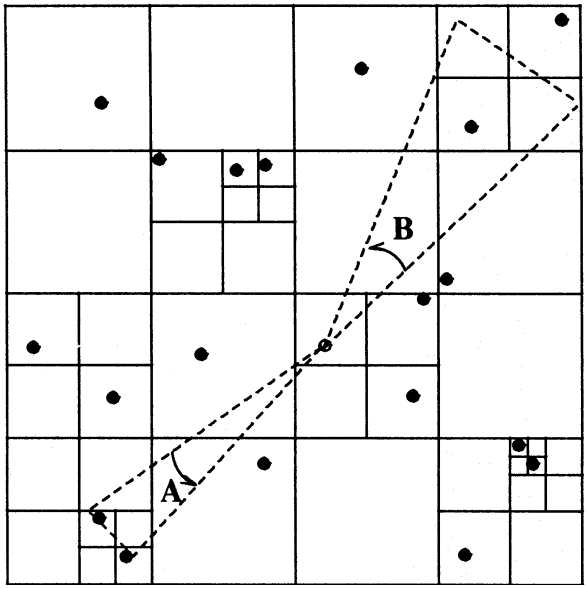

Figure 3.4: Example of tree code cells: in the integration of the forces acting on the central particle, angle B is sufficiently large for the subtending cell to be divided into it subcells for the force calculation; angle A, instead, is sufficiently small for the subtending cell to be treated as a single distribution with its multipole moments pre-calculated to quicken up the code. From [D.C. Richardson, 1993]

3.2 The tree code

A precise N-body interaction simulation must at every step determine N^2 interaction forces, which rapidly make the calculation burdensome as N increases. To alleviate this, `pkdgrav` implements for the calculation of the forces the hierarchic tree system proposed in [J.E. Barnes, P. Hut, 1986], which limits to a precise computation only the nearby particles interactions, while for far-away particle clusters it only considers the effects of a multipole expansion truncated at the desired order.

The tree code consists in the subdivision of the whole space in cubic bins in the following way: starting from the global cell corresponding to the whole space, every time it finds a particular cell to contain more than 1 particle, it divides the cell into 8 *children* subcells of (linear) size half of the *parent* cell's, and proceeds then in the same way to the analysis of each subcell (see figure 3.4).

The subdivision proceeds up to the point where every non-parent cell contains at most 1 particle, or when a prearranged sublevel limit l is reached, beyond which it is allowed for a l-level subcell to hold an arbitrary number of particles.

It is to note that the subcells are created only where needed: a cell containing 0 or 1 particles is not subdivided further, to limit the quantity of allocated memory and simplify the computations.

Position, speed and spin are recorded for every particle.

For every cell containing more than one particle[3] multipole moments are also computed relative to the internal distribution with respect of the cell's centre of mass.

To the order 0 (monopole), the field generated by the cell is approximated by that of a single particle of corresponding mass located in the centre of mass of the distribution:

$$\mathcal{M} = \sum_n m_n \tag{3.1}$$

$$\boldsymbol{\mathcal{G}}^{(0)} = \frac{\mathcal{M}\mathbf{r}}{r^3} \quad . \tag{3.2}$$

This requires the memorization of few data per cell, but it is generally a too rough approximation.

The gravitational dipole, calculated with respect to the centre of mass, is always zero

$$\mathcal{D}_i = \sum_n m_n x_{n;i} = 0 \quad , \tag{3.3}$$

so that the following order is the quadrupole moment:

$$\mathcal{Q}_{ij} = \sum_n m_n (3 x_{n;i} x_{n;j} - \mathbf{r}_n \delta_i j) \tag{3.4}$$

$$\boldsymbol{\mathcal{G}}^{(2)} = \frac{\mathcal{M}\mathbf{r}}{r^3} + \frac{\boldsymbol{\mathcal{Q}} \cdot \mathbf{r}}{r^5} - \frac{5}{2} \frac{(\mathbf{r}^t \cdot \boldsymbol{\mathcal{Q}} \cdot \mathbf{r})\mathbf{r}}{r^7} \tag{3.5}$$

which, being symmetric, requires the memorization of 5 additional elements.
Subsequent terms are of course usable for bigger precisions, but the quadrupole is generally sufficient for most cases.

Let's now consider a generic particle of which we want to integrate the motion, and be $\mathbf{r}$ the distance of the centre of mass of a generic cell containing more than 1 particle and d the linear dimension of the cell; we have that when

$$\operatorname{arctg}\frac{d}{r} \leqslant \theta_c \tag{3.6}$$

the effect of the masses contained in the cell considered is approximated with the multipole expansion; otherwise, the cell is resolved into the 8 daughter cells, and the (3.6) criterion is reconsidered for each of them (cf. fig.3.4).
Obviously, in the presence of a cell containing but 1 particle, its effect is calculated normally regardless of (3.6).

The θ_c is of course the key determining, as it is increased, the computation swiftness to the detriment of precision.

For a generic distribution of particles, a dependence of the integration time as a function of the particle number has been empirically noticed being of $O(N \log N)$.

The code is based on an evolution of an idea originally born for the study of planetary rings and protoplanetary discs, and it is particularly efficient in the case of a scattered distribution with the occasional bunch of objects whose effect on the supposedly many distant particles can be approximated with a consequent noteworthy time saving.

[3] and thus normally divided into subcells, unless it already is in the last allowed sub-level

The case of a single self-gravitating body is on the other hand the one where `pkdgrav` is less efficient: the high concentration of particles in a small space makes the multipole computation for every cell superfluous in most cases, as generally only cells containing a relatively small quantity of particles are treated as a single multipole contribution, all other subtending too large angles for every particle of the set, failing the (3.6) test.

As a consequence, in previous studies ([P. Tanga et al., 2009 II]) we found in fact a more prosaic N^2 dependence of computational time on the particles number.

An advantage of the tree system is nevertheless that of giving a precise and rapidly accessible hierarchy about the nearby particles, which is very useful in collisions foreseeing (see § 3.4).

3.3 The integration of the equation of motion

Particle integration happens by discrete and constant time steps whose length is selectable by the means of a parameter τ (`pkdgrav` having been written for Solar System dynamics, its internal system of units is so that $G=M_{\odot}=a_{\oplus}=1$ and the time unit is thus year$/2\pi$).

The algorithm used is the so-called *Leapfrog* which consists in the alternated integration of position and velocity with a $\tau/2$ phase lag.

Every step is composed of three parts: firstly, the stored velocities of the particles are linearly updated for a time $\tau/2$ with constant acceleration equal to the simple ratio between the total force acting on the particle and the particle's mass (as calculated at the start of the step); secondly, integration of the positions is performed at constant velocity for a time τ; finally, velocities are updated again by integrating them for another $\tau/2$ interval.

At the end of each step, the tree is then rebuild with the particles new positions.

The alternative way of integrating position-velocity-position, instead of velocity-position-velocity, is characterized by the same approximation level, but from experimental tests it appears to be slower.

3.3.1 the choice for the timestep

The length of the timestep to use in `pkdgrav` must be sufficiently low not to cause visible computational errors in the particles' velocities and positions, but not too much to overload the computation.

As the rubble-piles simulations are based on gravitational interactions, it is natural to use the characteristic free-fall time (the characteristic time needed for a cloud of size R, mass M and density $\rho = M/(4\pi R^3/3)$ to collapse under its own gravity)

$$t_{ff} = \frac{\pi R^3}{\sqrt{2GM}} = \sqrt{\frac{3\pi}{8G\rho}} \tag{3.7}$$

as a reference, and to choose a sensibly lower value (e.g. $\sim 1\%$ has been used in [P. Tanga et al., 2009 II], a previous work of ours briefly exposed in § 3.10.2).

3.4 Collisions detection

When updating the positions, the possibility for two particles to come at contact must be considered, in which case the couple is to be separately treated.

To foresee a possible future collision within a timestep, it would be necessary to determine for every particle pair whether they are approaching or not, that is whether

$$\mathbf{v} \cdot \mathbf{r} < 0$$

holds, with $\mathbf{r}$ and $\mathbf{v}$ relative position and velocity, and in such case compute the time necessary for them to collide, which is the lesser positive root of

$$t_{coll} = -\frac{\mathbf{r} \cdot \mathbf{v}}{v^2} \left[1 \pm \sqrt{1 - \frac{r^2 - (R_1 + R_2)^2}{(\mathbf{r} \cdot \mathbf{v})^2} v^2} \right] \quad , \tag{3.8}$$

where R_1 and R_2 are the two particles radii. If t_{coll} is less than the position integration step τ we are in the presence of a collision within the step.

In case that more than one collision is detected, the one relative to the shortest t_{coll} is of course processed first.

In practice, however, such a calculation is burdensome and of little relevance: what `pkdgrav` does when searching for collisions is instead considering for every particle only the nearest N_s ones, detected thanks to the tree disposition, with N_s a fixed parameter for each simulation (typically 32 is used).

In the case of a collision has been detected to occur, the code proceeds in the following way:

1. the smallest t_{coll} among all pairs is looked for: the corresponding collision is dealt with first
2. integration of positions happens at first up to time t_{coll} only
3. the post-collisional velocities of the particles are calculated (see § 3.5), and used to update the old, pre-collision velocities
4. a revision of all the future collisions involving the two particles takes place
5. the possible following collision is determined by comparison of the new set of t_{coll} values

until no further collisions are detected inside the timestep.

3.5 Collisions solving

Once a collision is detected to occur, it is necessary to determine the exit configuration, i.e. the after-impact linear and angular velocities of the two particles.

Be m_1 and m_2 the two particles masses, R_1 and R_2 their radii, $\mathbf{r}_1$ and $\mathbf{r}_2$ their positions, $\mathbf{v}_1$ and $\mathbf{v}_2$ their velocities and $\boldsymbol{\omega}_1$ and $\boldsymbol{\omega}_2$ their spins, and let the following quantities be defined:

$$\begin{gathered}
\mathbf{r} = \mathbf{r}_2 - \mathbf{r}_1 \qquad \mathbf{v} = \mathbf{v}_2 - \mathbf{v}_1 \\
\hat{\mathbf{n}} = \frac{\mathbf{r}}{r} \\
\mathbf{R}_1 = R_1\hat{\mathbf{n}} \qquad \mathbf{R}_2 = -R_2\hat{\mathbf{n}} \\
\boldsymbol{\sigma}_n = \boldsymbol{\omega}_n \times \mathbf{R}_n \qquad \boldsymbol{\sigma} = \boldsymbol{\sigma}_2 - \boldsymbol{\sigma}_1 \\
\mathbf{u} = \mathbf{v} + \boldsymbol{\sigma} \\
\mathbf{u}_N = \hat{\mathbf{n}}(\mathbf{u}\cdot\hat{\mathbf{n}}) \qquad \mathbf{u}_T = \mathbf{u} - \mathbf{u}_N \\
M = m_1 + m_2 \qquad I_n = \tfrac{2}{5} m_n R_n^2 \quad .
\end{gathered}$$

Let then the after-impact quantities be marked by " $'$ ".

Because of (linear) momentum conservation,

$$m_1(\mathbf{v}_1' - \mathbf{v}_1) = -m_2(\mathbf{v}_2' - \mathbf{v}_2) \quad . \tag{3.9}$$

As a consequence of the relative velocities of the contact points, each of the two particles will exert a torque on the other altering their rotational states:

$$I_n(\boldsymbol{\omega}_n' - \boldsymbol{\omega}_n) = m_n \mathbf{R}_n \times (\mathbf{v}_n' - \mathbf{v}_n) \quad . \tag{3.10}$$

Finally, to consider the dissipative forces between the two spheres,

$$\mathbf{u}' = -\epsilon_N \mathbf{u}_N + \epsilon_T \mathbf{u}_T \tag{3.11}$$

is imposed, where ϵ_N and ϵ_T are two suitable coefficients of elastic restitution, which take care of dissipating part of the energy of the collision ($\epsilon_N = \epsilon_T = 1$ is the completely elastic, no friction case, while $\epsilon_N = \epsilon_T = 0$ is the completely inelastic one).

The solutions of (3.9)-(3.11) then give the after-impact quantities, which are assigned to the two particles.

3.5.1 inelastic collapse and `dCollapseLimit`

A fact to be considered in the use of `pkdgrav` is that, by its own nature, it is not capable of managing two particles at rest in mutual contact. This creates a problem when two particles collide with too small a relative speed: because of the speed loss in the collision, they might tend to collide again after a small interval and so on, reducing the collision interval more and more, causing a block of the software.

To avoid this, `pkdgrav` uses a suitable "`dCollapseLimit`" parameter (henceforward, `dCL`) expressing a speed threshold so that any impact happening at lower speed is considered elastic, ignoring the passed parameters ϵ_N and ϵ_T. `dCL` is expressed as a fraction of the mutual escape velocity of the two particles, given by

$$v_e = \sqrt{\frac{2G(m_1 + m_2)}{R_1 + R_2}} \quad , \tag{3.12}$$

and is typically set at a sufficiently low value not to have any too visible large-scale effect.

The practical effect of this expedient is that of leaving, stored as random agitation of the particles, a certain residual "temperature" in a system in equilibrium, i.e. when the typical mutual speed of the particles has reached down values of order $v \sim \texttt{dCL} \cdot v_e/2$.

Such "thermal energy" can out of curiosity be compared to the gravitational energy:

$$\left|\frac{E_T}{E_G}\right| \approx \frac{Nm(\texttt{dCL} \cdot v_e)^2}{\frac{G(Nm)^2}{N^{1/3}R}} \approx \frac{\texttt{dCL}^2}{N^{2/3}} \quad , \tag{3.13}$$

and, for the typical values like those used for this thesis ($\texttt{dCL}=10^{-4}$, $N = 1000$), it is, with respect to the latter, negligible.

In [C. Comito, 2008], some tests have been performed to control if this value does create spurious effects, confirming it to be a good choice.

3.5.2 merge on collision

It is possible to set the outcome of collisions to either merge or bounce off the particles based on the impact speed. When merging, the two particles are removed from the simulation and replaced with a new one with the same total mass and linear and angular momenta (and with density either the same as the colliders' or a selectable value).

This is not used in the present work's simulations where all particles experience repeated slow-speed collisions, which would immediately collapse a compact body to a single particle in but a few steps.

3.6 Parallel computation

`pkdgrav` is specifically written for parallel computing. The routines can deftly assign different particles cluster far away from each other to different processors for faster processing, trying to minimise inter-processors exchanges as much as possible: this is normally favoured by the tree code and the reduced computations performed when the (3.6) condition is respected.

In the case of compact bodies, however, the situation is problematic: rarely the (3.6) condition is respected as long as intra-aggregates computations are considered and θ_c is set to a reasonable value. This has the different processors exchange a considerable quantity of data about smaller and smaller children cells, which slows down the computation.

In fact, the time saved by the parallel integration is often less than the time wasted by inter-processors data exchange, considerably slower than if all the computations were performed by a single CPU; this is so the case that actually simulation time increases the more processors are used! The best performances being attained by using a single processor, eventually the option of compiling `pkdgrav` without the expressly parallel subroutines resulted in a further time gain[4].

[4] the parallel environment may be more interesting for much higher N, though the absolute times involved are, as for now, prohibitive

This is a problem that appeared while we were performing tests to increase the efficiency of the computations, about mid-way of the doctorate work. As a consequence, all computations since then have been performed with 1 processor at a time, whichever was at the moment free at the OCA Mésocentre to accept a run without waiting for the most performing ones.

3.7 The heliocentric frame

To deal with Solar System simulations, `pkdgrav` also has a special *heliocentric frame* option. By using it, the frame of reference is changed from a strictly inertial one to one where the origin is fixed on a virtual mass of selectable size.

The resulting computation is slightly slowed for low particle density simulations due to the non-inertial frame. However, besides the convenience of having the coordinates referenced with the Sun (the difference being neglectable in most cases), this option has an advantage over simulating the Sun as a separate particle in the simulations of a single aggregate in heliocentric orbit. The latter choice would in fact create a much wider space to consider for the `pkdgrav` tree-code, forcing the creation of many empty cells and reducing the efficiency for collision searches among nearby particles.

This option has been used for the simulations in chapter 4.

3.8 Some relevant parameters

At call time (that is, when the programme is launched), `pkdgrav` accepts a series of parameters from an input file, upon which to set some internal variables used during the particles integration and collision routines.
A short list of those relevant to the present simulations follows:

dDelta : the timestep length, as discussed above

dTheta : the opening angle for the resolution of the cubic cells (see eq. 3.6)

nSmooth : the number of nearest neighbours checked for collision with each particle each step (to quicken the computational time, collisions are looked for only with those); set at 32 for all simulations - setting at lower values does not considerably save time

dEpsN : the normal coefficient of restitution for collisions; normally set at 0.8 [5]

dEpsT : the tangential coefficient of restitution; which we normally set at the same value as `dEpsT` [6]

dCollapseLimit : as discussed in § 3.5.1; normally set at 10^{-4} or lower[7]

iOverlapOption : this parameter regulates `pkdgrav` behaviour in the case a particle overlap is detected: see below

[5] in the range of values typical from literature
[6] a value of 1.0 is typical in literature
[7] there exists a similar limit also for the case of inelastic sliding, which is however of lower concern

3.8.1 `iOverlapOption`

It is possible that, because of rounding problems, two particles may be found overlapping. It is not normally a concern for low particle dentity systems like those for which `pkdgrav` was originally written, this kind of event being rare and the choice of one or the other of the following solutions having little effect. For dense systems like gravitational aggregates this happens frequently, and the choice of the solution can have dramatic consequences, as evidenced below.

`pkdgrav` offers four possible workarounds when an overlapping is found:

backstep : the particles are integrated back in time to a position just before the overlapping occurs, and a collision is resolved at that time

adjpos : the particles are moved away along the line connecting the centres for the smallest possible non-overlapping distance

repel : the particles are simply allowed to overlap (within limits), but the mutual gravity is substituted with a repulsive force, to somewhat simulate matter elasticity

merge : the particles are merged (cf. § 3.5.2).

As the `merge` option is useless for dense systems (cf. § 3.5.2), and the `adjpos` option has the possible outcome of being too rough, only the `backstep` and `repel` settings have been considered.

Both options have a controlling parameter:

dBackstepLimit : the maximum backstep time (or infinity): if a greater one is needed, an error is reported and `pkdgrav` halts

dRepelFactor : the magnitude of the repulsive force, as a fraction of mutual gravity (i.e. for a couple of overlapping particles the mutual gravity is effectively multiplied by $-dRepelFactor$).

Initially, we intended to perform a brief comparison between the two, to control their effective weights in determining the results (the difference should remain little for internal consistency).

However, we noticed some problems with the `backstep` case: in the course of long evolutions with massive aggregates, characteristic "explosions" may occasionally occur with no physical reason (see fig. 3.5).

These were likely due to the `backstep` option trying to backtrack particles in a dense system, causing successive backtracks for the new configuration an so on in a chain reaction that eventually manifests macroscopically or, alternatively, particles may be jammed in such a way that one is backtracked a while just to be found overlapping again in a short time, similarly causing a runaway series of backsteps, but the details are not clear. Initially, we found no way to circumvent the problem, and so sticked for precaution with the `repel` option.

Eventually, we found that another linked option could be in part responsible: the `bStrictOverlap` option can be set to ignore overlaps between receding particles (i.e.

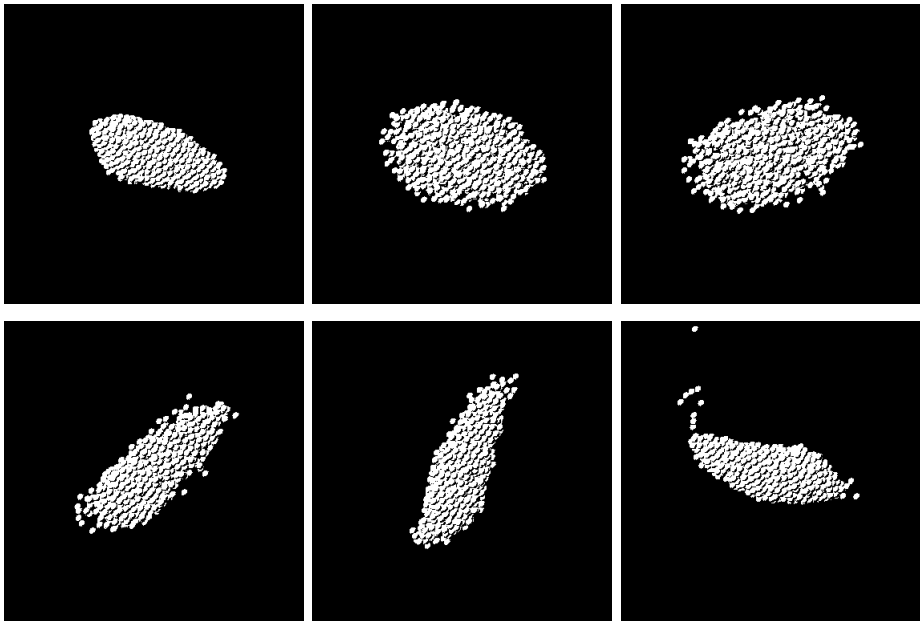

Figure 3.5: An "explosion" sequence occurring with the `backstep` setting for `iOO` during a simulation. Panels to be read left to right, top to bottom as a single sequence; the represented body is rotating anticlockwise (polar view). See § 3.8.1

if the overlapping problem is being solved by itself), thus decreasing the number of detected "effective overlaps". This apparently makes the problem disappear; though, no extensive tests have been performed to further investigate the matter.

The limited number of (correct) runs performed with `backstep` does not have us to believe the overall effect of the `iOO` option chosen to be of importance.

3.9 `rubble pile analizer`

`rubble pile analyzer` (`rpa`) is a companion programme to `pkdgrav` that extracts statistical data from a given `pkdgrav` particle distribution data file (this stores the mass, radius, position, velocity, spin for each particle, among other things such as simulation time).

3.9.1 identification of aggregates

The first and foremost problem to face is the detection of the aggregates themselves: as in `pkdgrav` two particles never rest on each other (cf. § 3.5.1), we cannot simply impose contact between particles to identify the aggregates. Instead, one has to recognise and isolate the aggregates in a generic particle dispersion, trying to understand which of these are in fact part of a single object, on the basis of the available data on particle positions.

To that purpose, `rpa` uses a recursive test to determine and isolate the aggregates trying to accumulate two of them into one if they are found at a sufficiently small distance, based on a settable *linking scale* parameter $\geqslant 1$.

`rpa` starts considering every particle as a separate aggregate, and then follows the algorithm:

1. analyses one aggregate at a time and looks for the nearest aggregates in a similar way to that used by `pkdgrav` to detect collisions (see § 3.4); if on all the neighbours the test has already been performed, it proceeds to the next aggregate

2. for each neighbour it determines if the spheres centred in the two centres of mass and having as radii the respective semimajor axes multiplied by the *linking scale* overlap at least partially (for axes determination, see below § 3.9.2): in the case the test fails, the merging is not considered, and the following neighbour is considered

3. in the case of a positive outcome, it determines if the two aggregates are both single particles, in which case the overall test is considered as positive, the two particles are considered a single aggregate, and the following neighbour is tested

4. otherwise (i.e. in the case of multi-particle aggregates) it checks whether at least one of the following is true:

   - the two spheres centred on the centres of mass and with radii the respective semiminor axes overlap
   - the centre of one of the two aggregates is found within the imaginary ellipsoid (see below) with which the other is modeled, scaled with the *linking scale*

   in which case the two aggregates are considered in fact part of the same, otherwise they are not; in both cases, the next neighbour is considered

5. a cycle of analyses being finished, if at least a pair of aggregates has been merged into one, another cycle is performed, otherwise the algorithm ends.

The algorithm used by `rpa` for the determination of aggregates is quite powerful so as to allow it to work in most cases without issues.

However, it presents some limits in the case of particularly elongated bodies or in cases where a secondary is found in orbit around the primary in a particularly close passage (e.g. at pericentre), both cases being however of little issue.

In the first case, contrary to a simple visual analysis, with the typical values used for the *linking scale* ($1.1 \div 1.2$), very elongated aggregates are detected as multiple (usually 2) bodies. This kind of problem arises for unnaturally long, cigar-shaped objects that have nonetheless been observed in our simulations as stable figures of equilibrium for fast rotating gravitational aggregates. In chapter 4 we deal mainly with body disruption and the following re-accumulation, which generally produces overall spherical bodies, but the problem is somewhat more present in chapter 5.

This behaviour appears strictly linked to the random nature with which `rpa` examines the particles configuration in search for aggregates, and to its accumulating process

used to aggregate the rubble piles as they are being detected in the recursive procedure shown above.

Normally, when two of the particle aggregates that are being recognized have encompassed all the particles that are between them and come into contact, they are simply merged due to them passing the test performed in point 4. It may be the case that, however, two quite elongated fragments do meet with an unfavourable configuration, where their separation is of the order of the semimajor axes, too high for them to pass the test. If no other particle or aggregate is left nearby that can join either of the two fragments and so possibly favouring a future merging test, the two fragments can remain formally separated, and manual intervention is needed, when discovered.

This usually is simply a manual increase of the *linking scale* from its standard value of 1.1 to values of 1.11, 1.12 or 1.2 . In some cases, this is not sufficient due to the internal configuration of the particles within the aggregate, and a more brutal use of a high *linking scale* is used.

This has, again, no practical issues until the fear arises that some particles may detach from the primary and remain close to the surface before possibly resettling down, a relevant event that alters the measurements and is missed from detection if a high *linking scale* is used.

The second problematic case is the opposite one: in some cases the instabilities can produce a cloud of fragments orbiting a large and usually fast rotating primary typically near the threshold of losing more particles due to centrifugal forces. The cloud itself is unstable, and as it evolves particles settle onto the primary as new may come off: during this time the exact limit of the primary is difficult to determine, as any near particle risks being included in the aggregate (and distorting the perceived size and shape, see below), and manual adjustments to the *linking scale* are to be made to give results consistent with the visual observation as far as possible.

The process can be at times tricky to distinguish between the two cases, but is generally manageable.

Moreover, the behaviour of the algorithm is not monotone in the *linking scale*(!), and in certain cases we experienced this directly. This is due to the fact that, once the *linking scale* is augmented somewhat from λ to $(\lambda + \delta\lambda)$, it is possible for a merging test to pass between an aggregate and a neighbour of its at a distance $R(\lambda + \delta\lambda/2)$ (R being the aggregates dimension), which would have failed with *linking scale*=λ: in this case, the centre of mass changes position, and this can affect the following tests performed upon the fragment, for example a merging with a third fragment at distance $R(\lambda - \delta\lambda/2)$ from the original aggregate, now too far away, which would have passed had the first test failed.

3.9.2 determination of dimensions

Once an aggregate is found, `rpa` tries to give an estimation of their dimensions, with the supposition of them being approximately ellipsoidal. It takes care of determining the centre of mass, and then the direction of the axes by the computation of the inertia

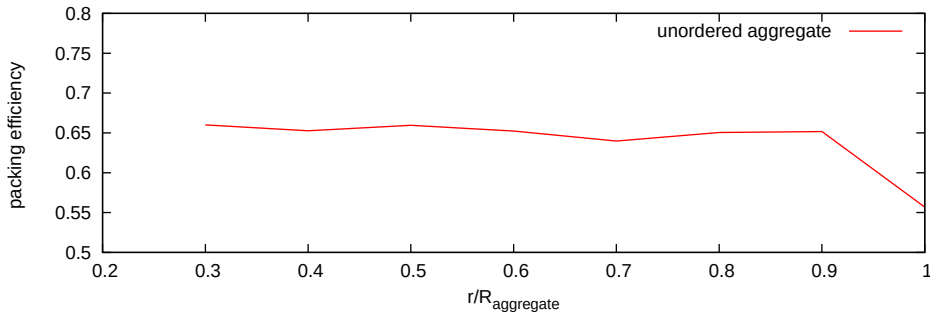

Figure 3.6: trend of the packing efficiency within a rubble-pile: on the x-axis the considered fractional distance from the centre of the aggregate where "1" indicates the size detected by `rpa`, and on the y-axis the packing efficiency (spheres volume / total volume) of the spheres lying inside the ellipsoid whose axes are those declared `rpa` multiplied by the corresponding x value; the density is constant up to 90% of the measured dimension and well corresponding to the experimental results described in § 3.1.2

tensor

$$\mathsf{I}_{ij} = \sum_n m_n(\delta_{ij}x_n^2 - x_{n;i}x_{n;j}) \quad , \tag{3.14}$$

of which the eigenvectors are found: these give the direction of the axes, i.e. the spatial orientation of the ellipsoid.

To determine the effective lengths it considers, starting from the centre of mass, the distance of the farthest particles in the three considered directions:

$$a_i = \max_n |\mathbf{r}_n \cdot \hat{\imath}| \tag{3.15}$$

where the $\mathbf{r}$ are the distances from the centre of mass, and $\hat{\imath}$ is the orientation of the i-th axis, finding the candidate values for the ellipsoid axes lengths. From here, it keeps increasing all three found dimensions of a factor $(1 + 10^{-3})$ at a time a number of times needed so that all particles lie within the virtual ellipsoid, maintaining the mutual ratios of the three.

One of the problems in the axes estimation by `rpa` lies in the fact that it tries to include within the ellipsoidal shape all the particle. Even the case of a single surface particle in a position too far from an hypothetical "smooth" surface can determine the artificial increase of the detected axes lengths: as a result, a low-density surface layer is included in the aggregate, thus invalidating the measures of dimensions, as well as all the related quantities (above all, density and the normalization factors for $\overline{L}$ and $\overline{\Omega}$), even if the axes ratios may be correctly measured (the re-scaling happens homogeneously for all three lengths) as long as any problematic particle lies far from the six "poles".

Our estimates performed for [P. Tanga et al., 2009 II] have told us that the error may be contained within 10% of the values estimated by `rpa` (see fig. 3.6), with 95% as a best value, at least for approximately ellipsoidal shapes.

Particularly elongated or flat objects can cause more problems, as for a 1000-particle

object minor axes can be as short as a couple of particle diameters, and incertitudes can cause more hassle[8].

Even more problematic are obviously non ellipsoidal objects, such as those found in chapter 5 preluding a fission. To have an order of magnitude for the incertitudes over the dimensions, we can estimate an error within a particle diameter on the measured axes lengths. By considering a 10% excess on $\bar{a}$ ($\sim$ a particle diameter over the radius of a 1000 particles spherical aggregate), we obtain an error on $\sqrt{GM^3\bar{a}}$ (the normalisation factor for $\overline{L}$) of $\sim 5\%$. This has been somewhat corrected by assuming a fixed packing efficiency of $\sim 2/3$, in line with both the measures obtained with the more regular bodies and the theoretical results of § 3.1.2.

Not being $\bar{a}$ too crucial a parameter for the interpretation of results, we sticked to 0.95 times the results given by `rpa` if an absolute length was needed.

A slightly different problem lies in the estimation of the axial ratios incertitudes, the issue being in determining how much of the axes length error is systematic on all three axes (and so being, irrelevant for the ratios).

It is to note that for stable bodies obtained at the end of simulations, the measured axes ratios do not vary over time, suggesting an overall regular surface without free wandering particles on it (which would tend to settle in one of the holes of the surface in short time). Besides, as a matter of fact, even a reasonably high of $R_p/R_{aggregate} \sim 5\%$ (for a 1000-particle aggregate, less for greater N) does not invalidate any of the thesis results, and so we simply accept the given values when needed.

3.9.3 determination of angular velocity

The angular velocity $\mathbf{\Omega}$ is determined by inverting

$$\mathbf{L} = \mathsf{I} \cdot \mathbf{\Omega} \tag{3.16}$$

where the angular momentum with respect to the centre of mass $\mathbf{L}$ is easily calculated from the particles' positions and velocities.

There not being significant sources of error in the calculation of $\mathbf{\Omega}$ for a stable body, the main problem comes from the fact that binary bodies, which we simulate here, do interact with timescales (the mutual orbits) comparable with the rotation periods themselves. We consequently tried to measure rotation periods for the components of a binary when at large mutual elongation.

3.9.4 tracking of orbital parameters

By itself, `rpa` does not calculate the relevant physical and orbital parameters for the minor (not primary) bodies beyond controlling if their instantaneous orbits are stable (i.e. e<1 and pericentre distance>primary radius). We added the relevant routine as to have `rpa` output the desired quantities in a convenient way. We also added the calculations for the gravitational and kinetic energies, and a suitable procedure has been added in order to trace these quantities.

[8] these are, however, mainly "pathological" cases

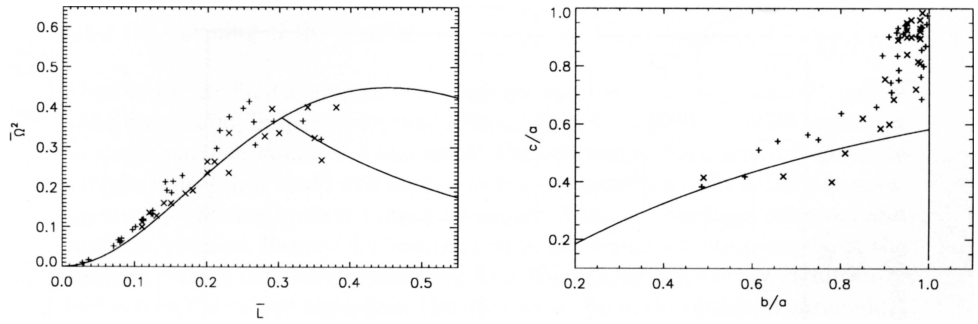

Figure 3.7: Results of [P. Tanga et al., 2009 I] compared to the Maclaurin and Jacobi sequences: + for simulations with N=500 particles, × for simulations with N=1000 particles. A tendency of forming Maclaurin spheroids when the initial cloud is spherical has been evidenced, while Jacobi-like bodies can only be obtained in the case of elongated clouds. No objects are formed with $\overline{L} > 0.4$. From op. cit.

3.10 Some previous results on perfect rubble-pile models

3.10.1 re-accumulation studies

In a past work ([J.F. Consigli et al., 2006], [P. Tanga et al., 2009 I]), we performed a study on the re-accumulation process of particles from an initial cloud with a certain velocity dispersion.

The general results showed how the obtained shapes are in general well represented by the classical hydrostatic sequences (see fig. 3.7).

An interesting feature has been that, independently of which kind of cloud shape, velocity dispersion or initial angular momentum was imposed to the system, no resulting aggregate could be formed with an $\overline{L}$ significantly higher than 0.4.

3.10.2 equilibrium of gravitational aggregates

As seen above (cf. fig. 2.6), by examining the shape distribution of asteroids it appears that these are far from the classical hydrostatic sequences.

A previous work of ours ([P. Tanga et al., 2009 II]) had shed light on the connection between finite-size aggregates and hydrostatic theories.

To simulate a relaxed population of asteroids, we considered a series of different rubble-piles, modeled with `pkdgrav`, of different shapes, and put them under a rigid body rotation at different angular momenta to observe the shape they would assume in the subsequent evolution.

starting conditions

We used as the starting objects for our simulations a number of ellipsoidal configurations composed of homogeneous spheres. We created ellipsoid of different shapes by varying

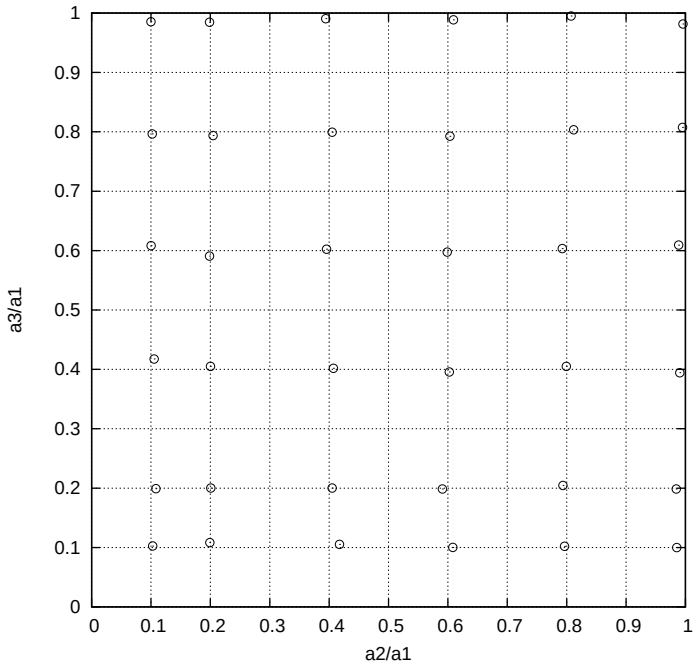

Figure 3.8: initial configuration for the aggregates

the axes ratios $(\alpha_2; \alpha_3)$ in the set

$$0.1 \quad 0.2 \quad 0.4 \quad 0.6 \quad 0.8 \quad 1.0$$

for a total of 36 configuration sampling the whole $(\alpha_2; \alpha_3) = [0; 1] \times [0; 1]$ configuration space.

The aim was to use N=1000 particles aggregates, a number which does not overburden the computation yet allows for a variety of shapes to be assumed. To obtain aggregates with unordered packing in all the desired shapes, the actual bodies have been obtained by carving them out of a 5000 particle aggregate that we obtained by the collapse of a disperse cloud with an initially zero particle velocity. To carve the more extreme shapes of low α_2 and/or α_3 and fit their length within the sphere diameter, theoretical a sphere of some 10^5 particles would be needed, too burdensome[9] to be created with a random process. The trick of deforming the 5000 particle object has been used, by having it spin at high angular velocity to increase the equatorial radius before carving out those problematic shapes. Yet, the most extremes of these were not possible to obtain in a 1000 particle configuration, and we had to stick with 800 and 500 particles respectively for the ($\alpha_2 = 1; \alpha_3 = 0.1$ and vice-versa) and the ($\alpha_2 = 0.1; \alpha_3 = 0.1$) cases (see fig. 3.8).

All bodies were set with particle density $\rho_p = 3000\, kg/m^3$ and radius $R_p = 50\, m$, typical for asteroid rock densities[10] and large fragment lengths for rubble piles (some-

[9] with the available hardware, the time to calculate a single integration step grows to beyond a day

[10] we remember that ρ_{bulk} for an unordered packing of spheres is $\sim 2/3\rho_p$

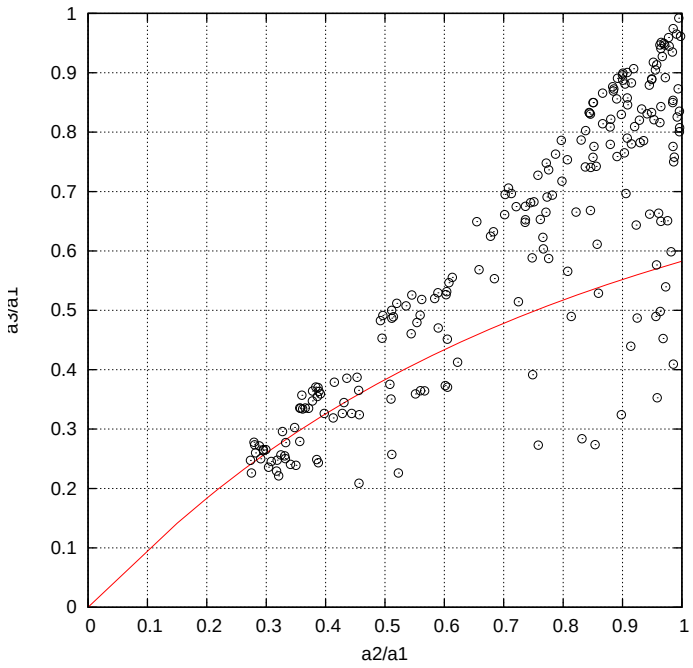

Figure 3.9: Final equilibrium shapes found in [P. Tanga et al., 2009 II] for bodies of different initial shapes and $\overline{L}$ between 0 and 0.5 compared with the Jacobi (traced line) and Maclaurin (right border) sequences. cf. fig. 2.6.

what smaller than Itokawa's two main components - cf. fig. 1.4).

We run different simulations for each of the bodies, by giving it different initial rigid body rotations along the a_3 axis so as to sample $\overline{L}$ in intervals of 0.1 from 0 to 0.5, an upper bound for the reshaping mechanism without mass loss, and letting each of them free to evolve. As timestep (cf. § 3.3.1) we chose $\tau = 8 \cdot 10^{-6} \frac{yr}{2\pi} \simeq 40\,s$, being $\sim$1% of the t_{ff}. 500 steps ($\sim$ 5.5 hours) have been used for each simulation, which were more than enough for each to reshape and reach the equilibrium.

results and comparisons

Our expectation was that they would follow the gradient of the gravitational+kinetic energy content, dissipating energy by internal friction, before coming to rest at a more energetically favourable shape at constant angular momentum.

By studying the energy content for the different ellipsoidal shapes (see fig. 3.10) supposed at equilibrium at a given $\overline{L}$, we verified that the simulated rubble-piles did indeed migrate towards the minima (which are in fact the MacLaurin and Jacobi figures). Yet, due to the internal frictions, this migration was stopped prematurely, and a dispersion of shapes resulted.

The striking results were that the final distribution of bodies at equilibrium (fig. 3.9) has a strong resemblance to the observed asteroid shape distribution (see fig. 2.6).

By examining the final results, an estimation of the angle of repose for a perfect

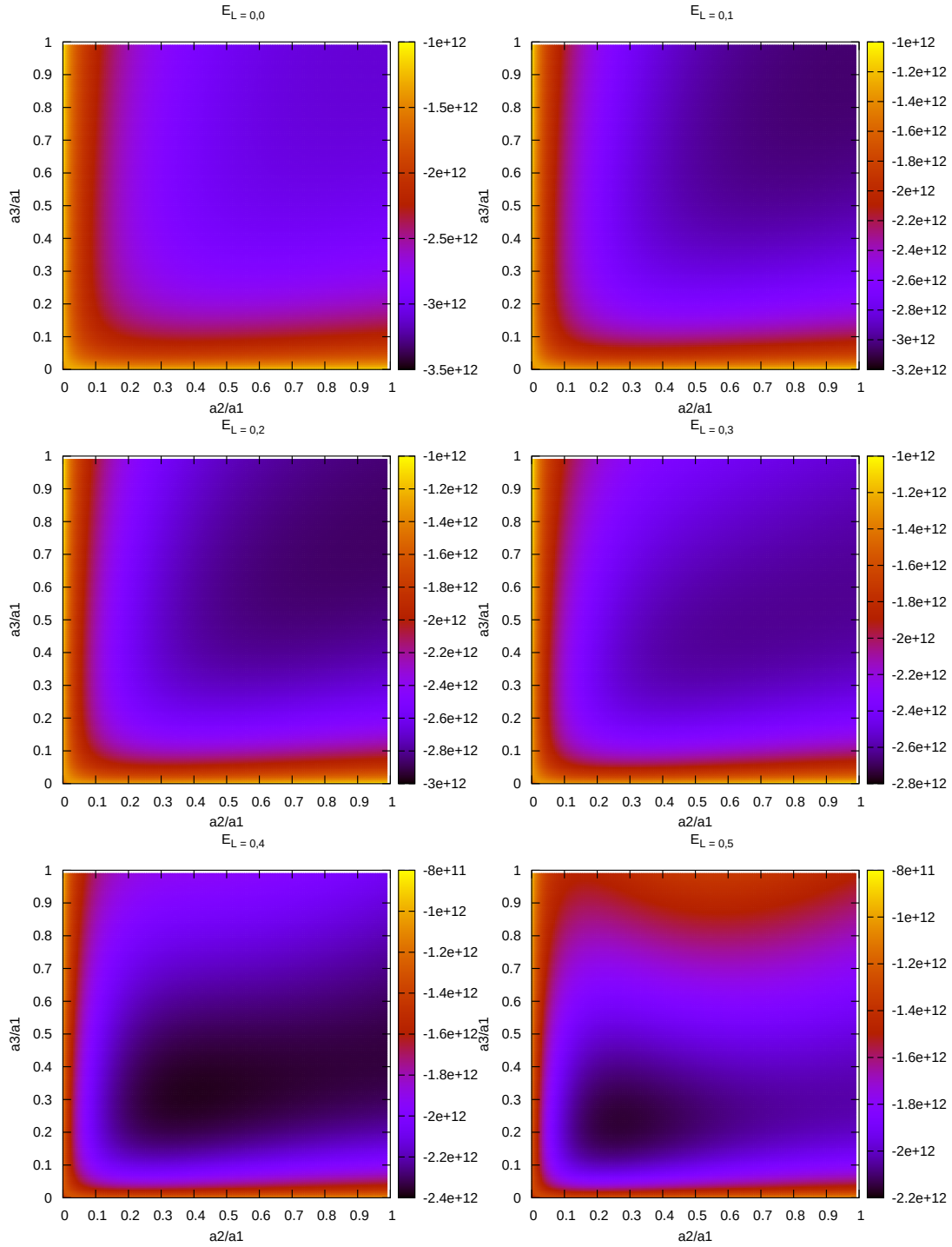

Figure 3.10: Trend of the content of the kinetical+gravitational energy content (arbitrary scale) for ellipsoidal bodies supposed at equilibrium ($E_{\overline{L}}$) for increasing values of angular momentum from $\overline{L} = 0$ to 0.5: the minima correspond to the Maclaurin and Jacobi sequences of fluid equilibrium (1 Maclaurin shape per value of $\overline{L}$, and 1 Jacobi shape per $\overline{L} >\approx 0.304$). Similar figures exist for the angle of repose needed to sustain each shape (cf. fig. 3.11). images from [C. Comito, 2008]

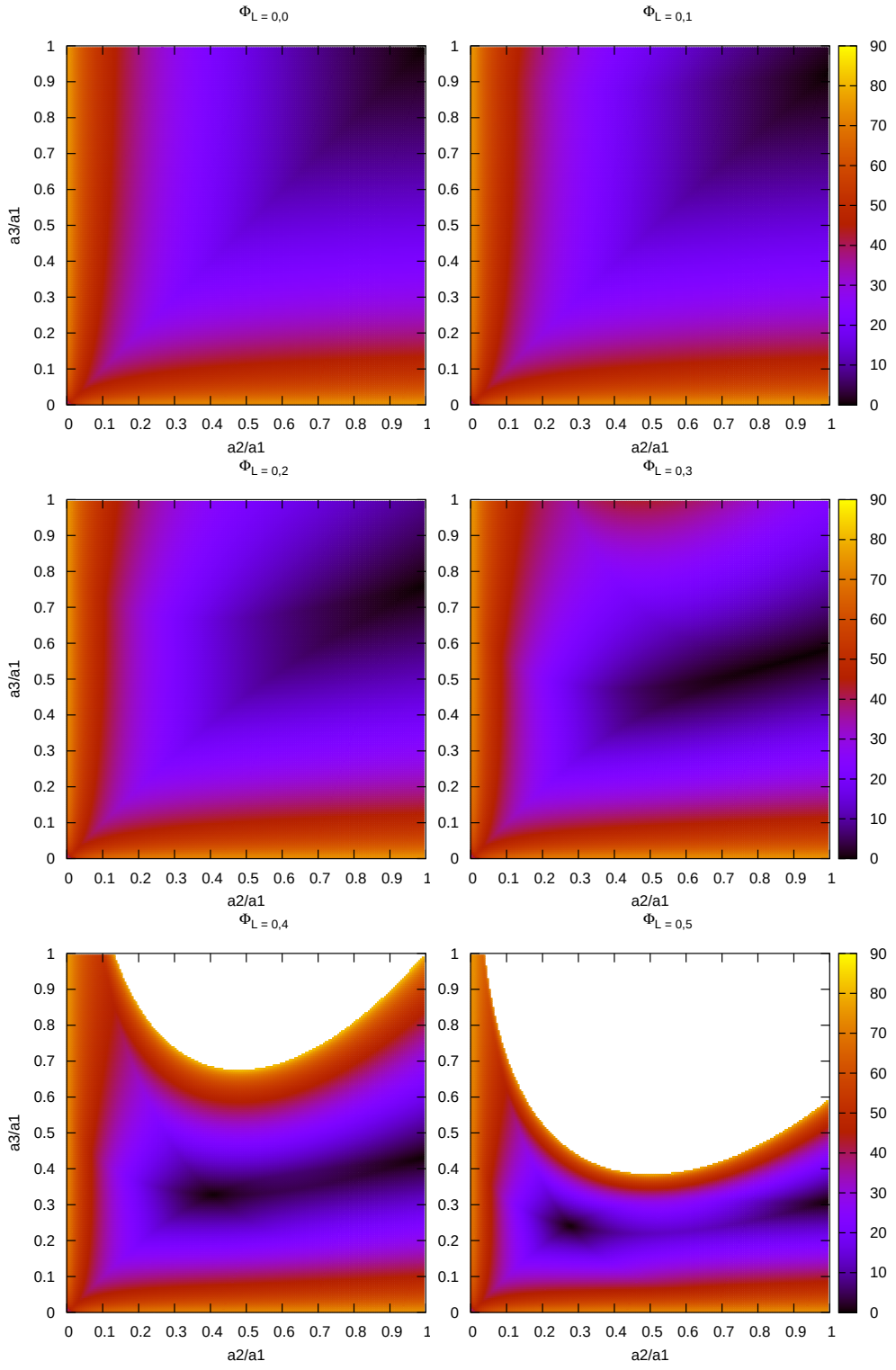

Figure 3.11: Trend of the minimal angle of repose to sustain a given ellipsoidal shape supposed at equilibrium for increasing values of $\overline{L}$ from 0 to 0.5: the zeros correspond to the Maclaurin and Jacobi figures for each specific $\overline{L}$. For high angular momentum, some shapes become unbearable without an active cohesion (the white zones). cf. fig. 3.10. images from [C. Comito, 2008].

rubble pile of equal sized spheres could be given at $\approx 5^{\circ}$ (cf. also fig. 3.11)[11].

This study set the background for the simulations we present in chapter 4, where we explored the behaviour of the bodies under faster rotations in search of a binary formation process.

[11]This angle of repose is, for cohesionless materials, the same as the maximum angle at surface between the local normal to such surface and the perceived gravity+centrifugal field direction for these ellipsoidal bodies, giving a link between the macroscopic and the microscopic physic levels

Chapter 4

High Angular Momentum Simulations

To have a view about the likelyhood and stability of a catastrophic binary-forming process we ran different series of simulations starting from a unitary rubble pile body setting it to a large angular momentum content.
This simple choice of approach was dictated by multiple reasons.

Firstly, it is a general approach unbound from the specific characteristic of the impact that may have created it.

Secondly, it is of help in describing a general unstable situation to study the main trends that the objects may take, under a variety of different kind of processes: one such example would be, in a case similar to those studied in chapter 5, where a slow increase of angular momentum due to external factors does bring a partly fragmented but still mildly cohesive body outside the stability region for cohesionless bodies (cfr § 2.1.5) before the centrifugal force can definitively tear it apart.

Thirdly, it allows us to study the possibilities of (at least short-time, see § 4.3.3) stability for a high angular momentum system, and the likelyhood for it to survive for a significant time.

Finally, this study integrates and complete a previous work ([P. Tanga et al., 2009 II], see § 3.10.2) that examined the stability for rubble-pile bodies under low angular momentum content, showing how the actual observed asteroid shape distribution is compatible with a relaxed rubble-pile population. While there we were interested in mass conserving reshape, here we explore the possibility of forming a binary from a highly unstable starting body.

4.1 Initial configurations

4.1.1 the initial shapes and parameters used

In the simulations we used as starting particle configurations the same bodies used in [P. Tanga et al., 2009 II]. Briefly, these are 36 different ellipsoidal shapes of axes ratios α_2 and α_3 each assuming the values

$$0.1 \quad 0.2 \quad 0.4 \quad 0.6 \quad 0.8 \quad 1.0$$

each composed of 1000 equal spheres[1] of density and radius

$$\rho_p = 3000\, kg/m^3 \quad R_p = 50\, m$$

organized with the "amorphous" packing (cf. § 3.1.2).

The resulting bodies mean radius is $R \sim 620\,\mathrm{m}$ (this gives a scale for the different pictures showing the evolutions).

For ease, all considerations about shapes are given with reference to the ellipsoidal shape space (α_2; α_3). The initial configurations have been represented in fig. 3.8

For the coefficients of restitution we used

$$\epsilon_N = \epsilon_T = 0.8 \quad .$$

These are in line with the values used in [P. Tanga et al., 2009 II], and other values have there been shown not to significantly alter the results, as long as they remain lower than 1.

As timestep (cf. § 3.3.1) we chose to keep the [P. Tanga et al., 2009 II] value of $\tau = 8 \cdot 10^{-6} \frac{yr}{2\pi} \simeq 40\, s$, but run the simulations for a much longer time corresponding to 10,000 steps, or ~ 4.5 days.

`dCL` has been set at 10^{-4}.
For `iOverlapOption` we used the `repel` option, in accordance with § 3.8.1.

4.1.2 angular momentum content

As previously said, we created different sets at different angular momentum contents.

At a fixed angular momentum, only two ellipsoidal shapes can be in an equilibrium configuration (albeit unstable at high $\overline{L}$), corresponding to the MacLaurin and Jacobi shapes; for high $\overline{L}$, slightly deformed elongated shaped are also stable (see § 2.1.6). All objects are then either attracted towards these equilibrium shapes conserving all mass (and consequently all L), or the initial instabilities are too large and the body is fragmented in the reshaping process.

As seen in [P. Tanga et al., 2009 II], a value of $\overline{L} \sim 0.4 \div 0.45$ is the upper bound for which all objects can reshape without mass loss; this limit corresponds in fact to the maximum (§ 3.10.1) obtainable angular momentum content for re-accumulated bodies from a dispersed cloud with random initial particle velocities: the re-accumulation of higher angular momentum aggregates being prevented by the intrinsic instability of the these latter objects. Correspondingly, we started our search for asteroid binaries formation from the $\overline{L} = 0.5$ value, and increased it by 0.1 for each successive set.

For convenience, we aligned the initial rotation axis a_3 of the body with the z-axis of the inertial frame.

[1] save for 3 for which 800, 800 and 500 particles were used: see § 3.10.2 for details over construction of the initial bodies

To have a comparison with real objects, we note that for $\overline{L} \sim 0.7 \div 0.8$, an "average" prolate object ($\alpha_2 = \alpha_3 = 0.5$) of density $\rho \sim 2000\,\mathrm{kg/m^3}$ will have a rotation period near the limit spin observed for medium-sized to large asteroids (with more spherical objects reaching the limit rotation for lower $\overline{L}$ contents). A higher $\overline{L}$ is thus attainable only in a catastrophic collision event.

4.1.3 presence of the Sun

To simulate a more physical background, we inserted the Sun in the simulation. The latter is not actually created as an additional particle, but rather the `pkdgrav` *heliocentric frame* option (see § 3.7) has been used, and all objects have been initially put in a circular orbit around the Sun at a conventional distance of 2.5 AU. The orbital plane has been chosen to be the x-y plane: i.e. perpendicular to $\overline{L}$, with the object internal angular momentum aligned with the orbital one. We expect the presence of the Sun to only be significant for long term stability (several heliocentric orbits) or for high mutual distances for a formed binary (apocentre outside primary Hill sphere), being negligible for short-term dynamics at single rubble-pile scale.

4.2 Results: $\overline{L} = 0.5$

The $\overline{L} = 0.5$ case appears as a transition value between the lower $\overline{L}$ cases, where objects do not present cases of mass loss and are able to deform into equilibrium figures, and the higher spin ones described below.

The behaviours of the simulations are roughly classifiable into 2 different categories, depending on their initial shape:

- those starting far from the spheroid shape (i.e. with $\alpha_2 < 1$) tend to converge towards the stable Jacobi shape for $\overline{L} = 0.5$
- those starting as spheroid (i.e. with $\alpha_2 = 1$) tend to keep at least in a first phase a more axisymmetrical shape and migrate towards the corresponding MacLaurin figure

with both cases possibly showing some form of mass loss.

4.2.1 Jacobi-attracted

The first behaviour is the predominant one, due to the low stability of the MacLaurin shapes at high L. The final shape is invariably in the vicinity of the Jacobi figure for $\overline{L} = 0.5$.
About a 1/3 of them, whose initial shape is near the region in which the hydrostatic stable shape is located, show no mass loss at all.

As we consider shapes farther away from this semi-stable region around the Jacobi shape, mass loss starts to occur. This mass loss is in the form of single particles or little clusters (in many cases, less than 5 particles, corresponding to 0.5% of the initial mass). All the particles lost at this stage are from the "tips" of the ellipsoid. On the whole,

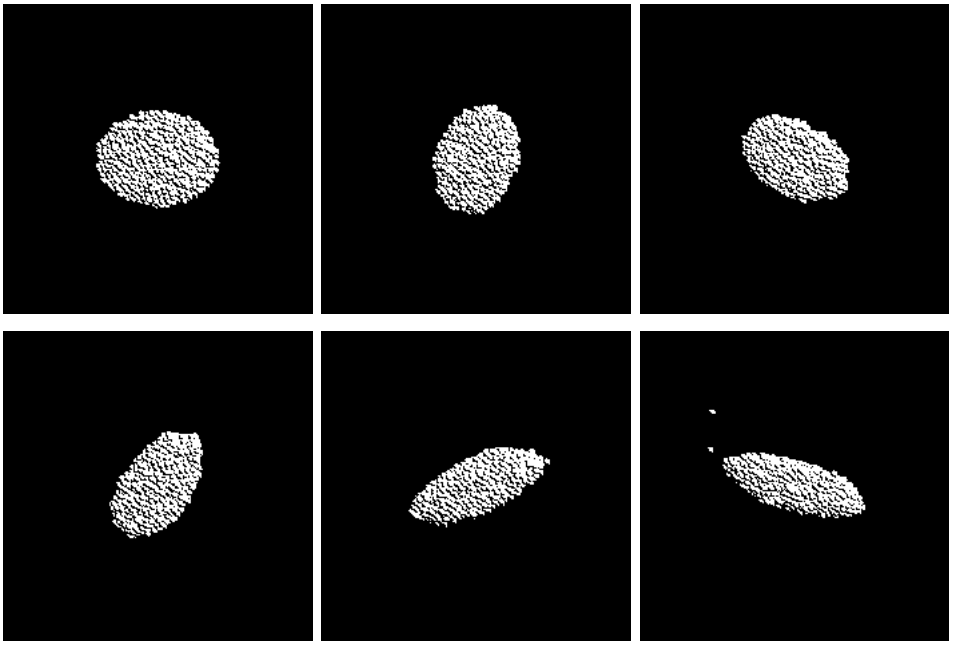

Figure 4.1: Sequence of evolution of the 5_8_2 body (see § 4.4 for nomenclature) seen from polar view; rotation proceeds anticlockwise. Initial shape and after 100, 200, 300, 500 and 700 steps; left to right, top to bottom. The body is towards the Jacobi ellipsoid with $\overline{L} = 0.5$. A small mass loss is evident. Typical behaviour for many bodies at median $\overline{L}$

about half of them lose no mass or less than 5 particles (0.5% of the initial mass) (see fig. 4.1).

In some cases, those farther from the stable Jacobi object, the mass loss is more important. It is of note that, due to the centrifugal nature of the mass loss, the lost particles are those with a high specific angular momentum content (with respect to the centre of mass frame of the object, neglecting in this phase the heliocentric motion). This entails a net loss of $\overline{L}$, which settles however in all cases between 0.42 and 0.5.

4.2.2 MacLaurin-attracted

The second kind of behaviour is more chaotic. The fluid MacLaurin shape for $\overline{L} = 0.5$ lies in the vicinity of the $\alpha_3 = 0.3$ point. This configuration has, however, low stability, and tends to lose its symmetry and transform into the Jacobi shape. Only one of the considered bodies, the one starting with $(\alpha_2; \alpha_3) = (1; 0.4)$, already near the point, is capable of maintaining a stable fully axisymmetric shape with no mass loss.

All others spheroids, while initially tending to migrate towards this point, do not manage to come to a stable configuration. The initial reshaping phase driving towards the MacLaurin equilibrium happens very fast, within 4000 to 10000s (1 to 3 hours, with reference to an initial rotation period of $\sim 6h$). The result of this fast deformation is a relatively flat, irregular body showing some asymmetries. Some particles may be expelled from the fast rotating body in the initial phase, generally remaining gravitationally bound to the primary and remaining in orbit around it. This configuration

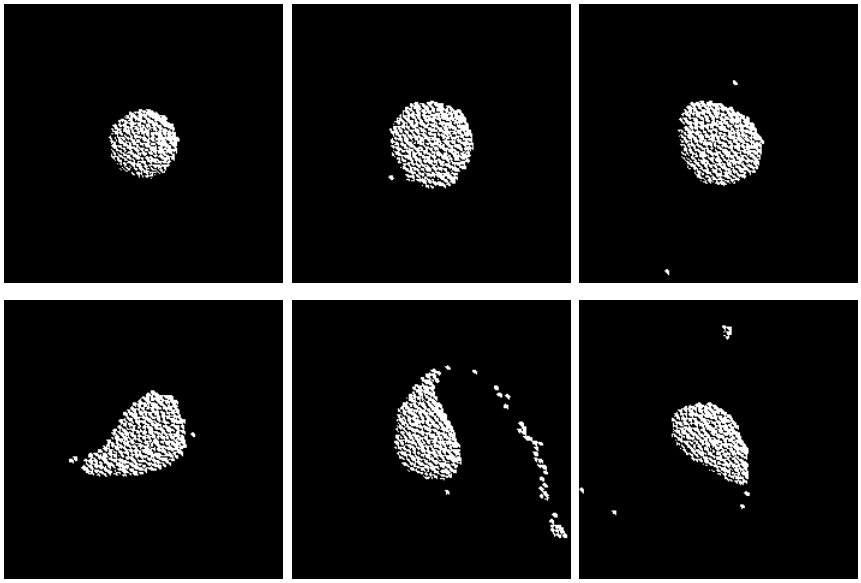

Figure 4.2: Sequence of evolution of the 5_A_6 body (see § 4.4 for nomenclature) seen from polar view; rotation proceeds anticlockwise. Initial shape and after 400, 1000, 1500, 1800 and 2500 steps; left to right, top to bottom. At first maintaining an approximately axisymmetric shape, it then collapse to a more favourable energetic configuration. Part of the mass expelled falls back to the primary while a part remains in orbit. Typical behaviour for initially spheroidal bodies at median $\overline{L}$

of the primary is not stable; in a relatively short time of typically $10^5 s$ (1 day), the asymmetries may grow, eventually leading to a more robust reshaping towards a more elongated shape. This transition is more brutal, and produces a loss of mass, which occur from the "tip" of the long axis, corresponding to the particles with the highest tangential velocity with respect to the centre of mass (see fig. 4.2). This mass loss is contained in a few percent of the total mass, and expelled at high speed in generally unbound, hyperbolic orbits, composed of mainly single particles with possibly a few small clusters.

The resulting configuration is a more or less elongated body which can be either ellipsoidal or drop-shaped, with a remaining $\overline{L}$ between 0.4 and 0.45, and possibly a few particles in orbit around it.

This behaviour is similar to the first stages of some chapter 5 results involving spheroidal initial bodies (cf. § 5.3.12).

4.3 Results: $\overline{L} = 0.6$ and higher

Starting from $\overline{L} = 0.6$, the behaviour starts to concentrate into four main classes, which can clearly be distinguished from the starting configuration. A qualitative map for the different behaviours is given in fig. 4.3-4.5.

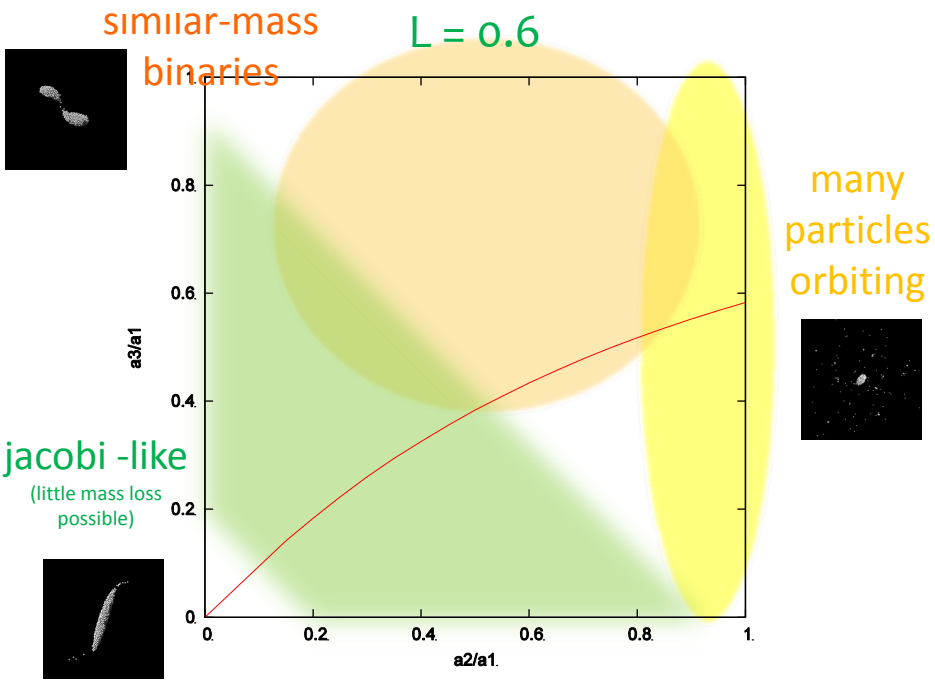

Figure 4.3: Map of the regions of different behaviours in funcion of the starting configuration for $\overline{L} = 0.6$. The different behaviours are discussed in § 4.3.1 and following. Extension of the regions is approximative and borderline behaviours exist.

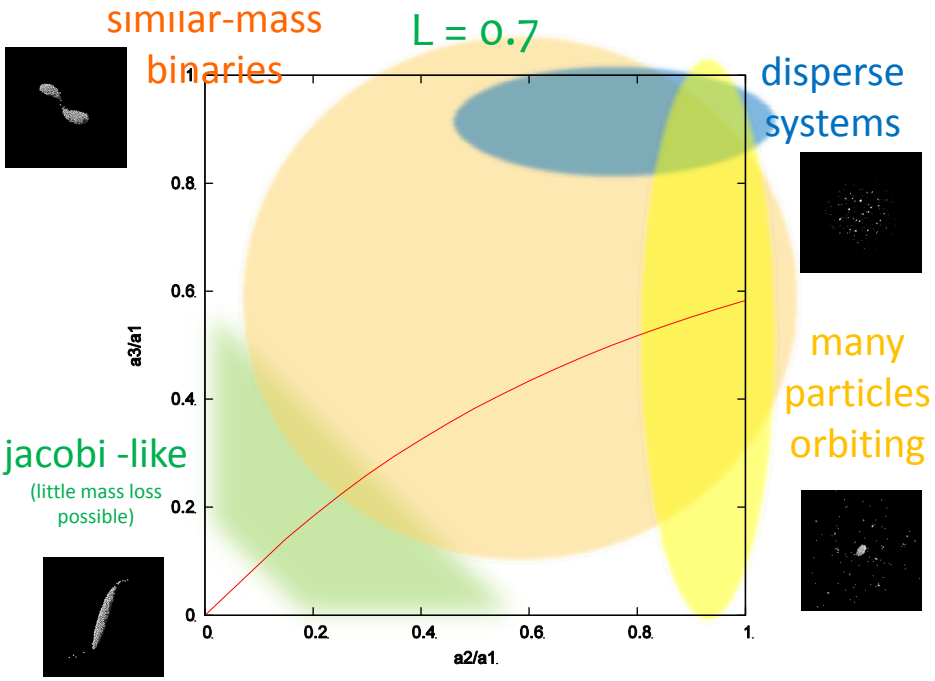

Figure 4.4: As for fig. 4.3, but with initial $\overline{L} = 0.7$. Dispersed systems also appear.

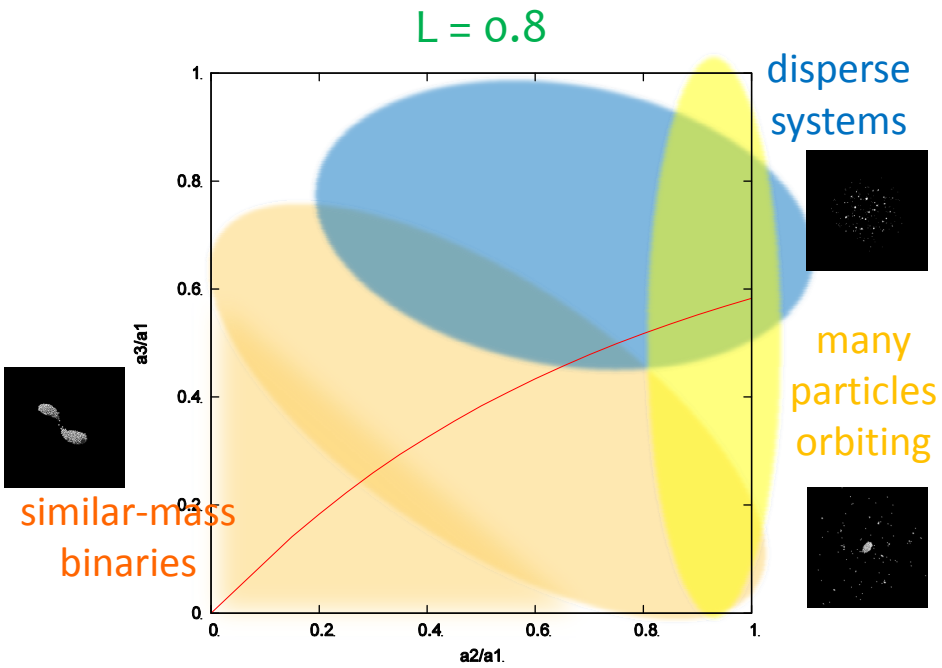

Figure 4.5: As for figg. 4.3 and 4.4, but with initial $\overline{L} = 0.8$.

4.3.1 Jacobi-like

This class is related to the general behaviour observed for the $\overline{L} = 0.5$ case. In a region around the corresponding Jacobi configuration, objects are generally capable of reshaping into an elongated ellipsoidal body, with however some particle loss from the ends of the long axis.
The more the initial angular momentum increases from 0.5 to 0.7, the more the region of the $(\alpha_2; \alpha_3)$ plane showing this behaviour shrinks, and the greater the mass loss become. The resulting configuration for this class are elongated bodies with rotation periods in the range $5.8 \div 8$h, depending on shape and $\overline{L}$. By the very nature of their history, generally these bodies are rotating with a spin just below the threshold of losing more mass by centrifugal force. No Jacobi-like figure is reached for $\overline{L} = 0.8$ and beyond.

4.3.2 many particles orbiting

This class is the heir of the second type of behaviour observed for the $\overline{L} = 0.5$ case, and is represented by the initially spheroidal bodies. In some cases, the spheroid may abruptly deform into an elongated shape with a consistent mass loss. In most cases, though, their axisymmetrical shape coupled with the high angular velocity results in an initial isotropic "equator explosion" and a following re-organization of the mass into a (usually slightly) elongated primary and a cloud of orbiting particles (see fig. 4.6).

It is to note that the loss of axial symmetry is a general process involving fast rotating bodies: this is in line with the classical hydrostatic theory according to which the MacLaurin sequence is unstable at high L.

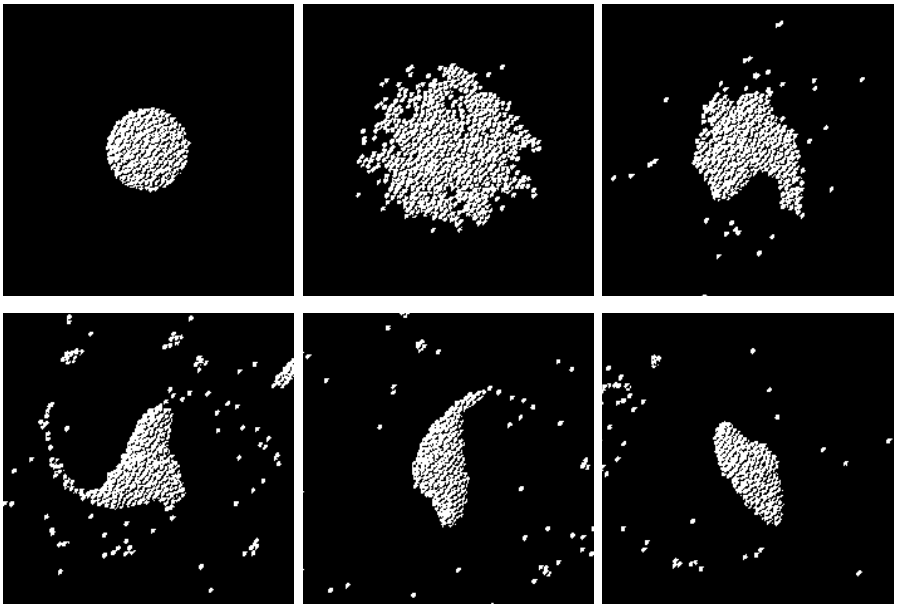

Figure 4.6: Sequence of evolution of the 7_A_4 body (see § 4.4 for nomenclature) seen from polar view; rotation proceeds anticlockwise. Initial shape and after 200, 500, 800, 1100 and 1400 steps; left to right, top to bottom. The body initially expands and then re-arrange its mass into an elongated primary and a cloud of orbiting particles. Small secondaries form and part of the mass is expelled from the system.

The particles and small clusters that separates are generally emitted with relatively low speed, under the escape velocity from the remaining body, resulting in a cloud of small satellites orbiting a fast rotating and possibly slightly irregular primary at close range. The primary, being simply what is left by the mass loss process driven by the centrifugal force, is as a consequence rotating at a speed just below further mass loss.

This system of irregular primary + cloud is in continual evolution: because of the chaotic interactions between the fragments, occasionally, particles from the cloud settle more of less gently onto the primary, while others detach from it. These latter are picked up from the ends, possessing a weight barely capable of having them stick to the primary surface, being easily put into orbit by the interaction with the cloud or by the slow reshaping process that the primary in undertaking. The primary, in turn, may deform driven especially in the beginning by the internal forces, and overall by the mass exchange with the cloud. The cloud itself presents an evolution, with the particles' orbits interfering and the particles themselves being directed towards one of three possible fates: colliding with the primary, being expelled from the system, or slowly coalescing with other particles into small clusters.

The number of bodies in the cloud starts decreasing by one of the described processes, the evolution timescale being of the order of a few days. The small satellites that grow around the primary tend to strongly interact and have chaotic orbits, having them follow one of the same fates of the single particles, in a process slightly reminiscent of that of a protoplanetary cloud.

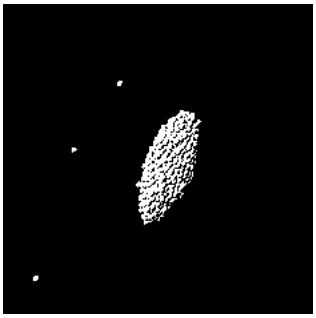

Figure 4.7: The primary of 7_A_4 after 10000 steps (4.6 d): its shape has been regularized (cf. fig. 4.6).

After the initially chosen run time, some configurations show a depleted cloud containing generally no consistent satellites. Some cases are more interesting, with a generally small but noticeable satellite composed of some tens of particles at most which has survived the initial chaotic phase, and has acquired an initially stable orbit. The clouds themselves are not completely dispersed by the end of the 4.5 days time, and a number of small 1-particle satellites often remain in orbit after a few days.
The primaries, with time, are slightly drawn to more regular, energetically favourable shapes (cf. fig. 4.7).

This behaviour, as $\overline{L}$ increases show a more and more pronounced initial fragmentation of the primary, sliding gradually towards the behaviour described in § 4.3.4.

4.3.3 similar-mass binaries (and multiple)

A third class of behaviour starts arising from the $\overline{L} = 0.6$ simulation. Examining the plots of the energy content and angle of repose necessary to maintain equilibrium for the different ellipsoidal shapes at different low-to-medium $\overline{L}$ (see fig. 3.10 and 3.11), one can note the appearance for the middle values of $\overline{L}$ between 0.3 and 0.5 of a range of shapes for which, regardless of the friction that can be present for the constituent material, no equilibrium is possible without a cohesion among the components. This unstable region is not too surprisingly initially contained within the $a_3 > a_2$ portion of the plane (i.e., the bodies rotating around the middle axis), which are known to be particularly energetically unfavourable. This region becomes wider the greater the considered $\overline{L}$, arriving with $\overline{L} = 0.5$ to comprise most of the considered ellipsoidal shape space.

Bodies originally within this region are too far from equilibrium to reach an equilibrium shape, as the strong centrifugal force works to tear them apart. What results is an extreme stretching of the aggregate, which then breaks into two big objects, with some mass possibly left over (see fig. 4.8 for a typical example).

The main characteristic of this class is thus the almost instant creation of a similar-sized couple, with most initial mass contained within the couple.

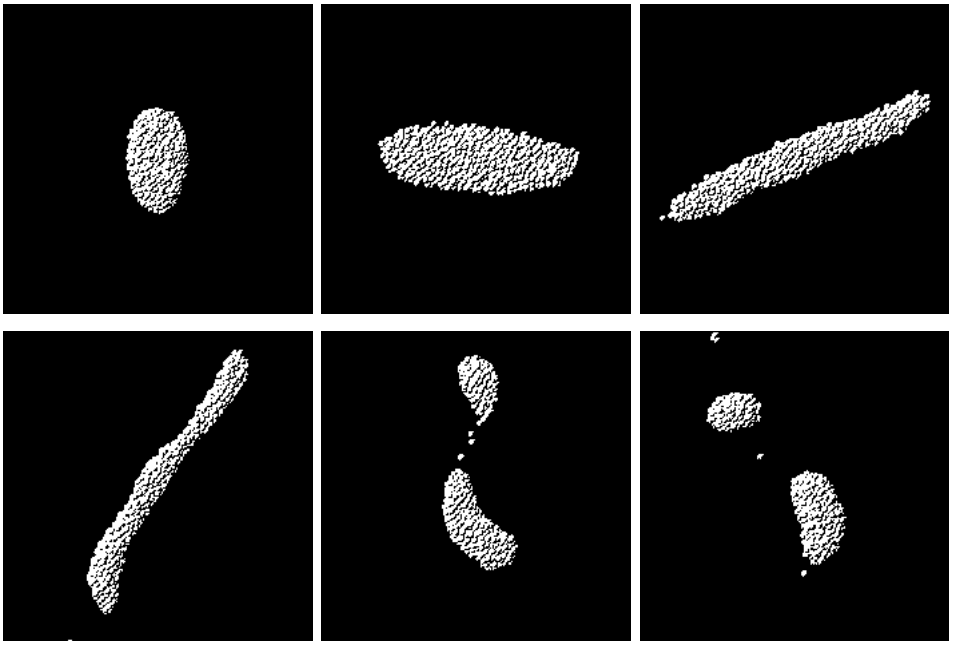

Figure 4.8: Sequence of evolution of the 7_6_4 body (see § 4.4 for nomenclature) from polar view; rotation proceeds anticlockwise. Initial shape and after 100, 200, 400, 600 and 800 steps; left to right, top to bottom. The high rotation rate stretches the aggregate, which eventually fission.

Considering the way it has been formed, the initial shape of the mutual orbit is invariably a very elongated or close one. In fact, the pericentre distance must be no greater than the value of the mutual distance of the two bodies at the instant they "formed", i.e. when the parent's material could be considered to be effectively been split into the newborn bodies, which in turn is typically of 2 or 3 initial parent diameters at most. The rotation status of the two bodies is, approximately, dictated by angular momentum conservation for the two halves of the parent, with the remaining angular momentum and energy (part of which dissipated by friction in the splitting process) determining the global a and e values.

The two members of the pair can generally be considered half or fully re-accreted bodies, and assume typically ellipsoidal shapes, generally fast rotating, with primary rotation periods mainly in the $2.5 \div 3.25$ h range (with some slower).

The initially planned time for each evolution is too short to follow the couple and study any mid-term evolution process. To obtain more interesting results in that direction, we chose some of the objects in this class to be followed more throughly along a longer period, as described in § 4.4.

ternary and multiple systems

Occasionally, and more and more as $\overline{L}$ increases, this binary forming process leads to the coalescence of 3 objects of comparable size, which may at first remain gravitationally bound.

As the number of created objects increases beyond 2, the system is driven more and more chaotic, with full 3-body interaction in play. Some systems have been followed throughly in § 4.4.

Eventually, as the number of created bodies grows along with more unstable configurations and higher starting $\overline{L}$, less and less mass remains bound to the primary, leading to a dispersed system.

4.3.4 dispersed systems

As $\overline{L}$ increases, eventually too unstable configurations are created. A region starts to appear at $\overline{L} = 0.7$ around $(\alpha_2; \alpha_3) = (0.8; 1)$, i.e. in the most energetically unstable zone, where the behaviour of cases 2 and 3 (§ 4.3.2 and § 4.3.3) is brought to an extreme.

These systems have a positive overall energy, and are disrupted by the high centrifugal forces into many fragments of different masses that begin to disperse. Some clusters may form around the most massive objects, which could lead to multiple bound subsystems orbiting the Sun with similar orbits (see fig. 4.9).

The transition from cases 2 and 3 into the disperse systems behaviour is not a sharp one, and the boundaries given in fig. 4.3-4.5 are approximative. A choice could be made of defining this region as where less than 50% of the initial mass remains bound within the most massive subsystem (primary and satellites), but even then the chaotic nature of the fragmentation process would only allow us to trace but an approximating boundary.

The dispersed systems have the potential of being a very interesting laboratory for asteroid binary formation, and one case has tentatively been followed for a longer time in § 4.4.

4.3.5 $\overline{L} = 0.9$ and above

The behaviour described in § 4.3.4 starts becoming predominant for $\overline{L} = 0.9$ and beyond, with more dispersed systems forming and with less mass conserved around the primary. We chose to stop simulation at $\overline{L} = 1.0$, where physical starting configuration are deemed too rare to give significant results.

4.4 Subsequent binary evolution

The relatively short time initially reserved for the systems to evolve is enough to draft a classification of the possible outcomes, as given in § 4.3. Generally, a first regime is reached in $\sim$ a day where the behaviour can be categorised according to the broad cases shown.

Border cases exist which can be classified as transition cases from one region to another.

In the most interesting case where a binary system is formed, however, the short time is only enough for 2 or 3 full orbits at most. To obtain a deeper understanding of the stability for those systems, as we previously said we selected a few of them preferentially in the "similar-mass binaries" case, and extended their simulation for a

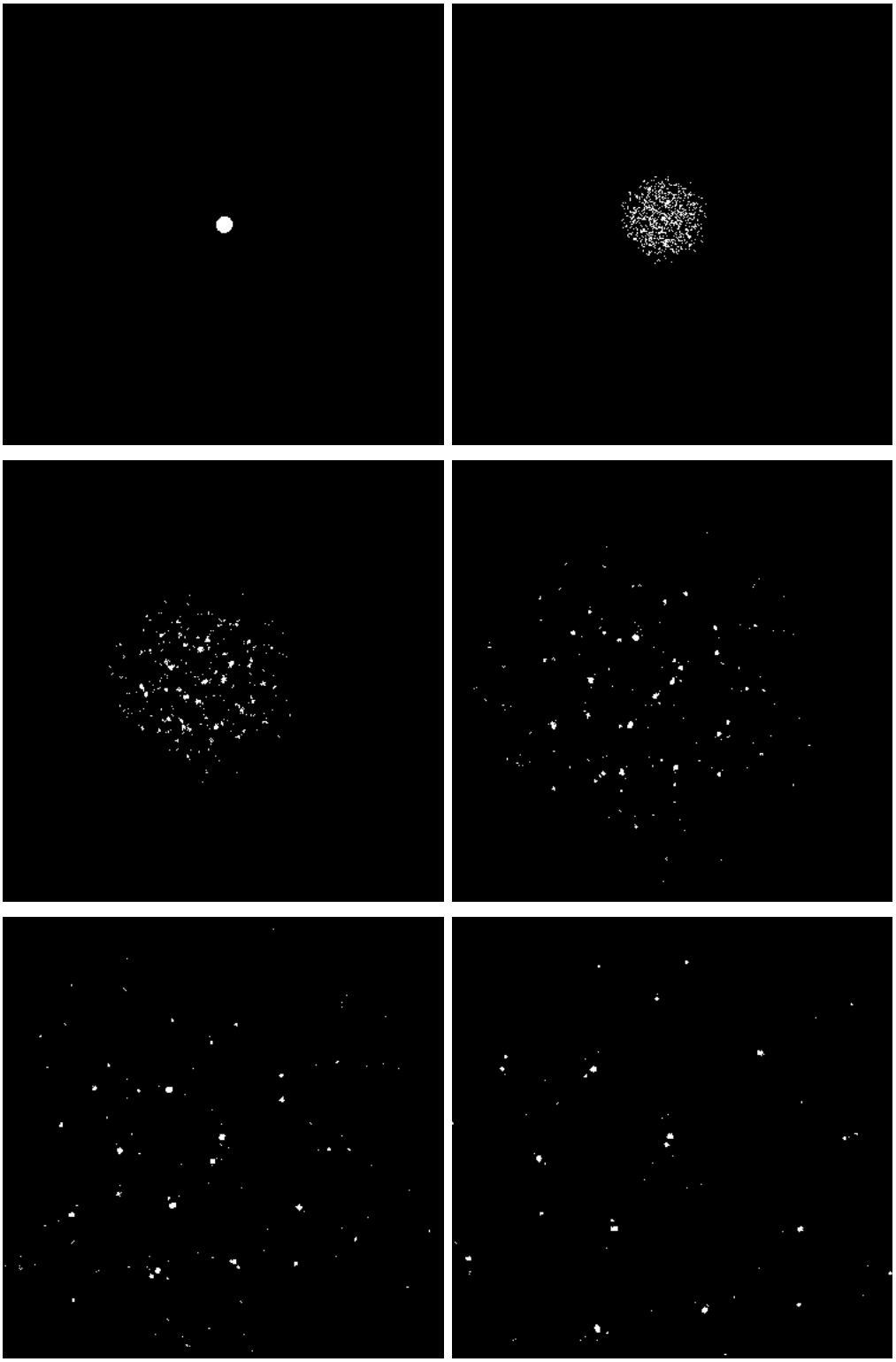

Figure 4.9: Sequence of evolution of the 8_A_6 body (see § 4.4 for nomenclature) from polar view. Initial shape and after 200, 500, 1000, 1500 and 2500 steps; left to right, top to bottom. The initial object is a spheroid of euatorial radius $\sim 750\,\mathrm{m}$; the images have a side length of $\sim 30\,\mathrm{km}$. The high angular momentum disrupts the body in multiple fragments. Some cluster may subsequently re-join or form isolated binary/multiple systems which remain in similar heliocentric orbits.

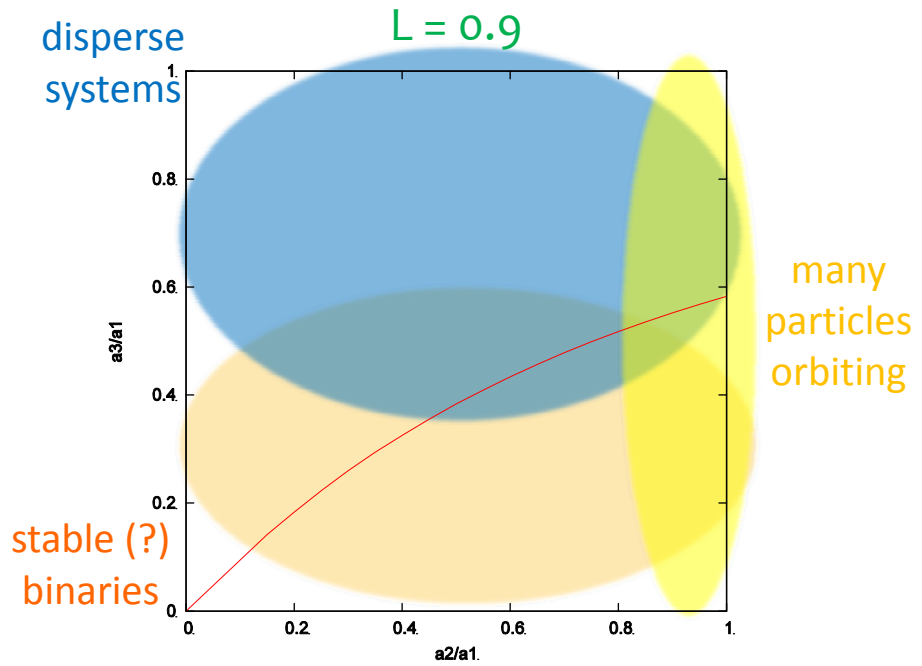

Figure 4.10: As for fig. 4.3, but with initial $\overline{L} = 0.9$. Dispersed systems are predominant, and many binaries formed by fission are not gravitationally bound.

longer time of 200h of CPU time each, which is the standard allotted time for medium-length simulations at the OCA Mésocentre, and corresponds to about 280,000 time steps, or $\sim$ 130 days (about 9% of a full heliocentric orbit at 2.5 AU).

The particular configuration of two large objects bound in an elliptical orbit is prone to different possible short- or mid-term scenarios. The pair will evolve under the action of the shapes-spin-orbit couplings, where all three elements vary in the process. Our general expectation is that, due to the continuing action of the other member, each aggregate would be continually stimulated, leading it to assume a more and more energetically favourable configuration, corresponding in principle to the Jacobi or Poincaré sequence of shapes, and thus a more regular one.

In a longer process, assuming the orbit proves to be stable, the spin-orbit periods would be moved towards each other by tidal forces to a synchronous binary like some that have been observed (cf. § 1.3.1).

The very nature of the often highly elliptical initial orbit is however the key in setting the whole after-the-split evolution as a chaotic process. The very close pericentre distance, of the order of a few primary radii, greatly enhances normal two-bodies interaction. In this scenario, the shape of the orbit is expected to abruptly change at each pericentre passage; this would not normally be an issue in an isolated system: as long as the total energy is negative, the couple is kept bound.

Here the Sun starts playing its disturbing role. The Hill radius for an asteroidal

object orbiting the Sun in a circular orbit at 1 AU is ~ 150 primary radii[2], and for the chosen distance for the simulations (2.5 AU) it is ~ 350.

It is natural to think that, if the mutual orbit of the two bodies of the asteroid couple is safely contained within the primary Hill sphere, the couple would remain bound.

If, on the other hand, the orbit deforms too much, the apocentre could be driven dangerously near the Hill radius, thus having the Sun enter play, eventually separating the couple.

As a general rule, every system behaves differently and any of the possible scenarios presented in § 4.4 is possible.

A brief description for each of them follows, to illustrate how the different final configurations can be formed. Each of the simulations is named with the triple X_Y_Z describing the initial conditions, where X denotes $10\times\overline{L}$, Y and Z respectively $10\times\alpha_2$ and $10\times\alpha_3$ ("A" has been used for the value of "1"), and in brackets the case to which it has been classified according to § 4.3 based on the evolution in the first 4.5 days.

Generally, the most intense phase is contained within the initial simulation, and a first regime is reached within $\sim$ a day. A summary is given in table 4.2.

4.4.1 5_6_A (Jacobi-like)

This is a particularly unstable case of $\overline{L} = 0.5$. A small-scale explosion of the outer layers of the initial body rapidly expels a fraction of the high angular momentum, settling the remaining body at $\overline{L} \approx 0.33$, along with a fraction of the mass, leaving the remaining primary in the proximity of the Jacobi figure for its $\overline{L}$ content and with $\sim 85\%$ of the initial mass.

A fraction of the expelled mass remains initially in orbit, including a small 6-particle secondary. These small satellites appear unstable, the small secondary itself being disgregated by tidal forces, and many particles are soon expelled from the system. A dynamical equilibrium arises where 4-7 single particles remain orbiting the primary in continually changing trajectories with close pericentre encounters (see fig. 4.11). They are strongly influenced by the irregularly shaped primary and the other satellites; occasionally some collide with the primary, while other particles may detach from its surface entering orbit.

4.4.2 6_4_8 (similar-mass binary)

This body quickly separates radially into different clusters, with a transient composition of two main bodies of 571 and 345 particles[3] (whence the classification), a tertiary of 54 particles, two minor clusters of 14 and 9 particles, and some free particles.

The formed secondary body does not however have enough momentum to enter into orbit; as a result, bodies 1, 2 and 4 quickly fall onto each other merging into a large primary, with the originally tertiary remaining in orbit around it. Quickly, all remaining mass is expelled from the system.

[2] though, orbits of the NEAs are eccentric, which decrease stability

[3] the total being of 1000 particles, it is easy to convert between particle number and mass fraction

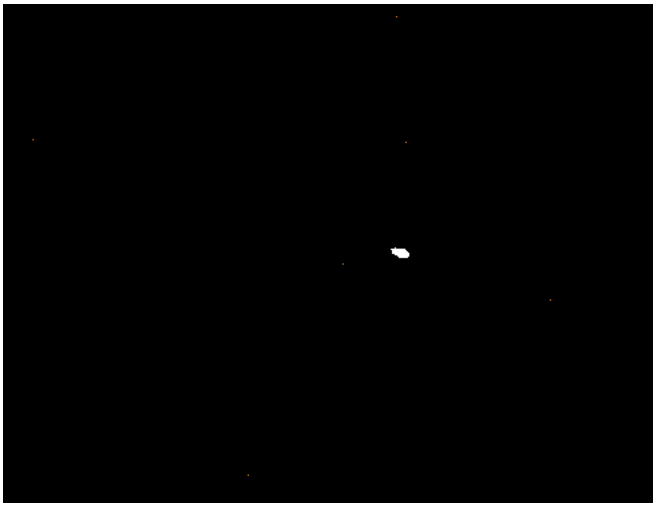

Figure 4.11: The system of 5_6_A after $\sim$ 80 days: a number of particles (coloured red to enhance visibility) are trapped into unstable elliptical orbits (some out of the picture). (cf. text)

The newly formed primary is reminiscent of its origin as a (gentle) collision between two similar-sized bodies, appearing elongated into a characteristic *contact binary* shape (see fig. 4.12).

The resulting orbit has an ellipticity initially oscillating in the band (0.39 ± 0.025), while by towards the end of the simulation it has risen to a value of 0.455 (see fig. 4.13).

4.4.3 6_6_4 (similar-mass binary)

This body reshapes at the beginning into a characteristic "peanut" shape with a prominent bulge. In short time, this evolves in the sense of separating the two component, with a resulting couple of 772 and 217 particles respectively. The relatively few remaining particles generally merge into one of the two main component or leave the system. The shapes of the two bodies are quite regular.

The ellipticity of the mutual orbit is high, a characteristic of the class of similar-mass binaries, but remains below 0.82 for all the simulation, while towards the end decreasing down to ~ 0.773

4.4.4 6_6_6 (similar-mass binary)

A similar case to 6_6_4, with the main difference being a small tertiary (9 particles) in an eccentric unstable orbit leading it to quickly collide with the secondary in the first close passage to the couple. The two bodies are composed of 740 and 234 particles, with an orbit with eccentricity decreasing along the simulation from $\sim$0.76 down to $\sim$0.67 by the end.

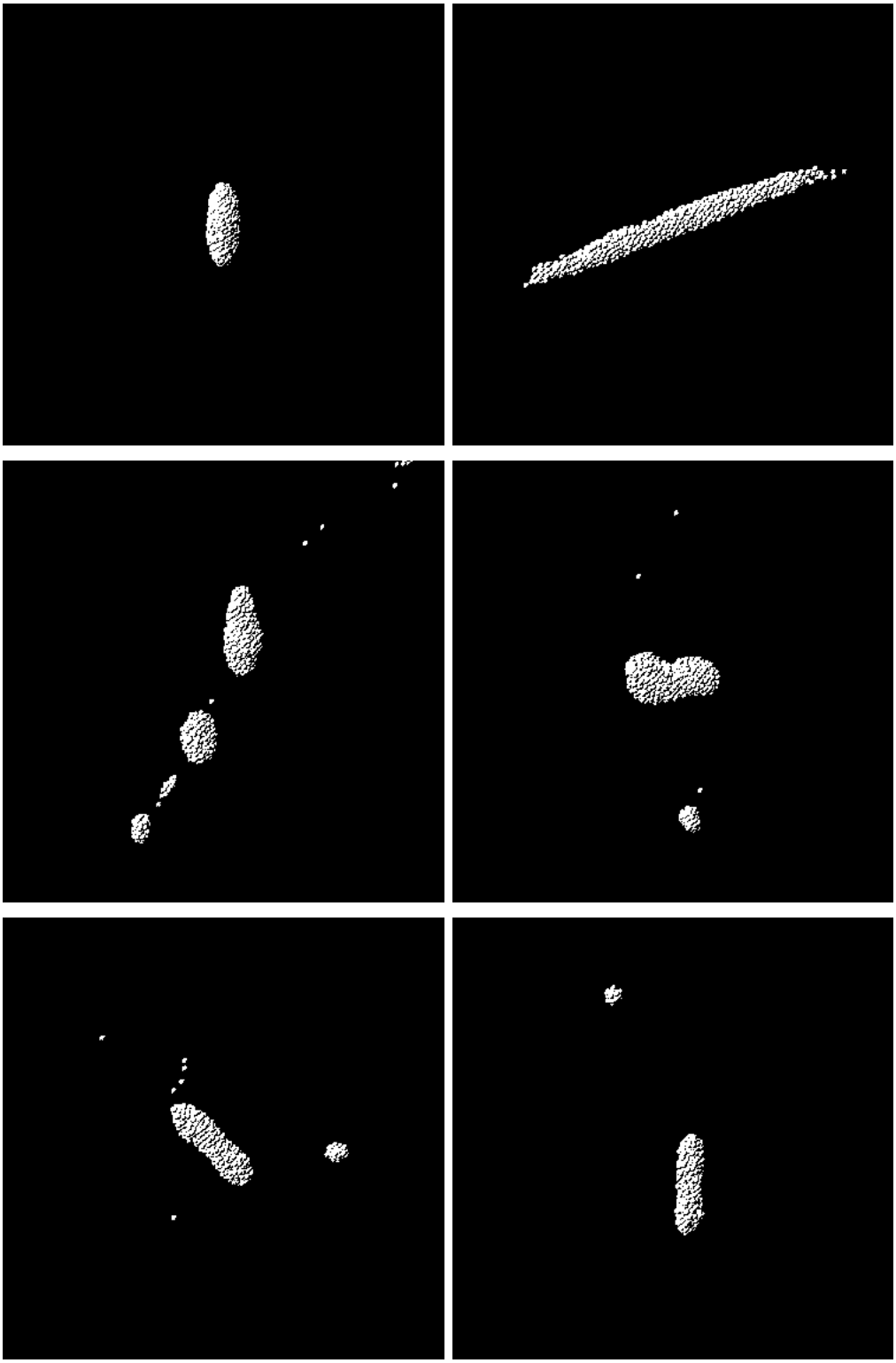

Figure 4.12: Sequence of evolution of the 6_4_8 body (cf. text) from polar view. Initial shape and after 200, 600, 900, 1300 and 14900 steps; left to right, top to bottom; all rotations proceed anticlockwise. The initial evolution shows a hint of multi-body dinamics. The final primary bears the mark of its origin as a contact binary.

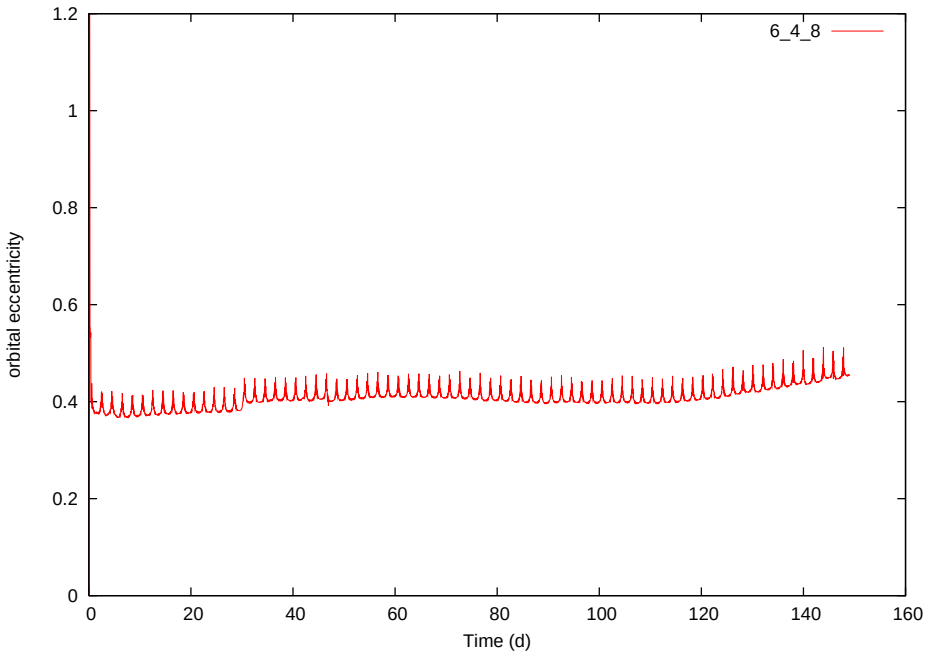

Figure 4.13: evolution of the eccentricity of the mutual orbit for the binary formed from the 6_4_8 body. the spikes are in correspondence to the pericentre passage, where the calculation of the (osculating) orbital parameters (based on the 2 point mass problem) carries a greater incertitude

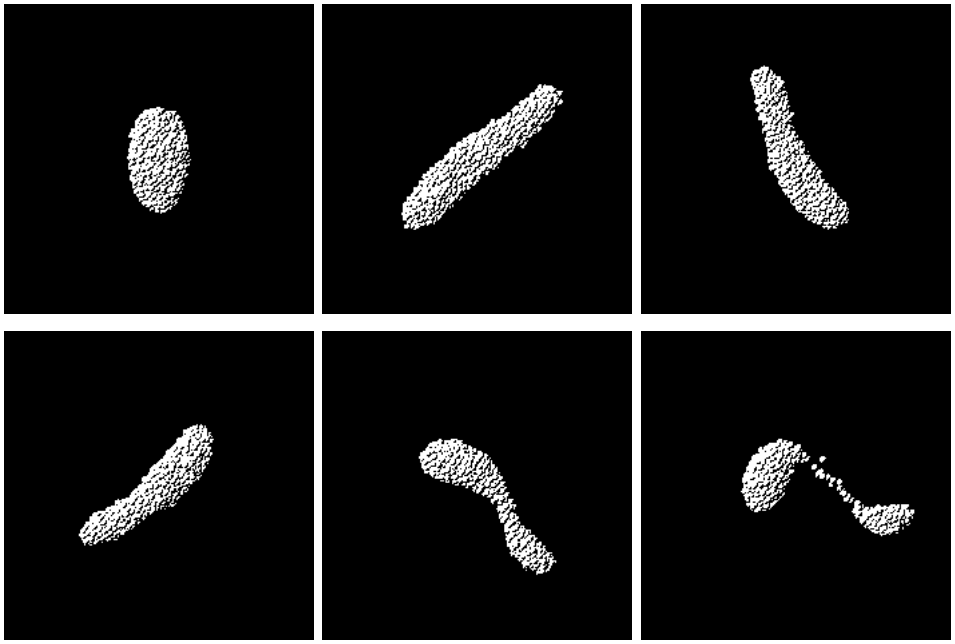

Figure 4.14: Sequence of evolution of the 6_6_4 body from polar view. Initial shape and after 200, 400, 600, 800 and 900 steps; left to right, top to bottom; rotation proceeds anticlockwise. The secondary is emitted in a highly elliptical orbit.

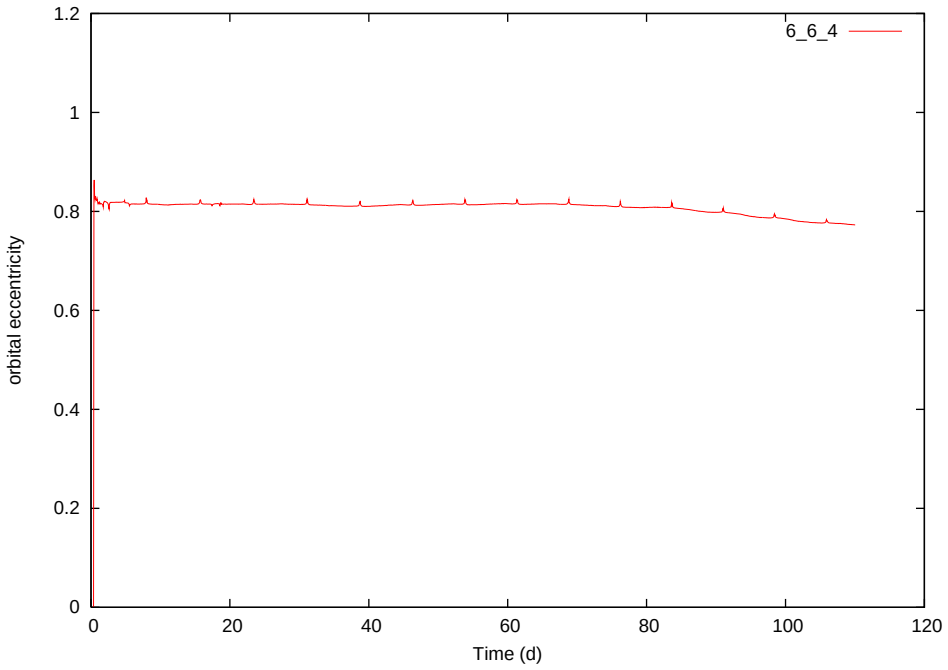

Figure 4.15: evolution of the eccentricity of the mutual orbit for the binary formed from the 6_6_4 body. the high eccentricity is typical of the binary fission process.

4.4.5 6_6_8 (similar-mass binary)

A similar case to 6_6_6, with a second small, eccentrically orbiting satellite surviving a first passage at pericentre while altering its orbit and eventually falling onto it at its second passage.

The two components are composed of 702 and 278 particles, with the eccentricity oscillating within the (0.54 ± 0.08) band.

4.4.6 7_2_4 (similar-mass binary)

The initial body separates into two fragments of 526 and 456 particles, with the little (1.8%) remaining mass escaping the system.

The orbit is eccentric, remaining around $\sim$0.8 for most of the simulation, with a sudden rise to 0.9 after the last recorded passage. The final apocentre of the orbit being located at $\sim$ 70 R_1, this is not as of itself a source of concern, but the final fate could be the dissolution of the couple if the eccentricity increases further.

4.4.7 7_2_8 (similar-mass binary)

Similarly to the 6_4_8 system, an originally 521 and 229 particles bodies fast re-collapse onto each other, leaving in orbit two relatively small satellites of 197 and 29 particles and some free particles, with a small fraction of mass escaping the system. The new originated primary proves unstable, and it quickly loses mass from its tip and remaining with a pear-like shape.

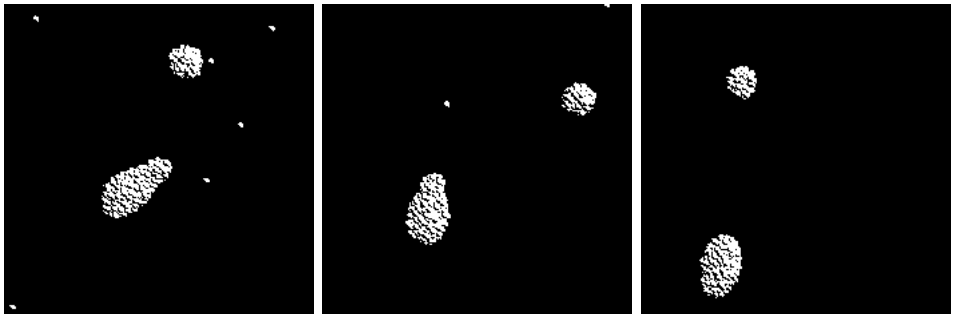

Figure 4.16: Smoothing of the primary in the evolution of the 7_2_8 system; from polar view. The system after 2100, 7000 and 52000 steps.

While the following evolution mostly dissipates the cloud of fragments in orbit, an interesting fact is that the primary is smoothed down towards more and more ellipsoidal shapes.

The tertiary satellite is eventually expelled from the system after a close passage with the secondary. The remaining couple orbits closely with a moderately eccentric orbit ($e \sim 0.39 \pm 0.015$) and a few single particles having survived the initial chaotic phase. A relatively high fraction of angular momentum is lost in the forming stage, with remaining $\overline{L} = \sim 0.55$.

4.4.8 7_4_8 (similar-mass binary/multiple)

The initial body breaks into different main components of 343, 295, 235, 78 and 29 particles, with the two smallest ones, along with most remaining mass, directly released into unbound orbits. Similarly to the 6_4_8 case, the 1st and 3rd bodies quickly merge. The remaining satellite's orbit is very eccentric (e>0.9), and after a first pericentre passage it increases further; the resulting orbit has an apocentre distance of $\sim 185 R_1$, and the two bodies eventually collide by the next encounter.

4.4.9 7_6_1 (similar-mass binary)

This very flat initial configuration initially deforms into a peanut shape which quickly separates into two similar-mass components of 549 and 451 particles, which remain bound in an orbit of eccentricity within the $(0.6 \div 0.75)$ range.

4.4.10 7_6_4 (similar-mass binary)

This initial body breaks into two fragments: an elonganted primary of 702 particles and a more spherical secondary of 266 particles. A number of free particles remain orbiting, which occasionally exchanges mass with the primary.

The eccentricity oscillates around 0.2 for all the observed period, with little evolution of the mutual orbit.

4.4.11 8_2_4 (similar-mass binary)

The body fission into two main fragments of 537 and 440 particles, in a close but fairly circular orbit, the eccentricity remaining below 0.1 for the whole simulation. Occasionally, some particles are detached from the primary surface, and collide back with either of the two bodies.

4.4.12 8_2_6 (similar-mass binary)

The initial body separates into 5 fragments which in a process similar to that of 6_4_8 coalesce into 3 main bodies of 577, 333 and 62 particles, plus minor fragments and free particles.

Initially, the two larger fragments are bound in a quite eccentric orbit with e$\sim$ 0.79 and a pericentre distance barely larger than the sum of their radii, which is highly unstable. The tertiary possesses a similar apocentre distance and an initially safer pericentre distance, which would by itself be a better chance of survival in the initial phases of evolution.

The presence of 3 bodies in a close configuration is however unstable. By the first orbit of the tertiary, the three bodies interact dramatically (see fig. 4.17): an exchange of angular momentum is performed between the bodies, with the tertiary actually changing the direction of its orbital angular momentum with respect to the centre of mass of the system and being expelled.

The remaining 2-body system (which has not exchanged any mass with the tertiary) has on the other side quite circularized its orbit (e$\sim$0.27, see fig. 4.18) with a safer pericentre distance, the couple remaining stable for the whole simulation.

This is a manifest example of the inherent chaoticity of N-body simulation processes. It is a mere accident, here, that the complex 3-body interaction leaves the system in its actual configuration, as even a small difference in the fragmentation process, or in the following reshaping can dramatically alter the overall system evolution.

4.4.13 8_4_2 (similar-mass binary/multiple)

The initial body separates into 4 fragments, of 552, 331, 88 and 27 particles. The smallest body is simply expelled from the system, and the two larger ones remain bound into a close circular (around e$\sim$ 0.055) and very stable orbit, with no appreciable initial evolution.

The tertiary is actually initially put into a very elongated orbit. When the latter returns in the proximity of the binary couple, its close passage has it collide and merge with the secondary, modifying its orbit into a wider one (cf. fig. 4.19).

The following evolution shows no further appreciable change apart from the mutual orbit eccentricity decreasing from the post-impact value of 0.18 to its final value below 0.1.

Similarly to the 8_2_6 case, this is another evident example of macroscopic chaoticity, a small difference in some parameters possibly having large consequences on the tertiary close encounter.

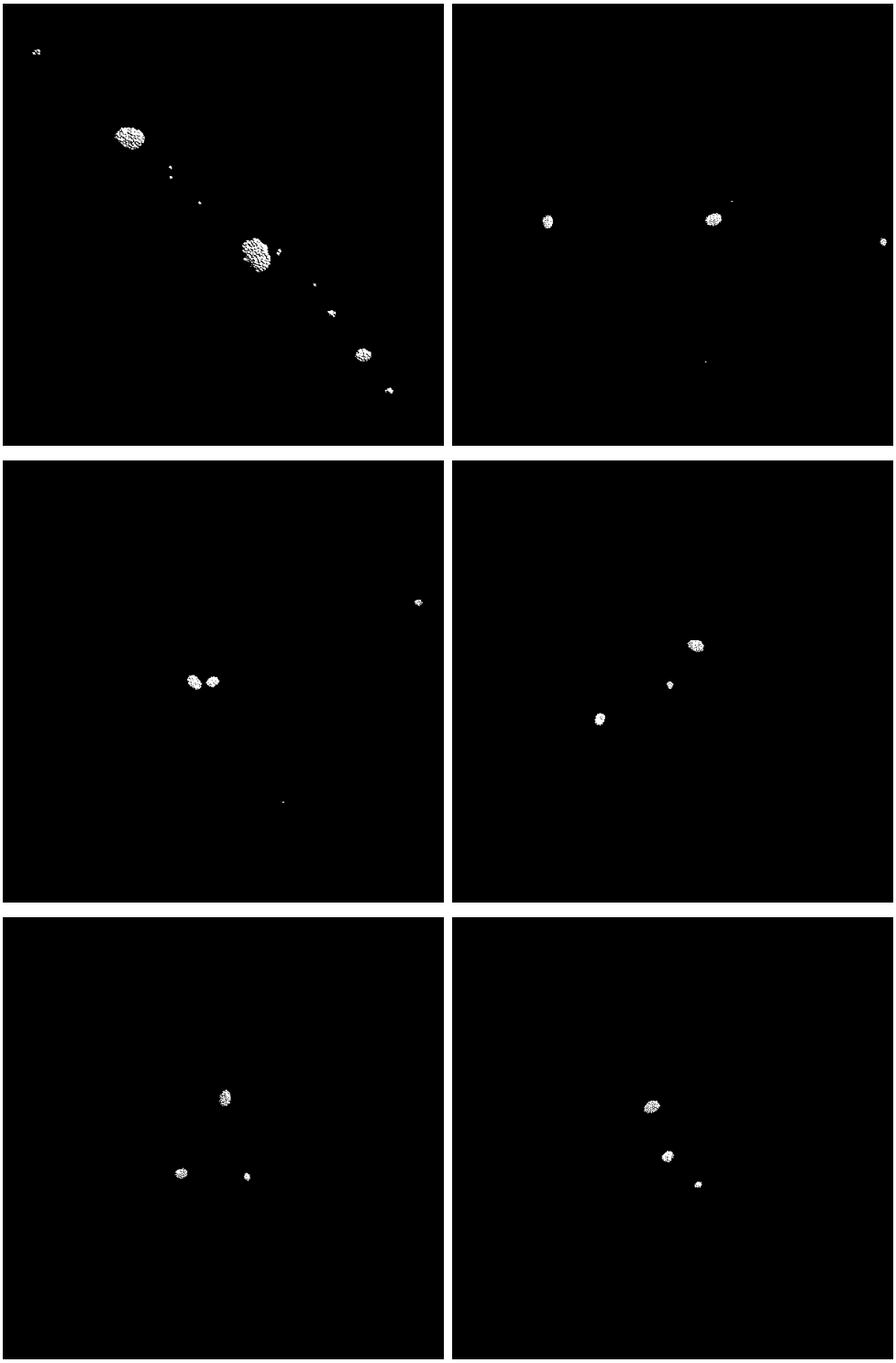

Figure 4.17: An example of a strongly chaotic behaviour in the evolution of the 8_2_6 body (cf. text). Polar view; left to right, top to bottom; all rotations and revolutions proceed anticlockwise. (1) the three main bodies form. (2) the apocentre passage for the two satellites. (3) the first pericentre passage of the secondary: the orbit is very eccentric. (4) the pericentre passage of the tertiary. (5)-(6) the two satellites interact with an exchange of angular momentum that changes their orbits: the secondary is pulled away from the primary in its course towards the pericentre. (continues on next page)

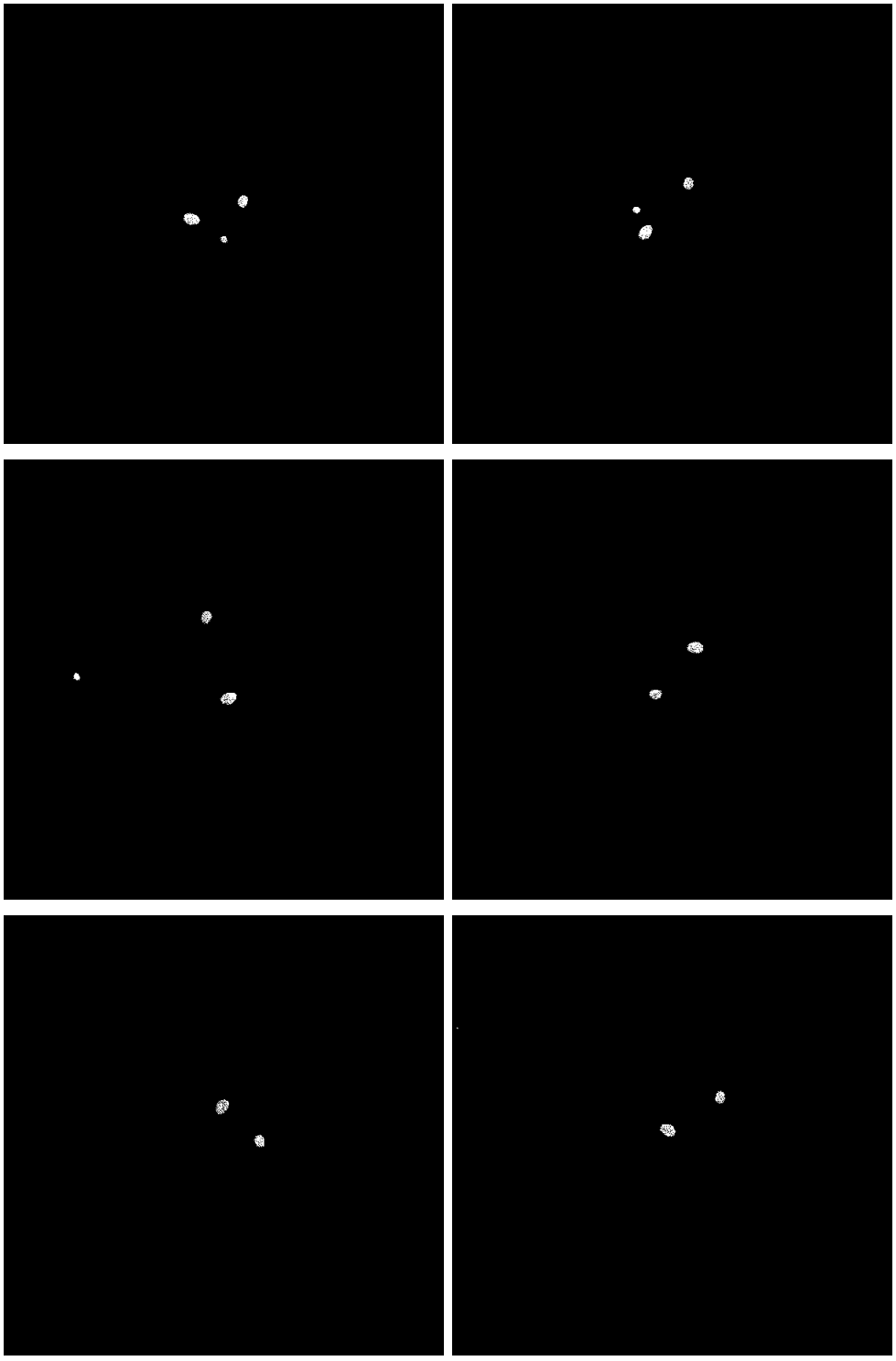

Figure 4.17: (continuing from previous page) - left to right, top to bottom - (7) the tertiary has had its angular momentum change direction. (8)-(9) the tertiary is expelled from the system. (10)-(12) the binary has been left with a more circular orbit (see also fig. 4.18).

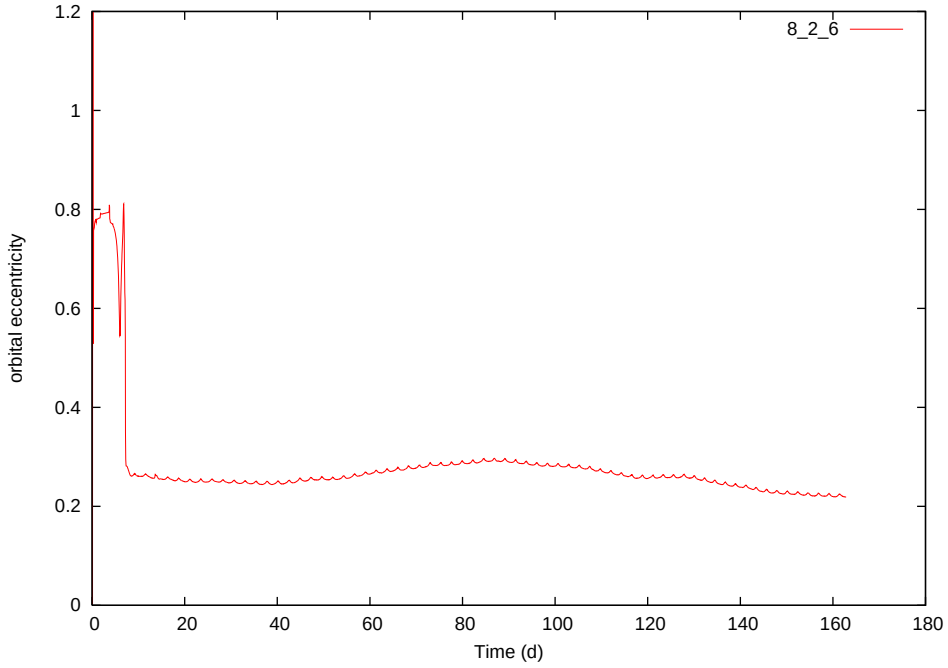

Figure 4.18: evolution of the eccentricity of the mutual orbit for the binary formed from the 8_2_6 body: note the circularising action of the tertiary in the first phase. the final system looks stable.

4.4.14 8_6_1 (similar-mass binary)

The initial body breaks into 2 main aggregates that quickly englobe all remaining bound particles. The resulting pair is composed of 2 bodies of 501 and 495 particles, with an orbital eccentricity oscillating in the (0.635 ± 0.020) range.

4.4.15 8_8_4 (similar-mass binary/multiple)

From an initial fragmentation of the body, three main bodies emerge in what essentially appears a chaotic process: a contact-binary primary (the result of a previous collision) of 706 particles and two spherical satellites of 154 and 54 particles.

The mutual orbits are unstable similarly to the 8_2_6 and 8_4_2 cases. The two smaller body, having in the meantime collected most part of the cloud of fragments in orbit, and interestingly conserving for a while a sub-satellite system of their own, collide after a few orbits, leaving a roughly spheroidal secondary of 254 particles. The primary, in turn, slowly regularize its shape in a process akin to that of the 7_2_8 case, being reduced to 698 particles by the time of the secondaries merger.

The couple appears stable in the following evolution.

4.4.16 5_A_A (many particles orbiting)

Almost the model for its category, the primary $\overline{L}$ quickly drops to ~ 0.35 while reshaping into the corresponding Jacobi figure. A cloud of fragments forms orbiting the primary,

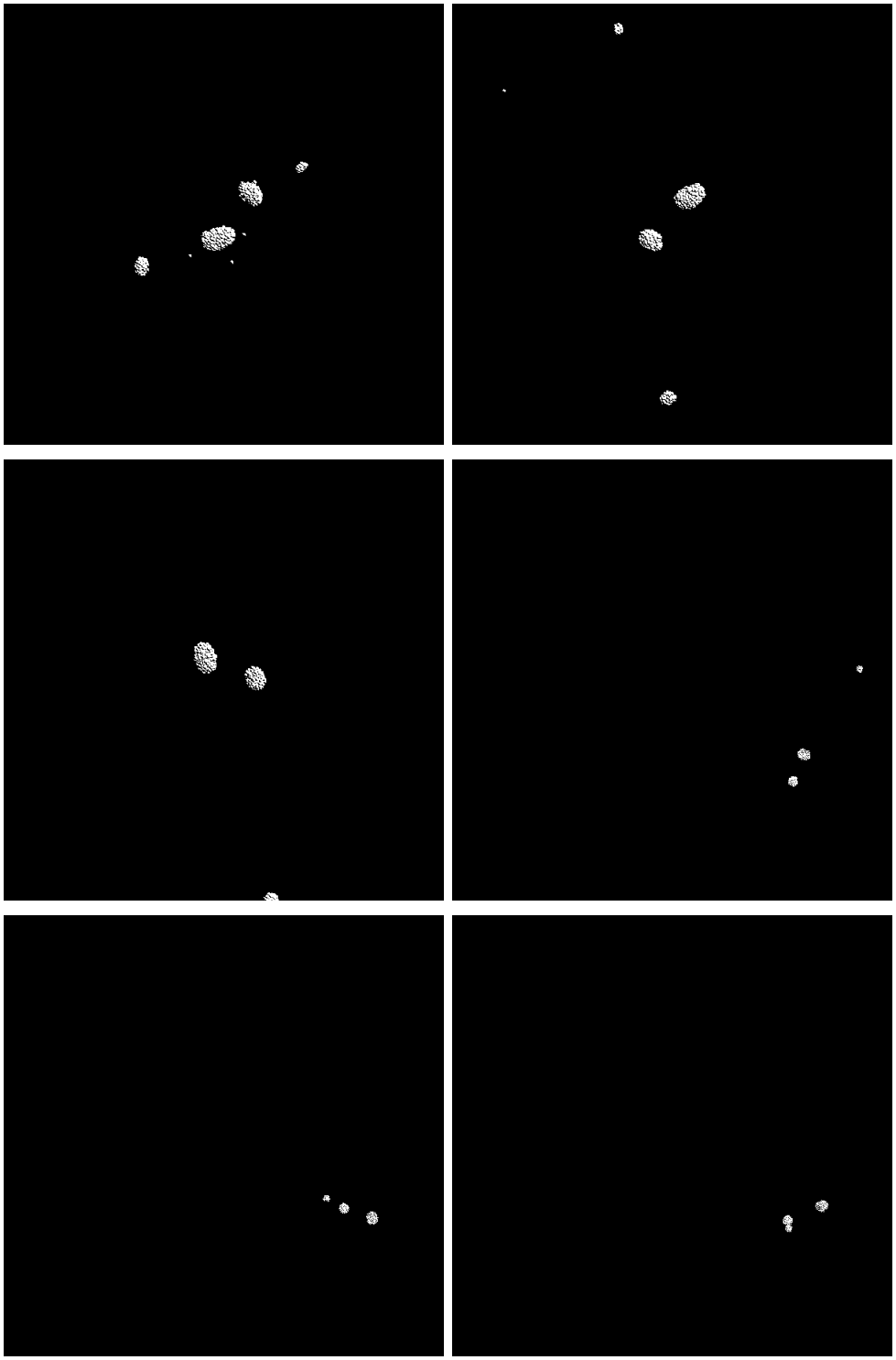

Figure 4.19: Sequence of evolution of the binary formed from the 8_4_2 body. Polar view; left to right, top to bottom; all rotations and revolutions proceed anticlockwise. (1) initially, the parent body is split into four main aggregates. (2) the 4th body is expelled from the system, and the tertiary is bound in a very eccentric orbit. (3) the remaining couple is left bound in a very close circular orbit. (4) much later ($\sim$ a month - smaller scale: the centre of mass of the couple has moved from a strictly circular heliocentric orbit and is no longer centreed in the heliocentric circularly rotating frame) the tertiary returns in the vicinity of the couple (5)-(6) the tertiary passes near the secondary and collides. (continues on next page)

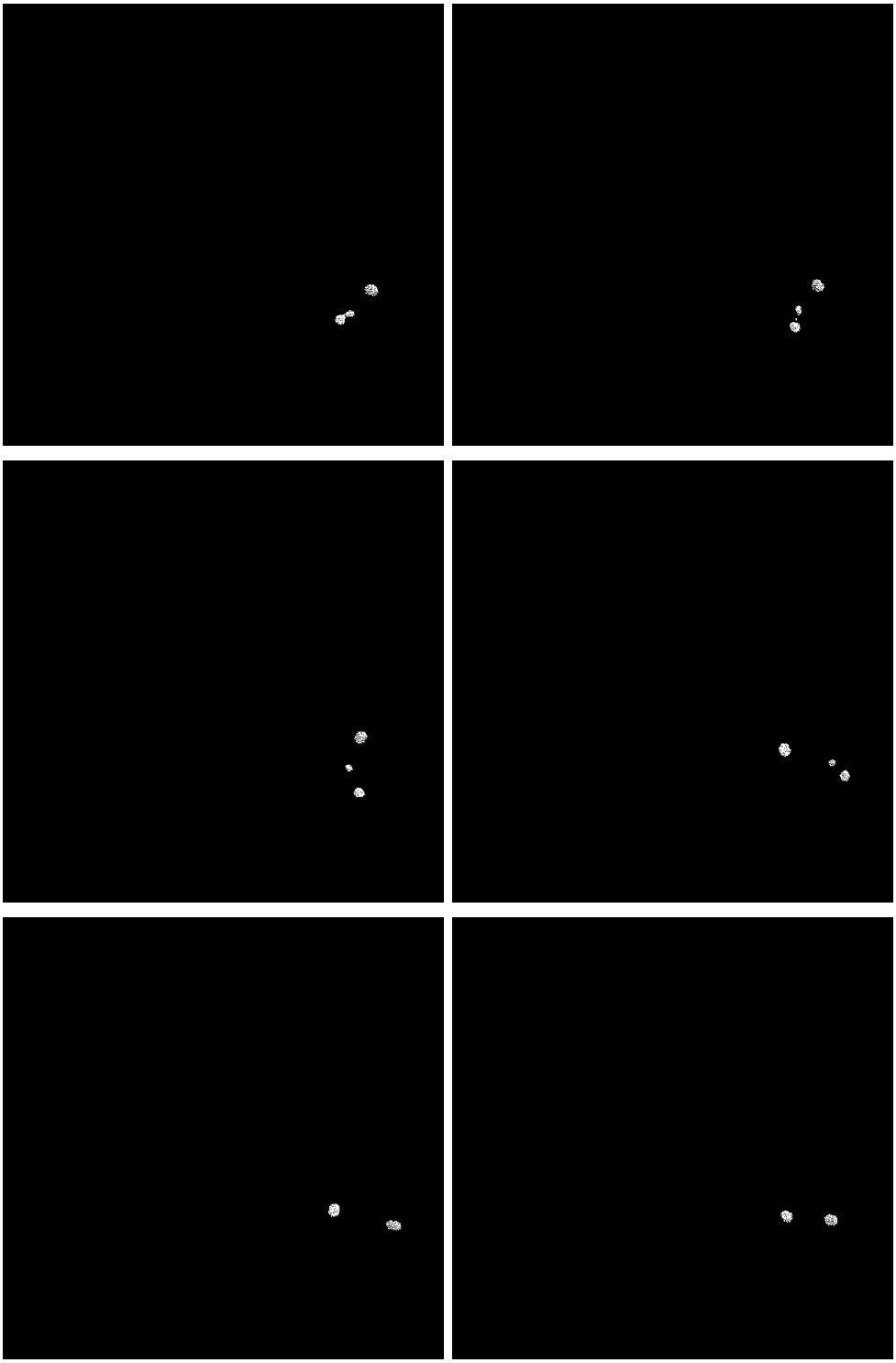

Figure 4.19: (continuing from previous page) - left to right, top to bottom - (7)-(9) the tertiary initially bounces off the secondary. (10)-(11) the tertiary collides again with the secondary and the two merge into a larger secondary. (12) the new couple is left with a wider orbit (cf. also fig. 4.20).

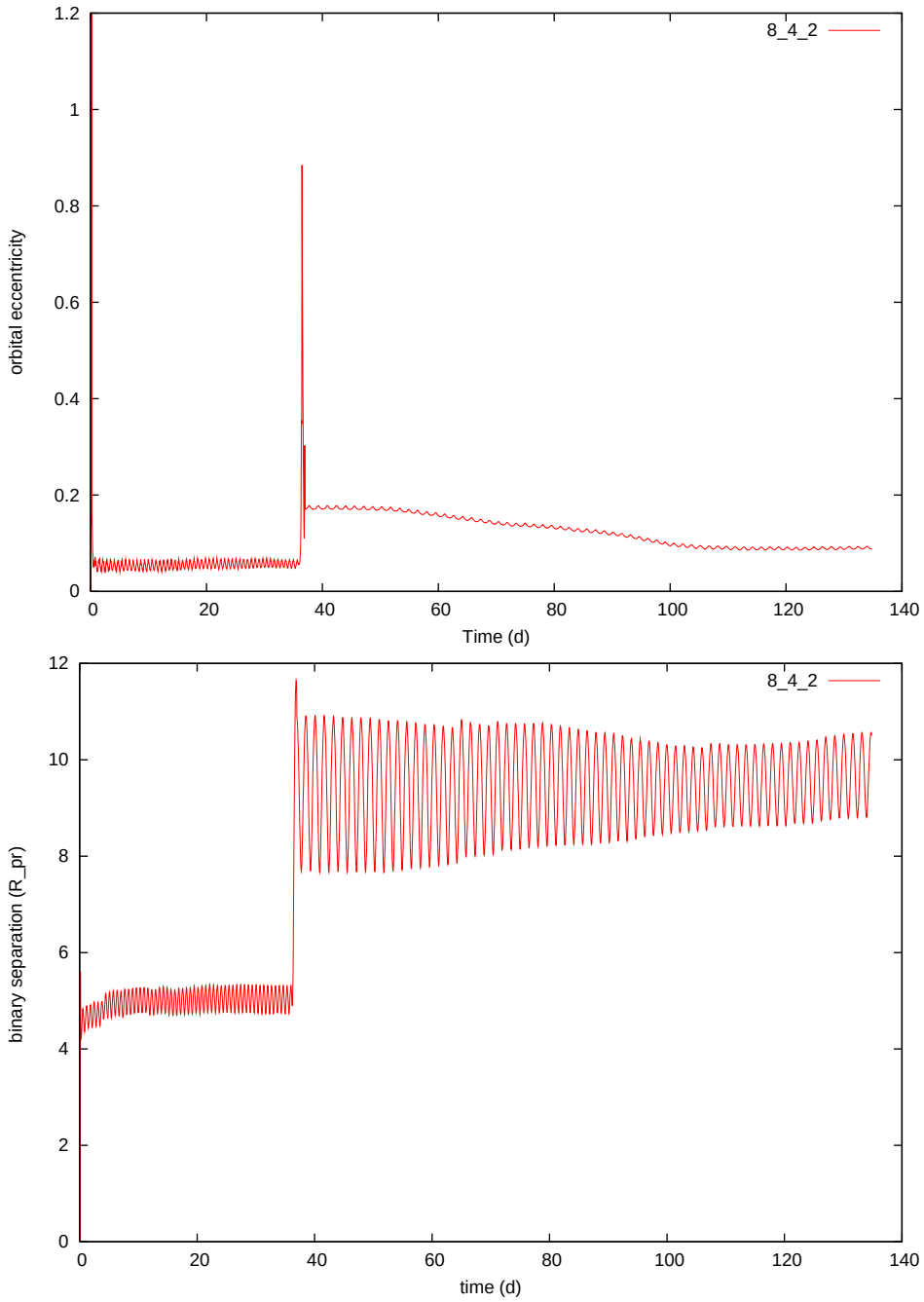

Figure 4.20: evolution of the eccentricity and mutual separation for the binary formed from the 8_4_2 body. Note in particular the tertiary impact on the secondary that, by chance, widens the couple instead of disrupting the system (see text ang fig. 4.19 for details).

which slowly dissipates and in which a secondary satellite is capable to grow coalescing particles onto itself (see fig. 4.21).

By the end of the simulation, the system is composed of a primary of 853 particles, a secondary of 45 particles and a number of single particles still orbiting.

4.4.17 6_A_6 (many particles orbiting)

A similar case to 5_A_A. The resulting system is however more composite, with several multi-particles clusters still gravitationally bound to the primary at the end of the evolution.

4.4.18 7_A_6 (many particles orbiting / similar-mass binary)

A border case between § 4.3.2 and § 4.3.3. The initial body is highly shattered by the rapid rotation, with the largest fragments then re-accumulating into an irregular primary. This rapidly rotating primary, in turn, fission by centrifugal force into two fragments of 591 and 276 particles. The remaining cloud of particles dissipates very quickly, leaving the two main bodies as the sole remnants of the system along with 2 single particles (see fig. 4.22).

The following evolution, after an initially apparently stable period where the ellipticity of the orbit oscillates between ~ 0.4 and 0.7, suddenly presents a quickly increase in the orbit elongation and ellipticity, leading to an abrupt separation of the couple within 106 days, after about 60 mutual orbits.

4.4.19 8_A_6 (dispersed system)

The initial body shatters into multiple fragments, with a number of them re-accumulates over the course of the month following the initial break-up (see fig. 4.9).

At the end of the simulation, corresponding to 185 days, the largest body has grown to a 357 particle body, with a satellite of 121 particles in a elliptical orbit. Other aggregates show no consistent satellites; their consistency and spins are tabulated in tab. 4.1.

4.5 Shape-spin-orbit interactions

One of the goals of the simulations was to study the evolution of simulated binary rubble-pile asteroids, following in particular the interactions among shape, spins and mutual orbit. This would allow to try to extrapolate some macroscopic characteristics of the perfect rubble pile model (like its dissipation function Q, see [Sol.Syst.Dyn., eq. 4.138]) which can be useful for future applications, comparison with real rocky objects estimates, and trying to analytically predict the behaviour of the systems beyond the relatively short simulation run times.

A first measurable result is the observation of the dependence of the spin period of some primaries with their shapes as these evolve under the action of a secondary. An example is given in fig. 4.24, where some abrupt changes in shape correspond to sharp changes in the rotation period.

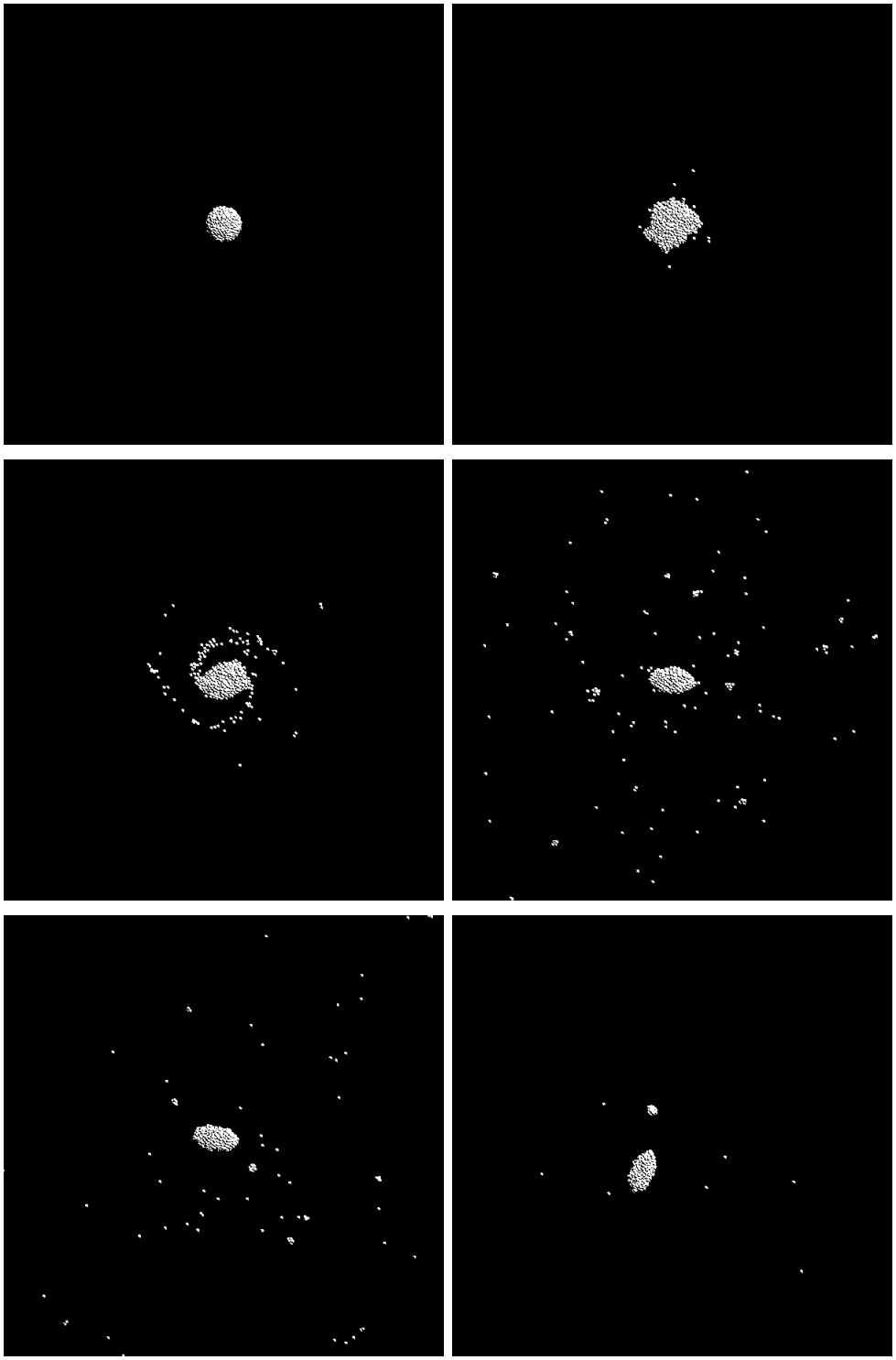

Figure 4.21: Sequence of evolution of the 6_4_8 body (cf. text) from polar view; left to right, top to bottom; all rotations and revolutions proceed anticlockwise. Initial shape and after 400, 700, 2000, 5000 and 20000 steps. Initially, the body flattens; then rapidly develops into an ellipsoidal shape with consistent mass loss in the form of many particles that remain in orbit. Slowly, a small secondary forms in orbit gathering mass from the orbiting particles.

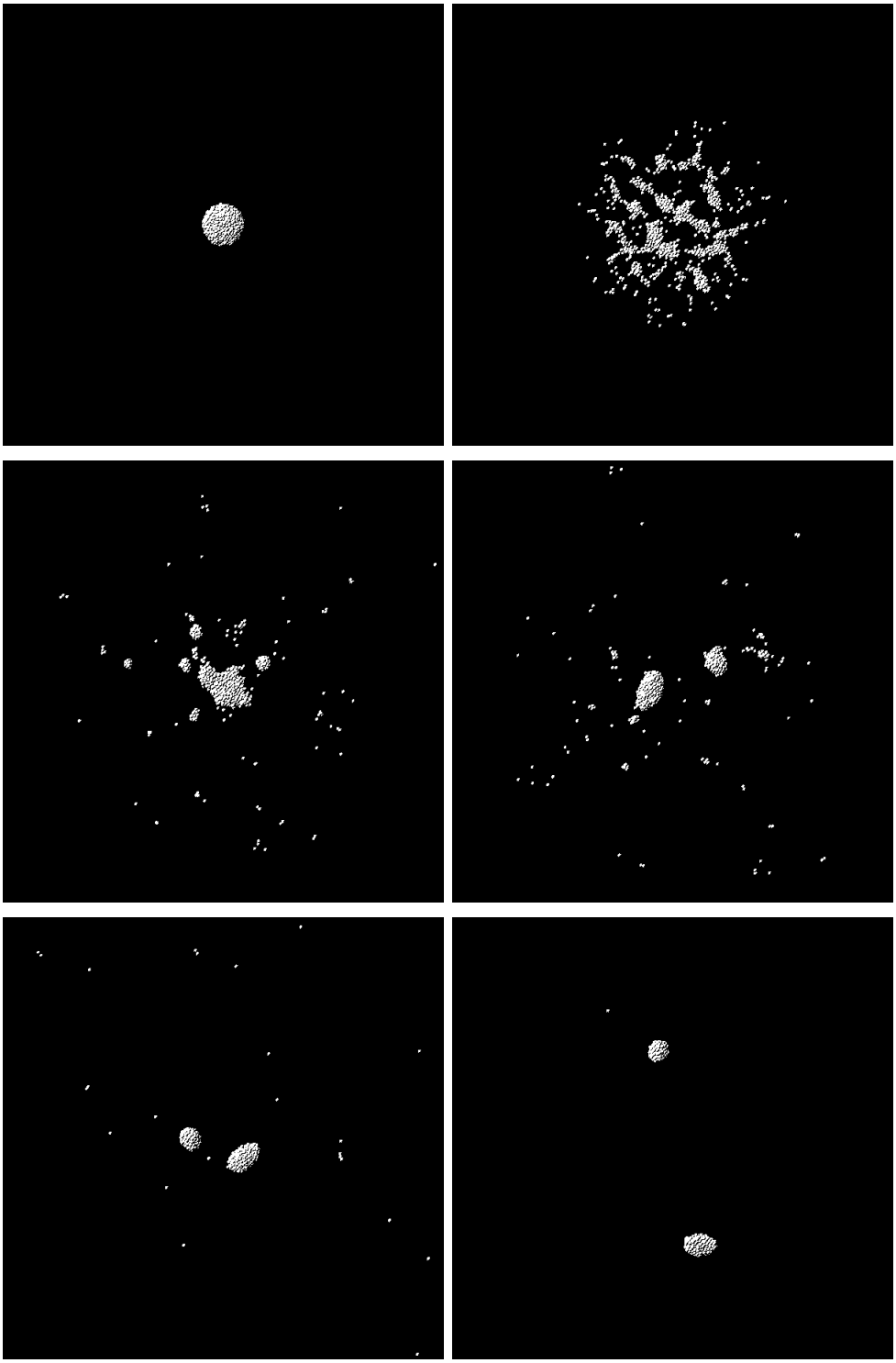

Figure 4.22: Sequence of evolution of the 7_A_6 body (cf. text) from polar view. Initial shape and after 300, 800, 1300, 4000 and 12000 steps; left to right, top to bottom. The body shatters and then re-accretes; two main aggregates emerge, which rapidly deplete the cloud of orbiting single particles.

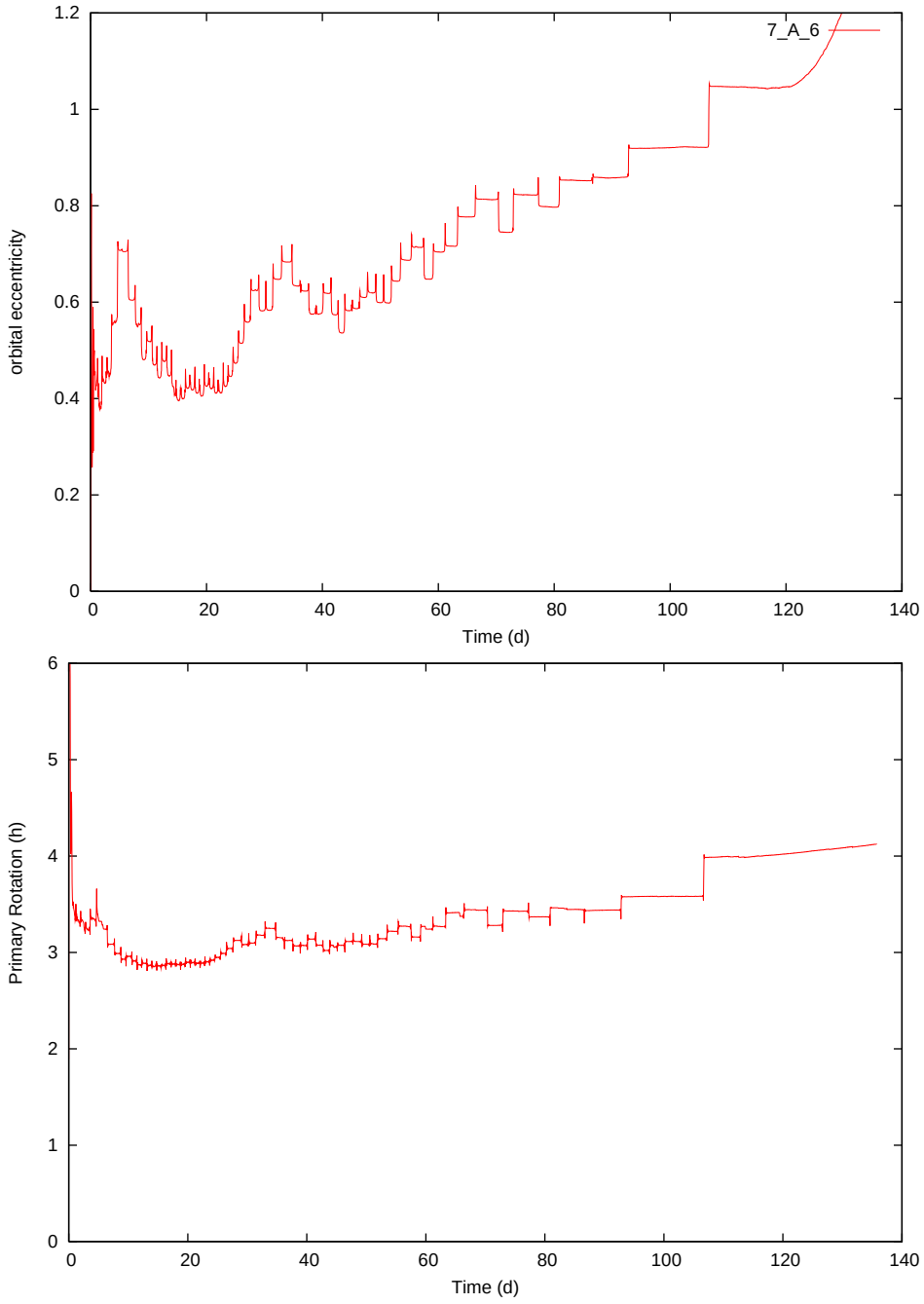

Figure 4.23: evolution of the eccentricity of the orbit and rotation period of the primary for the binary formed from the 7_A_6 body. The evolution is irregular, and eventually the couple breaks apart: the necessary energy is extracted from the rotation of the primary in the last close interaction after $\sim$ 3.5 months (cf. text). For the increase in the primary rotation rate after the couple dissolution, see § 4.6.

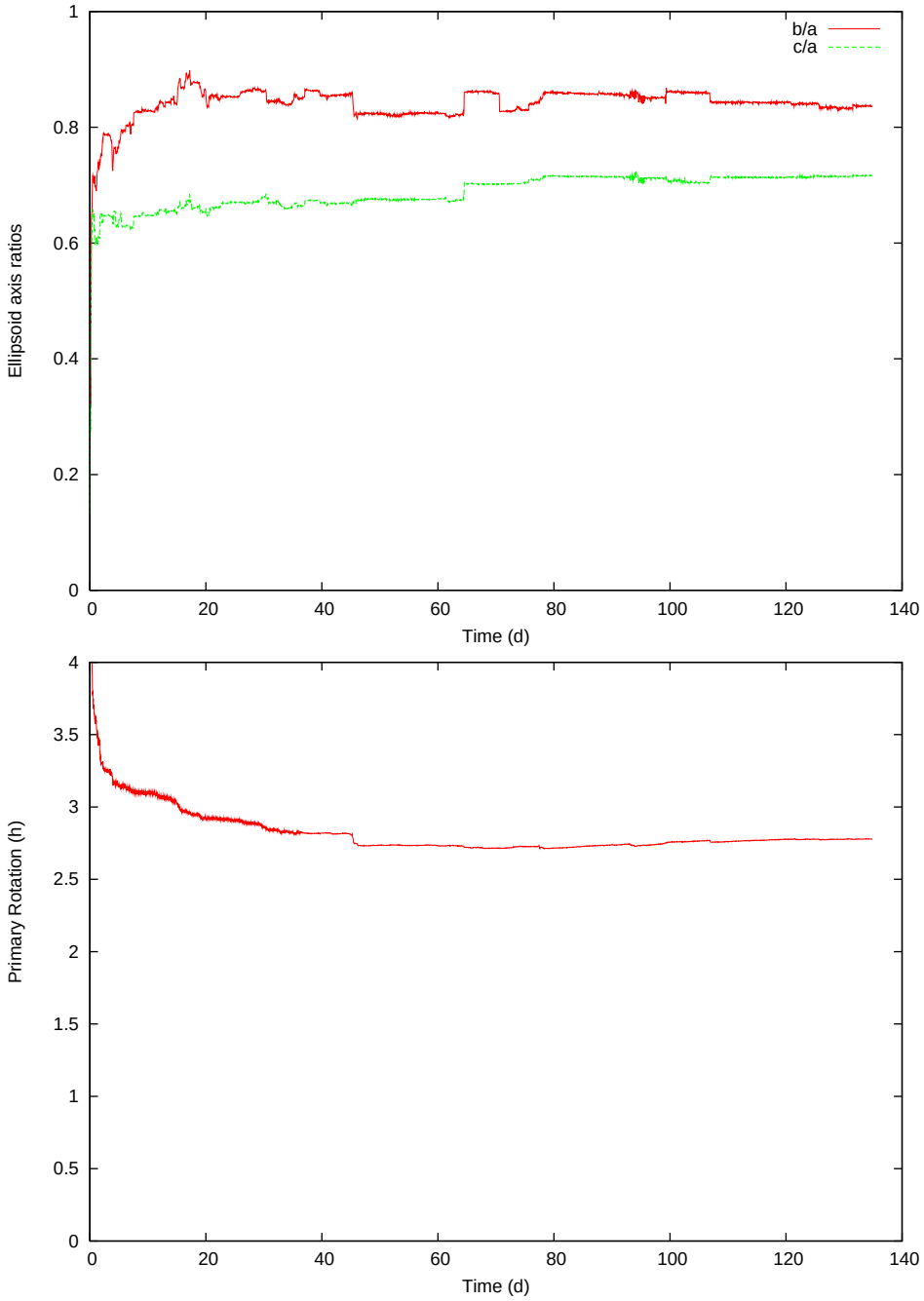

Figure 4.24: evolution of the axes ratio and spin of the primary for the binary formed from the 8_4_2 body under the perturbing action of the secondary: the abrupt change in the shape of the primary observed at ∼45 days is reflected in the rotation period; smaller bumps are also visible.

part. #	P(h)	satellites
357	7.3	a 121-particle (P_{rot} ~2.9h, e=0.76, a/R_1 ~ 20) + a single particle
160	3.1	4 single particles
66	3.4	2 single particles
52	3.1	2 single particles
49	7.0	a 2-particle satellite
23	3.8	-
18	4.7	-
11	4.3	1 single particle (?)
11	4.8	1 single particle (?)
10	4.6	-

Table 4.1: Aggregates of 10 or more particles (1% of parent's mass) resulting from the fragmentation and re-accumulation of the 8_A_6 body. Plotted are the masses in particle numbers (1000 initial particles), rotation periods in hours, and notes about satellites. Only the most massive has a significant secondary. 32 aggregates (2+ particles) have been detected in total, in addition to 46 free particles.

body	M_1(%)	P_1(h)	M_2/M_1	a/R_1	e	$\overline{L}$	notes
5_6_A	87.3	2.7			only single particles in unstable orbits		
5_A_A	85.3	2.7	0.053	7.5	0.43	0.38	single particles also orbiting
6_4_8	92.7	4.4	0.060	4.1	0.46	0.54	contact binary
6_6_4	77.4	2.5	0.28	17	0.73	0.66	see § 4.6
6_6_6	73.9	2.9	0.32	12	0.67	0.59	tertiary-secondary merger
6_6_8	70.2	2.7	0.40	5.7	0.57	0.55	
6_A_6	80.1	2.9	0.064	7.1	0.19	0.38	multiple small satellites
7_2_4	52.6	2.9	0.87	29	0.90	0.61	
7_2_8	70.1	2.8	0.29	3.6	0.39	0.49	smoothed contact binary
7_4_8	87.6	3.3	0.089	unbound - original secondary merged with primary			
7_6_1	54.9	2.5	0.82	13	0.69	0.69	no particle loss; see § 4.6
7_6_4	70.2	3.0	0.38	4.1	0.20	0.67	
7_A_6	61.4	4.1	0.51	unbound - secondary escapes after ~60 orbits			
8_2_4	53.7	2.8	0.82	5.5	0.058	0.75	
8_2_6	57.8	2.6	0.58	8.0	0.22	0.81	tertiary lowers ecc.
8_4_2	55.2	2.8	0.76	8.0	0.088	0.74	tertiary widens orbit
8_6_1	50.1	2.7	0.99	13	0.65	0.82	
8_8_4	69.6	3.2	0.37	10	0.60	0.75	smoothed contact binary
8_A_6	35.7	7.3	0.45	20	0.76	0.55	dispersed system

Table 4.2: Final results for the long simulations. M_1 is the mass fraction of the parent body ending up composing the primary, P_1 is the primary rotation period, M_2/M_1 the mass ratio of the two components, a the semimajor axis of the orbit (in primary average radii), e the orbit eccentricity. For description of the notes, see text. All primaries (except for the dispersed system) are fast rotators. The resulting close orbits are in line with those observed for the actual binary asteroid population.

Generally, though, any study of complex interactions is hampered by the conserva-

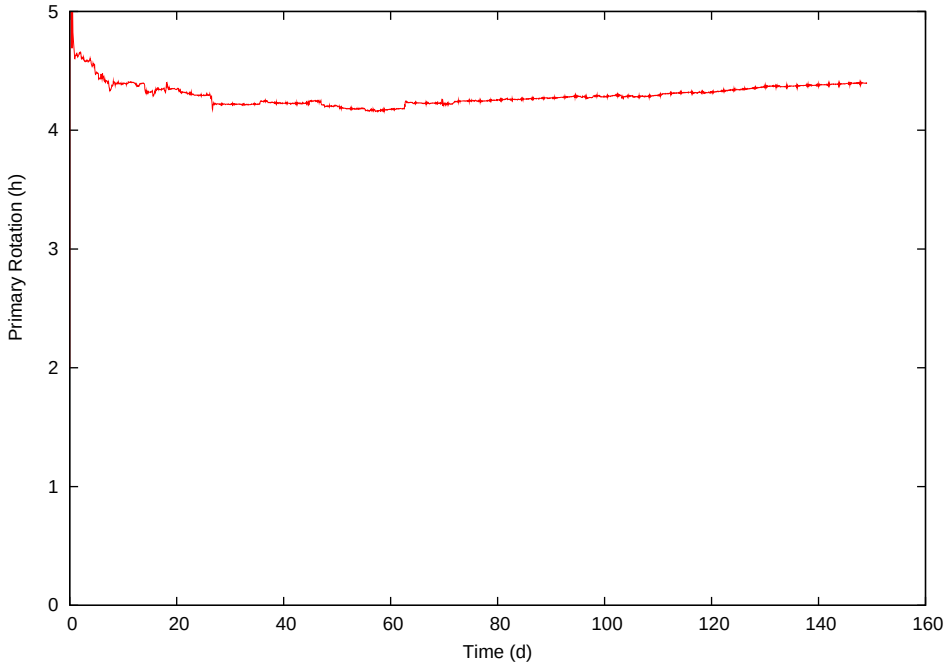

Figure 4.25: evolution of primary spin rate from the 6_4_8 simulation. the steady increase is not due to primary-secondary synchronisation (see § 4.6).

tion problems shown by `pkdgrav` (see § 4.6).

4.6 The limits of `pkdgrav` and the validity of the simulations

Another interesting observation derived from some simulations is the gradual steady increase of the primary rotation period (see fig. 4.25). We initially linked this to a classical tidal mechanism of braking dissipation that could lead, with time, to a partially or fully synchronous system. Yet, its constant nature instead of a discontinuous behaviour (greatest near close encounters, minimal near apocentre) was a first clue that there were more to it.

As we developed more refined measurements, an analysis of some binary angular momentum trends (see fig. 4.26) was the definitive evidence that drew some limit about the long-term precise rendering of compact bodies by `pkdgrav`.

While we expected a somewhat not perfect conservation of quantities like binary angular momentum (the systems being in orbit around the Sun), the variations were at most of $\pm \sim 1\%$ over $\sim$4 months for many simulations, except for some exceptional cases like 7_6_1 (cf. fig. 4.26), where a variation of more than 10% can be observed in a 5-month period. As this fact warranted more investigations, we run a few tests to locate the problem. Repeating the simulation with the Sun removed, the results were similar; as in the 7_6_1 simulation all the mass was contained in the pair, there couldn't be any doubt that the problem lied somewhere within `pkdgrav` code. We performed other tests trying to "freeze" the two asteroids into rigid body configurations (see § 3.1.3) to

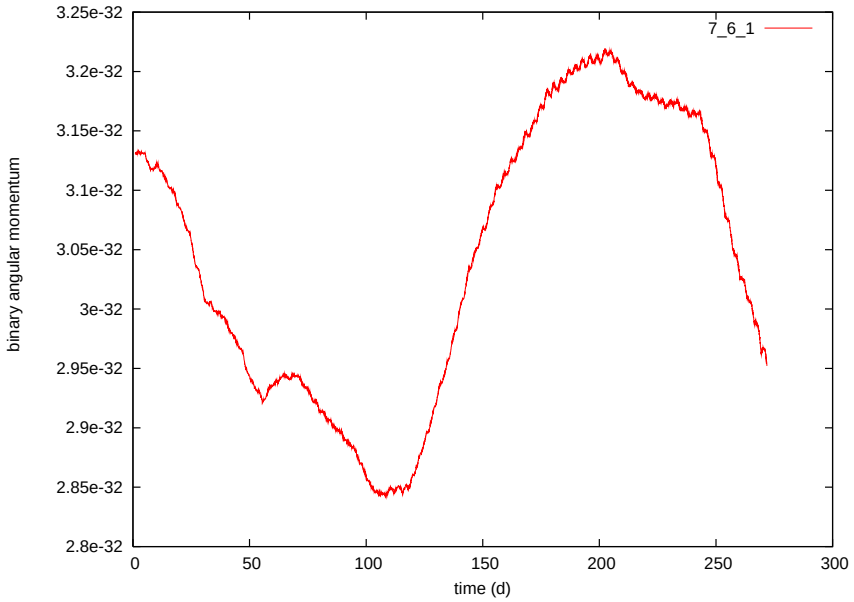

Figure 4.26: Evolution of angular momentum content of the binary from the 7_6_1 simulation. While it is not the only simulation presenting a significant variation of the angular momentum content, this was peculiar in both sinuous trend, amplitude ($\pm 5\%$ and more) and the fact that no other aggregates were present but the two members of the couple. a test without the Sun confirmed this to be a spurious `pkdgrav` effect.

eliminate all internal particle interactions, trying to change `iOO` (see § 3.8.1) from "repel" to "posadj" and "backstep", by decreasing the timestep length, and even eliminating the secondary (!); yet, the problem persisted.

In the end we found no real clue as for the reasons of such behaviour, or why some cases are more of an issue than others.

The "frozen rubble-piles" test was also performed to test the physical consistence the primary de-spinning patterns (as seen e.g. in fig. 4.25). The results showed no appreciable change in the slope of the rotation period change (see fig. 4.27), differently to what could be expected if that behaviour were due to tidal forces, which act by energy dissipation by friction at the interior of the bodies which are continually deformed: by turning off the deformation, this mechanism should be eliminated.

A question arises on the validity of the results obtained.

If a first consequence is that the code is not (yet) fit to precisely follow compact bodies evolution for more than a few days if precise measurements are needed, the overall errors obtained are largely covered by the general chaoticity of the simulations themselves, where small initial changes (in the relative positions of the particles inside the bodies, in the nature of the physical event that brought the bodies to an instability in the first place, etc...) can greatly alter the subsequent macroscopic quantities (the break-up of the initial bodies, their subsequent reshaping, the orbital parameters of the objects formed, and so on) and the overall history of the systems.

In this sense, the results obtained, both regarding the "overall behaviour regions"

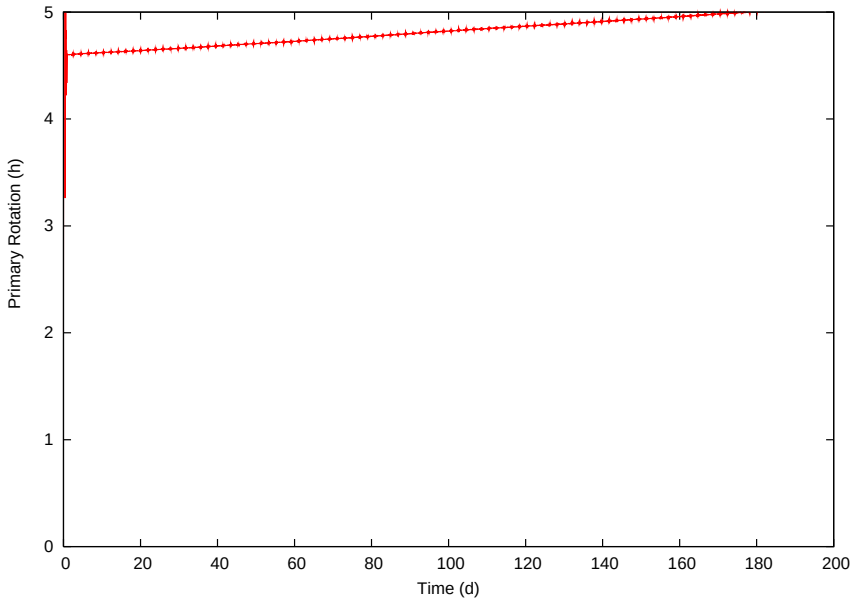

Figure 4.27: evolution of primary spin rate from the 6_4_8 simulation with the aggregates being "frozen" at fixed shape shortly after formation. the steady increase in the primary spin period does not change from the normal case (fig. 4.25), indicating that it is not due to tidal forces, which are suppressed in the rigid body configuration. this was an additional proof that `pkdgrav` may not be suited for long-term precise integrations of compact bodies.

described in § 4.3 and the mid-term evolutions, can only be interpreted statistically, to provide a general overview of the possible systems that can be obtained. Under this limit, we can safely assume the results to be correct.

4.7 Size dependence

The initial $R_p = 50\,m$ was chosen in [P. Tanga et al., 2009 II] because it is the typical size of the objects in the transition region between monolithic asteroids and rubble piles, and thus of the typical size of the large fragments we expect to find inside the actual rubble piles (somewhat less than the length of the main Itokawa components, cf. fig. 1.4).

In [P. Tanga et al., 2009 II] we also found that size was completely irrelevant for that work's results, at least within a factor of 10. To complement the results obtained here, we performed two runs increasing R_p by a factor 20

$$R_p = 1km$$

keeping ρ_p fixed (8000-fold increase of mass), and repeating the 7_6_4 and 6_A_6 simulations (L being correspondingly changed to keep $\overline{L}$ constant). This brings the overall dimensions somewhat larger than the sizes of the largest of the small binary asteroids (group B in the Pravec & Harris classification, see fig. 1.12).

The results are shown in table 4.3, and show no significant change compared to the $R_p = 50m$ case. Together with the results obtained from the simulations in [P. Tanga et al., 2009 II], we can trust the results to be valid for a wide category of sizes.

body	$M_1(\%)$	P_1(h)	M_2/M_1	a/R_1	e	$\overline{L}$	notes
6_A_6	80.1	2.9	0.064	7.1	0.19	0.38	multiple small satellites
6_A_6_{R20}	84.0	3.2	0.054	7.0	0.19	0.43	some single particles orbiting
7_6_4	70.2	3.0	0.38	4.1	0.20	0.67	
7_6_4_{R20}	74.6	3.8	0.30	7.8	0.27	0.65	

Table 4.3: comparison between the original and the simulations where the initial linear dimensions were multiplied by a factor of 20; final results are similar within the incertitudes of general behaviour

4.8 Conclusions

In general, we show how binaries are a natural outcome for unstable cases of shattering and re-accumulation.

A comparison with the real asteroids is presented in fig. 4.28.

In general, the systems retain a mildly strong memory of the initial $\overline{L}$ content; by comparing them to some groupings of binary asteroids, we can see how the systems starting with $\overline{L} \geqslant 0.8$ conserve generally too much angular momentum to be representatives of actual observed asteroid pairs. This could mean that the initial conditions are not representative of actual situations (for example, hardly a body could be allowed to accumulate such a high initial angular momentum before breaking, as this would correspond in general with a rotation period < 2h)[4].

On the other hand, the $\overline{L} = 0.5 \div 0.7$ cases are well within the possibility of being the parent scenario for some observed asteroid pair. In particular, if with time the binaries are allowed to reach the full synchronous state, they can be superposed to the region of synchronous small secondaries of the main belt.

The large, small mass-ratio binaries from the main belt (Pravec and Harris group L) have generally small satellites ($\sim 0.1\%$) and may originate in a wide variety of ways, including the simulations of this chapter and chapter 5.

The history of some couples shows how the primary can be smoothed in a relatively short time (months) from an irregular pear-like or contact binary shape. A comparison with the same simulation where all other orbiting particles and satellites have been removed shortly after the formation of the system shows how, in this case, the shape remains irregular (see fig. 4.29): this allows us to interpret the smoothing as due to the stresses induced by the secondary and/or matter exchange with a (possibly present) cloud of small particles. This in part confirms the experimental fact of many primaries of actual asteroid pairs being more regular and near to equilibrium figures ([D. Hestroffer, P. Tanga, 2005]).

[4] they are in line with the $\overline{L}$ content of Patroclus, though

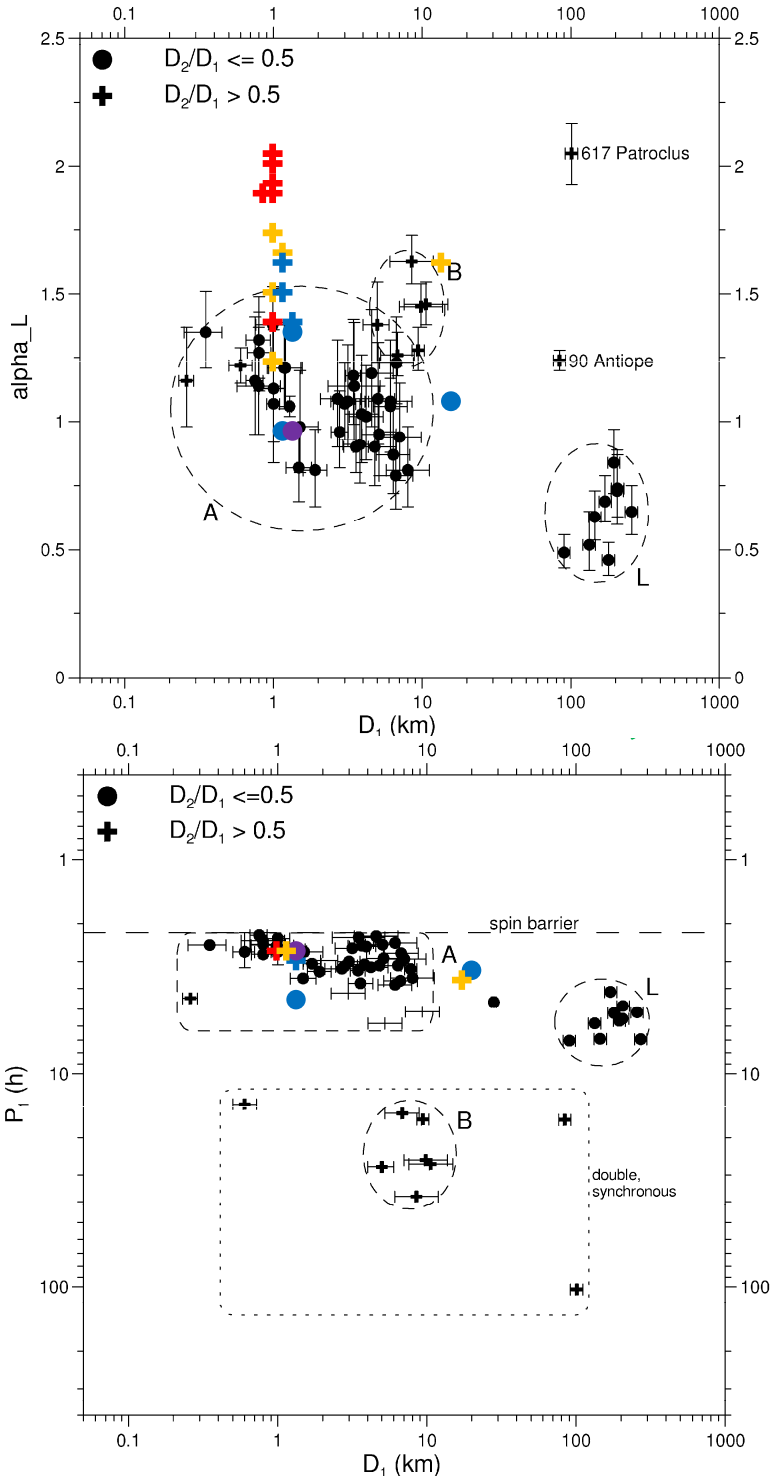

Figure 4.28: Plot of some relevant quantities for the objects issued from the long (some months) runs, compared to the groupings by [P. Pravec, A.W. Harris, 2007] (background image is the same as fig. 1.12, from op. cit.). Colour discriminates among starting $\overline{L}$: violet 0.5, blue 0.6, orange 0.7, red 0.8. Circles and crosses discriminate the size razio as per the original image's key. The rightmost objects are those from § 4.7 (but note that, as simulations scale well with size, each point can as well be though of as a horizontal bar; discriminating between sizes must be made according to physical considerations external to the simulations). In the $(D_1 - P_1)$ plot, results are largely overlapping. The results are compatible with the small binary asteroid population, even considering the mass ratio (not plotted here). With time, they may become synchronous and fit within group B. Patroclus system might be compatible with the $\overline{L} = 0.8$ bodies.

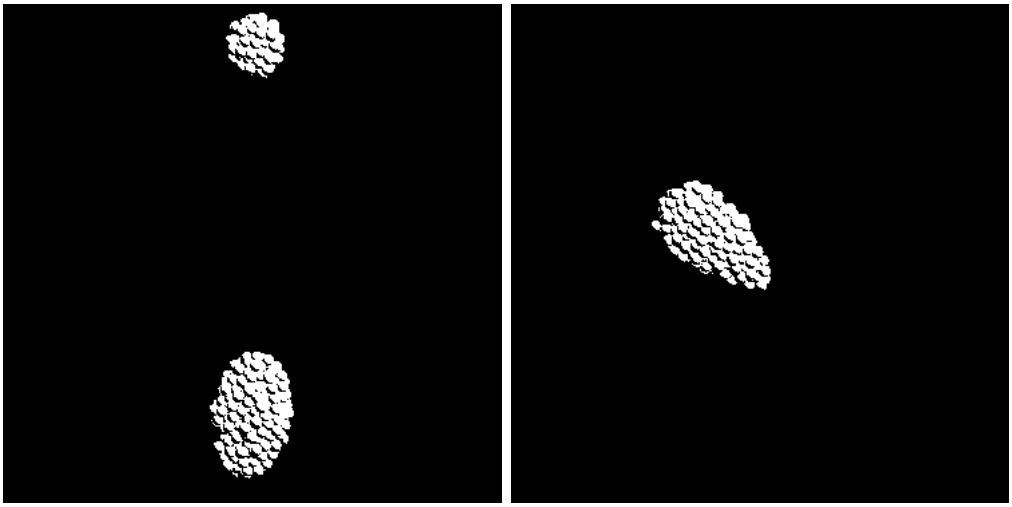

Figure 4.29: Smoothing of the primary in the evolution of the 7_2_8 system (left) is prevented (right) if all satellites are removed early in the simulation. Both images show the object after 52000 `pkdgrav` steps of 40 s each.

Some primaries do resist better, however, and retain their irregular shape, like the contact binary primary of 6_4_8.

Chapter 5

Spin-up Simulations

As shown by previous simulations (chapter 4, [J.F. Consigli et al., 2006], [P. Tanga et al., 2009 I]) equilibrium figures for bodies described by hard particles can sometimes differ from regular triaxial ellipsoids. A question then arises about their evolution when these different shapes undergo some gradual change in angular momentum.By looking at the possible range of equilibrium figures (cf. fig. 2.4), it is normal to wonder whether it is possible to actually explore some of them: in particular those close to the bifurcation towards binaries, to see if they can actually act as a passageway for binary formation processes, as suggested for example in [P. Descamps, F. Marchis, 2008] (cf. fig. 1.13).

Here we present the exploration of some shapes with a technique similar to that of [K.J. Walsh et al., 2008], but with a different premise and dramatically different results.

The approach we follow here is radically different from what was presented in chapter 4, where a sudden excess of angular momentum was introduced. As told in § 1.3.3, YORP effect has in the past decade been suggested as a possible responsible for pushing the asteroids beyond the stability limits of the simple ellipsoidal-like shape into binary asteroid formation, especially for those smaller than $\sim 25 \div 50$ km. Some studies have been performed to test its validity, as we discuss in § 1.3.3. Small collisions, YORP, periodical close encounter with the inner planets or other slow effects that may alter the equilibrium for a body are imagined to act on a much longer scale than the self-gravitational forces. While for example the YORP torque modifies the rotational state of an aggregate, the latter has time to readjust itself to the continually modified conditions in a quasi-static evolution.

We intended to explore the possible fission events and their issues, aiming at clarifying the dependency from initial conditions, and looking for those shapes that can more efficiently lead to a binary asteroid.

The idea is to simulate this kind of slow acting effects by subjecting the bodies to small angular momentum increases followed each by a suitable time left to the body to adjust its shape.

Here we just stress that we impose a gradual, regular change in spin which is independent from the object shape. This approach is not fully consistent with the nature of the YORP effect in itself, which may include spin-down periods and re-orientation of the rotation axis, possibly dependent on small details of the asteroid shape as shown

in [T.S. Statler, 2009]. A full consintent YORP simulation is possible in principle, but vastly increase the computational time involved, and is beyond the scope of this work.

Rather, the spin-up mechanism must be seen as a numerical method for approaching a shape to its spin limit, not as a process finely reproducing the real spin evolution of an object. We can however assume that, when close to splitting, our simulations could reproduce the effect of a gentle spin-up due to YORP.

5.1 Initial configurations and chosen parameters

5.1.1 initial rubble-piles

Since our previous simulations both from chapter4 and other sources (e.g. [P. Tanga et al., 2009 II]) have put at our disposal a large variety of shapes, sometimes presenting strong asymmetries, it seemed natural to try to use as wide a gamut of shapes as possible, to further examine the role of the initial shape in the possible binary formation process.

A first batch of shapes has been selected among the primary remnants of our 1000-particles simulations, with the choice based mainly on two criteria:

1. the high number of initial particles, to ensure an adequate rubble-pile behaviour, too few particles not being capable to assure a wide variety of shapes in response to the changing environment (rotation increase)

2. the variety of initial shapes.

The 12 selected shapes are generally composed of

$$N \sim 850 \div 1000$$

particles with the same characteristics of the simulations in chapter 4:

$$R_p = 50m \quad \rho_p = 3000kg/m^3 \quad .$$

To increase the range of bodies on which to study, we added in 6 more objects that resulted from other simulations, with the following characteristics:

$$N \sim 1200 \div 1500 \quad R_p \sim 86m \quad \rho_p = \sim 1000kg/m^3$$

of different shapes.

All resulting bodies have sizes $\sim 1\,\mathrm{km}$.

For the lack of a suitable way to classify those shapes, we used a (rough) visual appearance criterion, individuating the following kinds of shapes:

ellipsoidal (*ell*) shapes

double-pointed (*dbp*) shapes are similar to elongated ellipsoids, but with sharpened tips, a result of some previous particle loss

drop shaped (*dro*), which are bodies generated similarly to the previous ones, but more asymmetrical, with the mass loss having occurred only on one side; the most elongated may resemble the "egg-like" Poincaré shapes[1]

hamburger shaped (*ham*), a very flat spheroid

triangular shaped (*tri*), a flat three-spiked object

bilobated / contact binary (*cbi*), a contact binary object

irregular (*irr*): other unclassified shapes.

where the 6 low density body are additionally marked with *-ld*. Additional relevant information about their different shapes is given for the single bodies in § 5.3.

Most bodies are already in a high rotational state with generally $\overline{L} > 0.4$, but are in an initially stable equilibrium. It is posited that instability-creating mechanisms can really start to influence the binary creation process only from this stage on, for example by pushing the angular momentum beyond the quantity that a single rubble pile can hold without breaking.

5.1.2 chosen `pkdgrav` parameters

The coefficients of restitutions and the θ_c angle have been kept at

$$\epsilon_N = \epsilon_T = 0.8 \quad \theta_c = 0.5 \quad ,$$

as for the chapter 4

For the dynamical parameters, as we wanted to reproduce small incremental transformations, we decided to act on the side of caution, to try to limit as much as possible random numerical "noise" coming from `pkdgrav` and considering the results in § 4.6.

We took for the $\rho_p = 3g/cm^3$ objects a very conservative timestep of

$$t = 8 \cdot 10^{-7} yr/2\pi \approx 4s$$

i.e. 10 times less than for the high angular momentum simulations, and considerably less than [K.J. Walsh et al., 2008][2]. The 1500-particles $\rho_p = 1g/cm^3$ simulations have been run with a timestep re-scaled by $\rho^{-1/2}$ to $\approx 1.39e-6yr/2\pi$ (corresponding to $\approx 6.29s$), in order to maintain the same accuracy. We also decreased the `dCL` down to 10^{-6} for a higher precision than for the simulations of chapter 4.

For `iOO` we used the `repel` option, in accordance with what exposed in § 3.8.1.

Because we are primarily interested in studies on body deformations, differently than for the simulations in chapter 4, we did not use the heliocentric reference frame option (see § 3.7), as it unnecessarily slows the computation.

[1] cf. the instabilities of the Jacobi sequence in § 2.1.5

[2] they mainly used a 50 s timestep length (K. Walsh, private communication)

5.2 The simulations structure

The simulations run are each composed of a repeated cycle of three steps:

1. a `pkdgrav` integration of 50k timesteps of $\sim 10^{-3} t_{ff}$ under the sole role of self-gravity and inter-particle collisions
2. a semi-automated search to look for any mass loss or secondary that may have been formed
3. a sudden increase of 1% of the angular momentum of the body (the so-called "spin-up kick"), in the case no secondary has appeared

5.2.1 `pkdgrav` integration

To ensure a suitable time passes between angular momentum increases, we left the system evolve untouched for 50,000 timesteps, corresponding to $\sim$50 t_{ff}, a time much higher than what has been observed in [P. Tanga et al., 2009 II] as necessary for the reshaping into a new equilibrium. Overall, this mechanism reproduces the slow spin-up performed for example by the YORP effect on a small asteroid.

As the initial bodies were selected as remnants from previous simulations where mass loss had occurred, some may present single particles or small cluster initially detached from the real primary. We thus chose to start with a 50k step integration before the first "spin-up kick" to allow these particles to settle down and be sure the initial bodies are effectively at equilibrium.

5.2.2 search for secondaries and elimination of the escaping minor fragments

While the rubble-pile is left free to evolve in the `pkdgrav` integration, its shape is allowed to change to adjust for the higher angular momentum content since the last spin-up kick. In this process, after several kicks, it is inevitable for some mass to eventually escape the body.

After each `pkdgrav` integration, each body is examined with `rpa` (see § 3.9) to detect the presence of any fragment having detached from the aggregate.

A first automated examination is performed with the *linking scale* set to 1.2. If only one aggregate is detected (i.e., apparently no mass loss has occurred), we accept the result, and proceeded to the next spin-up kick.

This procedure, while speedy, has the potential for a "false-negative" mass loss detection if a single particle or small cluster is found very close to the body surface, as told in § 3.9.1. Yet, this exception is soon detected by the following step, when the spin-up kick, applied to all particles, pushes free bodies orbits further away, allowing their detection. As the particle has been detected in the following cycle, a rapid visual inspection of its story will lead to a reconsideration of the previous step, if the need arises to keep the particle[3].

[3] i.e. in the case the particle is just "jumping" from one location to another on the surface of the body

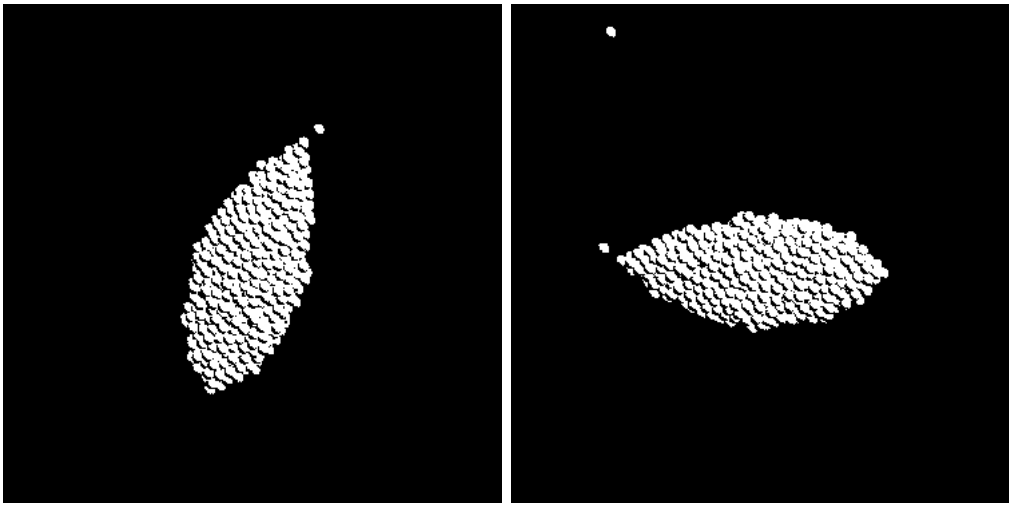

Figure 5.1: Loss of particles from the tip of a body (polar view, rotation proceeds anticlockwise). Emissions of single particles or very small clusters happen frequently during the spin-up simulations as the bodies are accelerated; mostly, these are emitted in hyperbolic orbits. As this carries away angular momentum excesses, often the primary mass is simply rearranged as to keep the overall shape similar than before the loss.

If the output of `rpa` indicates an actual mass loss, the test is repeated with different *linking scale* values (generally from 1.05 up to a value of 5 or 10), to check for consistency between the outputs. Again, if the results are in agreement (as they usually are), they are simply accepted as such. Otherwise, a visual examination is performed to check for the consistency of the secondaries.

As we look for a large-binary formation event, our idea was generally to eliminate before the next "spin-up kick" any particle or cluster that do not remain in orbit around the leftover primary.

For the purpose of the binary forming process, different kinds of mass loss can take place, with each case deserving a separate description.

single particles escaping the primary

The most frequent case of mass loss consists of single particles escaping the body from one of the tips. For the most part, these are emitted at high velocity on a hyperbolic trajectory (see fig. 5.1).

As our goal is the observation of satellite formation, and these particles no longer play any role in the reshaping of the body, they are simply ignored and removed from the system.

single particles remaining in orbit

In some instances, emitted single particles can remain in orbit around the primary. This is especially the case with the least elongated objects, and in particular in the first

phases of the *hamburger* and *triangle* simulations, similarly to the cases examined in § 4.3.2.

These objects are midway to our goal of capturing a secondary formation event. There are two main reasons as to why these objects should be kept in the simulation, although they are not relevant for directly producing significantly large secondaries ($>\sim 5 \div 10\%$ in mass).

First, if many small fragments are allowed to enter orbit during different "spin-ups", this cloud of fragments could, in a process already observed in some high angular momentum simulations (see § 4.3.2), lead to an aggregation in orbit of a consistent secondary. This is precisely the process observed in [K.J. Walsh et al., 2008] examined in § 1.3.3). For the same reasons discussed there, single particles detaching from the primary and entering orbit should be excluded from the system by the following step, simulating their escape in times shorter than needed for the next mass loss.

Yet, it could be the case for a considerable number of particles to be emitted at once, forming a cloud. In these cases, a real satellite could be formed by coalescence of fragments, as observed in some simulations in chapter 4. In such (rare) extreme cases where a big cloud of fragments is produced, we chose to adopt an ad hoc technique to simply allow the cloud to evolve naturally with a longer `pkdgrav` integration before applying the next spin-up kick.

Secondly, some small satellites have been observed that amount to only a tiny fragment ($\sim 0.1\%$, see § 1.3.1) of the primary mass, in line with a $\sim 1/1000$ ratio of a single particle to the whole aggregate. Again, there is no guarantee as to the stability or the origin of these configurations. Moreover, our goal is an understanding of the formation process of at least consistent medium to large sized secondaries.

These considerations lead us to simply remove from the system any single particle, regardless of its orbit being initially bound or not.

By the same line of reasoning we can also remove very small clusters (a few particles at most) that occasionally form.

large fragment emissions

The single particle (or very small cluster) mass losses do usually very little in reshaping the primary: while some mass is expelled in small batches of particles from the tips of the aggregates, new one coming from elsewhere on the body take its place, and the resulting shape often resembles the pre-mass loss one[4]. In some instances, however, after many spin-up cycles, it is possible for the aggregate to slowly deform out its initial shape, especially in the case of little mass loss during the evolution. This produces in the overall shape a narrowing in the figure, and the growth of a protuberance; eventually, this detaches from the primary in a sort of "budding" or "fission" process (see figure 5.2) creating a separate secondary aggregate.

[4] interestingly, a similar phenomenon is also observed with the crystalline (i.e. rigid) packing in [K.J. Walsh et al., 2008], where it ensures the steady supply of mass for the secondary to form up

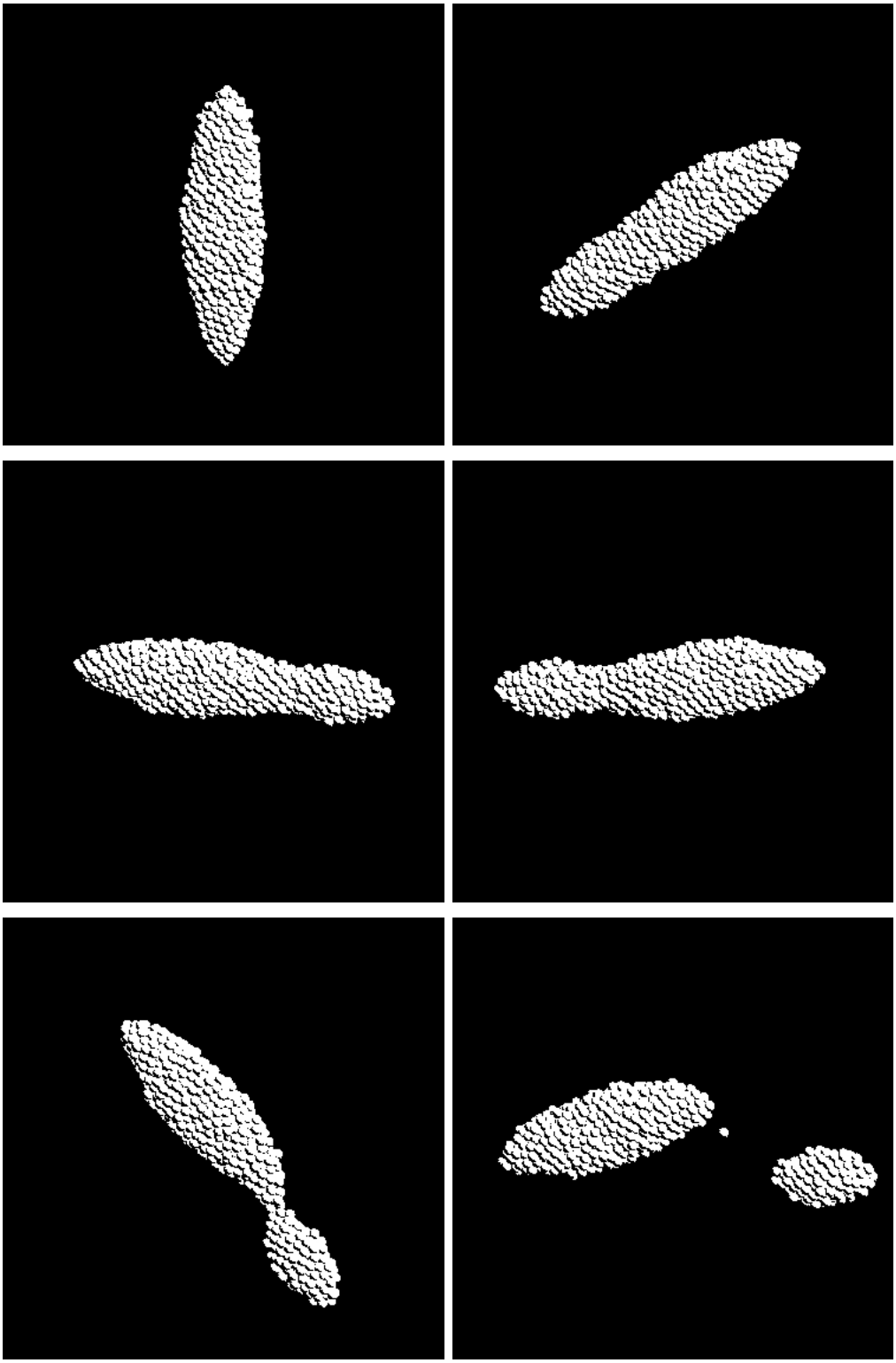

Figure 5.2: Sequence of evolution of the **dro3** body, from polar view; left to right, top to bottom. (1) the initial configuration; (2) after 15 "spin-up kicks", the shape has evolved a protuberance; (3)-(6) after 18 kicks, in a fast process (the images describe the last (clockwise) rotation period of the parent body) the protuberance quickly detaches forming a sizable secondary (mass ratio 0.25). see § **large fragment emissions** in 5.2.2

These secondaries can be emitted either in elliptical or in hyperbolic orbits.

As the aim of our study was to try to form asteroid binaries, we ignored and eliminated from the simulation any secondary emitted in a hyperbolic orbit, similarly to the single particles mass loss, and applied the next spin-up kick.

Conversely, we stopped the simulation if a stable secondary has formed, and no more spin-up kicks are applied. A short study on the stability of the mutual orbit is then performed.

5.2.3 spin-up kick

If no (initially stable) secondaries are formed, and after the elimination of any fragment detached from the primary to speed and the simulation and keep it "clean", the remaining object is spun up to simulate the slowing action of e.g. YORP in accelerating the object.

We wrote a small automatic routine that increases the angular momentum of a rubble pile by multiplying by a specified amount (here 1.01) all the velocity and spin vectors of their component particles with respect to the centre of mass of the body.

In all cases, we used a kick of 1% increase (the same used by [K.J. Walsh et al., 2008]).

The resulting spun-up aggregate is then fed back to `pkdgrav` for the next integration.

5.2.4 negative simulation ending

After many cycles without a positive stable secondary formation, the practical question of whether stopping the simulation or not arises.

We had initially planned to continue the cycle until a pre-determined fraction (for example 1/3) of the initial mass had been lost. However, this has revealed as too time-consuming, as the single particle mass loss showed to be a very slow process. As some bodies did fission, while some others kept losing mass without any pattern evolution (shape $\sim$ constant), ultimately we decided that after ~ 50 "spin-up kicks" without any significant secondary formation, the simulations were stopped anyway.

5.3 Simulation results

5.3.1 the angular momentum barrier

Some first conclusions can be drawn by examining the points in the simulations in which there is a mass loss. There appears to be in particular an "angular momentum barrier" (L-barrier), around $\overline{L}$ 0.4 to 0.5 (slightly different for each body), which is an upper bound for the internal angular momentum content. When, in the course of the simulations, $\overline{L}$ grows too much, an inevitable mass loss appears that drops $\overline{L}$ down to a lower value (see fig. 5.3).

This is in agreeing with both the hydrostatic theory for fluid bodies (cf. § 2.1.5) and previous results of chapter 4 and elsewhere (cf. 3.10) for the re-accumulation of aggregates from a dispersed cloud of fragments, where the formation of bodies with $\overline{L}$ beyond 0.4 is strongly suppressed.

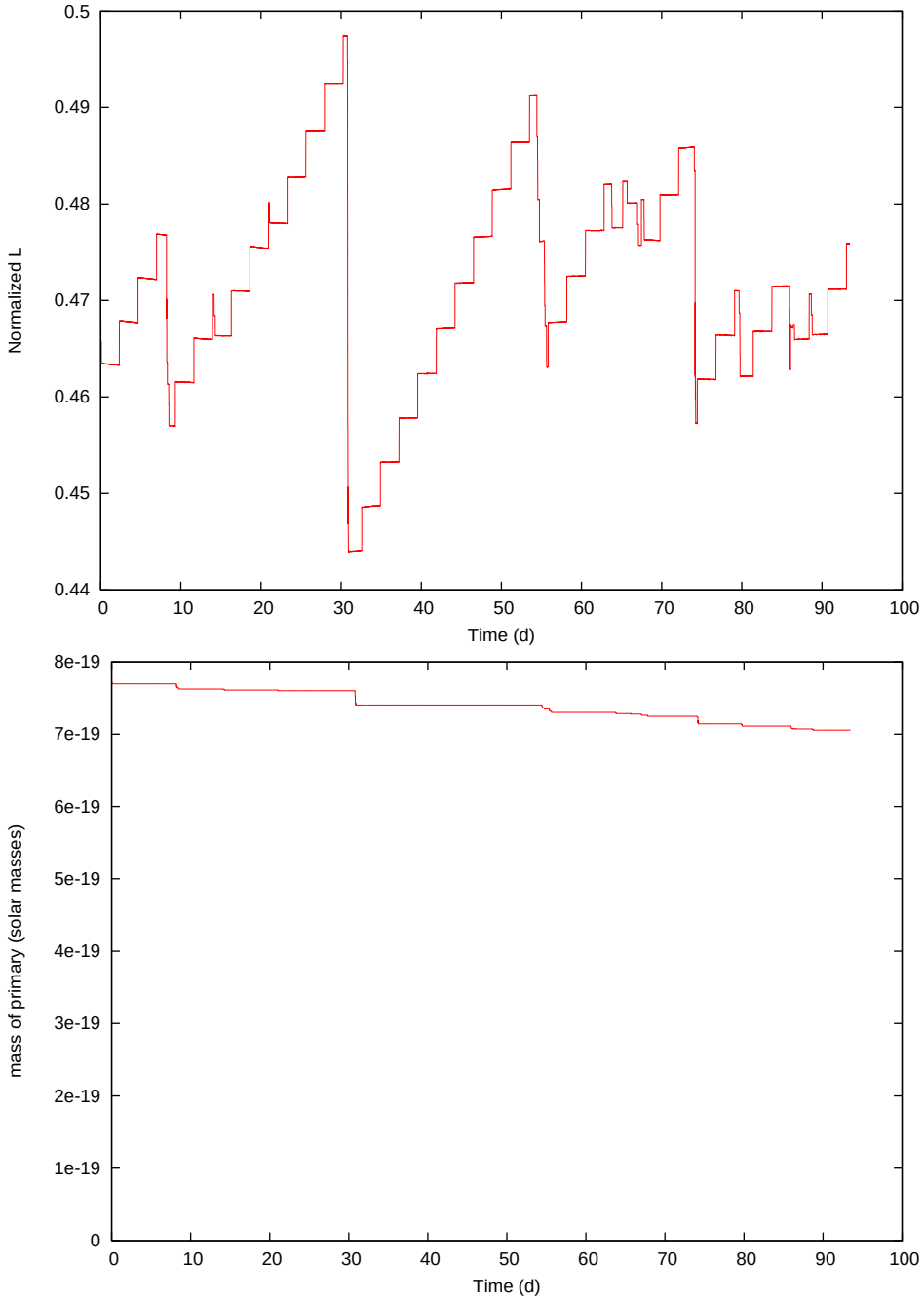

Figure 5.3: (above) evolution of $\overline{L}$ for the **dbp1** body (see text for nomenclature). the "spin up kicks" are visible as the steps of the stair-like pattern. occasionally, as a certain limit $\overline{L}$ (in this case, between ~ 0.47 and 0.50, and cf. § 5.3.1) is reached, mass loss occurs. (below) the parallel evolution of the mass of the primary. Most times, mass loss is due to groups of single particles and very small fragments violently emitted from the ends of the body into hyberbolic orbits. In this case, no stable secondary is formed.

A brief description of each simulated body follows; each one is identified by the three-letter symbol denoting its initial shape (see § 5.1.1) and by a progressive number to distinguish them. The 6 low-density bodies have been marked with "ld".

5.3.2 dbp1

An initially elongated body with sharpened ends, this object after some early minor mass loss in the form of particle emissions, slightly deforms into a pear-like one. It clearly present a L-barrier at $\overline{L} \sim 0.485 \pm 0.015$ (see fig. 5.3). The most interesting feature in the evolution is certainly the bump that start forming on the tip. This fails to transform into a real binary formation event, as the process is interrupted by the too early detachment of the mass, which breaks into several minor clumps and is dispersed (see fig. 5.4).

The subsequent part of the simulation does not show any further noteworthy shape change.

5.3.3 dbp2

This body starts as a squatter shape than *dbp1*, and is capable to accumulate angular momentum with little mass loss or reshaping. Eventually, the bump-forming mechanism starts, and when the body reaches $\overline{L} \sim 0.52$ the protuberance regularly evolves to form a small secondary of $\sim 15\%$ the mass of the remaining primary, in an initially bound orbit. The evolution of this body is plotted in fig. 5.5 - 5.6[5].

It is the smallest bound satellite formed; however, it is subsequently lost (cf. § 5.5).

5.3.4 dro1

A quite elongated object, it suffers little shape change and only a small significant mass loss. It eventually develops a secondary of $\sim 30\%$ of the primary mass through the process described in § 5.2.2.**large fragment emissions** (see fig. 5.7).

Here, the $\overline{L}$ value increases beyond ~ 0.55 by the time of splitting.

5.3.5 dro2

A similar initial shape to *dro1*, this body follows a different route. Presenting a L-barrier at $\overline{L} \sim 0.47 \pm 0.01$, it frequently presents minor mass emissions that never remain in orbit; see fig. 5.8.

5.3.6 dro3

An initially similar object from *dro2* , this body presents the opposite behaviour. It shows no mass loss at all, gathering an $\overline{L} \sim 0.6$ before splitting in two with a secondary of $\sim 25\%$ the mass of the primary (see fig. 5.9 and 5.10).

[5]we remind the meaning of the dimensionless angular velocity $\overline{\Omega} = \Omega/\sqrt{\pi G \rho}$ for a body, which have been introduced in (2.29)

Figure 5.4: the mass loss of the **dbp1** body occurring after kick number 13 (cf. also fig. 5.3); polar view; left to right, top to bottom; rotation proceeds anticlockwise. (1) the initial body (obtained from other simulations; the two free particles visible are expelled from the system and removed before the first kick). (2) by the 13th kick, a small protuberance has formed. (2)-(6) in the course of one rotation this protuberance is lost, with its fragmented mass emitted in hyperbolic orbit.

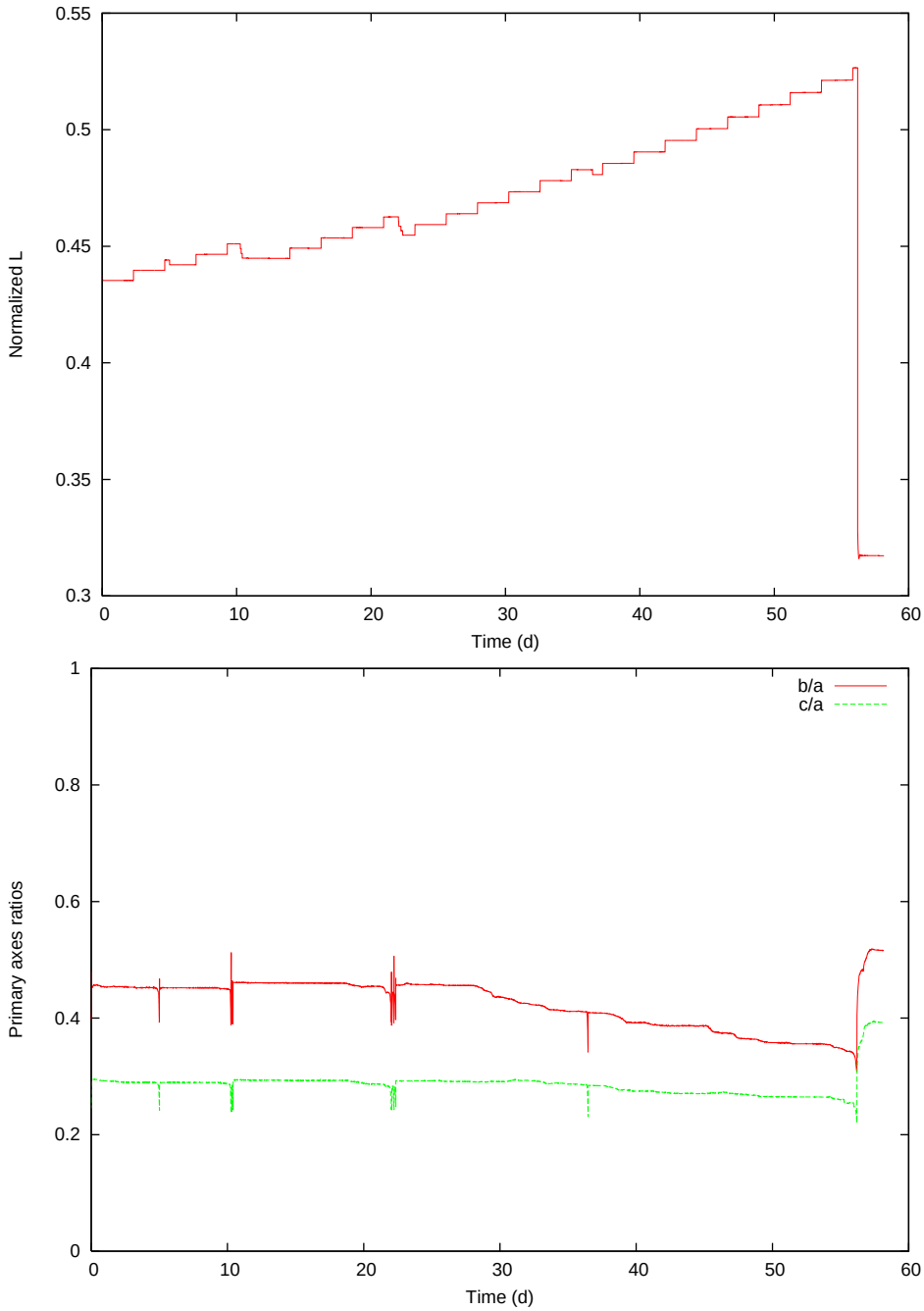

Figure 5.5: (above) Evolution of $\overline{L}$ for the **dbp2** body. Little mass loss occurs until the secondary forming process. (below) The corresponding evolution of the axes ratios of the body; the spikes are due to mass emissions that interfere with the `rpa` algorithm (see § 3.9). Initially, the body does not deform. When the angular momentum reaches a certain amount, the body starts to deform into more and more elongates shapes typical of the corresponding Jacobi shape for the corresponding $\overline{L}$, eventually producing a protuberance that in the final step separates forming a secondary of mass $\sim 15\%$ that of the remaining primary. cf. also fig. 5.6.

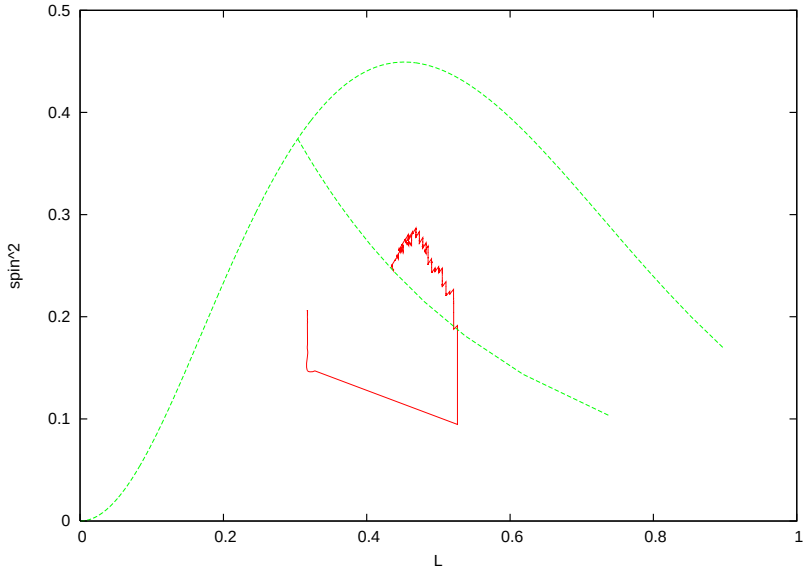

Figure 5.6: Evolution of the **dbp2** body (red line) in the $(\overline{L}-\overline{\Omega}^2)$-plane (Maclaurin and Jacobi sequences in green for comparison). The body starts near the centre of the figure. At first, the $\overline{L}$ increase reflects exclusively on a greater spin rate. Once a limit for the stability has been reached, the body starts to elongate (cf. fig. 5.5), covering a path parallel to the Jacobi sequence. Eventually, the body fission: the abrupt turn donward corresponds to the separation event. Sebsequent evolution is for the primary recompacting its material. (cf. below, § 5.6.2)

5.3.7 dro4

The initial body is similar to the *dro1*, *dro2* and *dro3* cases, and its evolution presents no appreciable shape change while it slowly but steadily releases particles from its tip, maintaining a Poincaré-like shape. The slow L-barrier at $\overline{L} \sim 0.45$ is probably connected to this behaviour (see further § 5.6.3). See fig. 5.11 and 5.12 for its evolution.

5.3.8 dro5

Another elongated body. A similar case to *dro4*, it has a L-barrier around $\overline{L} \sim 0.47 \pm 0.01$, several small mass losses and no appreciable shape change in the observed period.

5.3.9 dro6

This body is more spherical than the other *dro* cases, with an initial α_2 value of 0.6. It initially develops into a pear-like structure, with the head eventually detaching into a small "secondary" of $\sim 4.5\%$ of the primary mass, dispersing into an unbound orbit: see fig. 5.13.

After 19 more kicks, a similar process repeats itself.

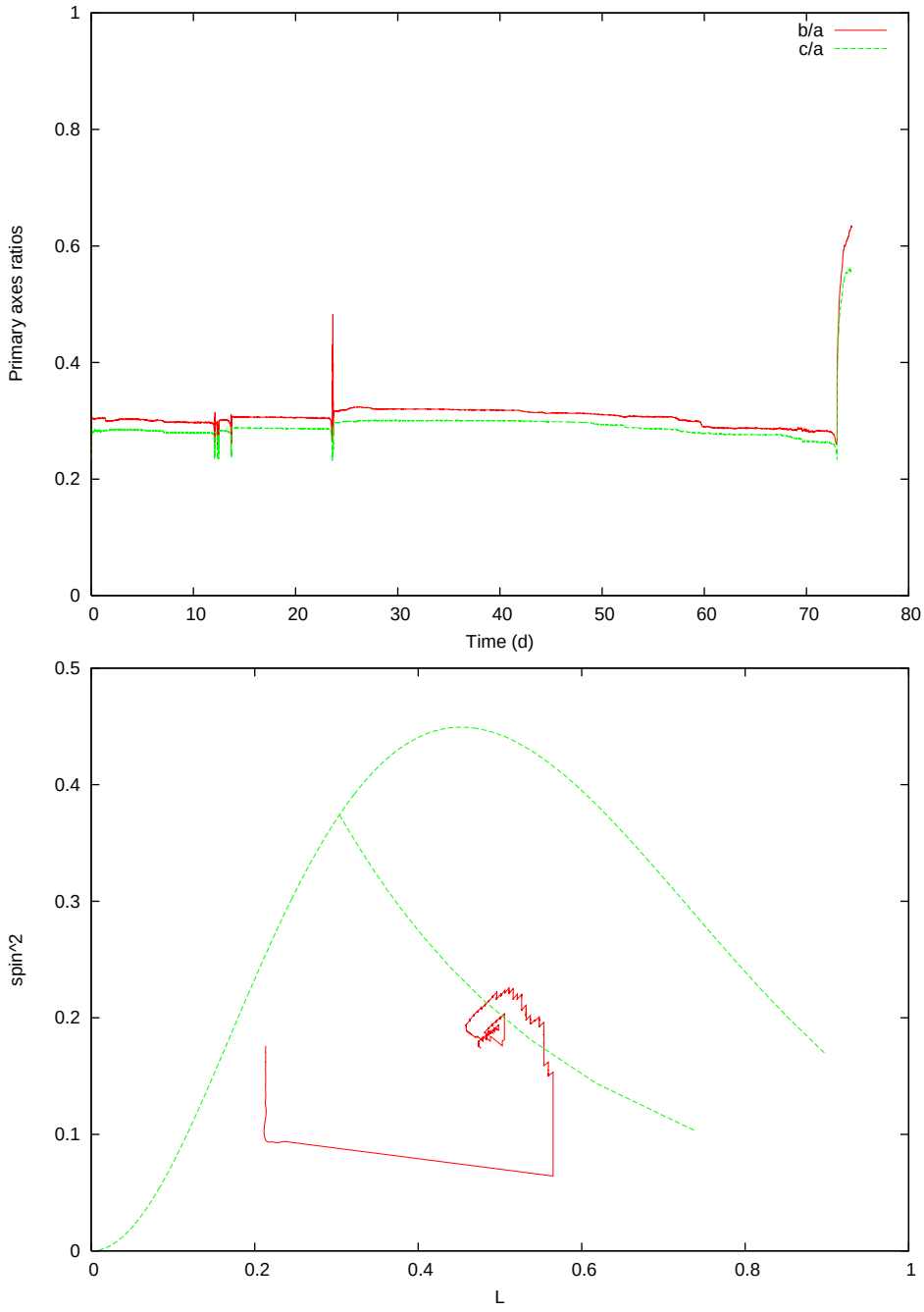

Figure 5.7: (above) Shape evolution for the **dro1** body. (below) the trajectory of **dro1** (red line) in the$(\overline{L}-\overline{\Omega}^2)$ plane compared to the hydrostatic MacLaurin and Jacobi sequences (green): the path followed is similar to dbp2 (cf. fig. 5.6). The formed secondary has a mass of $\sim 30\%$ that of the leftover primary.

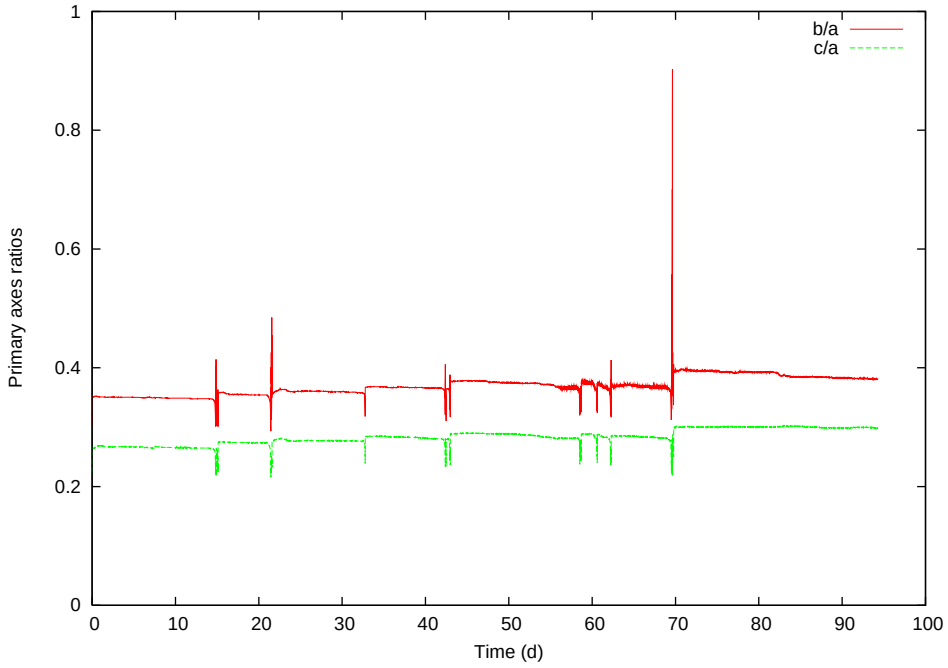

Figure 5.8: Shape evolution for the **dro2** body. It keeps a $\sim$ constant shape throughout the evolution. cf. also 5.9.

5.3.10 dro7-ld

An initially ellipsoidal object, it evolves into more elongated shapes by each kick. By the end of the simulation (67 kicks), it has reached a drop-like shape, with no sign of settling at a preferential shape (see fig. 5.14). It may fission if the simulation is allowed to continue, but no time scales can be foreseen and because of time limitations we did not investigate further.

5.3.11 dro8-ld

An elongated egg-like object. It maintains the overall shape throughout the simulation. The most significant event is a mass loss of $\sim 3\%$ concentrated in 2 small clusters and some free particles, emitted into hyperbolic orbit.

5.3.12 ham1

This body starts as a spheroid with $\overline{L} \sim 0.51$, an unstable configuration (cf. § 2.1.4), which with successive mass losses gradually transforms into a more elongated object. The initial mass losses are similar to those of the spheroidal objects of the high angular momentum simulation (cf. § 4.3.2).

In the second part of the simulation it presents no significant mass losses before fissioning at $\overline{L} \sim 0.50$ producing a secondary/primary mass ratio binary of ~ 0.26. The evolution is shown in fig. 5.15 and 5.16.

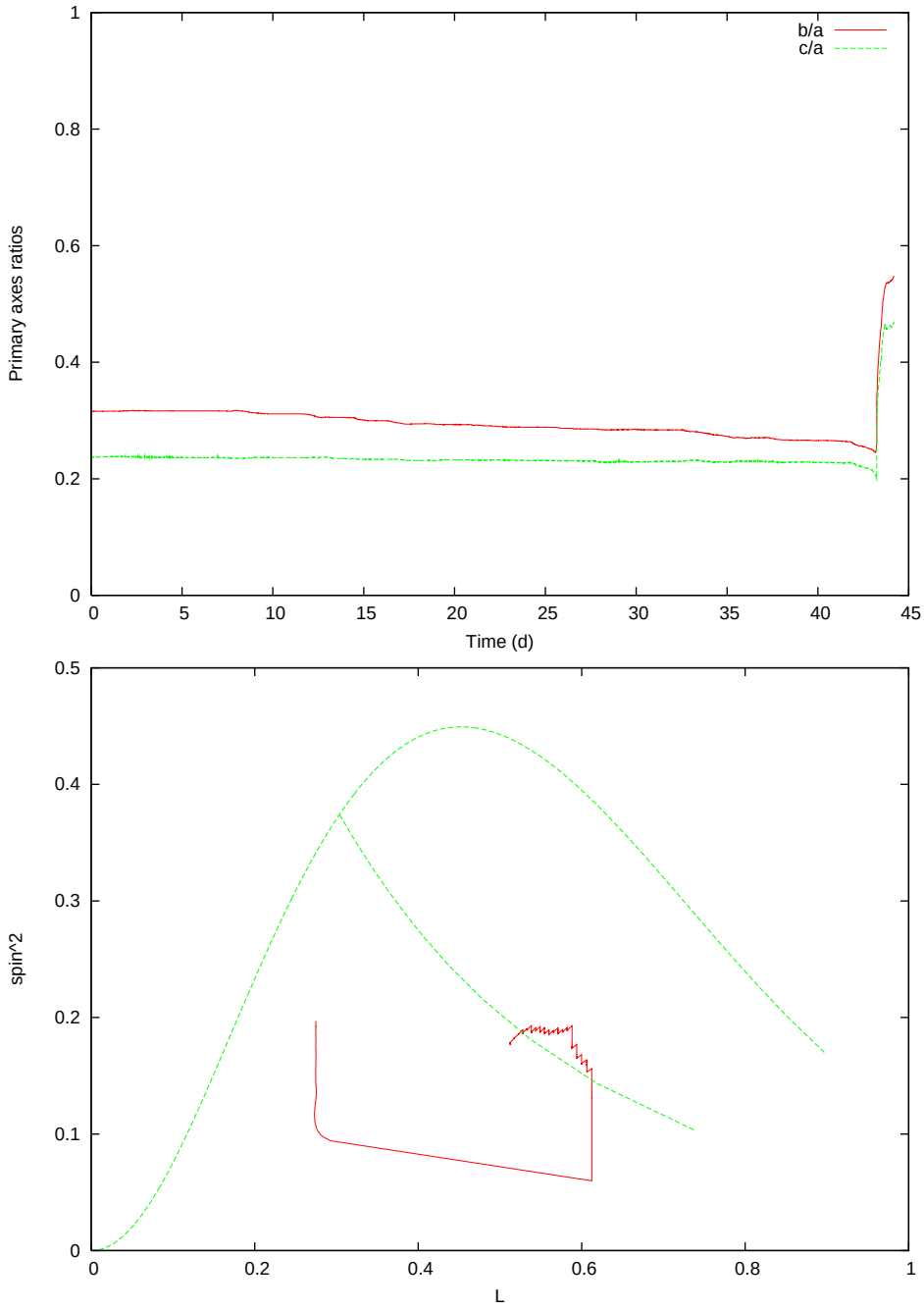

Figure 5.9: Evolution of the **dro3** body, which forms a satellite with $\sim 25\%$ of primary mass. (above) Axes ratios, cf. with 5.8. (below) Trajectory in the $(\overline{L} - \overline{\Omega}^2)$ plane (red line) compared with the Maclaurin and Jacobi figures (green): this is similar to fig. 5.6 and 5.7.

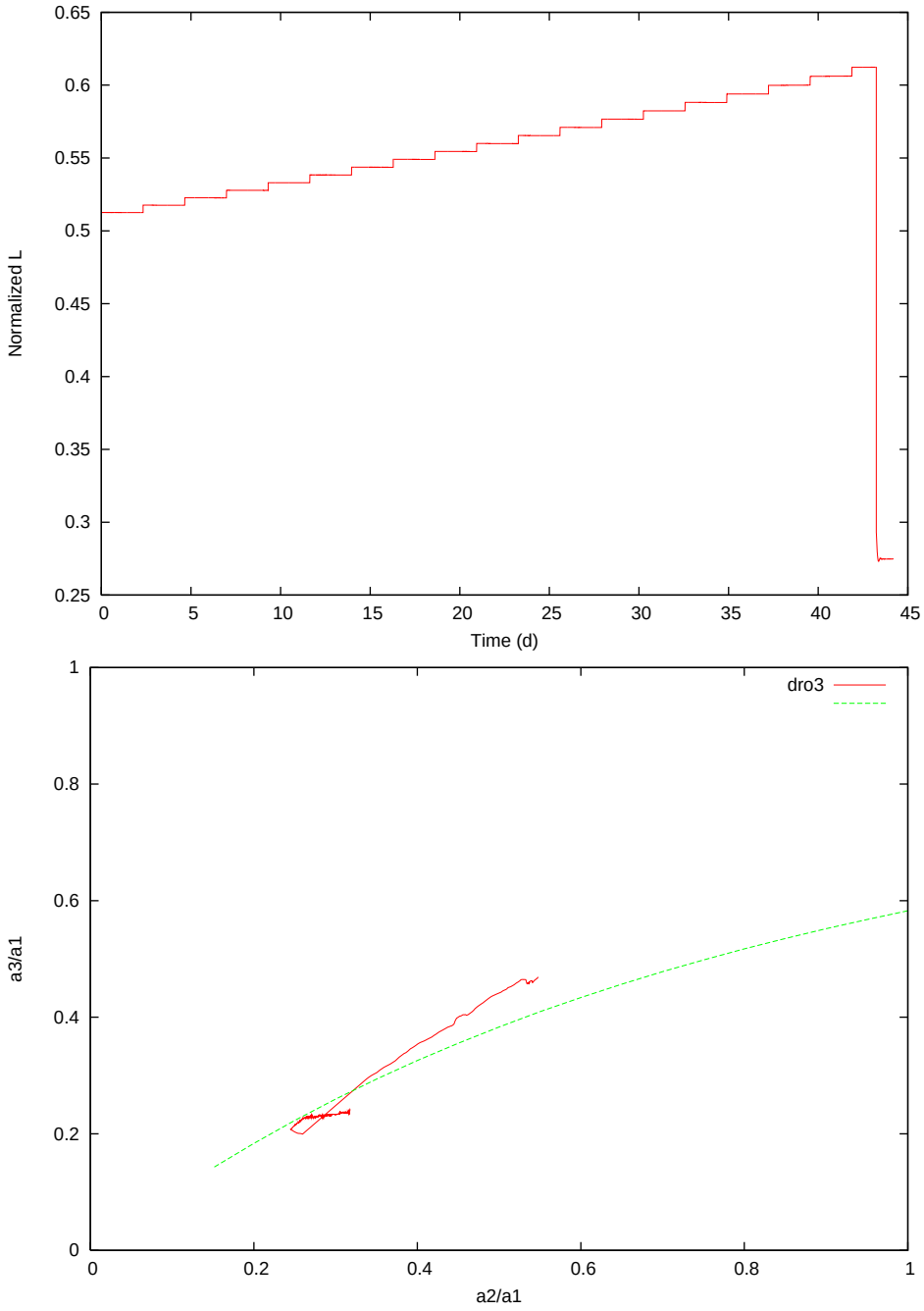

Figure 5.10: (above) **dro3** manages to accumulate a very high $\overline{L}$ without mass loss. (below) trajectory of the shape in the $(\alpha_2 - \alpha_3)$ plane compared to the Jacobi sequence (green): the body starts as a very elongated Jacobi object near (0.3; 0.2). It evolves slightly before fissioning (the U-turn in the trajectory).

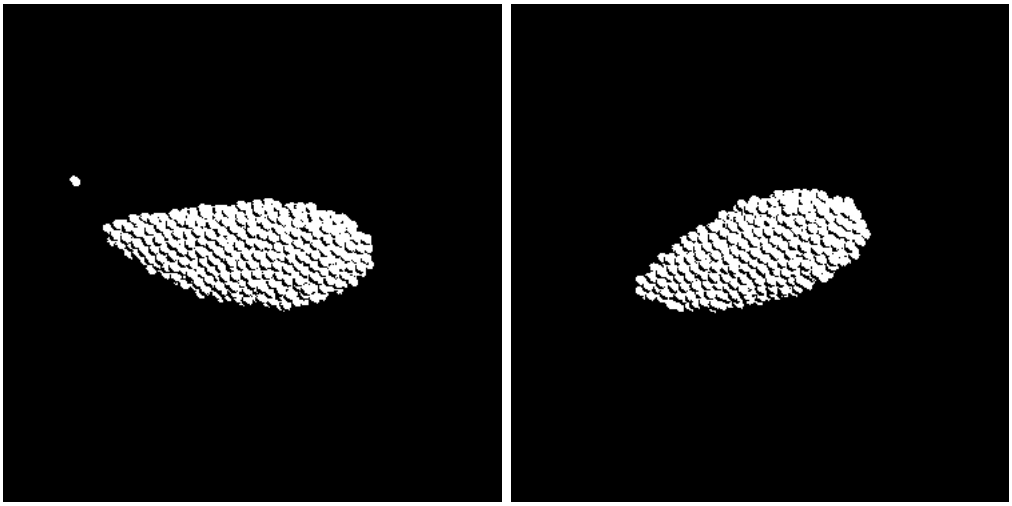

Figure 5.11: (left) initial shape of **dro4**. (right) its shape after 46 kicks. little evolution has occurred in the process. cf. also fig. 5.12.

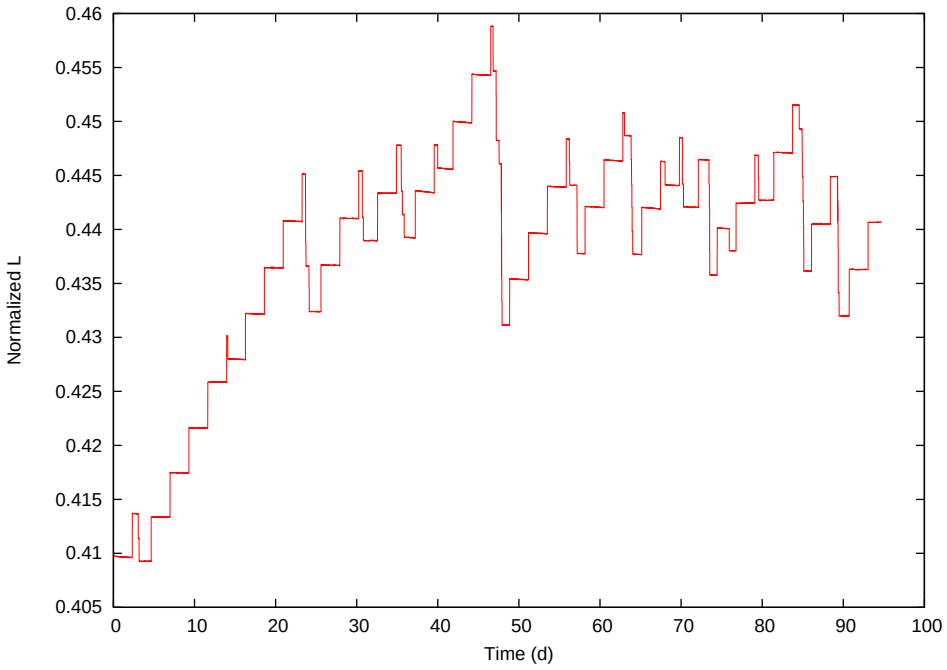

Figure 5.12: Evolution of $\overline{L}$ for the **dro4** body. The low angular momentum barrier at $\overline{L} \sim 0.45$ produces many small mass losses with particles emitted into hyperbolic orbits.

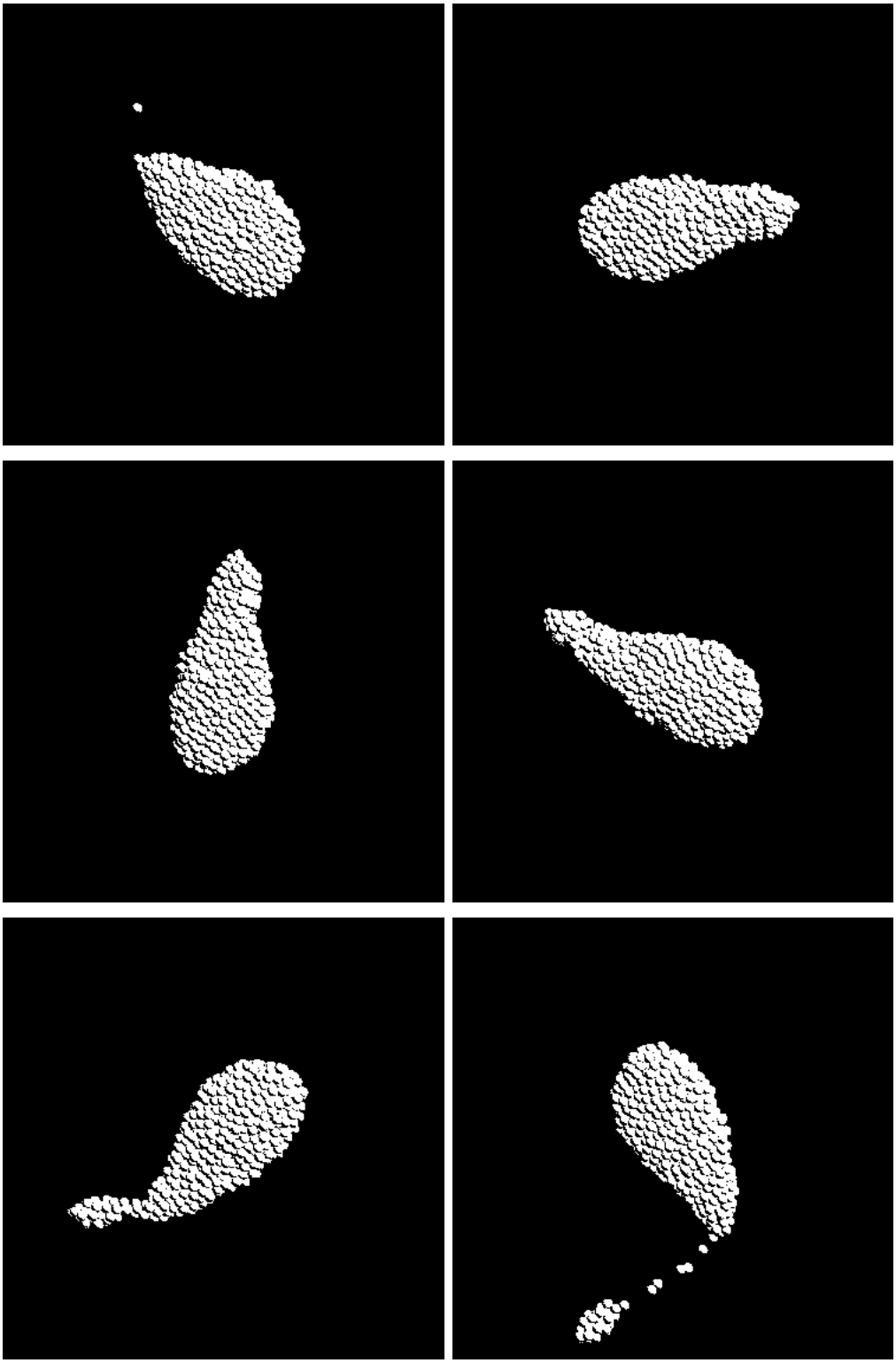

Figure 5.13: Sequence of evolution of the **dro6** body, from polar view; left to right, top to bottom. (1) the initial configuration; (2) by the 14th kick, the shape has evolved a protuberance; (2)-(6) at a point, this rapidly detaches (rotation proceeds anticlockwise) into a small gravitationally unbound cluster. A similar process repeats after 19 more kicks.

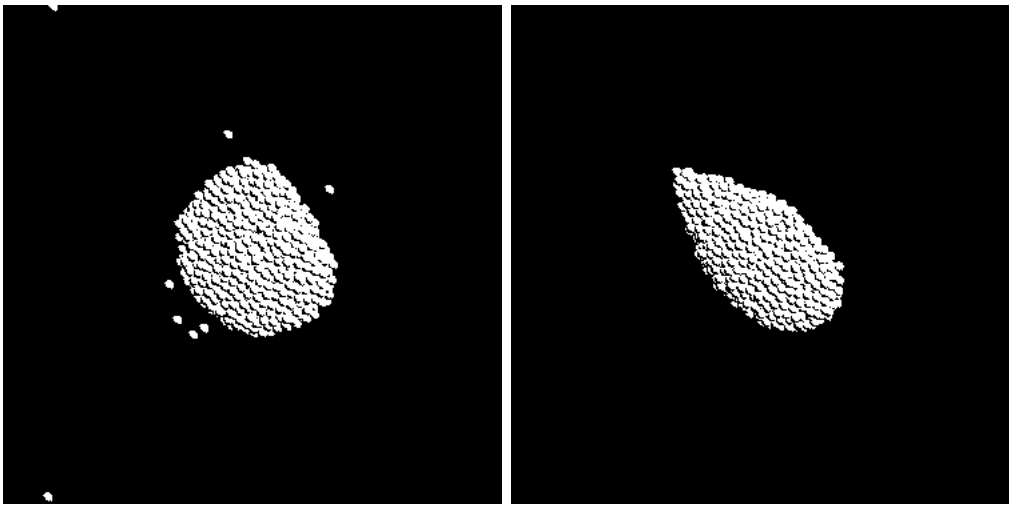

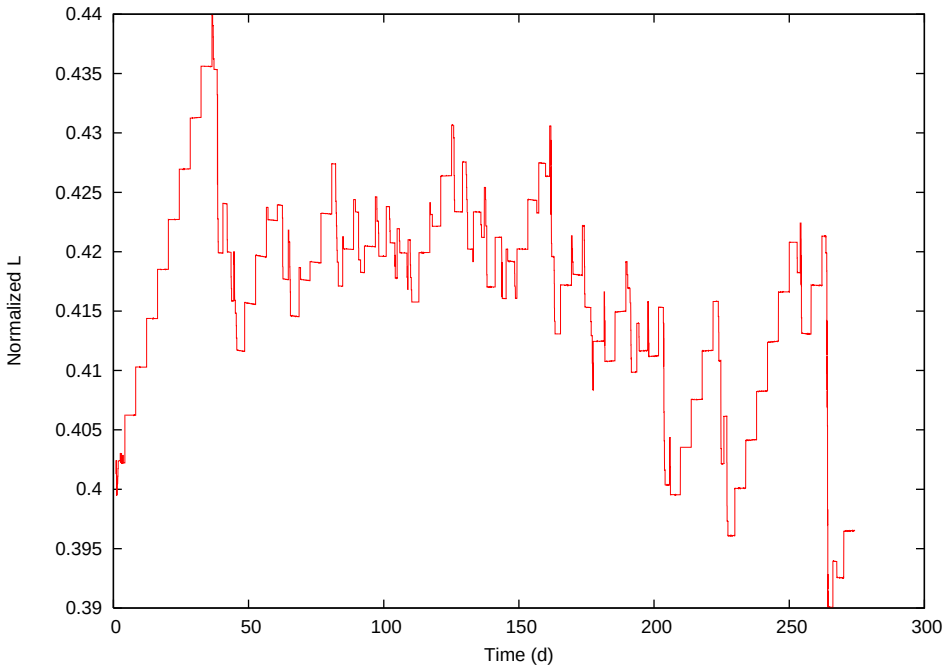

Figure 5.14: Evolution of the **dro7-ld** body. (above) Initial and final shapes (67 total kicks); the shape has changed and apparently the evolution is still ongoing (cf. § 5.3.10). (below) Evolution of $\overline{L}$; the low "L-barrier" probably prevents secondaries to form.

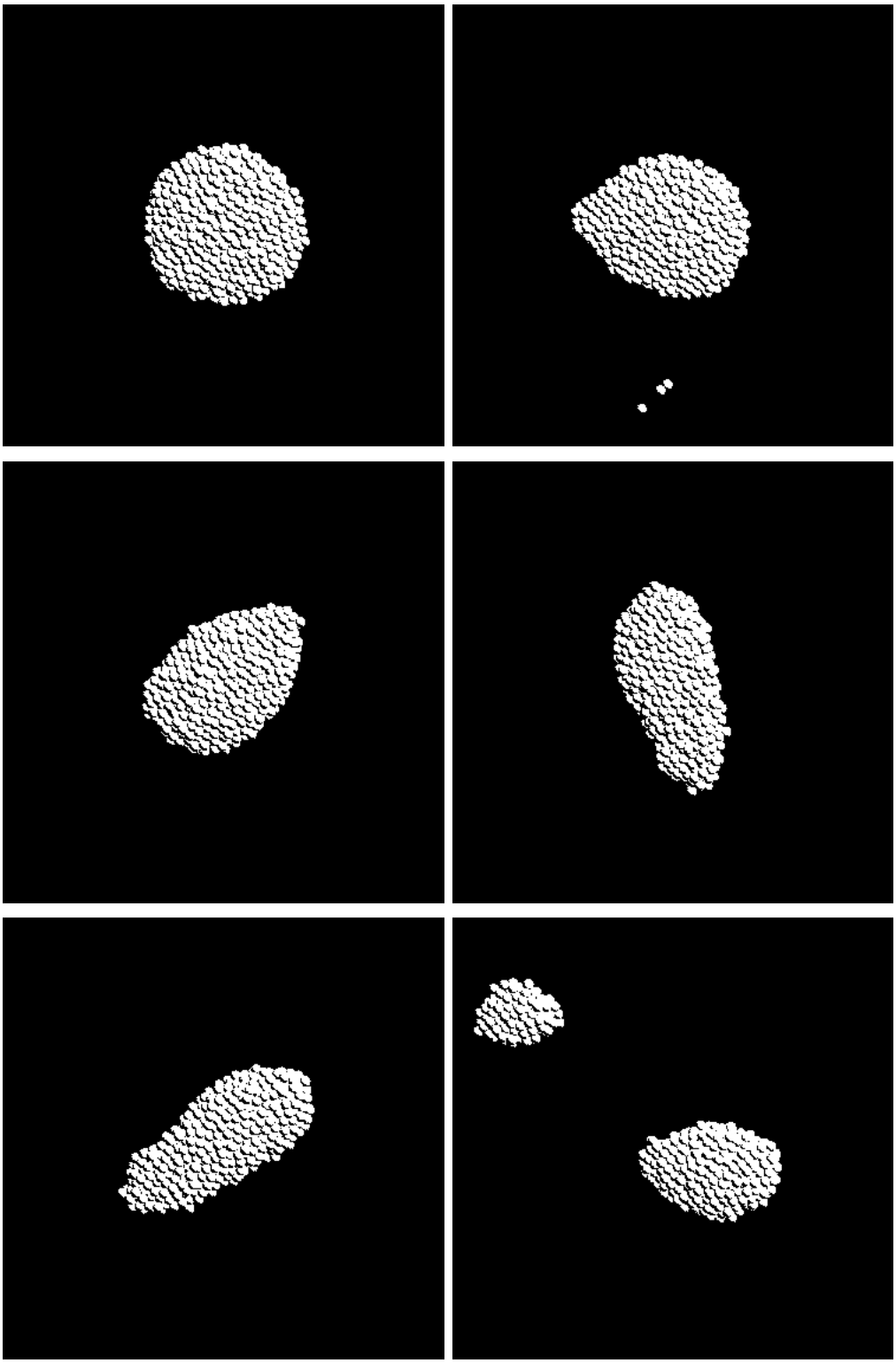

Figure 5.15: Sequence of evolution of the **ham1** body, from polar view; left to right, top to bottom. Initial shape and after 5, 10, 15, 20 and 25 kicks. See § 5.3.12 and fig. 5.16.

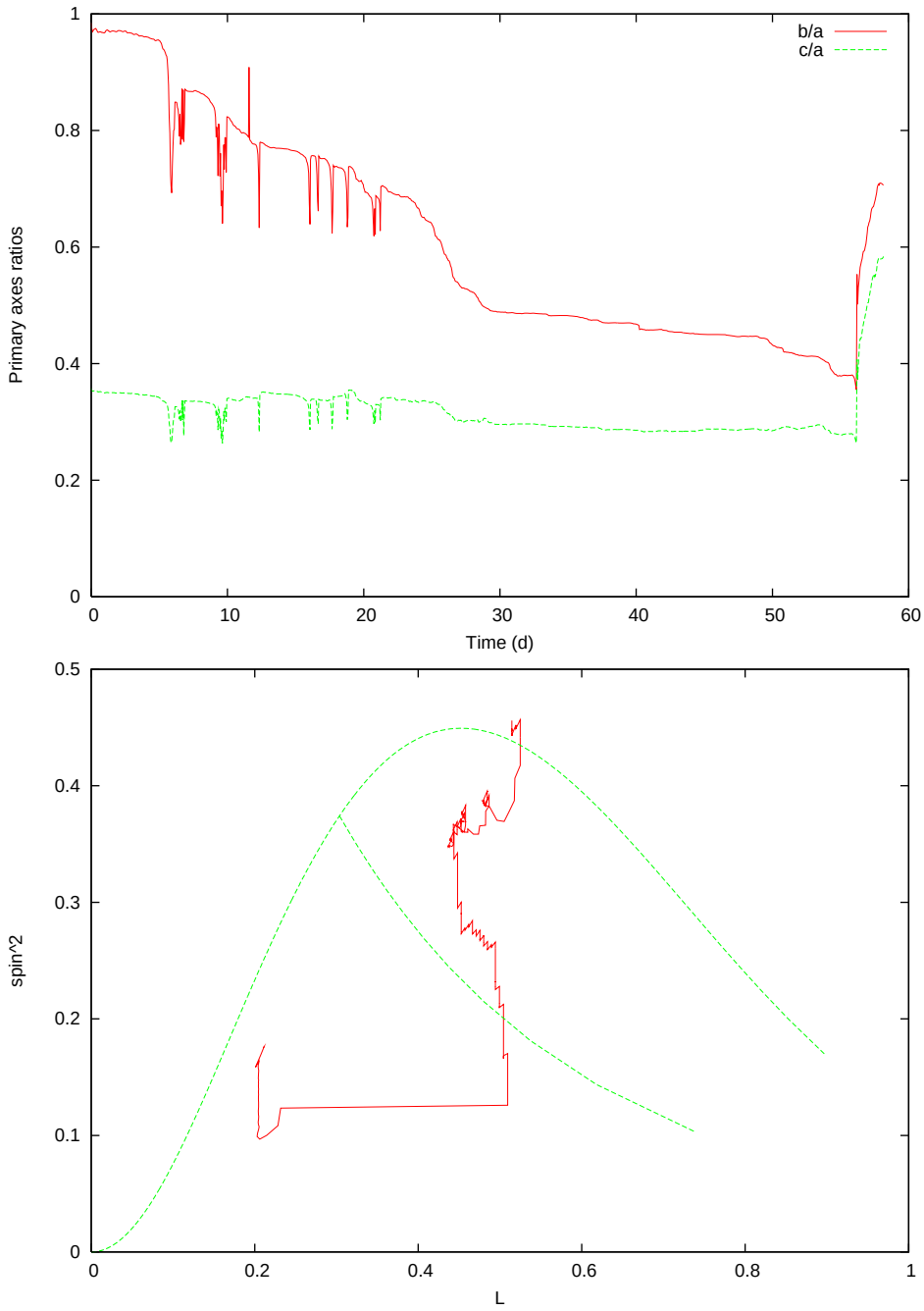

Figure 5.16: Evolution of the **ham1** body, which forms a satellite with $\sim$ 26% of primary mass. (above) Axes ratios; initially starting as a spheroid, at each kick it reshapes into a more elongated, energetically stable configuration with mass losses. (below) Trajectory in the $(\overline{L} - \overline{\Omega}^2)$ plane (red line) compared with the Maclaurin and Jacobi figures (green): the body start on the Maclaurin sequence, in the upper part of the figure. After reaching the vicinity of the Jacobi sequnce, the evolution is similar to those of dbp2, dro1 and dro3.

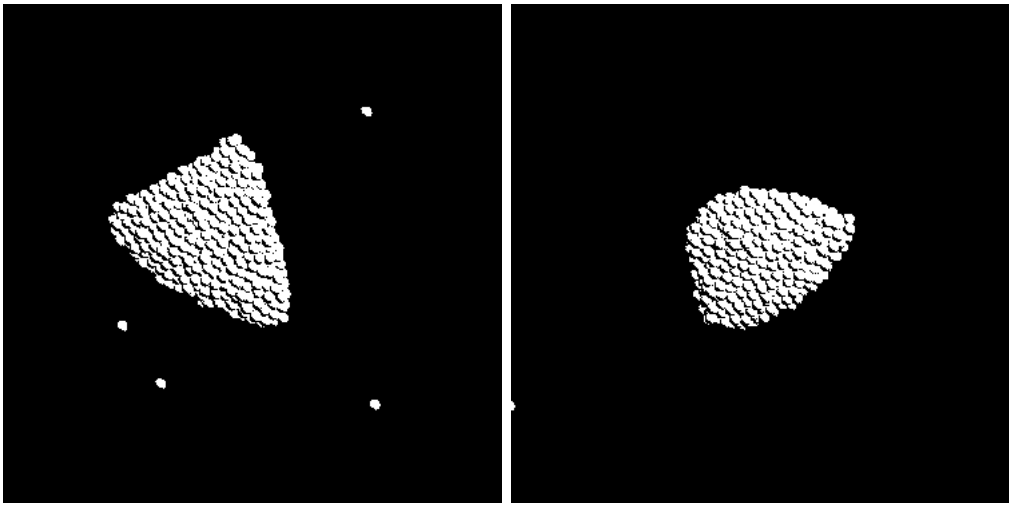

Figure 5.17: (left) initial shape of **tri1**. (right) its shape after 46 kicks. There are many particle loss events, but no stable secondaries form.

5.3.13 tri1

This body presents a L-barrier at $\overline{L} \sim 0.42$ and several mass losses, with the shape slowly turning into a squat drop-like object (see fig. 5.17). No stable secondaries are observed during the simulation.

5.3.14 ell1-ld

This object is initially drawn towards more and more elongated shapes, while some minor mass losses occur. Eventually, a secondary is formed similarly to the previous cases (cf. *dbp2*, *dro1*, *dro3* and *ham1*). The fission event occurs at the relatively low $\overline{L}$ value of ~ 0.46. The secondary produced has a mass of $\sim 16\%$ that of the primary. See fig. 5.18-5.19 for the evolution.

5.3.15 ell2-ld

A similar shape to *ell1-ld*, evolves differently. It has a low L-barrier at $\overline{L} \sim 0.42$, with frequent mass losses. The object is drawn to a more elongated shape in the course of the simulation. No secondaries form. See fig. 5.20.

5.3.16 ell3-ld

An initially ellipsoidal object similar to *ell1-ld* and *ell2-ld*, its shape elongates during the simulation (cf. fig. 5.21), though it appear to settle after a while with subsequent mass losses not changing it further. The L-barrier is apparently as low as $\overline{L} \sim 0.40$.

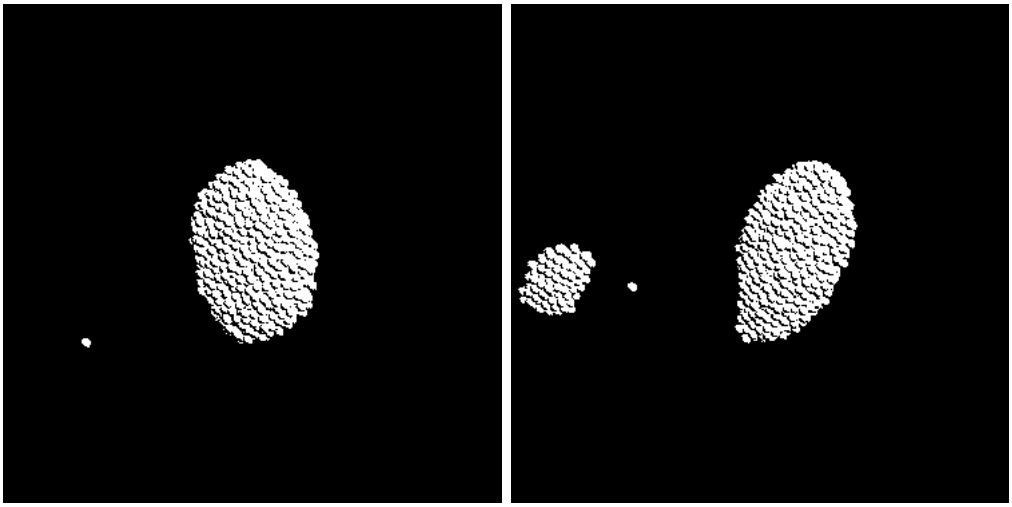

Figure 5.18: (left) initial shape for the **ell1-ld** body. (right) the resulting binary after 49 kicks; mass ratio is $\sim 16\%$.

5.3.17 cbi1-ld

This body is a contact binary. Its fission is thus strongly expected. It follows an evolution without mass loss, up to eventually separating the two components at a $\overline{L} \sim 0.55$. The formed secondary has $\sim$51% of the primary's mass. See fig. 5.22.

5.3.18 irr1

This body presents a L-barrier around $\overline{L} \sim 0.45$ and several mass losses that slowly turn its shape into a more elongated egg-like one (see fig. 5.23). No stable secondaries are observed during the simulation, though the reached shape may suggest that a future fission may occur; time limitations and the dubiousness of such an event made us not investigate further.

5.3.19 irr2

An initially irregularly shaped aggregate, this object slowly develops a quasi pear-like structure, though an early mass loss prevents this process to reach a secondary formation event (see initial and final shapes in fig. 5.24). No stable secondaries are observed during the simulation. Presenting a low L-barrier at $\overline{L} \sim 0.42 \pm 0.1$ for most of the simulation, towards the end starts pushing this threshold to a somewhat larger value of $\overline{L} \sim 0.46$.

5.4 Parameters variation

To analyse the impact of some key parameters, we investigated the effects of variating them. We already have as a basis the results in [C. Comito, 2008] by which no relevant differences are detected in size and density variations, so we do not expect these quantities to be an important factor.

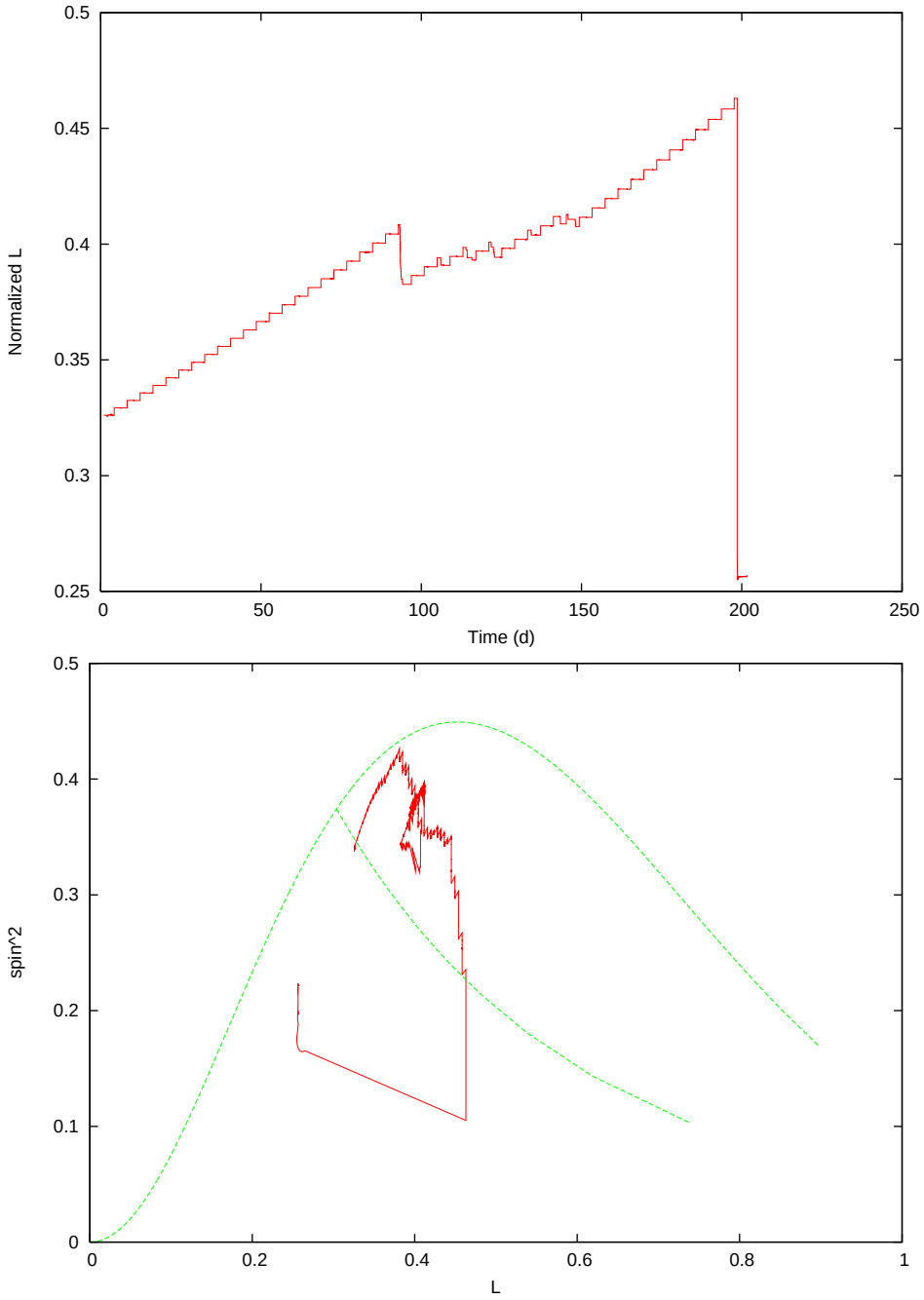

Figure 5.19: Evolution of the **ell1-ld** body, which forms a satellite with $\sim$ 16% of primary mass. (above) Evolution of $\overline{L}$. After the object has reached a limit angular momentum, some minor mass losses occur. Eventually, the mass losses stop and the body reaches $\overline{L} \sim 0.46$ where a fission occurs. (below) Trajectory in the $(\overline{L} - \overline{\Omega}^2)$ plane (red line) compared with the Maclaurin and Jacobi figures (green): the final stages of the evolution are similar to the other cases of binary formation.

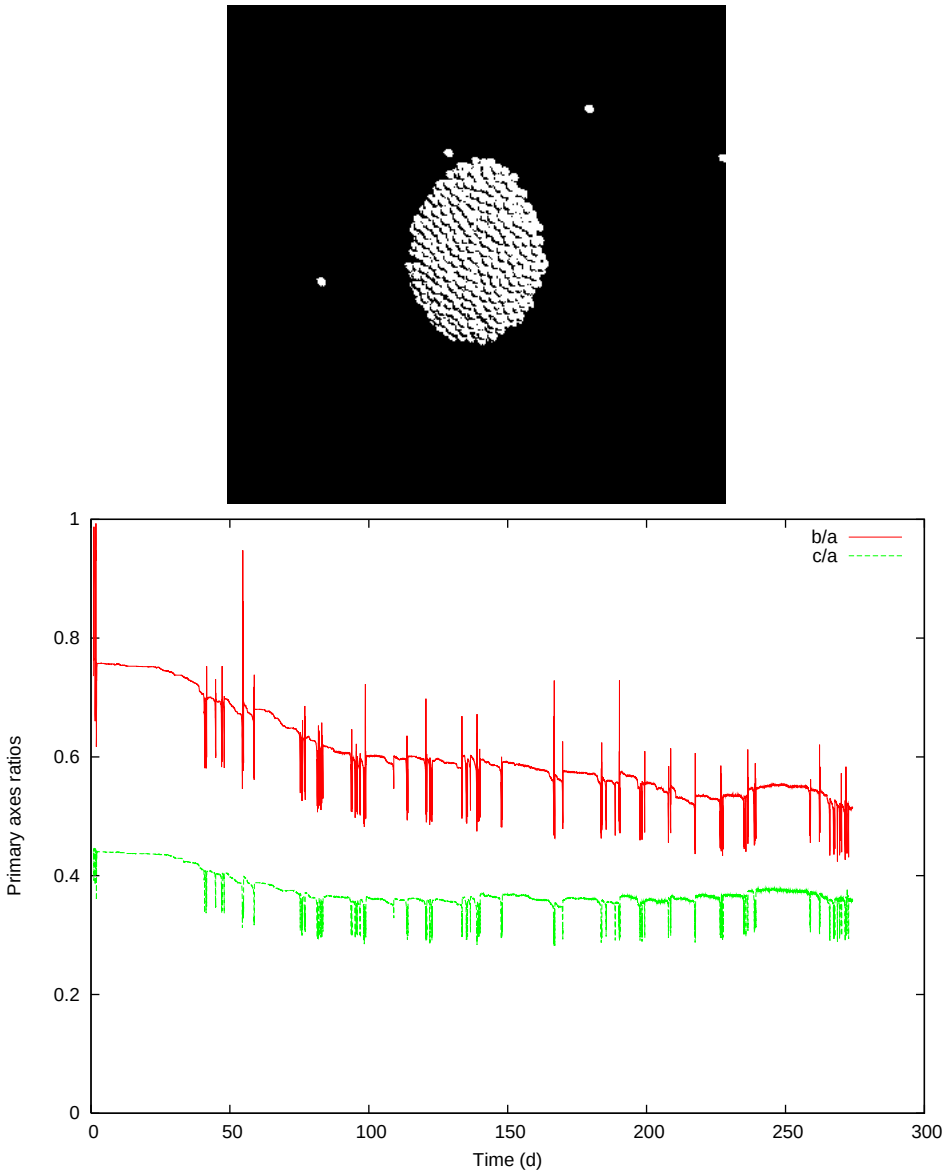

Figure 5.20: (above) initial shape for the **ell2-ld** body. (below) Evolution of the axes ratio. Similar in shape to *ell1-ld* (cf. fig. 5.18 and 5.19), it presents frequent mass losses and no stable secondary after 67 "kicks".

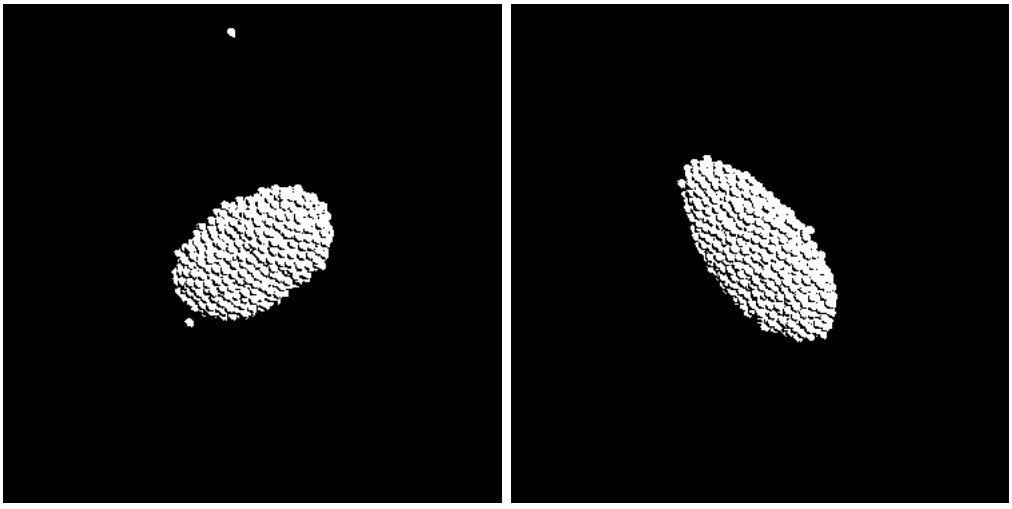

Figure 5.21: (left) initial shape for the **ell3-ld** body. (right) the final shape after 67 kicks.

Body	R_0	$M_1(\%)$	P_1(h)	M_2/M_1	a/R_1	e	$\overline{L}$	notes
dbp2	650 m	86	5.9	0.15	29	0.89	0.53	nominal case
dbp2x10	6.5 km	no stable secondaries; single biggest loss 0.036 of remaining primary						
dbp2x100	65 km	87	6.0	0.16	30	0.92	0.53	

Table 5.1: Effects of the increased size (constant density) on the behaviour of the *dbp2* body. R_0 is the original body length, M_1 is the mass fraction of the original body ended up in the primary. Recorded e and a (in primary radii) are the values at binary formation. The size variation does not show a significant variability of behaviour apart from statistical uncertainty. The *dbp2* nominal case is the same as the one in table 5.4.

We mainly used as proof-case the *dbp2* body ($\rho_p = 3 \cdot 10^3$ kg/m^3), as it appears a good border case for validations: it presents in the nominal case a secondary formation of just the right size ($\sim$ 15% of primary mass) for it to be emitted in an initially bound orbit. It is consequently easy to test whether positive or negative (or neither) effects arise when varying some parameters, by seeing if the secondary forming process is substantially enhanced or suppressed.

5.4.1 dimension

To observe the validity of the secondary formation process, we proceeded to modify the *dbp2* body by increasing particle radius 10 times (volume factor 10^3) and 100 times (volume factor 10^6) at constant density, and with no consequent variation on the `pkdgrav` integration timestep. The results are as in table 5.1.

It is to note that, even if the first case has failed to produce a secondary, the second has. This confirms on one hand the fairly well scalability of the results with linear dimension (and consequently mass), and on the other hand the chaoticity of the process, where small differences can produce sensibly different results (cf. results in chapter 4).

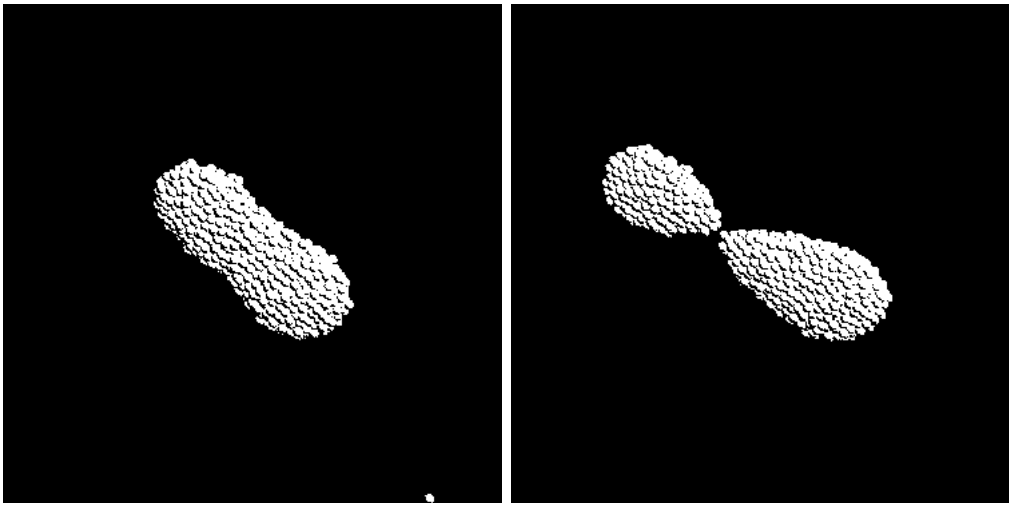

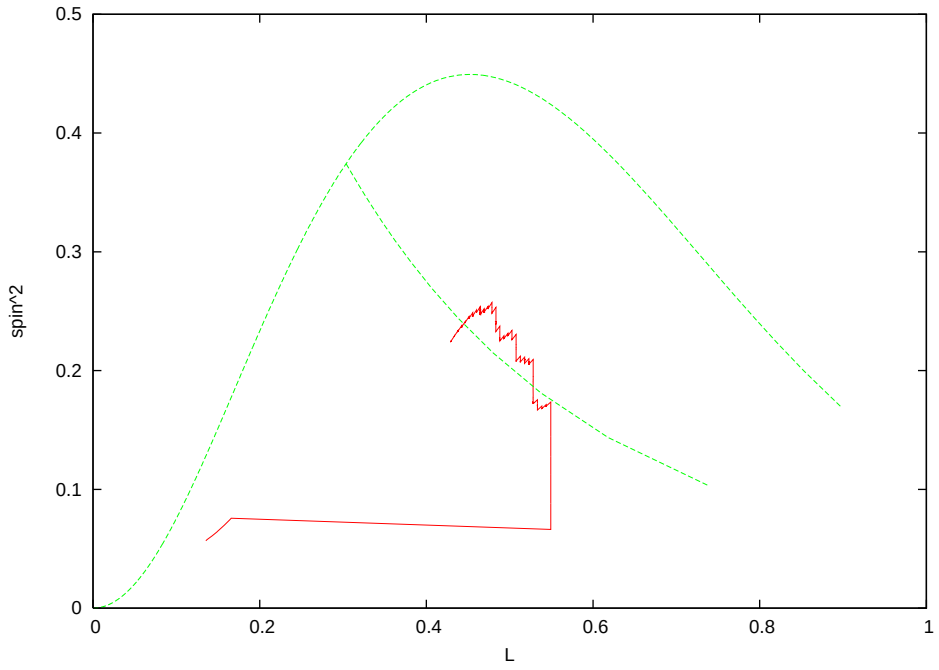

Figure 5.22: Evolution of the **cbi1-ld** contact binary. (above - left) Initial shape. (right) At the moment of fission after 25 kicks. (below) Trajectory in the $(\overline{L} - \overline{\Omega}^2)$ plane (red line) compared with the Maclaurin and Jacobi figures (green).

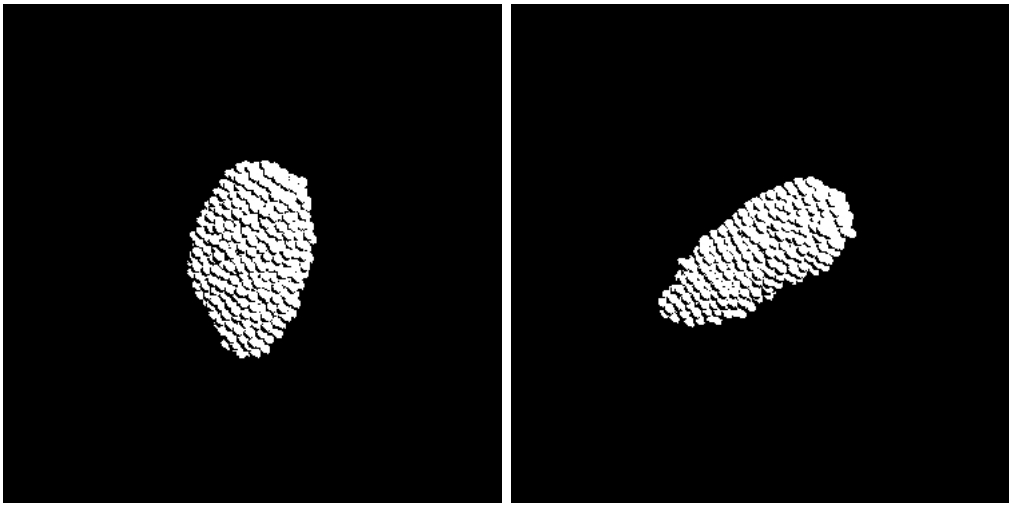

Figure 5.23: (left) initial shape of **irr1**. (right) its shape after 46 kicks. There are several particle loss events, but no stable secondaries form.

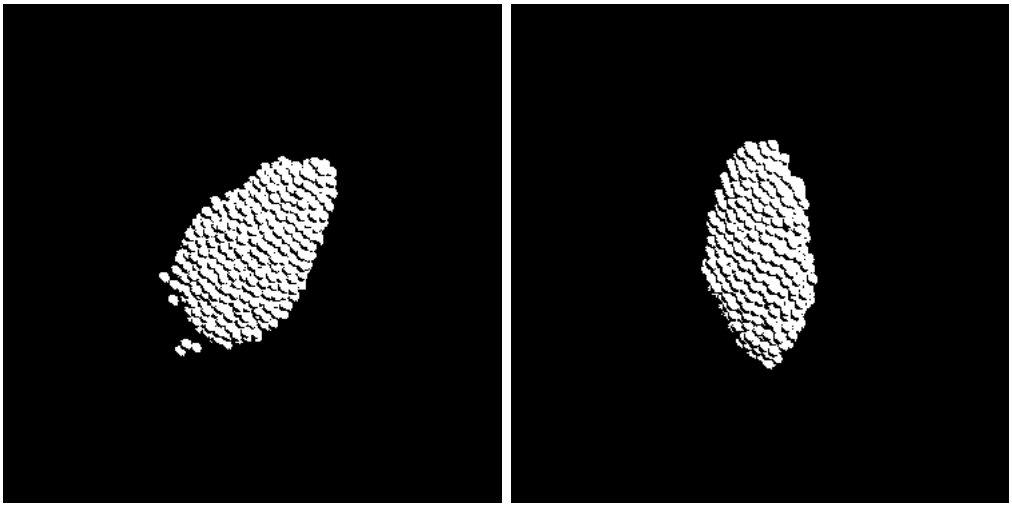

Figure 5.24: (left) initial shape of **irr2**. (right) its shape after 46 kicks. There are several particle loss events, but no stable secondaries form. The final shape being quite different than the initial one, the final fate is uncertain.

Body	ρ_{agg}	$M_1(\%)$	P_1(h)	M_2/M_1	a/R_1	e	$\overline{L}$	notes
$dbp2_{\rho 0.5}$	1.5	no stable secondaries; single biggest loss 0.038 of remaining primary						
$dbp2_{\rho 0.75}$	2.25	85	6.7	0.14	12	0.76	0.51	
dbp2	2.0	86	5.9	0.15	29	0.89	0.53	nominal case
$dbp2_{\rho 1.25}$	3.75	no stable secondaries; single biggest loss 0.073 of remaining primary						
$dbp2_{\rho 1.5}$	4.5	no stable secondaries; single biggest loss 0.034 of remaining primary						
$dbp2_{\rho 1.75}$	5.25	no stable secondaries; single biggest loss 0.013 of remaining primary						
$dbp2_{\rho 2}$	6	88	4.1	0.11	43	0.93	0.49	

Table 5.2: Effects of varying density (constant size) on the behaviour of the *dbp2* body. The recorded ρ_{agg} is recorded as 2/3 of the particle density. M_1 is the mass fraction of the original body ended up in the primary. Recorded e and a (in primary radii) are the values at binary formation. The density variation does not show a significant variability of behaviour apart from statistical uncertainty. The *dbp2* nominal case is the same as the one in table 5.4.

5.4.2 density

We varied the density for the *dbp2* body by exploring the particle density in the range $\rho_p = 1.5 \cdot 10^3$ to $6 \cdot 10^3 kg/m^3$ to test its influence in the results, with no change in size; we modified the `pkdgrav` integration time step according to the $\propto \rho^{-1/2}$ rule for the free fall time (cf. 3.7).

The results are as in table 5.2.

Similarly to the case in § 5.4.1, some cases (3 out of 8) do produce a secondary, and some do not, losing a comparable mass fraction in a more disordered way instead of in a single secondary. Again, as in § 5.4.1, this confirms the scalability of the secondary forming process in all the asteroid density range.

5.4.3 coefficients of restitution

In literature, and in particular in [K.J. Walsh et al., 2008] (cf. 1.3.3), the tangential coefficient of restitution is sometimes set to 1 (i.e., no tangential friction between fragments, and consequently no transfer between the particles internal angular momentum and the linear/angular momentum of the colliding one); in our simulations we preferred to work with a value smaller than 1, notwithstanding the increase in computational time, to provide a more physical result where such friction is present.

Nonetheless, we analysed the impact of setting this coefficient to 1. We used the *dbp2* and *dro1* bodies, both of which produce a secondary in the nominal case.

The results are given in table 5.3: the process of secondary formation appears delayed, but more stable. In both cases the lack of tangential stress produces a more even mass splitting event, with larger secondary/primary mass ratios (and more stable orbits), lower eccentricity and closer orbit.

Apparently, the lack of tangential friction may allow for a more fluid behaviour and a smoother transition into the binary state; a larger total mass loss has also been observed before the fissioning event, which is normal given the higher total angular momentum injected into the systems.

Body	# kicks	$M_1(\%)$	P_1(h)	M_2/M_1	a/R_1	e	$\overline{L}$	notes
dbp2	23	86	5.9	0.15	29	0.89	0.53	nominal case
$\text{dbp2}_{\epsilon_T=1}$	65	69	8.0	0.30	5.1	0.39	0.48	
dro1	31	75	6.3	0.30	10	0.64	0.55	nominal case
$\text{dro1}_{\epsilon_T=1}$	47	68	8.3	0.39	5.2	0.48	0.55	

Table 5.3: Effects of imposing an ϵ_T value of 1 on the behaviour of the *dbp2* and *dro1* bodies. The number of kicks necessary for the bodies to fission is recorded. M_1 is the mass fraction of the original body ended up in the primary. Recorded e and a (in primary radii) are the values at binary formation. The lack of tangential friction apparently causes delayed fissioning, larger secondaries and tighter orbits. The *dbp2* and *dro1* nominal cases are the same as the ones in table 5.4.

5.5 Long-term stability of binaries

A question arises on the stability of the formed asteroidal binaries. This is the same problem encountered in § 4.6. As we have ascertained, `pkdgrav` may have some structural problems in dealing with long-running compact bodies simulations. Nonetheless, we tried to follow the evolution of the formed binaries for $\approx$ 1.5M timesteps ($\sim$ 140 days for the $\rho_p = 3000\,kg/m^3$ systems).

Two aspects are to consider when examining the stability of the systems. The first is the total energy (gravitational+kinetic) stored within the system. In the case of it being positive, there is a high risk for the system to break up, unless the low eccentricity allow for the extra energy (stored in the two bodies internal rotation) to be with time dissipated by tidal forces; or alternatively the secondary may remain locked in a stable resonant orbit, as suggested in [S.A. Jacobson, D.J. Scheeres, 2011].

It remain to be seen if however `pkdgrav` allows for an efficient tidal dissipation, as for aggregates near the equilibrium, small scale dissipations by friction may be highly suppressed (cf. § 3.5.1).

Second, even in the negative energy range, where the system looks definitely bound, the case may arise for the apocentre to be located outside the primary's Hill sphere (cf. § 4.4), or dangerously near this limit for a prolonged time. For some instability-creating mechanisms like YORP or tidal encounters with the inner planets, the effect acts most prominently in the vicinity of the Sun (among the NEAs population), and a value of the apocentre distance of $\sim 75 \div 100$ primary radii should be regarded as dangerous for the long-time survivability of the couple.

Of the six found binaries, the *dbp2* system is the only found to escape the primary. It only manages to complete 5 full orbits with unstable values of e and a; after the last close passage, the eccentricity is increased to $\sim$1.1, and the couple is separated.

The *dro3* binary reaches mutual distances comparable with the Hill Radius at 1 AU from the Sun by the time of the last recorded orbit (see fig. 5.25).

In the other four cases, no problem is detected in the time considered.

Based on our results (see § 5.3 and table 5.4), we seem to be able to align similarly

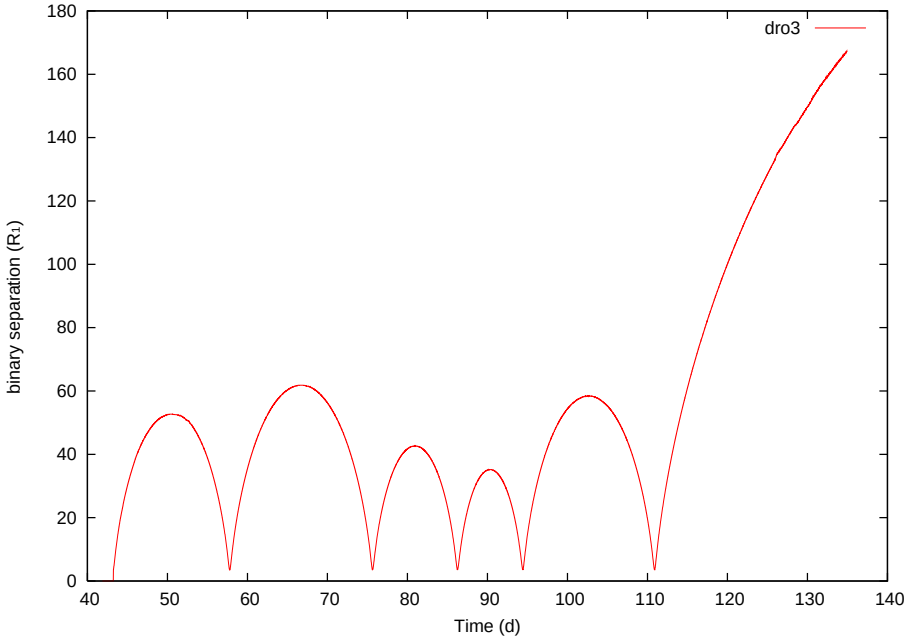

Figure 5.25: Evolution of the separation of the couple for the **dro3** system. By the last recorded (incomplete) orbit, the mutual distance reaches values comparable with the Hill radius for a body orbiting at 1 AU from the Sun with zero eccentricity ($\sim$ 200); for an eccentric NEA heliocentric orbit, this means the binary is easily separated.

to [S.A. Jacobson, D.J. Scheeres, 2011] regarding a lower limit for the mass of the secondary for it to be retained in a stable orbit, based mainly on simple dynamical reasons about energy conservation. They set an analytical limit at $\sim$ 20% of primary mass, with variations up to $\sim$ 28% depending on the shapes considered ([D.J. Scheeres, 2009 II], [P. Pravec et al., 2010]).

We can be roughly agree to a 30% limit ($dbp2_{\epsilon_T=1}$ has $\sim$0 free energy), for a net 0 free energy for the systems. The higher energy at separation with respect to [S.A. Jacobson, D.J. Scheeres, 2011] can be thought of as an additional energy necessary to win the body strength in the perfect rubble pile model with respect to a 2-ellipsoid model.

It is to note how [P. Pravec et al., 2010] do find asteroid pairs with mass ratios comprised in the whole $(0 \div 0.3)$ interval, which would indicate previous unstable binaries that separated with time because of positive free energy and spin-orbit coupling.

5.6 Results and discussion

In table 5.4, our results for the different cases have been summarised.

The recorded M_1 values are given as a reference, and a bias may be present: as we arbitrarily stopped our simulations after a number of kicks if no secondaries form, it may be the case that in some instances, by continuing the spin-up, a binary may be created. As further mass loss is possible in the process, the total mass (and thus M_1)

Body	ρ_{agg}	M_1(%)	P_1(h)	M_2/M_1	a/R_1	e	$\overline{L}$	notes
dbp1	2.0							
dbp2	2.0	86	5.9	0.15	29	0.89	0.53	lost after a few orbits
dro1	2.0	75	6.3	0.30	10	0.64	0.55	e reaches as high as 0.86 during the stability tests
dro2	2.0							
dro3	2.0	80	6.0	0.25	30	0.87	0.61	reaches limit of Hill sphere for NEAs distances after a few orbits
dro4	2.0							
dro5	2.0							
dro6	2.0		a number of clumps (biggest $\sim 5\%$ mass) detach over time and get lost					
dro7-ld	0.65							
lod8-ld	0.65							
ham1	2.0	73	6.3	0.26	7.0	0.52	0.50	
tri1	2.0							
ell1-ld	0.6	83	9.9	0.19	8.0	0.63	0.46	
ell2-ld	0.65							
ell3-ld	0.65							
cbi1-ld	0.65	66	20	0.51	5.3	0.30	0.55	initially a contact binary
irr1	2.0							
irr2	2.0							

Table 5.4: The results of our nominal cases for spin-up-induced binary formation. The body codenames represent the initial configuration (see § 5.1: dbp=double-pointed; dro=drop-shaped; ham=hamburger-shaped (high-$\overline{L}$ Maclaurin); tri=near-triangular shape; irr=irregular; lod=low-density particles); ρ_{agg} are a reference value for the bulk densities in g/cm^3 (which are considered as being $\sim 33\%$ lower than particle densities ρ_P, cf. § 3.9.2). M_1 is the mass of the primary as a fraction of the initial body's mass at the start of the simulation; eccentricity and semimajor axis (in primary radii) values are those at formation.

contained in these binaries may be lower than for the fissions observed here.

As for the results of chapter 4, the results are to be interpreted statistically, to verify the possibility of a fissioning mechanism following a slowly acting external agent and to examine the possible results in term of formed systems.

It is however clear that the slow action of an external perturbing agent can definitely lead to binary formation.

5.6.1 differences with the high angular momentum simulations

A difference must be noted with the results from chapter 4 (cf. table 4.2): the primaries obtained here rotate considerably slower (densities and binary $\overline{L}$ being equal). This is due to the fact that the primaries obtained with small incremental instabilities inherit the rotation rates of their elongate slowly-spinning parent. For the cases of chapter 4, instead, the primaries are usually a (at least partly) re-accumulation of mass of a more or less violent event, with the mass not allowed to fall unto the primary (for an excess of L) forming the secondary or being lost.

As the resulting binaries here have a similar $\overline{L}$ content than those obtained in the simulations of chapter 4.2 starting with $\overline{L} = 0.6$, the two mechanisms may both be responsible for synchronous binaries, where the information on the initial primary rotation rate has been lost.

5.6.2 the fissioning sequence

As a general trend (see fig. 5.6, 5.7, 5.9, 5.16, 5.19 and 5.22), the fissioning mechanism leading to large secondary formation tends to always follow a similar scheme. Namely, the aggregate tends to initially assume more elongated shapes, with possibly some minor mass losses, following the Jacobi sequence towards shapes characteristic of higher and higher $\overline{L}$. At a critical point the evolution takes then a detour towards a peanut-like shape before eventually accelerating the shape change and fissioning.

Following the hydrostatic classical results, which predict a MacLaurin shape not being stable for high $\overline{L}$ (and again verified in chapter 4), even where the body starts with a spheroidal (axisymmetric) shape this is as soon as possible catastrophically diverted towards the more stable elongated (triaxial, egg- or drop-shaped) ones, with violent reshaping and massive particle emission along the equator; for the *ham1* body, this reshapes is again diverted towards the same region of the $(\overline{L} - \overline{\Omega}^2)$ plane where the fissioning events occur.

Very interestingly, the position of this critical point in the $(\overline{L} - \overline{\Omega}^2)$ plane where the fissioning event occurs is quite constant across the different simulations (even if determining the exact location of a fissioning point is intrinsically difficult). In fact, it corresponds to the neighbourhood of the theoretic onset of the instabilities of the Jacobi sequence giving rise to the so-called "Dumbbell" sequence (see fig. 2.4 and 2.5), leading to symmetric body fission.

Although this sequence has been described with mathematical models it has, to our knowledge, never been observed "in action" in a simulation for a practical case of effective binary formation.

It must be noted, however, that the course of the sequence is only approximately followed. The complete run through the Dumbbell sequence leading from a triaxial Jacobi ellipsoid through a cigar-shaped object, a bilobate contact binary body, to symmetrical fission is complex and governed by very unstable equilibria, which are not entirely suitable for actual physical systems, especially finite-size grains, either actual or simulated.

Moreover, the course of the sequence is not monotone in angular momentum, while in our simulations the angular momentum is slowly rising during the evolution, and constant (whithin machine precision) during the last fissioning stage, with no mechanism for dispersion (mass loss does not occur during the last stages). Finally, the sequence is calculated for a perfectly symmetrical mass splitting, while in our cases a broad range of secondary/primary mass ratios is observed (in the most extreme case, of a ∼1-to-6 ratio).

The theoretical position of the sequence is nonetheless in good agreement with the onset of the final splitting process, confirming both our results and the applicability of classical fluidostatic results to gravitational aggregates, moreso if tangential friction between spheres is set to zero.

Moreover, it is in good agreement with the observations of synchronous and contact binaries (cf. fig. 1.13).

5.6.3 binaries or not? the hidden parameters

That there seems to be a more or less sharp separation between the single particles' emissions and the large clusters', with little observable middle ground.

The two creation mechanisms are indeed different: in the first case we have, following a spin-up, a local instability that is immediately resolved with the emission of some mass, mostly in the form of single particles, and of the excess angular momentum, restoring the initial equilibrium; in the second case, the reshaping occurs in a longer time frame, with the body altering its shape and developing a protuberance without losing mass and eventually releasing the mass all at once in a fissioning event of some tens of particles at least.

Global initial shape does not seem to be the main discriminant between presence or lack of binary creation; e.g. both initially elongated bodies, near to the "contact binary" region of the $(\overline{L} - \overline{\Omega}^2)$ plane (like *dro3*), and a spheroid (*ham1*) are capable of fissioning, while very similar bodies (*dro2*) are not.

A question thus arises as to why do some bodies develop into a binary systems and others, similar in shape, density and size, do not.

The problem has probably an answer in the internal configurations of the bodies, as different particles packing may distribute the internal forces in different ways. This is probably reflected at the macroscopic level in the generally higher values of the "angular momentum barrier" observed for the simulations forming a binary, whose particular packing may allow some of the spin-up kick energy to be transfered into the body shape (the growth of a narrowing in the body), allowing the rubble-pile to store it and eventually, after many "kicks", produce a secondary.

Even if strains and stresses computations are completely alien to `pkdgrav`, the different particle adjustments may nonetheless well reproduce some key aspects of granular systems (cf. 2.4), where apparently similar macroscopic configurations can in fact hide very different forces and structures at the microscopic level, which strongly dictate the dynamics of the systems (and where however other factors also kick in: contact forces, plasticity, or other). For real asteroids, this is ultimately a chaotic aspect (or at least a very poorly known or knowable one) that has connections with the formation history of the single rubble-piles themselves.

5.6.4 a comparison with previous independent studies

It can be observed (similarly to what has been found in [S.A. Jacobson, D.J. Scheeres, 2011]) both by the binaries we form and by all of the expelled clusters in the different runs that the larger the secondary, the greater the probability for it to be emitted in an elliptical stable orbit.

The difference with the results found in [K.J. Walsh et al., 2008] (cf. § 1.3.3) is evident. This is due to them using a crystalline packing. As they observe, they are unable to recreate the satellite forming mechanism with the unordered packing.

The mechanism by which they produce the satellite is highly suppressed using more fluid aggregates. In fact, the continually emission of particles into close circular orbits from the equator of a fast spinning spheroid is not possible as the fast spinning spheroid configuration is not a stable one unless the angle of repose for those asteroids be considerably higher than for the unordered spheres packing. Any mildly fluid spheroid allowed to continually accumulate angular momentum will quite soon turn into more elongated and more energetically favourable shapes, stopping the mechanism they observe.

Any reshaping is on the contrary prevented by the crystalline structure. This is what hides behind the "reshaping" of the elongated objects towards a spheroid apparently contrary to the classical hydrostatic results (i.e. it is no reshaping at all, but rather a slow particle removing process one at a time like from the top of a stack). If direct reshaping is prevented by the geometric packing, the only shape changing event is the possible loss, one at a time, of the surface particles at the equator due to the centrifugal force, to be replaced by other surface particles sliding "down" from higher latitudes.

Aggregates formed by well interlocked rocks may be described by this model, and their "hybrid" bodies (a geometrically packed crystal core surrounded by an unordered distribution of smaller particles) can also be a good middle ground, though the apparent contradiction between the mixing of the short gravitational timescale and the long YORP timescale (see § 1.3.3) remains to be addressed.

Conclusions

This work explores by numerical methods the behaviour of gravitational aggregates to improve our understanding on the possible origin of binary asteroids, and possibly to connect the initial conditions of the simulations to different classes of observed binaries.

Based on previous results both by us and in the literature, we have modeled an asteroid with an unordered "amorphous" packing of spheres, for avoiding the intrinsic geometric interlocking, especially when finer deformations where sought for, as in chapter 5.

The scenario we use in chapter 4 is representative of a system having accumulated a high amount of angular momentum, beyond the threshold for mass shedding for a cohesionless aggregate. This accumulation can be due to the presence of a small cohesion, or to a sudden event such as a major impact. We simulate the subsequent fragmentation of these bodies exploring a wide range of parameters.

We have shown that binary formation is common for a moderate angular momentum content ranging between the lowest limit typical of fluid equilibrium and the highest values possible for a rigid body preserving surface regolith.

Large secondaries / double asteroids are produced, formed by splitting and / or re-accumulation of the shattered body. Small satellites can accumulate in orbit, a scenario favoured by an initially axisymmetric shape of the body.

Our results have been compared with the available data on asteroidal bodies to show the resemblance in momentum, primary rotation rate and typical orbital distances. We find that an agreement with observed classes of binaries can be found.

In chapter 5 we explored the equilibrium sequence connecting single bodies to binary asteroids. The technique used is representative of the action of a slow perturbing force that may gradually draw a body to an unstable configuration.

We were able to show how a gradual shape deformation can drive an arbitrary shape to a bilobate aspect, then possibly fissioning and forming a multiple object. The observed bilobate shape is reminiscent of both the semi-analytical results for fluid bodies and the observed "contact binaries" among the asteroid population.

We investigated the long-term evolutions of the obtained binaries.

Both our approaches are original and have shed some light on poorly studied processes. In fact, theoretical studies of the dynamical evolution of binaries starting from

shapes in contact exist, but none of them can capture the richness of the phenomenology of fission, whose complex details and highly chaotic behaviour can strongly affect the formation (or not) of a (stable or unstable) binary object. Other numerical approaches also failed in capturing the complexity of the spin-up process, focusing on single aspects that we found to be not representative of the variety of possible situations.

In particular, for the first time we illustrate by numerical simulations the transition to instability for Jacobi ellipsoids, showing that in-orbit accumulation of small fragments is not the only mechanism forming satellites by spin-up.

Also, the path toward splitting appears to follow a typical development leading through a limited set of shapes, whatever the shape in the initial conditions.

During this study we have also identified several limitation of the numerical approach using hard spheres. Other approaches employing soft spheres are being investigated by other authors, but most probably dramatic advances will be obtained by future extensions towards irregular fragment shapes, certainly due in view of more realistic simulations and closer comparisons to the mechanisms identified in the domain of the physics of granular systems.

Approccio numerico a N corpi alla formazione ed evoluzione degli asteroidi binari

Malgrado ampi studi osservativi e teorici da Terra e dallo spazio, la natura profonda dei corpi minori del Sistema Solare rimane essenzialmente sconosciuta.

In particolare gli asteroidi, nello scenario comunemente accettato, hanno conosciuto un'intensa vita collisionale come risultato dei processi dinamici che hanno modellato il nostro sistema planetario. È comunemente accettato che processi catastrofici, come la frammentazione e la riaccumulazione gravitazionale, ne hanno profondamente modificato la struttura creando corpi altamente frammentati.

Almeno una frazione di questi avrebbero una coesione interna molto debole, che fa di essi oggetti tenuti assieme essenzialmente dalla gravità. Le proprietà interne di tali "aggregati gravitazionali" rimangono in ogni caso poco conosciute, in quanto la maggioranza dei vincoli derivati dalle osservazioni degli asteroidi riguarda le proprietà superficiali.

Gli asteroidi binari sono un caso particolare di rilevante importanza per la comprensione della fisica e dell'evoluzione di tali oggetti, in quanto le osservazioni ci forniscono in maniera agevole dati importanti riguardanti la loro struttura interna.

Come prima cosa, esse possono fornirci stime accurate della massa totale a partire dalle caratteristiche dell'orbita reciproca; siccome le curve di luce forniscono una misura diretta della taglia delle componenti e delle loro orbite anche per gli oggetti non risolti spazialmente, si può dunque ottenere una preziosa informazione sulla loro densità.

Anche gli stati rotazionali e le forme possono essere determinati più facilmente, permettendo di avere migliori stime sulle tensioni interne e più accurati modelli geomorfologici in condizioni di microgravità.

L'esistenza stessa dei binari e la loro varietà sono direttamente legate ai principali processi che hanno foggiato la fascia degli asteroidi, e qualsiasi determinazione delle loro proprietà fisiche è dunque fondamentale sia per ottenere un quadro complessivo della loro formazione e della loro evoluzione.

A.0.1 presentazione del lavoro

Molti possibili meccanismi sono stati proposti per l'origine degli asteroidi binari: dagli effetti mareali agli impatti craterizzanti energetici capaci di espellere materiale in orbita, dalla riac-

cumulazione in forma di binario di frammenti in seguito ad una collisione catastrofica alla fissione a causa di un aumento del momento angolare; tutti sono attualmente sotto esamina per mezzo dei dati osservativi e di modelli teorici.

Lo scopo del presente lavoro è di esplorare il comportamento degli aggregati gravitazionali in rotazione in prossimità del limite superiore del momento angolare prima di perdere massa: ulteriori accelerazioni oltre tale soglia offrono una visione del processo di fissione e di formazione di satelliti.

Gli asteroidi sono modellati numericamente per mezzo di un codice a N corpi specializzato come "cumuli di macerie perfetti": aggregati di sfere identiche soggette alla gravità reciproca e ad urti anelastici. In cerca di instabilità che possano condurre alla formazione di binari, la loro velocità di rotazione viene aumentata sino alla soglia a cui grosse instabilità si attivano, e vengono esplorate la deformazione risultante e la formazione di satelliti.

Si cerca inoltre di esplorare la questione della stabilità a lungo termine dei sistemi ottenuti, e vengono trattate le limitazioni attuali del nostro approccio.

I risultati sono infine esaminati in un constesto più vasto, comparandoli con altri studi teorici e numerici e con le osservazioni.

A.1 Gli asteroidi binari

Negli ultimi 20 anni sono stati scoperti un numero crescente di asteroidi binari, con caratteristiche molto diverse per dimensione del primario, rapporto di massa, separazione della coppia, momento angolare del sistema, e le scoperte future potranno presentare un immagine più precisa.

Una prima classificazione può comunque essere tentata (v. § 1.3.1), come per esempio in [P. Pravec, A.W. Harris, 2007] (cfr. fig. 1.12).

Si possono distinguere un gruppo di piccoli oggetti (dimensioni $< 10\,\mathrm{km}$) in forte rotazione (con periodi generalmente < 4 ore) e con secondari consistenti (rapporto di massa $1 \div 10\%$), distribuiti tra i NEO e la fascia principale[6]; un gruppo di piccoli binari sincroni di dimensione comparabile con i precedenti ma che hanno raggiunto la sincronia grazie all'elevato rapporto di massa (tipicamente $> 0{,}5$), che possono o meno essere una coda del gruppo dei piccoli binari[7]; un gruppo di grossi asteroidi localizzati all'interno della cintura principale con piccoli satelliti (rapporto di massa $<\sim 1\%$ ma principalmente $< 0{,}1\%$). Sono stati osservati anche sistemi "irregolari" che sfuggono alla classificazione, così come esempi di "binari a contatto" che, pur non essendo veri binari, testimoniano la loro storia di precedenti coppie i cui componenti si sono delicatamente posati l'uno sull'altro.

[6] è naturalmente presente un effetto di selezione che favorisce l'osservazione di sistemi più vicini

[7] per il momento, la grande maggioranza di essi è stata scoperta all'interno della cintura principale: un ruolo a questo riguardo può averlo il breve tempo a disposizione dei NEO prima di essere espulsi dal Sistema solare, comparabile con i tempi necessari per raggiungere la sincronia

A.2 La modellizzazione degli asteroidi

È generalmente accettato che la maggioranza degli asteroidi maggiori di ∼100 m sono fortemente fratturati o dei veri e propri "aggregati gravitazionali" di rocce tenuti assieme per autogravità (v. § 1.1.2).

Il primo modello perdescrivere la loro forma resta quello dato dall'idrostatica classica, che predice sequenze di forme stabili per oggetti autogravitanti in rotazione (v. § 2.1).

Conviene introdurre una normalizzazione per il momento angolare L, per eliminare ogni dipendenza dalla massa M e dalle dimensioni, definendo $\overline{L}=L/\sqrt{GM^3\overline{a}}$, con $\overline{a}$ raggio medio del corpo.

Le figure più semplici sono ellissoidi (siano a_1, a_2 e a_3 i tre semiassi, con a_3 asse di rotazione): si distinguono la sequenza di sferoidi[8] di Maclaurin, stabili a bassa rotazione ($\overline{L}$ <∼0,3), e la sequenza di ellissoidi triassiali di Jacobi, stabili per velocità di rotazioni più elevate ($\overline{L}$ tra ∼0,3 e ∼0,45). Esiste peraltro un numero infinito di sequenze matematicamente possibili, alcune di esse rappresentate in fig. 2.4.

La distribuzione delle forme degli oggetti reali è tuttavia apparentemente lontana da tali sequenze (cfr. fig. 2.6), il che comporta che altre modellizzazioni più elaborate devono essere utilizzate, considerando le forze interne capaci di sostenere forme non strettamente idrostatiche (cfr. § 2.3 - 2.4).

A.3 La modellizzazione numerica con i *perfect rubble-piles*

Questa tesi si occupa della modellizzazione numerica della formazione di asteroidi binari. A tal scopo, abbiamo utilizzato il programma `pkdgrav` ([D.C. Richardson et al., 2000]), un integratore gravitazionale a N corpi con gestione degli urti anelastici (v. cap. 3).

`pkdgrav` utilizza come unità di massa particelle sferiche rigide (v. § 3.1) sotto l'azione della loro gravità; questo permette di modellizzare un aggregato gravitazionale come un insieme di particelle libere di muoversi le une rispetto alle altre con una (limitata) libertà secondo la dinamica imposta dalle forze globali (v. fig. 3.3): tale configurazione viene chiamata un "perfect rubble-pile".

Studi precedenti (v. § 3.10) ci avevano permesso di dedurre alcune proprietà di tale modello, come l'osservare che per un aggregato è difficile contenere un $\overline{L} > 0.4$.

La maggioranza degli aggregati utilizzati per le simulazioni di questa tesi è stata formata con una densità di $\rho \sim 2\,g/cm^3$ e con sfere di raggio $R_p = 50\,m$.

A.4 Simulazioni a momento angolare elevato

Per testare la possibilità di formazione di asteroidi binari in uno scenario catastrofico, si procede simulando una situazione accidentale in cui un aggregato altrimenti stabile rimane

[8] ellissoidi di rotazione con $a_1 = a_2 > a_3$

vittima di un evento (come un impatto) che lo conduce improvvisamente verso una situazione di instabilità (v. cap. 4).

A tal fine abbiamo preso una serie di corpi ellissoidali con differenti rapporti assiali (v. fig. 3.8) in orbita (circolare) attorno al Sole, e abbiamo fornito loro un alto momento angolare sotto forma di campo di rotazione di corpo rigido su sé stessi. Abbiamo quindi seguito tali aggregati durante la loro evoluzione guidata dall'autogravitazione e dagli urti reciproci, alla ricerca in particolare dei casi in cui si formino sistemi binari (o multipli).

Abbiamo utilizzato differenti $\overline{L}$ da 0,5 a 1,0 per osservare il comportamento degli aggregati in condizioni differenti e comparare i sistemi risultanti. Si possono osservare quattro comportamenti tipo, a seconda della configurazione iniziale e del momento angolare posseduto. Degli schemi sono presentati nelle figg. 4.3, 4.4, 4.5, 4.10.

forme allungate con al più una piccola perdita di massa

Queste forme sono possibili quando $\overline{L}$ non superi $\sim$0,7.

primari circondati da una nube di piccoli frammenti

Questi sistemi sono la norma per le configurazioni inizialmente a simmetria assiale ($a_1 = a_2$), che rapidamente si portano verso vorme allungate perdendo massa isotropicamente. Quest'ultima rimane principalmente in orbita attorno al corpo principale nella forma di numerose particelle che formano una nube.

Nel corso di alcuni giorni si possono formare piccoli satelli (di massa qualche percento del primario) per accumulazione in orbita dei frammenti, mentre una parte della nube viene dispersa dagli effetti perturbativi reciproci delle particelle. Questo processo è tuttavia lento, e le nubi possono non riuscire a disperdersi nel tempo per cui ci è stato possibile seguire le simulazioni.

Alcuni esempi sono presentati nelle figg. 4.6 e 4.12.

binari con componenti di massa simile

Una gran parte dei sistemi con $\overline{L}$ compreso tra 0,6 e 0,8 evolve rapidamente verso la formazione di binari con componenti di massa comparabile (v. figg. 4.8 e 4.14).

Si tratta di un comportamento in cui l'aggregato viene sopraffatto dalla forza centrifuga e condotto verso forme fortemente allungate fino a separarsi in duo (o più) parti che restano, almeno all'inizio, in orbita reciproca.

Data l'origine di tali sistemi binari, l'orbita iniziale presenta una distanza al pericentro molto corta, dell'ordine di uno $\div$ tre diamtri del primario, ed ha la tendenza a evolvere molto rapidamente in maniera imprevedibile.

Per i sistemi ad alto momento angolare, la formazione di più corpi di masse comparabili può creare situazioni caotiche con interazioni multiple.

sistemi dispersi

Oltre $\overline{L}$ ~0,8 il comportamento dei sistemi è dominato dalla dispersione della maggioranza della massa iniziale, che si riaccumula in più corpi in orbita indipendente attorno al Sole, con possibilmente alcuni sistemi binari (v. fig. 4.9).

A.4.1 evoluzione a lungo termine dei sistemi

Tra gli scopi iniziali del lavoro di tesi ci eravamo proposti di studiare l'evoluzione nel tempo dei sistemi ottenuti. Tuttavia, un'evoluzione per più di qualche mese (in tempo simulato) è per il momento falsata da problemi numerici del codice (v. § 4.6).

A.4.2 conclusioni

Abbiamo mostrato come la formazione di distemi binari è una conseguenza normale per i casi di distruzione catastrofica dei corpi, con la possibile formazione di sistemi diversi tra loro.

È possibile comparare i sistemi ottenuti con le popolazioni di binari conosciute, osservando come per tutti i principali parametri essi possano ben rappresentare i binari reali (v. § 4.8 e fig. 4.28).

A.5 Simulazioni ad accelerazione progressiva

Una domanda si pone riguardo la possibilità di far evolvere un aggregato verso la formazione di un binario in maniera progressiva e senza salti.

Questo tipo di evoluzione può applicarsi a diverse situazioni, come incontri ripetuti di un NEA con i pianeti interni, piccoli impatti o per effetto YORP (v. § 1.3.3).

Per testare questa possibilità, abbiamo preso un insieme di aggregati stabili in forte rotazione ottenuti da simulazioni precedenti e li abbiamo sottoposti a cicli di piccole accelerazioni attorno al proprio asse seguite ciascuna da un periodo di evoluzione libera perché si assestassero alle nuove condizioni. Questo conduce gli aggregati in un'evoluzione di forme in modalità quasi-statica, simulando un'azione perturbativa esterna agente su tempi caratteristici più lunghi del tempo caratteristico autogravitazionale.

A mano a mano che gli aggregati accumulano momento angolare, essi sono spinti verso rotazioni non sostenibili da un corpo singolo, con una inevitabile perdita di massa per forza centrifuga. Se i corpi sono globalmente spinti verso le forme di Jacobi plus allungate, si possono distinguere, a prtire dal momento in cui queste forme sono raggiunte, due tipi di comportamento.

perdita di massa attraverso particelle singole

In certi casi, si separano periodicamente dal corpo principale delle particelle dalle "punte", disperdendosi all'infinito in orbite iperboliche (v. fig. 5.1). Queste particelle sono spesso sostituite da altre vicine, con in genere poco o nessun cambio di forma del corpo.

fissione del corpo

In alcuni casi, i corpi riescono a perdere solo poca massa per mezzo del meccanismo precedente, arrivando ad accumulare una parte dell'energia fornita dalle accelerazioni in una modifica della forma. Questa modifica consiste in una strozzatura che comincia a prodursi nel corpo, allargandosi con tempo, causando infine una fissione dell'aggregato e formando un binario (v. fig. 5.2) con orbita iniziale stabile.

A.5.1 la sequenza di fissione

Se si osserva nel diagramma $(\overline{L}; \overline{\Omega}^2)$ (con $\overline{\Omega}$ velocità di rotazione normalizzata $= \Omega/\sqrt{\pi G \rho}$) l'evoluzione dei corpi che presentano fissione (v. fig. 5.6, 5.7, 5.9, 5.16, 5.19, 5.22), si nota che tutti seguono uno stesso sviluppo che li porta verso le forme di Jacobi più allungate fino al punto in cui si distacca la sequenza teorica "dumbbell"[9] (cfr. fig. 2.4 e 2.5), che segue una trasformazione degli aggregati da una forma ellissoidale allungata verso un binario passando attraverso forme di binari a contatto. È nei dintorni di questa regione, dove si osservano i binari a contatto reali (cf. fig. 1.13), che si produce la fissione nelle nostre simulazioni.

A.5.2 conclusioni

Abbiamo mostrato come è possibile la formazione di binari con un meccanismo non catastrofico ad azione lenta, seguendo forme già previste a livello matematico.

Compariamo inoltre in nostro lavoro con [K.J. Walsh et al., 2008], in cui gli autori, usando un meccanismo simile al nostro, trovano risultati differenti, dovuti alle diverse strategie utilizzate nel formare gli aggregati originali.

Una questione interessante rimane riguardo al perché i corpi presentano comportamenti totalmente differenti a parità di forma esterna, cosa probabilmente dovuta all'organizzazione delle particelle all'interno degli aggregati.

A.6 Conclusioni

Questo lavoro esplora per mezzo di metodi numerici il comportamento di aggregati gravitazionali di sfere rigide per migliorare la nostra comprensione sulle possibili origini degli asteroidi binari, e possibilmente mettere in relazione le condizioni iniziali alle diverse classi di binari osservati.

Basandosi su risultati precedenti ottenuti sia da noi che nella letteratura, abbiamo modellato un asteroide come aggregato di sfere rigide.

Lo scenario utilizzato nel cap. 4 (v. § A.4) è rappresentativo di un sistema che ha accumulato una quantità di momento angolare oltre la soglia di perdita di massa per un aggregato senza coesione. Questo sovra-accumulo può essere dovuto alla presenza di una piccola coesione o ottenuto improvvisamente per mezzo di un impatto catastrofico. Noi simuliamo la conseguente frammentazione esplorando un ampio spettro di parametri.

[9] sequenza "a manubrio"

Abbiamo mostrato come la formazione di binari sia un evento ordinario per momenti angolari intermedi tra il limite superiore per i corpi in equilibrio idrostatico classico fino ai più grandi valori per i quali un corpo rigido può conservare la propria regolite.

Grandi secondari / asteroidi doppi vengono prodotti per rottura e/o riaccumulazione del corpo frammentato. Piccoli satelliti possono formarsi in orbita a partire da un aggregato inizialmente a simmetria assiale.

I nostri risultati sono stati comparati con i dati disponibili sugli asteroidi reali per mostrare la somiglianza di momento angolare, rotazione del primario e distanza orbitale tipica, trovando un buon accordo.

Nel capitolo 5 (v. § A.5) abbiamo esplorato la sequenza di equilibrio che raccorda i corpi singoli ai binari. La tecnica è rappresentativa dell'azione di una forza perturbativa che lentamente possa portare un corpo verso una configurazione instabile.

Abbiamo mostrato come una deformazione graduale può guidare un aggregato arbitrario verso una forma bilobata e una fissione, formando un oggetto binario. La forma bilobata osservata ricorda sia i risultati semi-analitici per i corpi fluidi sia i "binari a contatto" osservati tra gli asteroidi.

I nostri approcci sono originali e contribuiscono a far luce su processi scarsamente conosciuti. Studi teorici sull'evoluzione dinamica di binari a partire da oggetti in contatto esistono, ma nessuno ha potuto riprodurre la ricchezza fenomenologica della fissione, la complessità di dettagli e il comportamento altamente caotico della quale possono influire pesantemente sulla formazione (o meno) di un oggetto binario (stabile o no). Altri approcci numerici hanno inoltre mancato di riprodurre la complessità del processo di accelerazione progressiva (*spin-up*), limitandosi ad aspetti particolari che, alla luce dei risultati presentati qui, non rappresentano la varietà delle situazioni possibili.

In particolare, per la prima volta illustriamo con simulazioni numeriche la transizione degli ellissoidi di Jacobi verso l'instabilità, mostrando che l'accumulo in orbita di piccoli frammenti non è l'unico meccanismo per la formazione di satelliti per mezzo di *spin-up*.

Inoltre, il percorso verso la fissione appare seguire un cammino comune procedendo attraverso un insieme limitato di forme, qualunque siano le condizioni iniziali.

Nel presente studio abbiamo infine identificato varie limitazioni dell'approccio numerico con sfere rigide. Altri approcci che impiegano sfere plastiche sono in corso di studio da parte di altri autori, ma progressi importanti potranno essere ottenuti da sviluppi futuri verso particelle di forma irregolare, certamente necessarie per simulazioni più realistiche e somiglianze più strette con i meccanismi identificati nel dominio della fisica dei sistemi granulari.

sommario

Gli asteroidi binari hanno un ruolo d'importanza fondamentale nella determinazione di alcuni parametri asteroidali difficili da misurare da Terra, in particolare la massa. Studiando l'origine dei binari nel quadro generale degli aggregati gravitazionali, essi servono così da laboratori naturali per la fisica dei sistemi granulari a bassa gravità, e forniscono dati preziosi per la modellizzazione globale degli asteroidi.
Esiste una grande varietà nelle caratteristiche dei sistemi binari osservati, e numerose ipotesi sono state formulate per la loro origine (frammentazione catastrofica di un corpo e riaccumulazione sotto forma di binario, influenze mareali da parte dei pianeti, craterizzazione, YORP ...).
In questa tesi esploriamo, per mezzo di simulazioni numeriche a N corpi, la dinamica di un aggregato gravitazionale fuori dal regime di stabilità per un corpo singolo, alla ricerca delle configurazioni più favorevoli alla formazione di un sistema binario.
In una prima parte mostriamo come in uno scenario catastrofico la formazione di sistemi binari sia la norma, ben riproducendo la varietà nella popolazione osservata.
In un secondo studio esploriamo la possibilità di una deformazione progressiva di un aggregato in un sistema binario sotto l'azione di una forza perturbativa lenta che porti eventualmente alla fissione del corpo.
I nostri risultati offrono nuovi punti di vista nello studio della formazione degli asteroidi binari, come mostrato da un confronto con le osservazioni e la letteratura esistente.

parole chiave: *Sistema solare*, *asteroidi*, *formazione di satelliti*, *metodi numerici*, *YORP*, *meccanica celeste*, *mezzi granulari*

Approche numérique à N corps à la formation et évolution des astéroïdes binaires

Malgré des études extensifs observationnels et théoriques de la Terre et de l'espace, la nature profonde des corps mineurs du Système Solaire reste essentielement inconnue.

En particulier les astéroïdes, dans le scénario communément accepté, ont suffert une intense vie collisionnelle, comme résultat des processus ayant modelé notre système planétaire. Il est communément accepté que des processus catastrophiques, comme la fragmentation et la ré-accumulation gravitationnelle, ont profondément changé leur structure en créant des corps fortément fragmentés.

Au moins une fraction d'entre eux aurient une cohésion interne très faible, ce qui comporte des objets tenus ensemble que par gravité. Les propriétés internes de ces « agrégats gravitationnels » restent pourtant assez inconnus, étant que la plupart des contraintes observationnelles est liée aux propriétés superficielles des astéroïdes.

Les asteroïdes binaires sont un cas spécial d'importance fondamental pour comprendre la physique et l'évolution de ces objets, puisque leur observation fournit aisément des données sue leur structure interne.

Premièrement, ils peuvent fournir des estimes fidèles de leur masse totale à partir des caractéristiques de l'orbite mutuelle ; comme les courbes de lumière fournissent une mesure directe de la taille des composants et de leurs orbites, mêmê pour les objets non résolus spatialement, on peut donc obtenir une précieuse information sur leur densité.

Les états de rotation et les formes peuvent aussi être déterminées plus facilement, ce qui permet d'avoir des meilleures estimes sur les contraintes internes et des modèles géomorphologiques plus précis dans des conditions de microgravité.

L'existance mêmê des binaires et leur variété sont directement liée au processus primaires ayant façonné la ceinture d'astéroïdes, et toute détermination de leurs propriétés physiques est donc fondamentale pour une compréhension globale de leur formation et de leur évolution.

B.0.1 Présentation du travail

Beaucoup de mécanismes possibles ont été proposés pour l'origine des astéroïdes binaires : des effets de marée aux impacts craterisants énergiques expulsant de la matière en orbite,

de la ré-accumulation en forme de binaire des fragments après une collision catastrophique à la fission à cause d'une augmentation du moment cinétique ; tout sont actuellement testés avec observations et modèles théoriques.

Le but de ce travail est d'explorer le comportement des agrégats gravitationnels en rotation en proximité de la limite supérieure pour leur moment cinétique avant de perdre masse : des accélérations ultérieures au delà de cette limite fournissent des nouveaux regards sur les processus de fission et la formation des satellites.

Nous modelons les astéroïdes numériquement avec un code à N corps spécialisé comme des « tas de débris parfaits » : agrégats de sphères identiques sujettes à leur gravité mutuelle et à des collisions inélastiques. En cherchant des instabilités conduisant à la formation d'un binaire, nous augmentons leur vitesse de rotation jusqu'au seuil où des instabilités majeures s'activent, et explorons la déformation résultante et la formation de satellites.

Nous essayions aussi d'explorer la question de la stabilité à long terme des systèmes obtenus et traitons des limitations actuelles de notre approche.

Les résultats sont aussi examinés dans un contexte plus vaste, en les comparant avec des autres études théoriques et numériques et avec les observations.

B.1 Les astéroïdes binaires

Dans les 20 derniers ans plus et plus d'astéroïdes binaires ont été découverts, avec des caractéristiques fort différentes pour taille du primaire, rapport de masses, séparations du couple, moment cinétique du système, et les découvertes futures pourrons nous présenter une image plus précise.

Une première classifications peut néanmoins être tracée (voir § 1.3.1), comme par exaple par [P. Pravec, A.W. Harris, 2007] (cf. fig. 1.12).

On peut distinguer un groupe de petits objets (taille $< 10\,\mathrm{km}$) tournant très vite (généralement avec des périodes < 4 heures) et avec des secondaires consistants (rapport de masse $1 \div 10\%$), distribués dans les NEOs et la ceinture principale[10] ; un groupe de petits binaires synchrones de taille comparable avec les précédents mais ayant atteint la synchronicité grâce à l'important rapport de masse (généralement $> 0{,}5$), qui peuvent ou pas être une queue du groupe des petits binaires[11] ; un groupe de grandes astéroïdes localisés dans la ceinture principale avec des petits satellites (rapport de masse $<\sim 1\%$ mais principalement $< 0{,}1\%$). Des systèmes « irréguliers » qui échappent à la classification ont aussi été observés, tout comme des exemples de « binaires à contact » qui, bien que n'étant des vrais binaires, nous témoignent de leur histoire d'ancien couple dont les composants se sont posés délicatement l'un sur l'autre.

[10] il y a bien sûr un effet de sélection favorisant l'observation de systèmes plus proches

[11] pour l'instant, la grande majorité d'entre eux ont été découverts dan la ceinture principale : le court temps à disposition pour les NEOs avant d'être explulsé du Système solaire comparable avec le temps nécessaire pour attaindre la synchronicité peut y jouer un rôle

B.2 La modélisation des astéroïdes

Il est généralement accepté que la majorité des astéroïdes plus grands que ∼100 m sont fortement fracturés voir des véritables « agrégats gravitationnels » de rochers ténus ensemble par auto-gravitation (voir § 1.1.2).

Le premier modèle pour expliquer leur forme reste celui donné par l'hydrostatique classique, qui prédit des séquences de forme stables pour des objets autogravitants en rotation (voir § 2.1).

Il convient d'introduire une normalisation pour le moment cinétique L, pour éliminer toute dépendance de la masse M e de la taille, en définissant $\overline{L}=L/\sqrt{GM^3\overline{a}}$, $\overline{a}$ étant le rayon moyen du corps.

Les plus simples figures sont des ellipsoïdes (on nomme a_1, a_2 et a_3 les trois demi-axes, a_3 étant l'axe de rotation) : on distingue la séquence de spheroïdes[12] de Maclaurin, qui sont stables à faible rotation ($\overline{L} <\sim 0.3$), et la séquence des ellipsoïdes triaxiales de Jacobi, qui sont stables pour des vitesses de rotation plus importantes ($\overline{L}$ entre ~ 0.3 et ∼0.45). Il existe par contre un nombre illimité de séquences mathématiquement possibles, quelques unes entre eux étant visualisées en fig. 2.4.

La distribution des formes des objets réels est toutefois apparemment lointaine de ces séquences (cf. fig. 2.6), ce qui comporte que d'autres modélisations plus élaborées doivent être utilisées, en considérant les forces internes qui peuvent soutenir des formes non strictement hydrostatiques (cf. § 2.3 - 2.4).

B.3 La modélisation numérique avec les *perfect rubble-piles*

Cette thèse s'occupe de la modélisation numérique de la formation d'astéroïdes binaires. Pour le travail, nous avons utilisé le logiciel `pkdgrav` ([D.C. Richardson et al., 2000]), un intégrateur gravitationnel à N corps avec gestion de collisions inélastiques (voir chap. 3).

`pkdgrav` utilise comme unités de masse des particules sphériques rigides (voir § 3.1) sous l'action de leur gravité; ceci permet de modéliser un agrégat gravitationnel comme un ensemble de particules pouvant se déplacer les unes par rapport aux autres avec une (limitée) liberté selon la dynamique imposée par le forces globales (voir fig. 3.3) : on appelle cette configuration un « perfect rubble-pile ».

Des études précédents (voir § 3.10) nous avaient permis de déduire quelques propriétés de ce modèle, comme voir que pour un agrégat il est difficile de contenir un $\overline{L} > 0.4$.

La majorité des agrégats utilisés pour le simulations de cette thèse à été formée avec une masse volumique de $\rho \sim 2\, g/cm^3$ et par des sphères de rayon $R_p = 50\, m$.

[12] ellipsoïdes de rotation avec $a_1 = a_2 > a_3$

B.4 Simulations à moment cinétique élevé

Pour tester la possibilité de formation d'astéroïdes binaires dans un scénario catastrophique, on procède simulant une situation accidentelle où un agrégat autrement stable reste victime d'un évènement (comme un impact) lui conduisant soudainement vers une situation d'instabilité (voir chap. 4).

À cette fin nous avons pris une série de corps ellipsoïdales avec différents rapports axiaux (voir fig. 3.8) en orbite (circulaire) autour du Soleil, et leur avons donné un moment cinétique important dans la forme d'un champs de rotation rigide sur eux mêmê. Nous avons alors suivi ces agrégats durant leur évolution gérée par autogravitation et collisions mutuelles, en cherchant en particulier les cas où des système binaires (voir multiples) se forment.

Différents $\overline{L}$ de 0,5 à 1,0 ont été utilisés pour observer le comportement des agrégats dans des conditions différents et comparer les systèmes résultants. On peut observer quatre comportements type, selon la configuration initiale et le moment cinétique possédé. Des schémas sont présentés en fig. 4.3, 4.4, 4.5, 4.10.

formes allongées avec au plus une petite perte de masse

Ces formes sont possibles lorsque $\overline{L}$ ne dépasse pas ∼0,7.

primaires entourés par une nouage de petits fragménts

Ces systèmes son la norme pour les configurations initialement axisymétriques ($a_1 = a_2$), qui rapidement tournent vers des formes allongées en perdant de la masse isotropiquement. Cette-ci reste principalement en orbite autour du corps principale dans la forme de nombreuses particules formant un nouage.

Dans le temps de quelques jours, des petits satellites peuvent se former (avec masse quelques pourcents du primaire) par accumulation en orbite des fragments, tandis que une partie des nouages est dispersée par les effets de perturbation mutuelles des particules. Ce processus est pourtant lente, et les nouage peuvent ne pas se disperser dans le temps que nous à été permis pour suivre les simulations.

Des exemples sont présentés en fig. 4.6 et 4.12.

binaires avec composants de masse similaire

Une fraction importante des systèmes avec $\overline{L}$ entre 0,6 et 0,8 évoluent rapidement vers la formation de binaires avec les composants de masse comparable (voir fig. 4.8 et 4.14).

Il s'agit d'un comportement où l'agrégat initial est vaincu par la force centrifuge et conduit vers des formes fortement allongées jusqu'à se séparer en deux (voir plus) parties, qui restent, au moins au début, en orbite mutuelle.

Vu l'origine de ces systèmes binaires, l'orbite initiale présente un distance au péricentre très courte, de l'ordre de un ÷ trois diamètres du primaire, et a la tendance à évoluer très rapidement de manière imprévisible.

Pour les systèmes à haut moment cinétique, la formation de plusieurs corps de masses comparables peut générer des situations chaotiques avec des interactions multiples.

systèmes dispersés

Au delà de $\overline{L}$ ∼0,8 le comportement des systèmes est dominé par la dispersion de la majorité de la masse initiale, qui se ré-accumule en plusieurs corps dans orbites indépendantes autour du Soleil, avec possiblement des systèmes binaires (voir fig. 4.9).

B.4.1 évolution à longue terme des systèmes

Parmi les buts initiales du travail de thèse on se proposait d'étudier l'évolution dans le temps des systèmes obtenus. Toutefois, une évolution pour plus que quelques mois (en temps simulé) est pour l'instant faussée par des problèmes numériques du code (voir § 4.6).

B.4.2 conclusions

Nous avons montré comme la formation de systèmes binaires est une conséquence normale pour des cas de destruction catastrophique des corps, pouvant former un ensemble varié de systèmes.

Nous pouvons comparer nos systèmes avec les populations connues de binaires, en voyant comme pour touts les principaux paramètres on peut bien représenter les binaires réels (voir § 4.8 et fig. 4.28).

B.5 Simulations à accélération progressive

Une question se pose quant à la possibilité de faire évoluer un agrégat vers la formation d'un binaire de manière progressive et sans sauts.

Ce type d'évolution peut s'appliquer à différents situations, comme des rencontres répétés d'un NEA avec les planètes internes, des petits impacts, où par effet YORP (voir § 1.3.3).

Pour tester cette possibilité, nous avons pris un ensemble d'agrégats stables sous importante rotation issus de simulations précédents, et les avons soumis à des cycles de petites accélérations autour de leur axe suivies chacune d'un période d'évolution libre pour se tasser dans leur nouvelle condition. Ceci conduit les agrégats dans une évolution des forme de manière quasi-statique, en simulant une action perturbatrice externe agissant sur des temps caractéristiques plus longs que le temps de l'auto-gravité.

Au fur et à mesure que les agrégats accumules du moment cinétique, ils sont poussés vers des rotations qu'ils ne peuvent pas soutenir comme corps unitaire, avec une inévitable perte de masse par force centrifuge. Si tous les corps sont globalement poussés vers les formes de Jacobi plus allongées, on peut distinguer, à partir du moment où ces formes sont atteintes, deux sortes de comportement.

perte de masse par particules individuelles

Dans certaines cas, des particules se détachent périodiquement des « pointes » des corps se dispersant vers l'infini en orbites hyperboliques (voir fig. 5.1). Ces particules sont souvent substituées par des autres particules voisines, avec généralement petit ou nul changement de forme du corps.

fission du corps

Dans un nombre de cas, les corps sont capables de ne perdre que une quantité limité de masse avec le mécanisme précédent, arrivant à accumuler une partie de l'énergie fournie par les accélérations dans une modification de leur forme. Cette modification prend la forme d'un étranglement qui commence à se produire dans le corps, s'élargissant avec le temps et qui enfin produit une fission de l'agrégat et la formation d'un binaire (voir fig. 5.2) avec une orbite initiale stable.

B.5.1 la séquence de fission

Si on observe dans le diagramme $(\overline{L}; \overline{\Omega}^2)$ ($\overline{\Omega}$ étant la vitesse de rotation normalisé $= \Omega/\sqrt{\pi G \rho}$) l'évolution des corps qui présentent une fission (voir fig. 5.6, 5.7, 5.9, 5.16, 5.19, 5.22), on s'aperçoit que tous suivent un mêmê développement qui les porte vers les formes de Jacobi les plus allongées jusqu'au point d'où il s'écarte la séquence théorique « dumbbell »[13] (cf. fig. 2.4 et 2.5), laquelle suit une transformation des agrégats d'une forme ellipsoïdale allongée vers un binaire en passant par des formes de binaires à contact. Dans les alentours de cette région, où les binaires à contact réels sont observées (cf. fig. 1.13), la fission se produit dans nos simulations.

B.5.2 conclusions

Nous avons montré comment la formation de binaires est possible avec un mécanisme non catastrophique agissant lentement, en suivant les forme déjà prévues mathématiquement.

On compare notre travail avec [K.J. Walsh et al., 2008], où les auteurs, en utilisant un mécanisme semblable au notre, trouvent des résultats différents, dus aux différents stratégies utilisées pour former les agrégats originaux.

Une question intéressant reste sur pourquoi les corps présentent des comportements totalement différents à parité de forme extérieure, ce qui est probablement dû à l'organisation des particules dans les agrégats.

B.6 Conclusions

Ce travail explore par le moyen de méthodes numériques le comportement d'agrégats gravitationnels de sphères rigides pour améliorer notre compréhension sur les possibles origines des astéroïdes binaires, et possiblement connecter des conditions initiales aux différents classes de binaires observés.

En se basant sur des précédents résultats obtenus par nous et dans la littérature, nous avons modelé un astéroïde comme un agrégat de spheres rigides.

Le scénario utilisé dans le chapitre 4 (voir § B.4) est représentatif d'un système ayant accumulé une quantité de moment cinétique au delà du seuil de perte de masse pour un agégat sans cohésion. Cette suraccumulation peut être due à la présence d'une petite cohésion où

[13] séquence « à haltère »

soudainement par le moyen d'un impact important. Nous simulons la fragmentation qui suit en explorant un ample spectre de paramètres.

Nous avons montré comme la formation de binaires est un évènement ordinaire pour des moyens moments cinétiques allant de la limite supérieure pour des corps en équilibre hydrostatique classique jusqu'au plus grand valeurs pour lequelles un corps rigid peut conserver son régolithe.

On produit des grandes secondaires / astéroïdes doubles par cassement et/ou ré-accumulation du corps brisé. Des petits satellites peuvent se former en orbite à partir d'un agrégat initialement axisymétrique.

Nos résultats ont été comparés avec les données disponible sur les astéroïdes réels pour montrer la similarité en moment cinétique, rotation du primaire et distance orbitale typique, en trouvant un bon accord.

Dans le chapitre 5 (voir § B.5) nous avons exploré la séquence d'équilibre raccordant les corps simples aux binaires. La technique est représentative de l'action d'une force perturbante pouvant lentement porter un corps vers une configuration instable.

Nous avons montré comme une déformation graduelle peut guider un agrégat arbitraire vers une forme bilobée et une fission, en formant un objet binaire. La forme bilobée observée rappelle à la fois les résultats demi-analytiques pour les corps fluides et les « binaires à contact » observés parmi les astéroïdes.

Nos approches sont originales et contribuent à éclaircir des processus mal connus. Des études théoriques existent sur l'évolution dynamique de binaires à partir d'objets en contacte, mais aucun n'a pu reproduire la richesse phénoménologique de la fission, dont les détails complexes et le comportement fortement chaotique peuvent influer lourdement sur la formation (ou pas) d'un objet binaire (stable ou instable). Autres approches numériques ont aussi manqué de reproduire la complexité du processus d'accélération progressive (*spin-up*), se fixant sur des aspects particuliers qui, à la lumière des résultats présentés ici, ne représentent pas la variété des situations possibles.

En particulier, pour la première fois nous illustrons avec des simulations numériques la transition vers l'instabilité pour les ellipsoïdes de Jacobi, en montrant que l'accumulation en orbite de petits fragments n'est pas le seul mécanisme formant des satellites par *spin-up*.

De plus, le parcours vers la fission parait suivre un chemin commun en procédant à travers un ensemble limitée de formes, quelconque soient les conditions initiales.

Pendant cet étude nous avons aussi identifié plusieurs limitations de l'approche numérique utilisant des sphères rigides. Autres approches employant des sphères molles sont en train d'être examinées par des autres auteurs, mais des progrès importants pourrons s'obtenir par des développements futures vers des particules de forme irrégulière, certainement nécessaires pour des simulations plus réalistes et des comparaisons plus rapprochées avec les mécanismes identifiés dans le domaine de la physique des systèmes granulaires.

résumé

Les astéroïdes binaires ont un rôle d'importance fondamentale dans la détermination de paramètres astéroïdales difficilement mesurables de la Terre, en particulier la masse. En étudiant l'origine des binaires dans le cadre des agrégats gravitationnels, ils servent ainsi comme laboratoires naturels pour la physique des systèmes granulaires à basse gravité, et ils nous donnent des éléments précieux pour la modélisation globale des astéroïdes.
Vue la grande diversité existante de caractéristiques des systèmes binaires observés, nombreuses hypothèses ont été postulées pour leur origine (fragmentation catastrophique d'un corps et ré-accumulation sous forme binaire, influences de marée par les planètes, cratérisation, YORP ...).
Dans cette thèse nous explorons, grâce à des simulations numériques à N corps, la dynamique d'un agrégat gravitationnel en dehors du régime de stabilité pour un corps simple, en cherchant les configurations les plus favorables à la formation d'un système binaire.
Dans une première partie, nous montrons que dans un scénario catastrophique la formation de systèmes binaires est normale, ces-ci bien reproduisant la variété présente dans la population observée.
En suite, nous explorons la possibilité d'une déformation progressive d'un agrégat vers un système binaire sous l'action d'une force perturbante agissant lentement jusqu'à la fission éventuelle du corps.
Nos résultats proposent des nouveaux regards dans l'étude de la formation des astéroïdes binaires, comme montré par une comparaison avec les observations et la littérature existante.

mots-clés : *Système solaire*, *astéroïdes*, *formation de satellites*, *méthodes numériques*, *YORP*, *mécanique céleste*, *milieux granulaires*

abstract

Binary asteroids play a role of primary importance in determining some physical parameters difficult to measure from Earth, such as the mass. By studying the origin of binaries in the general frame of gravitational aggregates, we can use them as natural laboratories for granular system physics in microgravity conditions, thus obtaining valuable information for modeling asteroids in general.
A large variety exists as for the range of parameters of the observed binary systems, and many possible origins have been suggested for them (catastrophic shattering of a parent object and re-accumulation as multiple bodies, planetary tidal perturbations, cratering, YORP ...).
In this work we explore by numerical N-body simulations the dynamics of gravitational aggregates outside the limits of stability for a single body, looking for the most favorable configurations leading to binary systems formation.
First we show how common the formation of binary systems in a catastrophic scenario is, well reproducing the variety in the observed population.
As a second step we explore the possibility of a gradual shape deformation of an aggregate towards a binary system by the action of a slow perturbing force leading to a possible fission of the body.
Our results provide new insights into the formation of asteroid binaries, as shown by a comparison to observations and existing literature.

keywords: *Solar System*, *asteroids*, *satellite formation*, *numerical methods*, *YORP*, *celestial mechanics*, *granular media*

Bibliography

[ASTEROIDS II] R.P. Binzel, T. Gehrels, M.S. Matthews (edited by), *Asteroids II*, University of Arizona Press, 1989.

[ASTEROIDS III] W. Bottke, A. Cellino, P. Paolicchi, R.P. Binzel (edited by), *Asteroids III*, University of Arizona Press, 2002.

[Ell.fig.equil.] S. Chandrasekhar, *Ellipsoidal figures of equilibrium*, New Haven and London, Yale University Press, 1969.

[Phys.Sol.Sys.] B. Bertotti, P. Farinella, D. Vokrouhlický, *Physics of the solar system*, Kluwer Academic Publishers, 2003.

[Sol.Syst.Dyn.] C.D. Murray, S.F. Dermott, *Solar System Dynamics*, Cambridge University Press, 1999.

[C. André, 1901] C. André, *Sur le système formé par la planète double (433) Eros*, Astronomische Nachrichten 155 (1901), 27-30.

[J.E. Barnes, P. Hut, 1986] J.E. Barnes, P. Hut, *A hierarchical O(N Log N) force calculation algorithm*, Nature 324(4) (1986), 446-449.

[G. Beekman, 2006] G. Beekman, *I.O. Yarkovsky and the discovery of his effect*, Journal for the History of Astronomy 37-1 (2006), 71-86.

[M. Belton, R. Carlson, 1994] M. Benton, R. Carlson, *1993 (243) 1*, IAU Circular 5948 (1994) http://www.cbat.eps.harvard.edu/iauc/05900/05948.html

[W.F. Bottke, H.J. Melosh, 1996] W.F. Bottke, H.J. Melosh, *The formation of asteroid satellites and doublet craters by planetary tidal forces*, Nature 381 (1996), 51-53.

[C.R. Chapman et al., 1996] , C.R. Chapman, E.V. Ryan, W.J. Merline, G. Neukum, R. Wagner, P.C. Thomas, J. Veverka, R.J. Sullivan, *Cratering on Ida*, Icarus 120 (1996), 77-86.

[C. Comito, 2008] C. Comito, *Forme di equilibrio di aggregati gravitazionali: modelli numerici con applicazione agli asteroidi*, Master Thesis, Pisa, 2008 http://etd.adm.unipi.it/theses/available/etd-08272008-034805/

[J.F. Consigli et al., 2006] J.-F. Consigli, P. Tanga, C. Comito, D. Hestroffer, D.C. Richardson, *Formes d'astéroïdes et formation de satellites: le rôle de la réaccumulation gravitationelle*, Comptes Rendus Physique 8 (2007), 469-480.

[D.R. Davis et al., 1996] D.R. Davis, C.R. Chapman, D.D. Durda, P. Farinella, F. Marzari, *The formation and collisional/dynamical evolution of the Ida/Dactyl system as part of the Koronis family*, Icarus 120 (1996), 220-230.

[P. Descamps, F. Marchis, 2008] P. Descamps, F. Marchis, *Angular momentum of binary asteroids: Implications for their possible origin*, Icarus 193 (2008), 74-84.

[J.W. Dohnanyi, 1969] J.W. Dohnanyi, *Collisional models of asteroids and their debris*, Journal of Geophysical Research 74 (1969), 2531-2554

[L.T. Elkins-Tanton, 2006] L.T. Elkins-Tanton, *Jupiter and Saturn*, Chelsea House, New York, 2006

[P. Goldreich, R. Sari, 2007] P. Goldreich, R. Sari, *Tidal Evolution of Rubble Piles*, arXiv:0712.0446v1[astro-ph], 2007.

[R. Gomes et al. (2005)] R. Gomes, H.F. Levison, K. Tsiganis, A. Morbidelli, *Origin of the cataclysmic Late Heavy Bombardment period of the terrestrial planets*, Nature 435 (2005), 466-469.

[D. Gregory, 1702] D. Gregory, *Astronomiae physicae et geometricae elementa*, Edinburgh, 1702.

[I. Hacisu, Y. Eriguchi, 1984] I. Hachisu, Y. Eriguchi, *Fission sequence and equilibrium models of rigidity rotating polytropes*, Astrophysics and Space Science 99 (1984), 71-74.

[I. Hacisu, 1986 I] I. Hachisu, *A versatile method for obtaining structures of rapidly rotating stars*, The Astrophysical Journal Supplement Series 61 (1986), 479-507.

[I. Hacisu, 1986 II] I. Hachisu, *A versatile method for obtaining structures of rapidly rotating stars. II. Three dimensional self-consistent field method*, The Astrophysical Journal Supplement Series 62 (1986), 461-499.

[D. Hestroffer et al., 2002] D. Hestroffer, P. Descamps, M. Kaasalainen, P. Tanga, J. Torppa, J. Berthier, A. Cellino, M. Lattanzi, M. Di Martino, J. Piironen, V. Zappalà, *Comparison of topographic models for asteroids to the HST/FGS data*, Proceedings of Asteroids, Comets, Meteors (ACM 2002), 29 July - 2 August 2002, Technical University Berlin, Berlin, Germany (ESA-SP-500, November 2002).

[D. Hestroffer, P. Tanga, 2005] D. Hestroffer, P. Tanga, *Figures of equilibrium among binary asteroids*, Bulletin of the American Astronomical Society 37 (2005), 1562-.

[D. Hestroffer, P. Tanga, 2006] D. Hestroffer, P. Tanga, *Asteroids from Observations to Models*, Lect. Notes Phys. 682 (2006), 89-116

[K.A. Holsapple, 2001] K.A. Holsapple, *Equilibrium Configurations of Solid Cohesionless Bodies*, Icarus 154 (2001), 432-448.

[K.A. Holsapple, 2004] K.A. Holsapple, *Equilibrium figures of spinning bodies with self-gravity*, Icarus 172 (2004), 272-303.

[K.A. Holsapple, 2010] K.A. Holsapple, *On YORP-induced spin deformation of asteroids*, Icarus 205 (2010), 430-442.

[S.A. Jacobson, D.J. Scheeres, 2011] S.A. Jacobson, D.J. Sheeres, *Dynamics of rotationally fissioned asteroids: Source of observed small asteroid systems*, Icarus 214 (2011), 161-178.

[H.M. Jaeger, S.R. Nagel, 1992] H.M. Jaeger, S.R. Nagel, *Physics of Granular States*, Science 255 (1992), 1524.

[D.G. Korycansky, E. Asphaug, 2003] D.G. Korycansky, E. Asphaug, *Impact evolution of asteroid shapes 1. Random mass redistribution*, Icarus 163 (2003), 374-388.

[D. Lai et al., 1993] D. Lai, F.A. Rasio, S.L. Shapiro, *Ellipsoidal figures of equilibrium: compressible models*, The Astrophysical Journal Supplement Series 88 (1993), 205-252.

[S.C. Lowry et al., 2007] S.C. Lowry, A. Fitzsimmons, P. Pravec, D. Vokrouhlický, H. Boehnhardt, P.A. Taylor, J.-L. Margot, A. Galád, M. Irwin, J. Irwin, P. Kusnirák, *Direct Detection of the Asteroidal YORP Effect*, Science 316 (2007), 272-274.

[G.W. Lugmair, A. Shukolyukov, 2001] G.W. Lugmair, A. Shukolyukov, *Early Solar System events and timescales*, Meteorics & Planet. Sci. 36 (2001), 1017-1026.

[P. Magnusson, C. Neese, 1996] P. Magnusson, C. Neese (Eds.), *Asteroid Spin Vectors. EAR-A-5-DDR-ASTEROID-SPIN-VECTORS-V4.2. NASA Planetary Data System*, 1996.

[P. Michel et al., 2001] P. Michel, W. Benz, P. Tanga, D.C. Richardson, *Collisions and Gravitational Reaccumulation: Forming Asteroid Families and Satellites*, Science 294 (2001), 1696-1700.

[A. Milani, Z. Knežević, 1994] A. Milani, Z. Knežević, *Asteroids proper elements and the dynamical structure of the asteroid belt*, Icarus 107 (1994), 219-254.

[A. Morbidelli, 2005] A. Morbidelli, *Origin and dynamical evolution of comets and their reservoirs*, arXiv:astro-ph/0512256v1

[I. Newton, 1687] I. Newton, *Philosophiæ naturalis principia mathematica*, London, 1687.

[S.J. Paddack, 1969] S. J. Paddack, *Rotational bursting of small celestial bodies: Effects of radiation pressure*, Journal of Geophysical Research 74 (1969), 4379-4381.

[P. Pravec et al., 2000] P. Pravec, L. Šarounová, D.L. Rabinowitz, M.D. Hicks, M. Wolf, Y.N. Krugly, F.P. Velichko, V.G. Shevchenko, V.G. Chiorny, N.M. Gaftonyuk, G. Genevier, *Two-period Lightcurves of 1996 FG_3, 1998 PG, and (5407) 1992 AX: One Probable and Two Possible Binary Asteroids*, Icarus 146 (2000), 190-203.

[P. Pravec, A.W. Harris, 2000] P. Pravec, A.W. Harris, *Fast and slow rotation of asteroids*, Icarus 148 (2000), 12-20.

[P. Pravec et al., 2006] P. Pravec, and 56 others, *Photometric survey of binary near-Earth asteroids*, Icarus 181 (2006), 63-93.

[P. Pravec, A.W. Harris, 2007] P. Pravec, A.W. Harris, *Binary asteroid population 1. Angular momentum content*, Icarus 190 (2007), 250-259.

[P. Pravec et al., 2010] P. Pravec and 25 others, *Formation of asteroid pairs by rotational fission*, Nature 466 (2010), 1085-1088.

[S.D. Price, M.P. Egan, 2001] S.D. Price, M.P. Egan, *Spaced based infrared detection and characterization of near earth objects*, Advances in Space Research 28 (2001), 1117-1127.

[T.R. Quinn et al., 2000] T.R. Quinn, N. Kats, J. Stadel, G. Lake, *Time stepping N-body simulations*, arXiv:astro-ph/9710043v1

[D.C. Richardson, 1993] D.C. Richardson, *A new tree code method for simulation of planetesimal dynamics*, Monthly Notices of the Royal Astronomical Society 261 (1993), 396-414.

[D.C. Richardson, 1994] D.C. Richardson, *Tree code simulations of planetary rings*, Monthly Notices of the Royal Astronomical Society 269 (1994), 493-511.

[D.C. Richardson et al., 2000] D.C. Richardson, T. Quinn, J. Stadel, G. Lake, *Direct large-scale N-body simulations of planetesimal Dinamics*, Icarus 143 (2000), 45-59.

[D.C. Richardson et al., 2005] D.C. Richardson, P. Elankumaran, R.E. Sanderson, *Numerical experiments with rubble piles: equilibrium shapes and spins*, Icarus 173 (2005), 349-361.

[B. Rozitis et al., 2009] B. Rozitis, N. Murdoch, S.F. Green, T.-L. de Lophem, P. Michel, *Astex microgravity experiment: simulated asteroid regoliths*, 60th International Astronautical Congress, 12-16 October 2009, Daejeon, South Korea http://oro.open.ac.uk/24832/1/2009_Rozitis_et_al_IAC.pdf

[P. Sánchez, D.J. Scheeres, 2011] P. Sánchez, D.J. Scheeres, *Simulating Asteroid Rubble Piles with a Self-gravitating Soft-sphere Distinct Element Method Model*, The Astrophysical Journal 727 (2011) 120.

[V.S. Safronov, 1969] В.С. Сафронов, *Эволюция допланетного облака и образование Земли и планет*, Наука, 1969
[V.S. Safronov, *Evolution of the protoplanetary cloud and formation of the Earth and the planets*, Nauka, 1969, English translation by Israel Program for Scientific Translations, Jerusalem, 1972].

[D.J. Scheeres et al., 2006] D.J. Sheeres and 15 others, *Dynamical Configuration of Binary Near-Earth Asteroid (66391) 1999 KW4*, Science 314 (2006), 1280-1283.

[D.J. Scheeres, 2007] D.J. Scheeres, *Rotational fission of contact binary asteroids*, Icarus 189, 370-385.

[D.J. Scheeres, 2009 I] D.J. Scheeres, *Minimum energy asteroid reconfigurations and catastrophic disruptions*, Planetary Space Science 57 (2009), 154-164.

[D.J. Scheeres, 2009 II] D.J. Sheeres, *Stability of the planar full 2-body problem*, Celestial Mechanics and Dynamical Astronomy 104 (2009), 103-128.

[T.S. Statler, 2009] T. S. Statler, *Extreme sensitivity of the YORP effect to small-scale topography*, Icarus 202 (2009), 502-513.

[P. Tanga et al., 2002] P. Tanga, D. Hestroffer, A. Cellino, M. Lattanzi, M. Di Martino, V. Zappalà, *Shape and size measurements of asteroids by the HST fine guidance sensors*, Proceedings of Asteroids, Comets, Meteors (ACM 2002), 29 July - 2 August 2002, Technical University Berlin, Berlin, Germany (ESA-SP-500, November 2002).

[P. Tanga et al., 2004] P. Tanga, S.J. Weidenschilling, P. Michel, D.C. Richardson, *Gravitational instability and clustering in a disk of planetesimals*, Astronomy & Astrophysics 427 (2004), 1105-1115

[P. Tanga et al., 2009 I] P. Tanga, D. Hestroffer, M. Delbò, D. Richardson, *Asteroid rotation and shape: from disruption to gravitational reaccumulation by numerical simulations*, Planetary and Space Science 57(2) (2009), 193-200.

[P. Tanga et al., 2009 II] P. Tanga, C. Comito, P. Paolicchi, D. Hestroffer, A. Cellino, A. Dell'Oro, D.C. Richardson, *Rubble-pile reshaping reproduces overall asteroid shapes*, the Astrophysical Journal 706 (2009), L197-L202.

[K. Tsiganis et al., 2005] K. Tsiganis, R. Gomes, A. Morbidelli, H.F. Levison *Origin of the orbital architecture of the giant planets of the Solar System*, Nature 435 (2005), 459-461.

[K.J. Walsh, D.C. Richardson, 2007] K.J. Walsh, D.C. Richardson, *A steady-state model of NEA binaries formed by tidal disruption of gravitational aggregates*, Icarus 193 (2008), 553-566.

[K.J. Walsh et al., 2008] K.J. Walsh, D.C. Richardson, P. Michel, *Rotational breakup as the origin of small binary asteroids*, Nature 454 (2008), 188.

[J. Yarkovsky, 1888] J. Yarkovski, *Hypothèse Cynétique de la Gravitation Universelle en connexion avec la formation des élements chimiques*, Moscow 1888.